X-Ray topography of semiconductor silicon

Neil Loxley

X-Ray Topography of Semiconductor Silicon

Neil Loxley B.Sc.

Physics Department,

Durham University

Thesis submitted to the University of Durham in Candidature for the Degree of Doctor of Philosophy,

September, 1988

Abstract

This thesis describes the examination and characterisation of semiconductor silicon by the various methods of X-Ray Diffraction Topography.

A brief introduction is given to the dynamical theory of X-ray diffraction and its relevance to the formation of contrast in X-ray topographs. The experimental methods used and contrast formation mechanisms are introduced.

The design and construction of an inexpensive Automated Bragg Angle Controller (ABAC) is described, based around a microcomputer and using many of the existing features of the Lang camera. This enables Lang topographs of the whole of distorted crystals to be taken.

Using the ABAC, the contrast of defects in Lang topographs of cylindrically bent silicon wafers is explored. A comparison is made between this data and images in Hirst topographs and contrast differences between the techniques are attributed to the presence of an inhomogeneous bending moment. The change in contrast in section and Lang topographs upon homogeneous bending for asymmetric reflections is also investigated and mechanisms for the contrast changes are suggested.

A bipolar device wafer is examined with double crystal topography using synchrotron radiation and a highly asymmetric reflection with a glancing angle of incidence. By exploiting the wavelength tuneability of the synchrotron radiation, the depth penetration of the X-rays is varied and the optimum experimental conditions for observing both defects and devices determined. Using this technique it is

possible to image both devices and process related defects to a high resolution and contrast.

The Lang, section and glancing angle double crystal topography techniques are compared for the examination of a CMOS device wafer. The relative strengths and weaknesses of each technique are highlighted and many defects are imaged and characterised.

Finally, results showing the appearance of fringes in the double crystal topographs for low angles of incidence are presented. These are attributed to the presence of a long range strain, and the dependence of the fringes upon curvature is explored for moderate bending conditions ($R \sim 35m$).

Preface

This thesis describes work undertaken in the Solid State Group of the Physics Department, University of Durham and the S.E.R.C. Synchrotron Radiation Source (SRS), Daresbury Laboratories during the period October 1984 to September 1987. All of the work contained herein is the author's own and is previously unpublished with the exception of material contained in the list of publications. All collaborative work and material from other sources is duly referenced where appropriate.

List of Publications

N. Loxley and B.K. Tanner, "The Contrast of Dislocations in X-ray Topographs of Homogeneously Bent Silicon Crystals", Mat. Res. Soc. Symp. Proc. 82, 209

N. Loxley and B.K. Tanner, "X-Ray Double Crystal Topography of Processed Silicon Wafers", ibid., 215

Acknowledgements

I am thankful for financial support from the Science and Engineering Research Council and GEC Hirst Research Centre through a CASE award. Professor A.W. Wolfendale is thanked for the use of the facilities in the Physics department at the University of Durham and the S.E.R.C. for the use of facilities at the Synchrotron Radiation Source (SRS) at Daresbury Laboratories, Warrington.

During the course of my time at Durham, many people have offered invaluable help, advice and support. In particular, the following are gratefully acknowledged:

My supervisor, Dr Brian Tanner, for his continued enthusiasm and guidance, and the members of Alvey consortium 030 for many useful discussions. Dr Marian Suriowich and Dr Steven Barnett for invaluable practical help and discussions, Chu-Xi for help and company during soul-destroying visits to the SRS, Dr Martin Hill for help with the design of the electronics in the ABAC interface box and Dr Stephan Green for providing the simulations included in chapter 4.

Dennis Jobling and Paul Armstrong of the student workshop for the care and skill with which they built the bending jig.

And finally, Gabrielle, for the many hours spent preparing drawings, helping to print the final version and looking after me during the seemingly neverending period of writing up. Without her unstinting help, patience and love the writing of this thesis would have taken much longer.

For Mom and Dad

Contents

Note on figure captions:
(SRS) after a figure number indicates that the topograph was obtained using synchrotron radiation from the SRS, Daresbury Laboratories.

Chapter One

The Theory of X-ray Diffraction

1.1 The geometrical theory of X-ray diffraction.

In its simplest form, X-ray diffraction can be considered as the specular reflection of X-rays from lattice planes. This condition for diffraction, shown in figure 1.1 leads to the familiar Bragg condition:

$$2d_{hkl}\sin\theta_B = \lambda \qquad (1.1)$$

where θ_B is the Bragg angle, λ is the wavelength of the incident radiation and d_{hkl} is the distance between the reflecting planes. An alternative definition is given by the Laue equation (also shown in figure 1.1):

$$\mathbf{k}_g = \mathbf{k}_o + \mathbf{g} \qquad (1.2)$$

where $\mathbf{k}_o$ and $\mathbf{k}_g$ are vectors parallel to the incident and diffracted beams respectively, both with a magnitude of $1/\lambda$, and $\mathbf{g}$ is the diffraction vector ($\mathbf{g} = h\mathbf{a}^* + k\mathbf{b}^* + l\mathbf{c}^*$, where $\mathbf{a}^*$, $\mathbf{b}^*$ and $\mathbf{c}^*$ are unit reciprocal lattice vectors). h,k and l represent the Miller indices of the set of diffracting planes, multiplied by the order of the diffraction.

The geometrical theory is limited to giving the conditions at which the maxima of diffraction occur, and gives no information on the intensity of the diffracted beam. To calculate the diffracted intensity, either the dynamical theory or the more limited kinematical theory must be used and these are explained in the following sections.

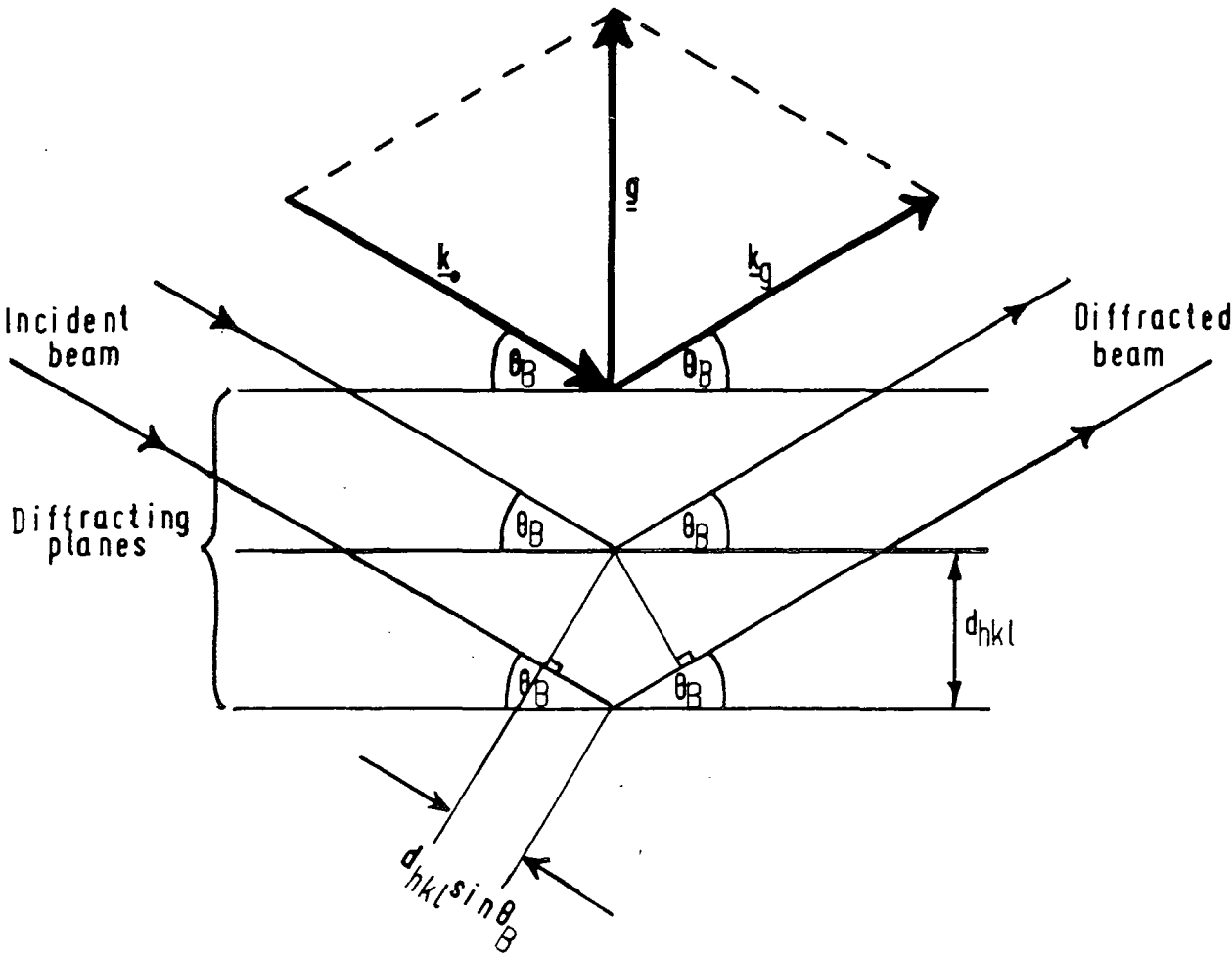

Figure 1.1

The Bragg and Laue conditions

1.2 The scattering of X-rays from a unit cell.

We first assume the dominant scattering mechanism to be elastic Thomson scattering, that is, the scattered wave is coherent with the exciting radiation and has the same wavelength. When a beam of X-rays is incident on an atom, the electric field component of the electromagnetic radiation sets the electrons in the atom into forced vibration with the same frequency as the exciting radiation. These electrons form an oscillating dipole and in turn, as expected from classical electromagnetic theory, emit radiation in all directions that is coherent in phase, polarization, frequency and amplitude with the incident beam.

Summing the contributions from the atoms within the unit cell leads to an expression for the structure factor F_g, which is defined as the ratio of the amplitude of the wave scattered by one unit cell to that scattered by a single free electron somewhere within the unit cell. Generally, for an arbitrary angle of incidence and wavelength this sum is zero due to destructive interference between the scattered wavelets from individual atoms. However, in cases where the Bragg condition is satisfied, constructive interference occurs and a diffracted beam is observed. If the atomic scattering factor f_j is now defined as the ratio of the amplitude of the coherent scattered radiation from the jth atom in the unit cell to that from a single free electron centred at the atomic centre, the expression for the structure factor can be written as:

$$F_g = \sum_j f_j \exp(2\pi i \mathbf{g}.\mathbf{r}_j) \qquad (1.3)$$

where N is the number of atoms in the unit cell and $\mathbf{r}_j$ is the position of the jth atom in the unit cell. The physics of the scattering process (including absorption) can be included phenomenologically in (1.3) by the use of a complex atomic scattering factor such that:

$$f = f_o + \Delta f' + i\Delta f'' \qquad (1.4)$$

where $\Delta f'$ and $\Delta f''$ are dispersion corrections (for non-absorbing crystals $\Delta f'' \equiv 0$). Tables of the atomic scattering factors and the dispersion corrections may be found in [1]. For centrosymmetric crystals the structure factor will be real when the origin is taken as the centre of symmetry. Since the structure factor gives the amplitude of the diffracted wave, the intensity of the diffracted wave will be proportional to $|F_g|^2$.

1.3 The kinematical theory of X-ray diffraction.

The kinematical theory has limited applications in X-ray topography and is therefore not discussed here in detail. Reviews of the theory may be found in [2-5].

The theory is based around the central assumptions that the diffracting units are small (less than 1μm) and that a negligible amount of energy is lost from the incident beam in creating a diffracted beam. These imply that the diffracted beam does not interact with the crystal or with the non-diffracted wave (the "direct" beam), and that all unit cells are subject to the same exciting field, of a magnitude equal to that of the incident wave.

The diffracted intensity is now found by adding the

contributions from all the unit cells within the crystal, giving a diffracted intensity which is proportional to both the square of the structure factor and the volume of the diffracting crystal.

To calculate the diffracted intensity for large perfect crystals, a theory is needed which takes account of all the waves propagating through the crystal. Such a theory is described below.

1.4 The dynamical theory of diffraction.

The derivation of the dynamical theory may be found in many excellent reviews of the subject [2-4], [6-10], and the reader is referred to these for a more thorough explanation. Simply, the problem is to solve Maxwell's equations:

$$\begin{aligned} \text{div } \mathbf{D} &= \rho_f & \text{curl } \mathbf{E} &= -\partial \mathbf{B}/\partial t \\ \text{div } \mathbf{B} &= 0 & \text{curl } \mathbf{H} &= \mathbf{j}_f + \partial \mathbf{D}/\partial t \end{aligned} \qquad (1.5)$$

for a complex, triply periodic electric susceptibility χ, where:

$$\chi = \sum_{\mathbf{h}} \chi_h \exp(-2\pi i \mathbf{h}.\mathbf{r}) \qquad (1.6)$$

and is related to the structure factor by:

$$\chi_h = \frac{-r_e \lambda^2 F_h}{\pi V_c} \qquad (1.7)$$

where r_e is the classical electron radius (= 2.818×10^{-15}m) and V_c is the volume of the unit cell.

The problem is further simplified by only allowing two waves with appreciable amplitude to exist within the

crystal, with wavevectors $\mathbf{k}_o$ and $\mathbf{k}_g$ connected by the Laue equation (1.2).

For a non-trivial solution we arrive at

$$\begin{vmatrix} k^2C\chi_g & k^2(1+\chi_o)-\mathbf{k}_o.\mathbf{k}_o \\ k^2(1+\chi_o)-\mathbf{k}_g.\mathbf{k}_g & k^2C\chi_g \end{vmatrix} = 0 \qquad (1.8)$$

where C is a polarisation factor, equal to unity for a σ polarised incident beam (electric vector // plane of incidence) and equal to $\cos 2\theta_B$ for a π polarised beam (electric vector ⊥ plane of incidence) and k is the magnitude of the wavevector in vacuo of the incident beam. Writing:

$$\alpha_o = (1/_{2k})\{\mathbf{k}_o.\mathbf{k}_o - k^2(1+\chi_o)\} \qquad (1.9a)$$

and

$$\alpha_g = (1/_{2k})\{\mathbf{k}_g.\mathbf{k}_g - k^2(1+\chi_o)\} \qquad (1.9b)$$

we obtain the fundamental equation of the dynamical theory:

$$\alpha_o\alpha_g = 1/_4k^2C^2\chi_g\chi_g \qquad (1.10)$$

It is also useful to define an amplitude ratio:

$$R = D_g/D_o = 2\alpha_o/(C\chi_g k) = C\chi_g k/(2\alpha_g) \qquad (1.11)$$

where D_g and D_o are the amplitudes of the direct and diffracted waves, related to the total wavefield D_{TOT} by:

$$D_{TOT} = D_o\exp 2\pi i(\nu t - \mathbf{k}_o.\mathbf{r}) + D_g\exp 2\pi i(\nu t - \mathbf{k}_g.\mathbf{r}) \qquad (1.12)$$

1.4.1 The dispersion surface.

A useful visualisation of the dynamical theory is the dispersion surface, a section through which is shown in figure 1.2. The surface is formed in the following way. In reciprocal space, two spheres of radius k (the magnitude of the vacuum wavevector) and $k(1+\chi_o/2)$ (the magnitude of the wavevectors corrected by the mean refractive index of the crystal) are drawn about both the origin O and the reciprocal lattice point G (where $OG \equiv \mathbf{g}$). In the kinematical theory the allowed wavevectors, defined by the Laue equation (1.2), would be $\mathbf{k}_o$ and $\mathbf{k}_g$, drawn from the Laue point L, to O and G respectively. In the dynamical theory however, allowed wavevectors are given by (1.9) and (1.10), and their magnitudes hence differ from $k(1+\chi_o/2)$ by α_o and α_g. This implies, if the spheres about O and G are approximated to straight lines in the region of L (valid since $\alpha_o \sim \alpha_g \sim 10^{-5}k$), that the tails of allowed wavevectors must lie on hyperbolae asymptotic to AB and CD. Including the two possible polarisation states gives four branches of the dispersion surface, marked 1σ, 1π, 2σ and 2π.

Each point (tie-point) on the dispersion surface now uniquely defines both a direct and a diffracted beam wavevector in amplitude, phase and direction, the tie-point that is excited by the incident wave being selected by the experimental conditions.

1.4.2 Boundary conditions.

Let us consider a plane, linearly polarised, incident wave incident upon the crystal (this can be extended to an

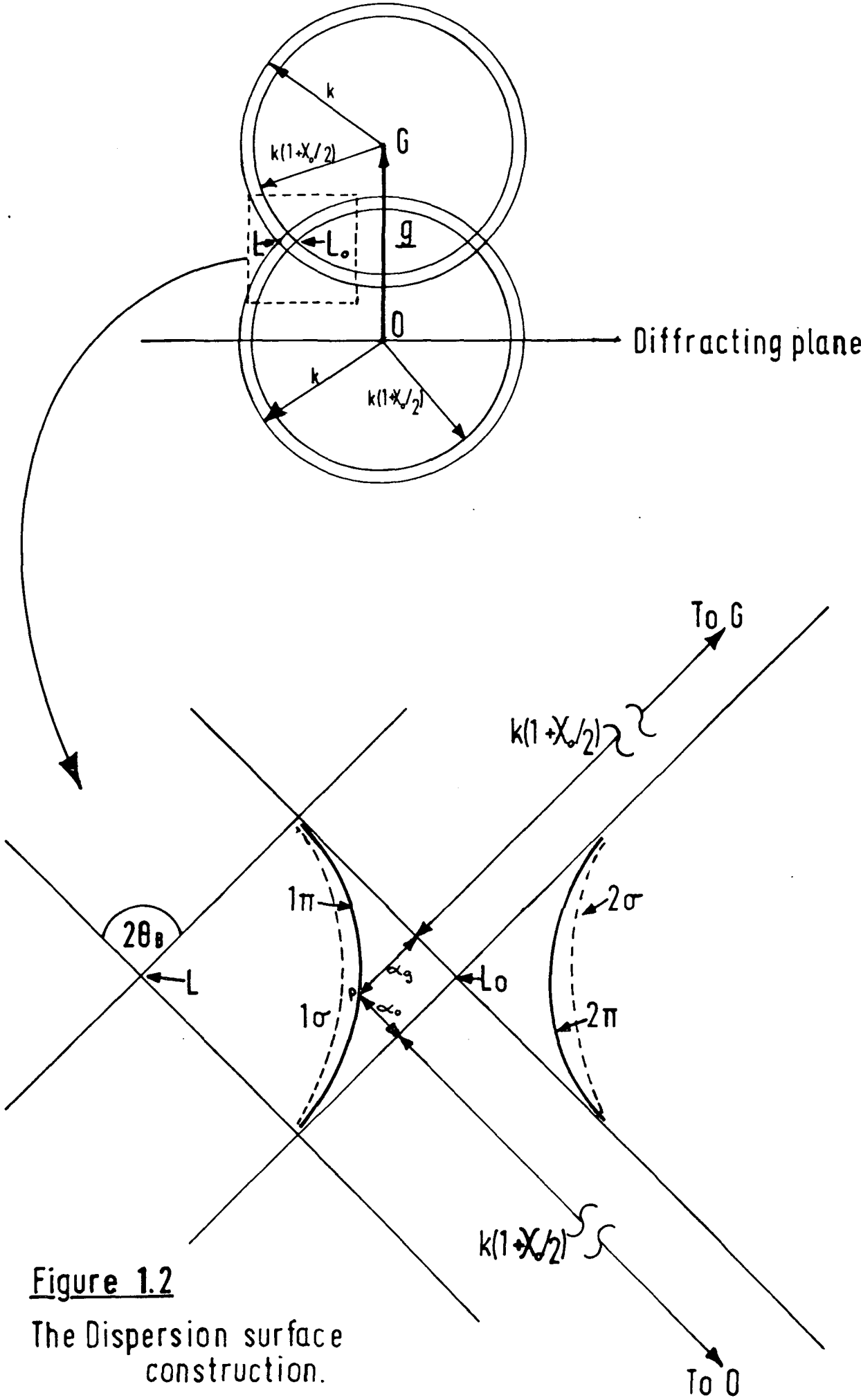

Figure 1.2

The Dispersion surface construction.

unpolarised wave by superposition of the two principle orthogonal polarisation states). Since the refractive index for X-rays is very close to unity, reflection of the incident wave at the surface is negligible and the electric field vectors can be considered, to a good approximation, to be continuous across the crystal surface.

For the wavevectors, we require there to be no change in amplitude or frequency on crossing the surface, which implies that the wavevectors can only differ by a vector along the surface normal, or:

$$\mathbf{k}_{oi}-\mathbf{k} = \mathbf{k}_{gi}-\mathbf{k} = \delta n \qquad (1.13)$$

where $\mathbf{k}$ is the external wavevector and i is equal to 1 or 2 depending on the branch of the dispersion surface.

The tie-points selected by this condition now become clear when it is drawn on the dispersion surface construction. Figures 1.3 (a) and (b) show sections through the dispersion surface in the region of L for the symmetric Laue geometry (beam enters and exits through different surfaces) and the symmetric Bragg geometry (same entrance and exit surface) respectively. The tie-points are given by the intersection of a line parallel with $\mathbf{n}$ drawn from the tail of $\mathbf{k}$, with the dispersion surface. The point(s) at which the surface normal cuts the dispersion surface will now be dependent upon the position of the tail of $\mathbf{k}$, and hence upon $\Delta\theta$, the deviation of the angle the incident beam makes with the diffracting planes from the exact Bragg angle.

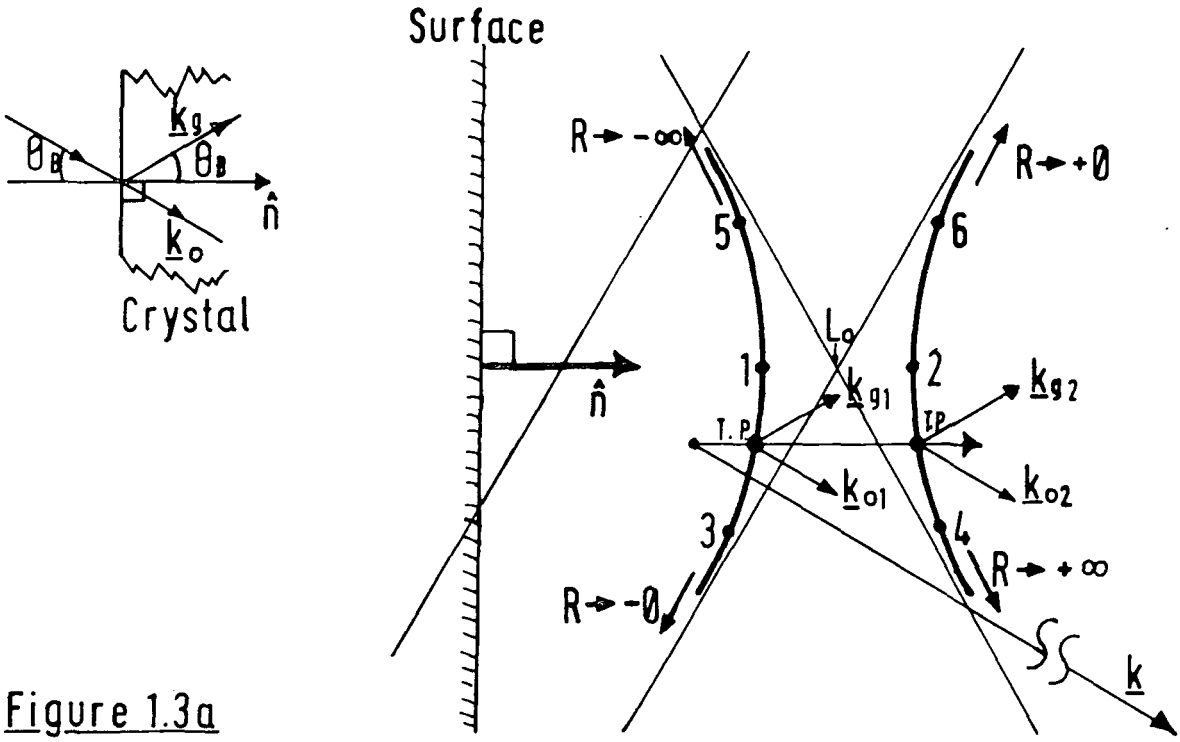

Figure 1.3a

Laue geometry boundary condition.

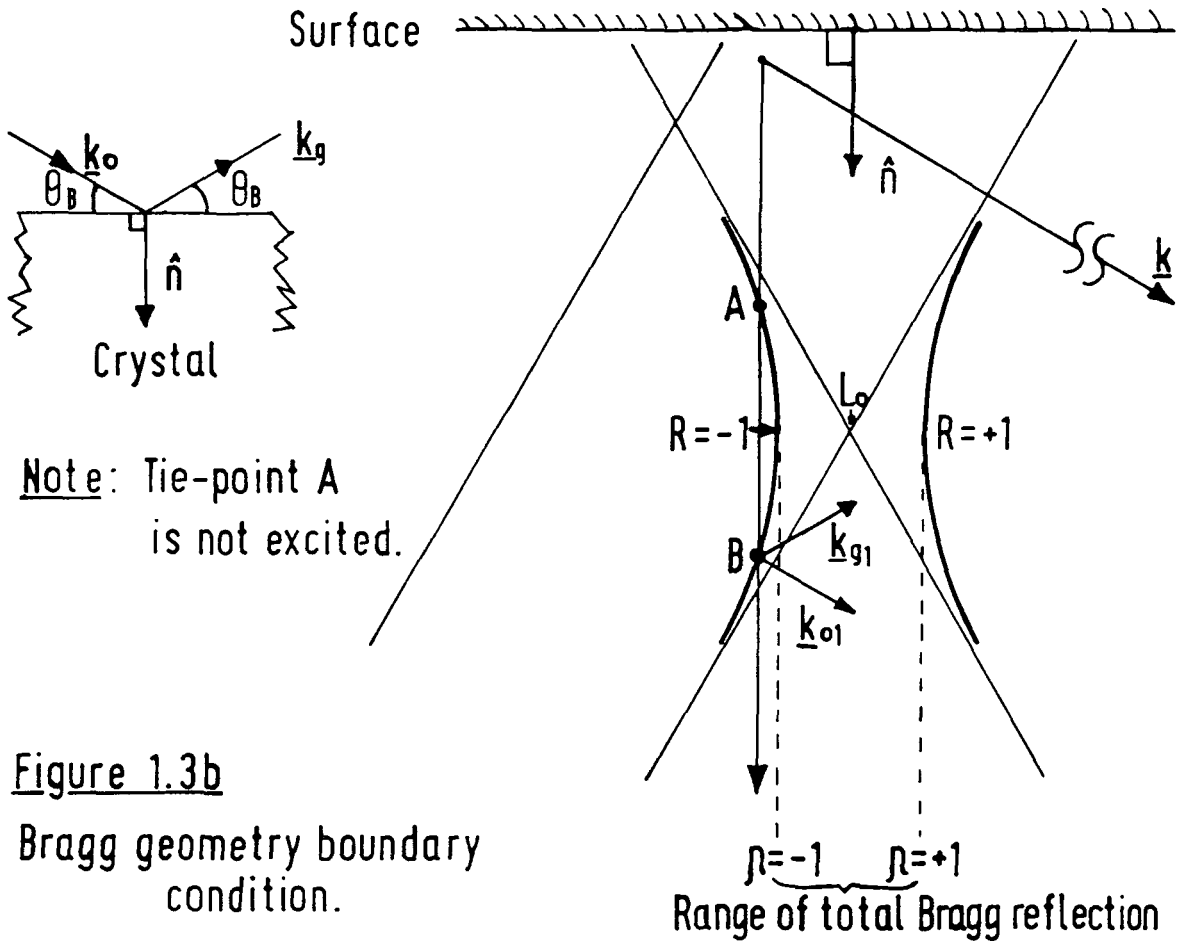

Note: Tie-point A is not excited.

Figure 1.3b

Bragg geometry boundary condition.

The deviation from the Bragg angle can also be written in terms of a deviation parameter which is proportional to $\Delta\theta$ such that:

$$\eta = 2\sin\theta_B k\Delta\theta/\Lambda_o \qquad (1.14)$$

where Λ_o is the diameter of the dispersion surface. For both the Laue and Bragg geometries, the surface normal passes through Lo, the Lorentz point when $\eta = 0$ (and hence when $\Delta\theta = 0$). The tie-points selected for a given η are different for the two cases and therefore they are treated separately below.

1.4.3 The Laue Case.

For $\eta = 0$, tie-points 1 and 2 in figure 1.3(a) are excited at the diameter points of branches 1 and 2 respectively. At this point $|R|=1$ and therefore the direct and diffracted beams have comparable intensities. As $\Delta\theta$ becomes negative, tie-points towards point A are excited. For tie-point 4, R tends to infinity and hence no incident wave can excite it (since an infinitely large D_g would be excited by the presence of any D_o). For tie-point 3, R tends to zero and therefore only a transmitted beam propagates. At the other extreme, where $\Delta\theta$ is large and positive, (tie-points 5 and 6) only the tie-point on branch 2 is active and again, since R tends to zero, only a transmitted beam can exist.

1.4.4 The Bragg case.

In the Bragg case, it is only possible to excite one branch (two branches if both polarisation states are included) of the dispersion surface for a given $\Delta\theta$, and although two tie-points on one branch are selected by an incident beam (see figure 1.3(b)), it can be shown [11] that in an infinitely thick crystal only those tie-points which give wavevectors associated with a flow of energy into the crystal have a physical meaning.

The relative strengths of the direct and diffracted beams for a given tie-point will be the same as for the Laue case, however it should be noted that there is a range of $\Delta\theta$'s ($-1<\eta<+1$) for which no tie-points are excited and hence no wavefields exist inside the crystal. This is the range of total Bragg reflection.

1.4.5 Energy flow.

The flow of energy within the crystal can be described in terms of the Poynting vector:

$$\mathbf{S} = \mathbf{E}\times\mathbf{H} \qquad (1.15)$$

which is the energy flow through a unit area perpendicular to **S** in a unit time. For our purposes however, it is adequate to use $\langle\langle \mathbf{S} \rangle\rangle$, a time averaged Poynting vector, which is also averaged spatially over one unit cell. This leads (after some manipulation) to the important result that the total energy flow corresponding to a tie-point is always normal to the dispersion surface at that point.

The total energy flow consists of three components such that:

$$\mathbf{S}_T = [\mu_o/\varepsilon_o]^{1/2}\langle\langle \mathbf{S} \rangle\rangle = \mathbf{S}_1+\mathbf{S}_2+\mathbf{S}_{12} \qquad (1.16)$$

where $\mathbf{S}_1$ is the effective energy flow associated with branch 1 of the dispersion surface, $\mathbf{S}_2$ the flow associated with branch 2 and $\mathbf{S}_{12}$ a coupling term between the two, which has a sinusoidal dependance on depth into the crystal with a period:

$$P = 1/(\mathbf{k}_{o1}-\mathbf{k}_{o2}) \qquad (1.17)$$

Now, if tie-points on both branches 1 and 2 of the dispersion surface are excited and the energy flows associated with these tie-points spatially overlap, the total energy flow exhibits the phenomenon of "Pendellosung". Here, the energy alternates between the directions $\mathbf{s}_o$ and $\mathbf{s}_g$ (unit vectors // $\mathbf{k}_o$ and $\mathbf{k}_g$ respectively), going to zero in the $\mathbf{s}_g$ direction and very nearly to zero in the $\mathbf{s}_o$ direction with a period P.

For the symmetric Laue case and $\eta = 0$, $1/P$ is equal to Λ_o; the period for this condition is called the extinction distance ξ_g where:

$$\xi_g = \frac{\pi V_c \cos\theta_B}{r_e \lambda C \sqrt{(|F_g F_{\bar{g}}|)}} \qquad (1.18)$$

For symmetric reflections with $\eta = 0$, all the energy flows along the diffracting planes, however for a non-zero η, energy associated with different branches will propagate in different directions and, if the crystal is thick enough,

will become spatially separated within the crystal. At the exit surface of the crystal each wavefield decouples into two beams, one in the direct beam direction and one in the diffracted beam direction. This means that we have the possibility of having eight exit beams produced by one incident unpolarised plane wave, four in the $\mathbf{s}_o$ direction and four in the $\mathbf{s}_g$ direction.

1.4.6 Absorption.

The use of a complex electric susceptibility ensures that absorption processes are included in the dynamical theory in the form of the imaginary parts of the wavevectors ($\mathbf{k}_o$" and $\mathbf{k}_g$"). The intensity of a wave propagating through the crystal being attenuated by a factor $\exp(-4\pi\mathbf{k}_o"\cdot\mathbf{R})$, where **R** represents the position in the crystal.

It is easy to show that $\mathbf{k}_o$" is parallel to the surface normal and hence the fronts of constant absorption are parallel to the crystal surface. It is laborious however, to put this in terms of the direction of energy flow (**j**), and the reader is referred to [6], [8] or [12] for a derivation. For a centrosymmetric crystal with the origin taken as the centre of the unit cell, the absorption is finally given by:

$$\mu(\mathbf{j}) = \frac{\mu_o \quad (1 \pm C\chi_g"/\chi_o")}{\cos\theta_B} \qquad (1.19)$$

close to the diameter point of the dispersion surface ($R \simeq \pm 1$). For R large, or close to 0, only one (direct) beam propagates which suffers essentially normal photoelectric absorption, μ_o.

Batterman and Cole [6] calculated μ for the 220 reflection off a 1mm slab of Ge with CuKα_1 radiation (μ_o = 38) and found:

Branch 1	R = -1	σ polarisation:	$\mu(j)t$ = 1.9
"	R = -1	π polarisation:	$\mu(j)t$ = 12.5
Branch 2	R = +1	σ polarisation:	$\mu(j)t$ = 63.5
"	R = +1	π polarisation:	$\mu(j)t$ = 74.0

where t is the thickness of the sample.

Hence, energy associated with branch 1 of the dispersion surface (and especially σ polarisation) suffers much less than normal photoelectric absorption, or is "anomalously transmitted". The concept of anomalous transmission (also called the Borrmann effect) can be explained by considering the standing waves in the crystal which are set up by an incident beam at the exact Bragg condition (η = 0). Describing the wavefields in the form given in (1.12) and utilising (1.2) and (1.11) we arrive at an expression for the total wavefield for a branch 1 tie-point:

$$|D_1|^2 = |D_{g1}+D_{o1}|^2 \propto 1+R_1^2+2R_1\cos(2\pi\mathbf{g}.\mathbf{r}) \qquad (1.20)$$

For branch 1, R is always negative and thus the electric field is a minimum for $\mathbf{g}.\mathbf{r}$ equal to an integer or zero and has a periodicity of g^{-1} = d normal to the Bragg planes. This means that the electric field is a minimum at the atomic sites and therefore suffers less than normal absorption (since the maxima are well away from the absorbing electrons, localised at the atomic sites). For a branch 2 tie-point, R is positive, giving maxima at the

atomic sites and enhanced absorption.

1.4.7 Primary extinction.

Primary extinction is implicitly incorporated in the dynamical theory, and should be considered as a correction to the kinematical theory. It is however, a useful concept when considering the passage of X-rays through a crystal, affecting the depth to which X-rays will penetrate into a crystal in the Bragg geometry and playing a large part in the formation of images in both Bragg and Laue geometry topography.

Neglecting ordinary photoelectric absorption, in the range of total Bragg reflection ($-1<\eta<+1$), all of the energy of the incident beam is transferred to form the diffracted beam. This means that the direct beam diminishes rapidly in intensity as it penetrates into the crystal, as though it were suffering severe absorption (even though in this case $\mu = 0$). The effect of this, is that for an incident beam close to the Bragg condition, only a small depth of crystal contributes to the diffraction process. A measure of this "skin depth" is given by the extinction distance as defined in (1.18).

Extinction, being a dynamical effect, is critically dependent upon the perfection of the crystal lattice and the lack of extinction is one cause of contrast on X-ray topographs. Extinction contrast is discussed in 2.2.2.

1.4.8 The dynamical theory for "real" X-rays.

The definition of the incident beam of X-rays as an

unbounded, linearly polarised, monochromatic plane wave is clearly inadequate to describe available X-ray sources. These will generally produce randomly polarised X-rays of finite spectral and angular divergence, which means that the theory so far described is not capable of describing the effects seen in the "real" experimental conditions described in chapter 2.

The effect of a randomly polarised wave is easily given by the superposition of the σ and π polarised waves and this approach is also useful when considering the finite divergence. The incident beam can now be thought of as a superposition of plane waves with wavevectors of slightly different magnitudes (spectral divergence) and directions (angular divergence). Such a wavepacket incident on a crystal at, or very near to the exact Bragg condition, will simultaneously excite the whole of the dispersion surface (because of the range of η's present) and will hence cause energy to flow in all directions within a triangle bounded by the direct and diffracted beam directions (the so-called Borrmann fan).

Close to the exact Bragg condition, the dispersion surface has a very large angular amplification effect, which decreases towards unity far from the centre of the dispersion surface. This leads to a high density of wavefields at the edges of the Borrmann fan, giving a greater intensity at the margins under conditions of low absorption. For $\mu t > 3$ however, the wavefields far from the exact Bragg condition are preferentially absorbed leading to lower intensity at the margins than at the centre of the

Borrmann fan.

Asymmetric reflections can be included in the dynamical theory by making use of the direction cosines γ_o and γ_g, the cosines of the angles between s_o and s_g respectively, and the inward facing surface normal. In terms of the dispersion surface, the asymmetry simply changes the direction of the surface normal with respect to the dispersion surface, and hence the tie-points selected by a given set of experimental conditions.

1.5 The Eikonal theory.

For small crystal distortions, the Eikonal theory of Penning and Polder [13], analogous to the optical case of a beam propagating through a medium with a continuously varying refractive index, may be used to describe the propagation of X-rays through the crystal lattice. The theory is explained well, though in a phenomenological way in Penning's thesis [10] and rigorously but in a less accessible form by Kato [14-16].

Essentially, we treat the X-ray wave packet as a well behaved ray, propagating in a crystal lattice which appears undeformed in the space of roughly one Pendellosung length, P. The deformed crystal can now be subdivided into regions which are misorientated with respect to each other or have different lattice parameters. Within each region the dispersion surface and hence the wavefields remain unchanged and upon crossing from one region to another, the beam remains well defined but the wavevector of a wave within the

ray will necessarily undergo a small change dk. This implies that the dispersion surface in each region is shifted with respect to its neighbours.

It is easier however, to consider the dispersion surface as fixed and the reciprocal lattice as the variable. The changing wavevector is now represented by the tie-point for a particular wavefield migrating along the dispersion surface as the beam progresses through the crystal. Since the direction of energy flow for a wavefield is at all times perpendicular to the dispersion surface at its tie-point, this leads to curved wavepaths. For a given deformation it can be shown that the tie-points move in the same direction for both branches of the dispersion surface. This means that rays from opposite branches of the dispersion surface will curve in opposite directions, branch 1 rays in the same sense as the curvature of the lattice planes and branch 2 rays in the opposite sense. Furthermore, the position of the tie-point uniquely defines R (eqn. 1.11) and therefore as it migrates, the relative intensities of the direct and diffracted components of the wavefield will also change.

Penning [10] considers several possible lattice distortions and the effects one may expect but only in terms of the direction of the rays. He does however cite the important result that for a crystal that is bent cylindrically, there is no change in the paths of wavefields for symmetric reflections. This is because the diffracting planes "fan out" with respect to each other under the influence of the curvature, but at the same time remain essentially flat.

Kato [16] using a similar Eikonal theory, shows that the integrated intensity of the diffracted beam increases at the expense of the direct beam intensity with increasing curvature of the diffracting planes. He also shows that Pendellosung fringes (see section 2.3.1) are drastically changed, contracting and finally disappearing as the curvature of the lattice planes is increased. These effects are all borne out by experiments, some of which are presented in chapter 5.

To maintain the concept of a ray, the Eikonal theory can only be used for small continuous distortions, leading to the condition that the diffracting planes must have a radius of curvature greater than a critical value R_c, such that:

$$R_c \approx g\xi_g^2 \qquad (1.21)$$

For curvatures greater than this, the ray cannot adjust to the rapid change in lattice parameter or orientation and the wavefields decouple into the direct and diffracted beam components.

1.6 Generalised Diffraction Theory.

The generalised diffraction theory, developed independently by Takagi [17,18] and Taupin [19] can be used to describe the passage of X-rays through a crystal with any type of distortion. The wavefield inside the crystal is described in the same form as (1.12), with the exception that D_o and D_g are now replaced by slowly varying functions of position $D_o'(\mathbf{r})$ and $D_g'(\mathbf{r})$ such that:

$$D_{TOT}(\mathbf{r}) = \sum_{g} D_g'(\mathbf{r})\exp(-2\pi i \mathbf{k}_g.\mathbf{r})\exp(2\pi i \mathbf{g}.\mathbf{u}(\mathbf{r})) \quad (1.22)$$

where $\mathbf{u}(\mathbf{r})$ is the local deformation vector of the crystal lattice and the sum has only components of o and g for the two beam case.

Introducing this expression for $D_{TOT}(\mathbf{r})$ into Maxwell's equations gives two coupled second order partial differential equations expressed along the directions s_o and s_g:

$$\partial D_o'(\mathbf{r})/\partial s_o = -i\pi k C \chi_g D_g'(\mathbf{r})$$

and (1.23)

$$\partial D_g'(\mathbf{r})/\partial s_g = -i\pi k C \chi_g D_o'(\mathbf{r}) + 2i\pi k \beta_g' D_g'(\mathbf{r})$$

where β_g', which represents the deviation of the incident wave from the exact Bragg condition, is given by:

$$\beta_g' = (k_g^2 - k_o^2)/2k^2 - (1/k)\partial/\partial s_g(\mathbf{g}.\mathbf{u}(\mathbf{r})) \quad (1.24)$$

For $\beta_g' = 0$, equations (1.23), the so-called "Takagi-Taupin" equations can be solved exactly, however, generally it is necessary to integrate them numerically. The most successful method for doing this being the half step derivative method [20].

Whilst the Takagi-Taupin equations are mathematically rigorous, the concept of the dispersion surface and hence details of the physics of the scattering process within the crystal are lost. They do however give the intensities of the direct and diffracted beams leaving the crystal, making them very suitable for the simulation of topographs. With the advent of powerful high speed computers, simulation is

now becoming a routine tool for X-ray topographers and its use is covered in detail in the review by Epelboin [21].

Chapter Two

Techniques and contrast formation in X-ray topography.

2.1 Introduction.

From chapter one we have seen how X-ray diffraction is dependent upon the perfection of the crystal lattice. Thus, we would expect to be able to use X-rays as a probe of local distortions in the lattice and it was with this aim that the various techniques of X-ray diffraction topography were developed.

Perhaps the simplest way for there to be a difference in the diffracted intensity between one region of a crystal and another is by there being a misorientation between the regions, greater than the divergence of the incident beam. In this case it is impossible for there to be simultaneous diffraction from both regions, which leads to a loss of intensity from one of them. This type of contrast is termed "Orientation Contrast" and may also arise if the misorientation is relatively large (e.g. low angle boundaries, grain boundaries, mosaic crystals) and the incident beam has a large spectral and/or angular divergence, as with a polychromatic or an uncollimated incident beam. Here, the diffracted beams from the two regions will have comparable intensities but different directions which, if the recording medium is placed sufficiently far from the crystal to allow spatial separation of the two beams, leads to a local loss of intensity at the boundary. This contrast is at the heart of the now little used Schulz technique [22] which uses a

microfocus X-ray tube with the crystal in the Bragg geometry, a similar technique in the Laue geometry having been developed by Guinier and Tennevin [23].

Contrast may also be caused by local distortions of the lattice, for example around the core of a dislocation, interfering with the propagation of wavefields through the crystal. This contrast can only be explained by using the dynamical theory and is described in more detail in 2.3.1.

Before going on to discuss the various techniques in detail, it is valuable to consider what information X-ray topography can and cannot give. It is possible non-destructively to image large areas of crystal (4 inch silicon wafers are now regularly examined), showing the direction and distribution of defects. As such, it is a very useful complementary technique to TEM, allowing the electron microscopist to isolate areas of specific interest, whilst giving information about the macroscopic nature and distribution of defects. Crystals up to several millimetres thick can be imaged (in standard techniques, providing μt is of the order of $\sim$ 0.5 to 3), some techniques are capable of giving a very high strain sensitivity (up to one part in 10^8), some can give information on the depth distribution of defects and some are very surface sensitive. By using a variety of techniques it is usually possible to fully characterise the sample.

On the negative side however, several factors conspire to limit the ultimate resolution of the technique to about 1μm. This arises in part because X-rays cannot be easily focussed and the refractive index for them for most crystals

is close to unity, meaning that topography is a non-magnifying technique and is thus dependent upon the resolution of the recording medium, usually film. It also depends however, upon geometrical factors and the sensitivity to small lattice distortions, which means that the strain field a long way from a defect will cause contrast on the film. These limitations are discussed in greater depth in 2.5. Another reason often cited for the relative unpopularity of X-ray topography, is the length of time it takes to image samples which can be up to tens of hours for large wafers on high resolution film. Whilst this can indeed be a drawback, there are now techniques available which can allow rapid imaging of even very large samples.

2.2 Techniques of X-ray topography.

Reviews of the various techniques may be found in many books and journals; however the articles the author has found the most useful are found in [24-27].

The vast majority of topographic techniques use an incident X-ray beam of limited spectral divergence (such as the characteristic emission line from a metal target), whose angular divergence has also been carefully controlled. Although some attempts have been made to use the Kβ characteristic line [28], [29], the Kα line is most commonly employed, which is where the first problem arises. The Kα emission is in fact a closely spaced doublet, consisting of the $K\alpha_1$ and $K\alpha_2$ wavelengths, which for a molybdenum target are separated by a $d\lambda$ of about 0.004Å. Simultaneous diffraction of the two lines will lead to two diffracted

beams with different directions and intensities, giving the possibility of a greatly reduced spatial resolution. Most of the techniques described below have been developed in part to remove or minimise this problem.

2.2.1 The Berg-Barrett technique.

The Berg technique [30], as refined by Barrett [31] is shown schematically in figure 2.1. The crystal is set to diffract the Kα doublet from an X-ray line focus source with a width of less than about 1mm. An asymmetric Bragg geometry is used, with a small angle of incidence and $2\theta_B$ as close to 90° as possible. In this geometry, a narrow incident beam is converted into a wide diffracted beam, allowing a large surface area of the crystal to be imaged. However, simultaneous diffraction of the Kα doublet is unavoidable and the film must be placed very close to the specimen to eliminate spatial separation of the two diffracted beams. The Berg-Barrett technique was further developed by Newkirk [32,33] who was the first person to report the imaging of individual dislocations by extinction contrast.

To obtain a suitable Bragg angle, it is usually necessary to use fairly soft (i.e. long wavelength) radiation, which also gives a small extinction distance. Thus this technique only images the first few microns of a crystal surface and is therefore particularly suitable for crystals with high dislocation densities ($<10^6$ cm^{-2}) and for studying surface related defects such as those formed by the fabrication of electronic devices [34], [35].

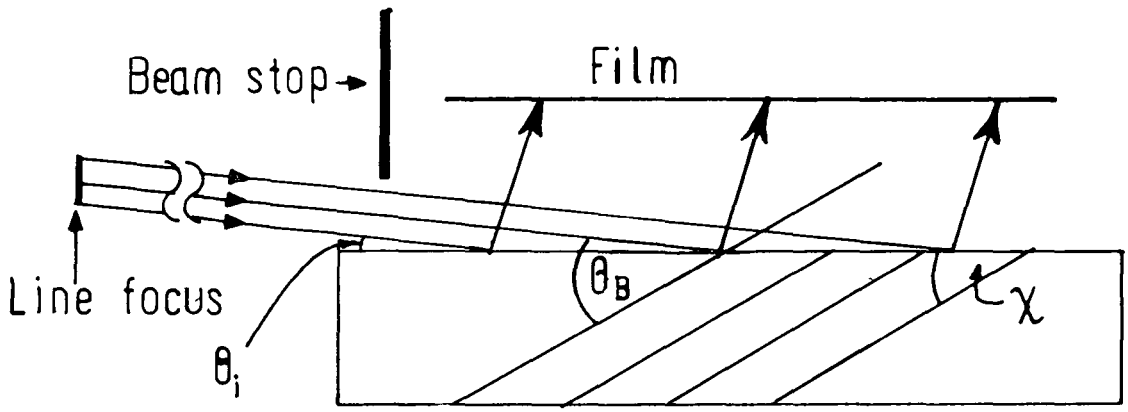

Figure 2.1

The Berg-Barrett Technique.

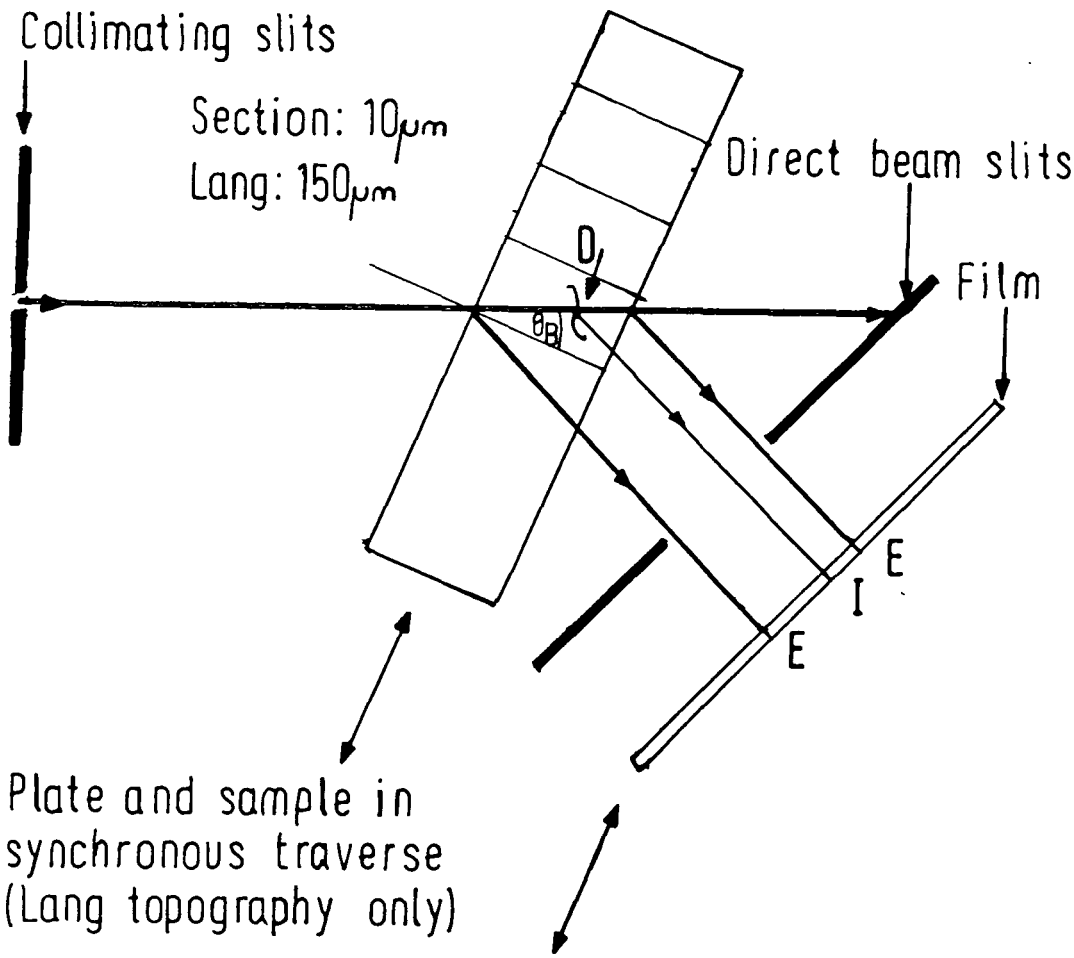

Figure 2.2

Section and Lang Topography Techniques.

2.2.2 Section Topography. [36]

The experimental set-up for section topography, shown in figure 2.2 is extremely simple. X-rays from a focus some distance away, typically 1m, from the sample are collimated into a ribbon beam with a height of up to several centimetres. The horizontal angular divergence is limited to $\sim 5x10^{-4}$ radians by slits of width 10-15μm. Since the divergence of the beam is less than the angular separation of the $K\alpha_1$ and $K\alpha_2$ reflections in the crystal, it is possible to obtain diffraction from only the $K\alpha_1$ line. Slits are placed between the crystal and the film (usually called the direct beam slits) to stop the diffracted beam, and also to remove stray reflections.

The small slit size serves two purposes in section topography, firstly it gives a spherical wavefront which excites the whole of the Borrmann fan as described in 1.5 and secondly, because the beam is narrow compared with the width of the Borrmann fan, the resulting topograph contains information on the direction of energy flow within the crystal. This effectively gives an image of a slice through the crystal, showing the depth of the defects within it. The phenomenology of image formation is discussed more fully in 2.3. However the reason why the section topograph should give information on the depth distribution of defects is briefly explained below.

Referring to figure 2.2, we see that the direct beam contains mostly X-rays which do not exactly satisfy the Bragg condition. When this beam passes through a heavily distorted region (D) such as close to the core of a

dislocation, some of these normally undiffracted X-rays will be diffracted very nearly in the direction $\mathbf{k}_g$. The intensity of the diffracted beam will be described by the kinematical theory, and will therefore be proportional to the volume of heavily distorted crystal. Since this diffracted beam does not satisfy the same Bragg condition as the crystal bulk, it will suffer less than normal primary extinction and will thus appear as an area of enhanced intensity on the topograph. This type of contrast is often called "extinction contrast". The depth at which the direct beam crosses the defect is thus clearly related to the position of the image (I) relative to the edges (E) of the section topograph.

Although section topography can be used to characterise defects in detail and gives information on the propagation of wavefields through the crystal, its usefulness is limited by the small volume of crystal bounded by the Borrmann fan imaged per topograph. To map out both the depth and distribution of defects across the whole sample it is possible to take a series of section topographs on the same plate, the sample and film being traversed by a small distance comparable to the width of the base of the Borrmann fan between exposures. An example of such an experiment is given in chapter 6. However, whilst this provides very detailed information about the perfection of a sample and can be done automatically using a step scanning technique [37,38], it can still take an excessive time to image a whole sample and is therefore most suitable for examining small areas in detail. For most purposes, it is usually better to image a large area of the crystal using the Lang

technique described in section 2.2.3 and then to use this to choose areas of interest to be examined by section topography.

2.2.3 Lang topography.

The Lang technique [39] is perhaps the most widely used topographic technique, and is capable of imaging large areas of even relatively thick crystals, providing that $0.5 < \mu t < 3$. The experimental geometry for this method is the same as in the section technique shown in figure 2.2, but with a collimating slit of width 100-200μm, sufficient to resolve the Kα doublet whilst retaining a reasonably high intensity of incident radiation. The crystal and film are now traversed synchronously back and forth across the X-ray beam to expose a larger area of the sample. Figure 2.3 shows the Marconi-Elliot Lang camera used at Durham University, with the direct beam slits pulled back to show the features, which are marked with the same notation as in figure 2.2. The camera has been interfaced to a microcomputer by the author and this is described in chapter 3.

The Lang topograph can be considered as a spatial integration of many section topographs, giving an image of the projection of the crystal volume and can be used to image crystals of a size limited solely by the size of the Lang camera. However, because the exposure time required to expose the film will vary linearly with the width of the sample, large crystals may take a prohibitively long time to image.

The Lang method gives a vertical magnification close to

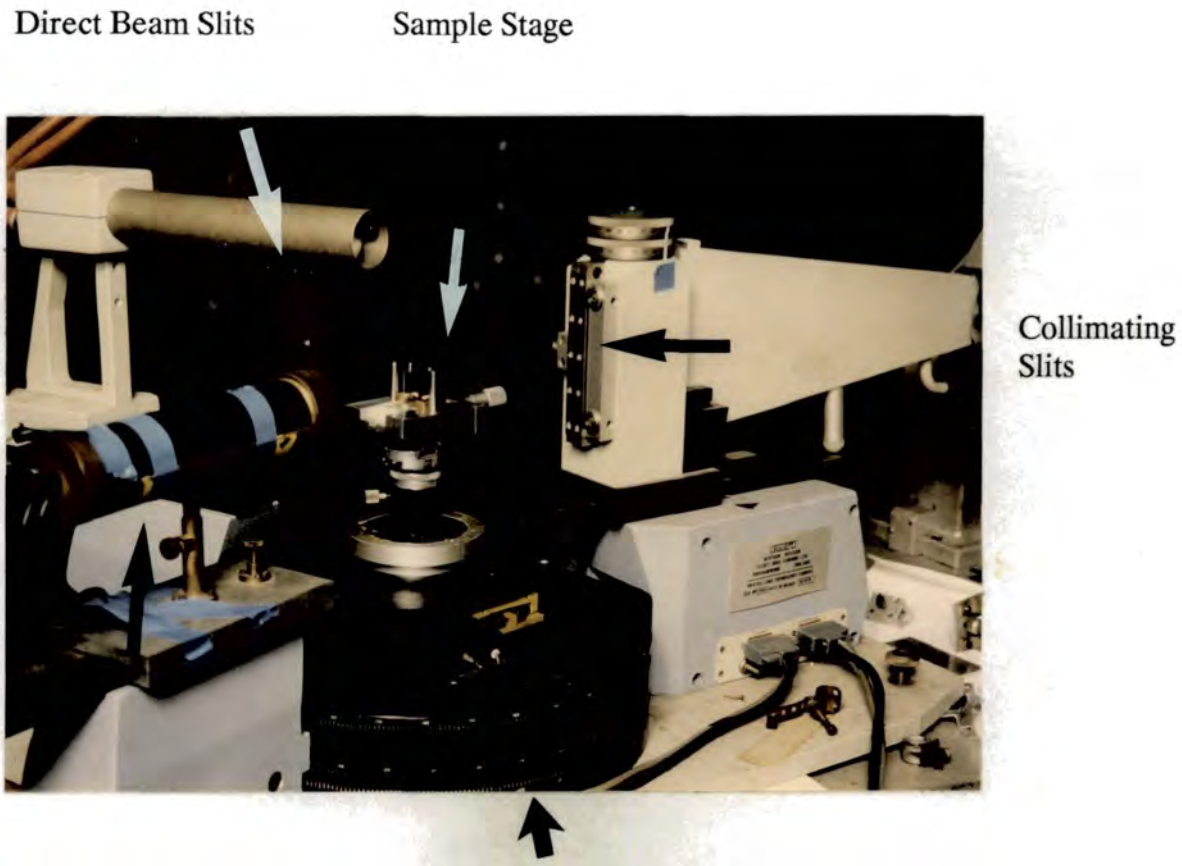

Figure 2.3.

The Marconi-Elliot Lang Camera in use at Durham University. Note that the Direct Beam Slits have been pulled back to show the sample stage.

unity. If the film is placed parallel to the exit surface of the specimen slab, the horizontal magnification is also unity. This arrangement, however, is usually undesirable since the diffracted beam now passes through the film at an angle to its surface normal, leading to a significant broadening of the image for all but the thinnest emulsions. To avoid this problem the film is usually placed perpendicularly to the diffracted beam and the image suffers from a horizontal magnification of $\cos(\theta+\chi)$.

2.2.4 Double crystal topography.

Although the single crystal methods so far discussed potentially have a high strain sensitivity (up to $\sim 10^{-5}$), they will in practice be unable to distinguish small changes in lattice parameter occurring over a long range, the best sensitivity to this being $\sim 10^{-3}$. These limitations are brought about because of the finite angular and spectral divergence of conventional X-ray sources. The double crystal technique as developed independently by Bond and Andrus [40] and Bonse and Kappler [41], can be used to reduce both the spectral and the angular divergence of the X-ray beam, hence improving the strain sensitivity.

Let us consider the parallel +- (or +m,-m) setting shown in figure 2.4, where the reference crystal and the specimen both have the same interplanar spacing, that is, d is identical for both crystals. In this way, all wavelengths diffracted by the first crystal are diffracted at the same relative angle by the second crystal, that is, the geometry is non-dispersive in wavelength. This leads to a very narrow

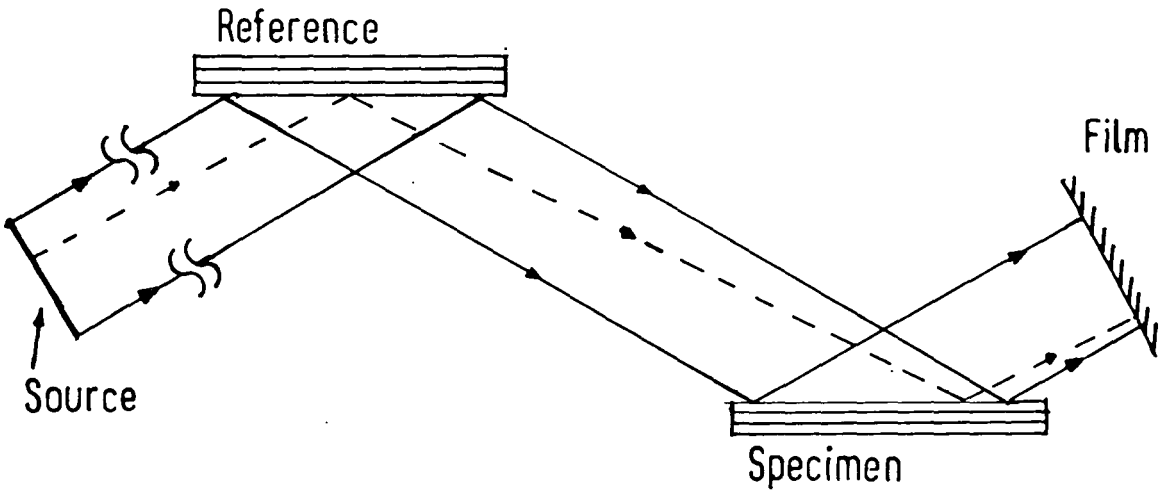

Figure 2.4

Double Crystal Topography (Non-Dispersive Geometry).

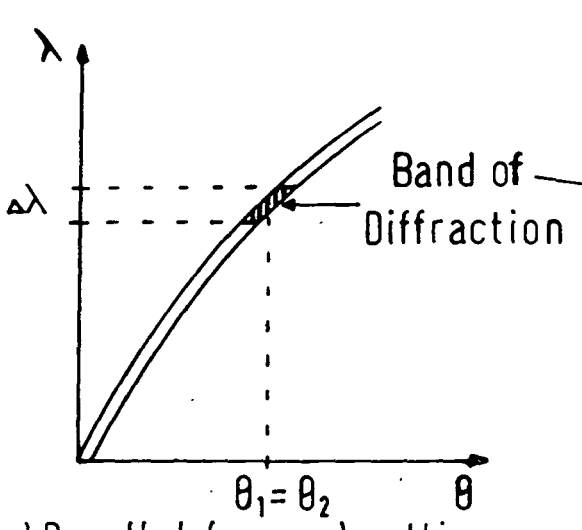

(a) Parallel (+m, -m) setting.

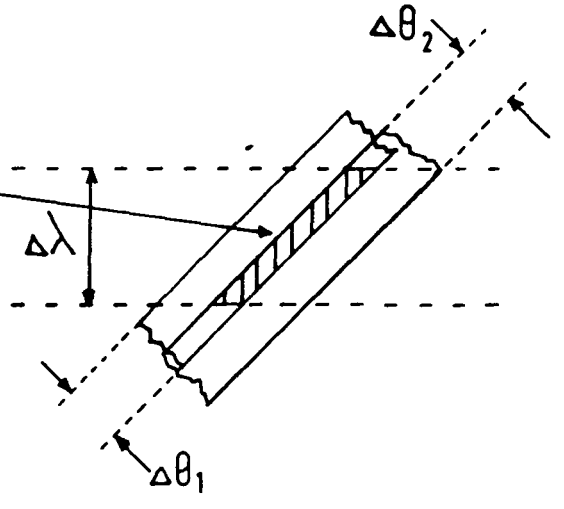

(b) Second crystal set on flank of rocking curve.

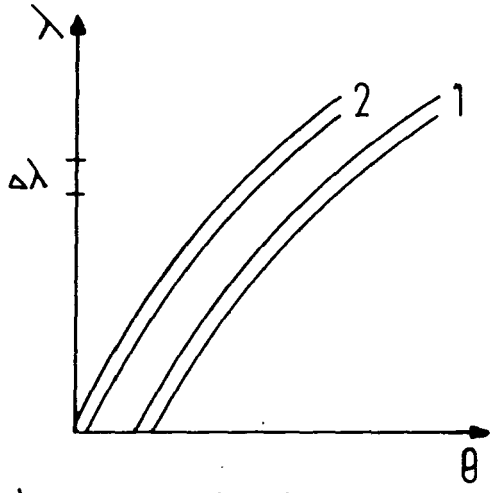

(c) Case for a local misorientation.

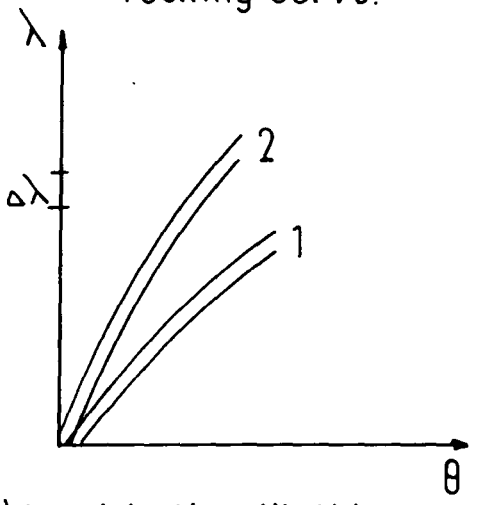

(d) Local lattice dilation.

Figure 2.5

The Du Mond Diagram

angular range of reflection as the second crystal is rotated relative to the first about the Bragg condition (the rocking curve); the reflecting range being the convolution of the two perfect crystal reflecting ranges.

If we consider the Du Mond diagram, a plot of the conditions which satisfy the Bragg condition against wavelength and angle, for this setting (shown in figure 2.5a), we can begin to understand its high sensitivity to lattice distortion. The region of overlap of the two curves gives the condition for simultaneous diffraction. When the two crystals are set exactly parallel, diffraction occurs for all wavelengths. However as the second crystal is rotated, the curve is translated relative to the first (figure 2.5b) and the amount of overlap is reduced, leading to a reduction of diffracted intensity. Thus, if the second crystal is locally misorientated it leads to a local loss of intensity; a local change of lattice spacing leading to the situation shown in figure 2.5d, with a corresponding loss of intensity. When the second crystal is set upon the steep flank of the rocking curve, the diffracted intensity will vary approximately linearly with the amount of distortion present. Using closely matched values of d for both crystals in the +- setting, a very high sensitivity to changes in lattice parameter is achievable and it has been used to detect changes of a few parts in 10^8 [42].

Whilst the +m,-m setting is non-dispersive in wavelength, it is angularly dispersive, leading to images in topographs being broadened because of the different directions of the diffracted beams for different

wavelengths. Also, the strain field relatively far from the core of a dislocation is sufficient to give contrast, leading to broad images. For these reasons, this setting is not particularly suitable for crystals with very high dislocation densities.

The angular dispersion can be reduced by using slightly different values of d for the two crystals, thus limiting the wavelength range diffracted by both crystals for one setting of the first crystal. Whilst this reduces the line width of the images of the dislocations, it also lowers the sensitivity of the technique due to the finite spectral dispersion.

Asymmetric reflections are often used for either or both of the crystals in double crystal experiments. When used for the first crystal with a glancing angle of incidence, they have the effect of converting a narrow incident beam into a wide one which can be used to illuminate a large area of the second crystal, and of reducing the angular divergence of the diffracted beam. An asymmetric second crystal, however, can be used to limit the depth of penetration of the X-rays and to illuminate a large area of the sample from a small incident beam. The latter arrangement is discussed in depth in chapter 5. A good introduction to the merits of double crystal topography using asymmetric reflections is given in the paper by Renninger [43].

When using the double crystal technique, care should be taken over the choice of the first crystal, since the final diffracted intensity, being a convolution of the diffraction

from both crystals, is equally dependent upon the first crystal as on the second. Thus, first crystals should be dislocation free, with a known, constant lattice parameter. If the first crystal is not defect free, images of these defects will appear on the final topograph albeit diffused, because of the distance between crystal and plate. Luckily, this is not much of a problem when using silicon, since high purity, zero dislocation density silicon crystals are now regularly grown for the semiconductor industry.

2.2.5 The Hirst topography technique.

For silicon wafers, the Lang technique suffers from the serious drawback that exposure times may be prohibitively long. For instance, with a generator running at 40kV and 40mA, a source size of 200μm and a source to sample distance of about 1m this may be upwards of 40 hours for a 4 inch wafer on nuclear emulsion. This makes X-ray topography unsuitable for the routine inspection of production line wafers. The Hirst topography technique [44] shown in figure 2.6 circumvents this problem by cylindrically bending the sample to a radius of curvature of twice the Rowland circle. For a symmetric reflection and a beam of X-rays divergent from a point source located on the Rowland circle, all X-rays in the plane of incidence make equal angles with the Bragg planes. By limiting the source size, it is possible to obtain simultaneous diffraction of only the $K\alpha_1$ emission line from the whole wafer. Oscillating Soller slits remove the transmitted beam, allowing the film to be placed relatively close to the sample.

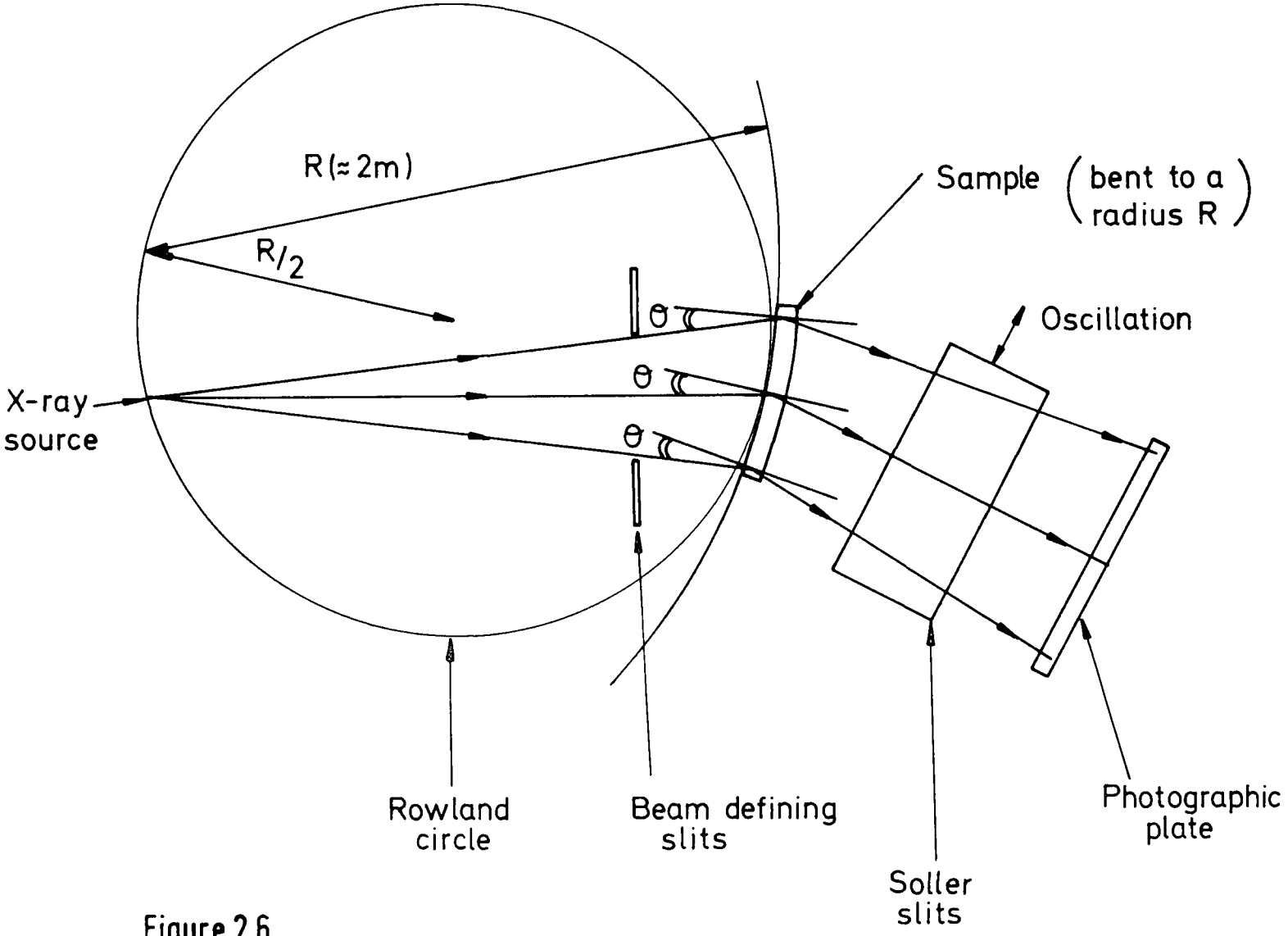

Figure 2.6

The Hirst Topography Technique.

In this way, topographs with a resolution comparable to that of the Lang technique are possible with greatly reduced exposure times (of the order of 1 hour). The contrast obtained from the Hirst technique is similar to that from the Lang technique, although important differences are apparent. The cause of the difference in contrast between the techniques is discussed in chapter 4.

2.3 Contrast on X-ray topographs.

2.3.1 Image formation in projection topographs.

Firstly, consider a section topograph of a perfect, parallel sided, lightly absorbing (i.e. $\mu t \approx 1$) crystal slab. As we know, the finite angular divergence of the incident beam excites all of the dispersion surface simultaneously, producing energy flow in all directions within the Borrmann triangle. Also, because of the slight difference in wavevector between them, wavefields from different branches of the dispersion surface travelling in the same direction will interfere. This interference, or Pendellosung, produces intensity maxima within the crystal, the loci of the maxima of all the wavefields lying on hyperbolae asymptotic to $\mathbf{s}_o$ and $\mathbf{s}_g$ in the plane of incidence and forming hyperbolic cylinders in the crystal slab. The exit surface of the crystal will intersect these cylinders as shown in figure 2.7a and straight parallel fringes are observed in the diffracted beam, shown in figure 2.7b.

If the crystal and film are traversed to form a Lang topograph, these fringes will not be present on the plate because we are now looking at the integrated intensity of

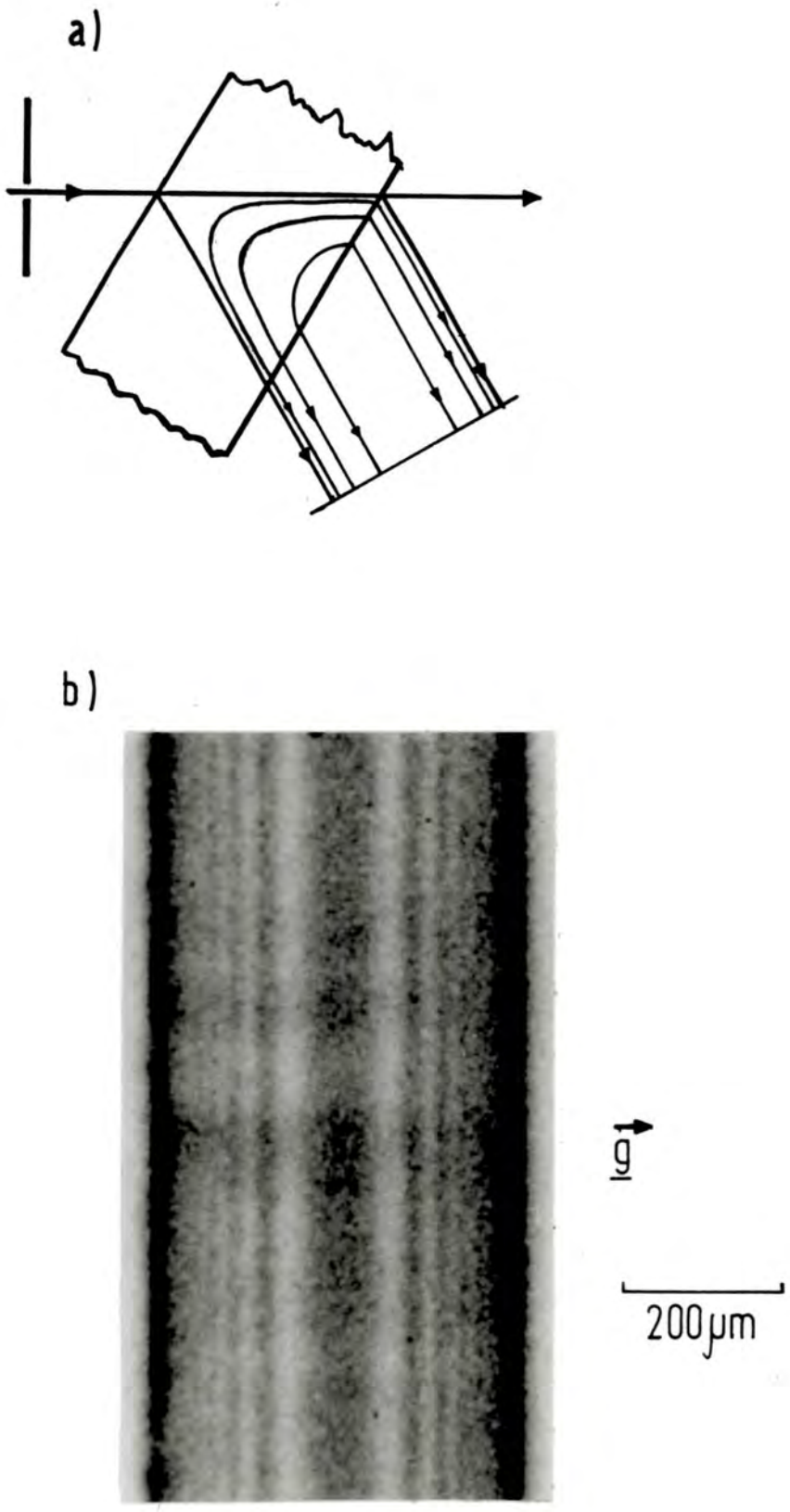

Figure 2.7

a) Formation of Pendellösung fringes

b) $\bar{4}40$ Section Topograph.

the crystal volume. If, however, the crystal is wedge shaped, hook shaped fringes are produced in the section topograph giving fringes in the Lang topograph which can be thought of as fringes of equal thickness.

Pendellosung, or Kato fringes were first observed by Kato and Lang [45] and can only be explained by the dynamical theory with an incident spherical wave [46]. Being a dynamical effect, they are easily distorted or destroyed by small deviations from crystal perfection and are therefore a good indicator of the presence of defects which may otherwise not be imaged on a topograph. The distortion of these fringes under the influence of lattice curvature is discussed in chapter 4.

Now consider the situation shown in figure 2.8, when there is a defect, in this case a dislocation, present at a certain depth within the crystal. As mentioned in section 2.2.2, when the direct beam cuts the dislocation line at D, a direct image of enhanced intensity is formed (1); the intensity of the image being roughly proportional to the volume of the heavily distorted region.

When the wavefield travelling in the direction AE crosses the strain field close to the dislocation core, it decouples into its direct and diffracted beam components, which excite new wavefields such as AF upon re-entering the perfect material below. This phenomenon is often described as interbranch scattering. Energy is thus removed from the original wavefield AF, leading to an area of diminished intensity on the plate, the dynamical image (3).

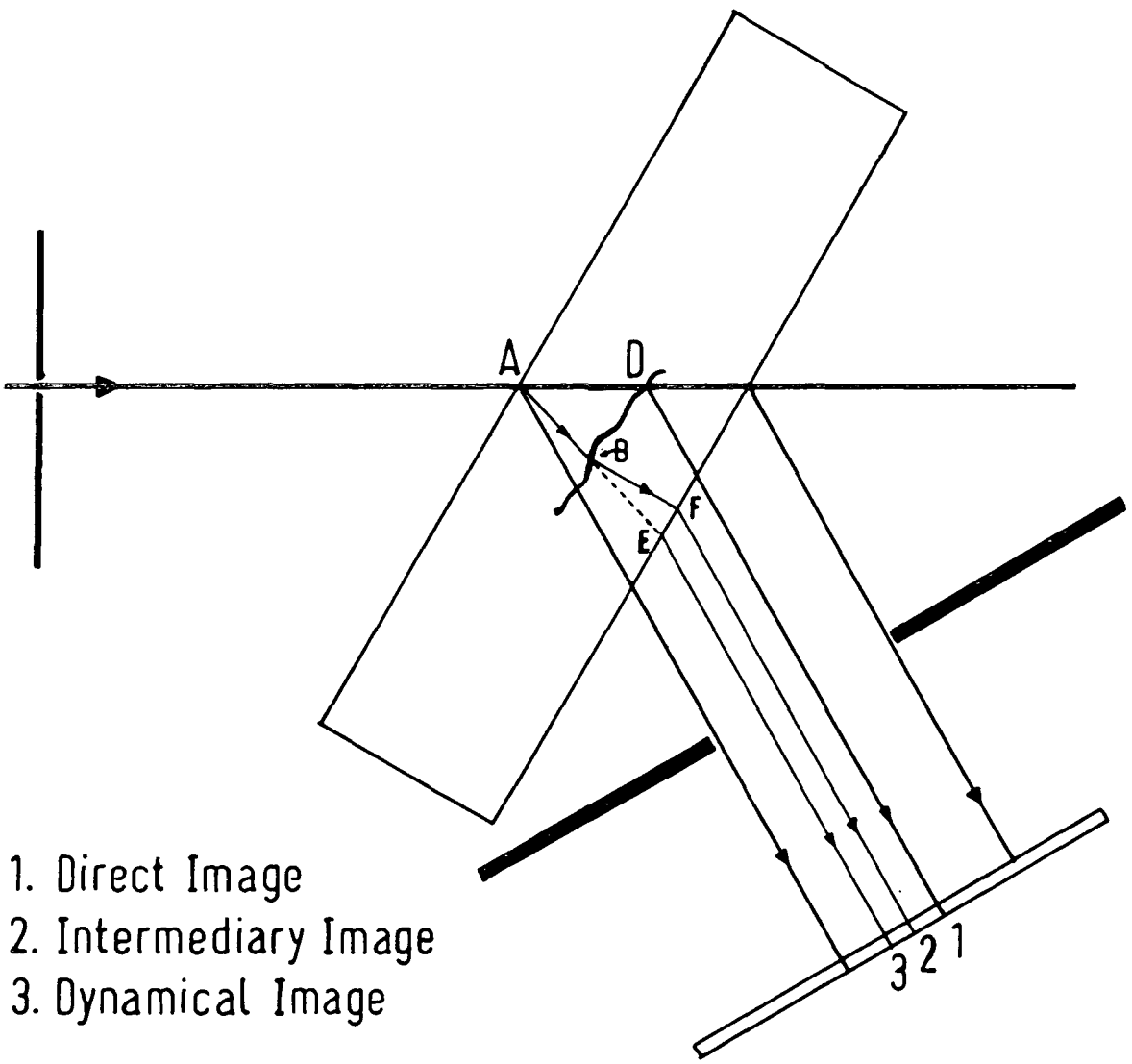

1. Direct Image
2. Intermediary Image
3. Dynamical Image

Figure 28
Defect Contrast in Section Topography

The newly created wavefields will now propagate in different directions from the original wavefields and may interfere with them, forming complex interference fringes, the so-called "intermediary image" (2).

In a Lang topograph, we can get an idea of the sort of contrast we expect by imagining a series of overlapping section topographs. Thus, the direct image becomes a projection of the dislocation through the crystal volume, and the dynamical image is now in effect a "shadow" of the direct image. One may still see intermediary fringes, providing that the dislocation line does not lie parallel to the crystal faces.

Under certain conditions, when the width of the perfect crystal rocking curve is narrow enough (e.g. for high order reflections), the direct image may appear as a double line [47]. This is because the misorientation around, for example, an edge dislocation is equal and opposite in lobes on either side of the dislocation line. Since the intensity of the direct image only depends upon the volume of heavily distorted material and not upon the sense of deformation, both lobes will give rise to direct images of roughly equal intensity. In low order reflections these images will normally overlap and the direct image appears as a single line, since the perfect crystal reflecting range is too wide to resolve them individually.

Generally, the image of a dislocation will only be visible when the defect produces a sufficiently large distortion of the diffracting planes. For a pure screw dislocation this implies that the image will be invisible

when **g** is perpendicular to the Burgers vector, that is, **g.b** = 0. For an edge dislocation, we have the added condition that **g.bxl** = 0 for complete invisibility, where **l** is a vector parallel to the dislocation line. A mixed dislocation therefore will never be completely invisible, although partial invisibility is often found for all dislocations for **g.b** = 0. By looking for invisibility in topographs of the same crystal taken with different reflections, it is often possible to determine uniquely the Burgers vector of a dislocation.

Inclusions, such as precipitates, have a radial strain field and therefore give different contrast to line defects such as dislocations. In order to give contrast, the strain field of such a defect must be great enough to cause a misorientation greater than the perfect crystal reflecting range. Perpendicular to **g**, the atomic displacements are parallel to the diffracting planes which consequently suffer no distortion in this direction. This leads to contrast consisting of two lobes separated by a line of no contrast perpendicular to **g**.

2.3.2 Contrast formed by surface films.

From section 1.6 we have seen how the propagation of X-rays through a medium with a small continuous distortion can be explained using an Eikonal or ray optics theory. This theory can be used to explain the contrast in topographs of crystals whose surfaces are locally strained by the presence of discontinuous films. Pioneering work by Meieran and Blech [48] showed local contrast at the edges of oxide films grown

on silicon wafers, whilst the intensity a short distance away from the edges was the same in both the oxidised and unoxidised regions. Further work [49-54], has identified the cause of this contrast and given it a theoretical basis. More detailed explanations will be given as the need arises, but the basic contrast effects are summarised below.

A thin film grown on an otherwise perfect substrate induces either a tensile or compressive strain due to the different thermal expansion coefficients. The strain in the substrate will be essentially normal to the surface everywhere but close to the edges of the film. Here, there is also a component of strain parallel to the surface and perpendicular to the film edge. When using a symmetric reflection, the diffracting planes beneath the film are undistorted and this area diffracts with equal intensity to the rest of the substrate. At the edges however, the diffracting planes are slightly curved, leading to a change in intensity which can be described by the Eikonal theory.

The use of an asymmetric reflection where the normal strain gradient under the film causes a distortion of the lattice planes close to the interface with the substrate has been used to obtain contrast from the whole of the covered area [55,56], and can be used as a measure of film adhesion.

In section topography the strain leads to the appearance of elliptical fringes which contract as they approach the interface. The appearance and contraction of these fringes has been extensively studied by Kato [14-16], and also by Hart [57].

2.3.3 Contrast in reflection topographs.

The situation in Bragg geometry topography is different in two important respects from that in the Laue geometry. Firstly, only wavefields from one branch propagate in the crystal and secondly, only a small surface skin of about ξ_λ contributes to the diffracted intensity. Extinction contrast is formed in much the same way as for projection topographs and the energy taken from the wavefield in forming the direct image creates a shadow, the white dynamical image.

Since only one branch of the dispersion surface can be excited for a thick crystal (two for unpolarized radiation) we do not expect interference effects as the wavefields within the Borrmann fan do not overlap within the crystal. Interference fringes have however been reported in reflection topographs by several people including the author and these are discussed in chapter 6.

Single crystal reflection techniques are quite insensitive to orientation contrast because of the divergence of the incident beam and therefore only gross misorientations such as grain boundaries will be imaged by this technique. Double crystal reflection topography is, however, sensitive to misorientations of the order of seconds of arc as a result of the narrow half-width of the rocking curve. This sensitivity may be used to map out contours of misorientation on distorted crystals such as silicon wafers, but can also be a nuisance because only a small area of a bent crystal can be imaged in one exposure. Contrast in double crystal reflection topography is explored more fully in chapter 5.

2.4 X-ray topography using synchrotron radiation.

Synchrotron radiation is produced when relativistic charged particles undergo centripetal acceleration, as at the bending magnets of an electron storage ring. The acceleration causes the electrons to emit dipole electromagnetic radiation in its frame of reference. Due to the relativistic transformation, this is confined in the laboratory frame to a forward directed cone tangential to the path of the electrons with an opening angle of $1/\gamma$ ($\gamma = \sqrt{(1-v^2/c^2)}$). The radiation is highly polarized in the horizontal plane, has a white spectrum extending from hard X-rays ($\lambda \sim 0.7$Å from the conventional 1.2T bending magnet) to visible light, and is very intense. The spectrum of the emitted radiation is shown in figure 2.9. Furthermore, the source size is small and the topography station is situated about 80m from the source, giving a divergence at the sample in the plane of incidence of only 4×10^{-6} rad.

The simplest experiment one can undertake with synchrotron radiation is white beam topography [58]. Here, the crystal is placed in an unmonochromated beam which covers the area of interest, often the whole sample. This gives Laue spots on the plate, each of which contain a topograph of the crystal. Since each spot represents the Bragg condition for a certain wavelength and reflection, a great deal of information is contained in one topograph which may only take seconds to expose. This method is equivalent in form to the Schulz method in the reflection geometry and the Guinier-Tennevin method in the transmission geometry, but because of the low divergence of the beam, the

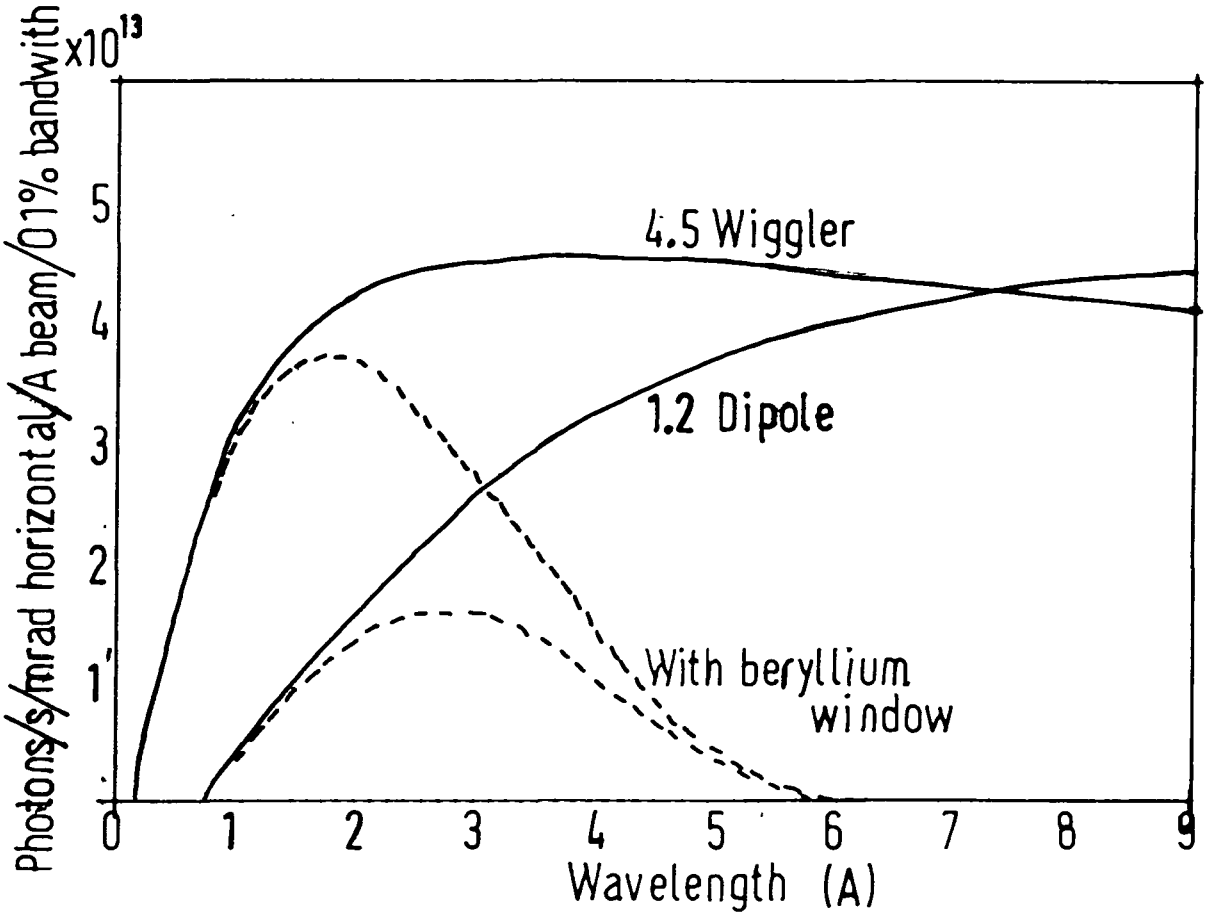

Figure 2.9

Spectral characteristics of the SRS

plate can be placed up to about 10cm away from the sample and still give a resolution comparable to the Lang technique [59,60]. This technique is insensitive to orientation contrast since misorientated regions diffract X-rays of slightly different wavelengths from the white radiation. Boundaries do however show either enhanced or diminished intensity because of the overlapping or separation of the diffracted beams respectively. Whilst useful for in situ experiments and Burgers vector analysis, the white beam technique can be difficult to interpret because of harmonic contamination (see section 5.3.2).

Synchrotron radiation is also very amenable to double crystal topography, giving several advantages over laboratory based experiments. The first crystal here is used to monochromate and condition the incident beam by use of a suitable reflection, with a continuous range of wavelengths available by simply rotating the crystal, i.e. the source is tunable in wavelength. Due to the highly polarised nature of the radiation, the experiment can be arranged to either use solely π or σ polarised radiation. The high photon flux reduces exposure times from tens of hours to minutes and the low divergence perpendicular to the plane of incidence means that the second crystal does not have to be finely adjusted for tilt as it does for divergent laboratory sources. Furthermore, the low divergence in the plane of incidence limits the range of wavelengths diffracted by the first crystal, giving a strain sensitivity in the non-parallel +- setting comparable to that in the parallel setting.

2.5 Factors affecting resolution on topographs.

Although this section is confined to the resolution in the Lang technique, the basic principles may be easily extended to most of the topographic methods.

In the Lang technique, the diffracting planes are perpendicular to the plane of incidence and therefore essentially no diffraction takes place in the vertical plane. The vertical resolution is thus only limited by geometrical factors and a point on the sample will produce a line of height

$$\delta = hb/a \qquad (2.1)$$

on the emulsion. Here, h is the apparent height of the X-ray source viewed from the sample, b is the sample to film distance and a the source to sample distance. If we take fairly typical values of h = 200μm, b = 2cm and a = 1m we see that δ = 4μm. This can sometimes be improved by the use of a fine focus X-ray tube or by placing the film as close to the sample as possible, but in most cases it is practically impossible to obtain a vertical resolution of better than 1μm.

The horizontal angular divergence of the X-ray beam is of the order of 5×10^{-4} rad and therefore geometrical factors are not a problem. Horizontal resolution is however affected by the spectral line width dλ of the characteristic line from an X-ray target. This leads to a spread in the Bragg angle $d\theta_B$ of:

$$d\theta_B = (d\lambda/\lambda)\tan\theta_B \qquad (2.2)$$

which consequently gives a spreading dx of the image of a point in the sample of:

$$dx = bd\theta_B \qquad (2.3)$$

For $CuK\alpha_1$, b = 1cm and $\theta_B = 24°$ this leads to a horizontal resolution of 1.7μm, of the same order as δ. In fact, the spread due to the spectral line width is only really a problem for large values of θ_B, when care should be taken to minimise b.

2.6 Photography.

Since topographs are recorded at a magnification of unity, it is vital to have a recording medium capable of reproducing the contrast to a resolution of at least that dictated by the factors in the previous section. Furthermore, it must have a high absorption factor for X-rays and a wide usable density range. Ilford L4 nuclear emulsion plates are generally accepted to be the best medium for X-ray topography, having small (0.14μm swelling to 0.25μm upon processing), tightly packed grains with a high proportion of silver halide, giving a good stopping power for fairly thin emulsions. The use of L4 plates and their characteristics are described in detail in [61] and therefore only a brief description is given here.

L4 plates are supplied in a variety of emulsion thicknesses, since harder radiation will be less strongly absorbed for the same thickness as soft radiation. The thicknesses of emulsion required to absorb roughly half of the incident radiation are 25μm for $CuK\alpha_1$, 50μm for $MoK\alpha_1$

and 100μm for $AgK\alpha_1$, although 50μm should preferably be used for $AgK\alpha_1$ whenever possible because of the long processing times and possibility of distortion with the 100μm emulsion. 25μm emulsions are always used at the synchrotron radiation source since there is a very high photon flux available and the thin emulsion gives a significant reduction in processing time. The thin emulsion is also more tolerant to beams passing through the emulsion at an angle without giving a significant loss of resolution.

The emulsion is stuck to one side of a glass plate and may be viewed under red light. Care must be taken at all times to avoid contact with the delicate emulsion and the plate should always be mounted with the emulsion side towards the diffracted beam, since glass is a good absorber of X-rays!. The plates may be identified by gently scratching a number in one corner of the emulsion, which removes the protective light filter and leads to the number appearing black on the developed plate.

Unfortunately, the high packing of grains also leads to lengthy processing times because the diffusion rate of developer through the emulsion is slow. To achieve uniform development, the development rate must be reduced to be comparable to the diffusion rate and this is done by developing the plates close to ice temperature in the body of a domestic fridge. A typical processing schedule for 50μm plates is given in table 2.1. Developer deteriorates quickly upon dilution and should therefore be changed regularly, whilst fixer can be used repeatedly. All solutions should be made with deionised water and kept as clean as possible.

	Thickness	
	50μm	25μm
	Time (minutes)	
Soak in filtered deionised water	10	5
Develop in 1:3 D19b to deionised water close to ice temperature	30	10
Stop in 1:100 acetic acid to deionised water	5	5
Fix in 1:9 Kodak Unifix to deionised water	120	30
Wash in filtered tap water	>120	>60
Dry under cover		

Table 2.1

Processing schedule for Ilford L4 Nuclear Emulsion Plates

For high resolution work, it is essential to use L4 plates. They are however very expensive and require lengthy and careful processing making them unsuitable for routine work. For alignment and test exposures, Kodak dental film is extremely useful, coming in individually wrapped packets and requiring short exposure times, with the added advantage that it can be developed and fixed to an acceptable standard within one or two minutes. Dental film is used at Durham for checking the height and position of the incident beam

relative to the sample, the tilt of the sample and the position of the direct beam slits. It can also be used to give a low resolution topograph, giving sufficient resolution to show large defects and can show enough detail to align crystals for section topographs.

Medium to high resolution topographs of large crystals can be exposed on polyester backed sheet film, the most common being the Agfa "D" range. D7 is a reasonably fast, medium resolution film capable of showing many types of defects and is regularly used for examining large crystals such as silicon wafers. The resolution is usually sufficient to pinpoint areas which deserve closer inspection with higher resolution films. D2 is a high resolution film, requiring the same exposure time as L4 plates but giving a smaller range of usable density. It does however have the advantages over L4 plates of being much cheaper and having shorter processing times.

Topographs in this thesis were enlarged using a Wild photomacroscope with a continuously variable magnification between 3.9x and 80x, and a maximum field of view of 27mm. Negatives of the plates were taken using Ilford FP4 9cm x 12cm sheet film with the plates being viewed by transmitted light. All the topographs presented here are printed as positives, that is, dark images represent enhanced intensity.

Chapter Three

The design and construction of an automated Bragg angle controller.

3.1 Introduction

As a result of the high angular collimation inherent in the Lang technique, crystals which are in some way distorted quickly deviate from the exact Bragg condition as they traverse, causing the diffracted intensity to drop and leave underexposed (or in some cases, unexposed) areas on the photographic plate. This makes the unmodified Lang camera unsuitable for the examination of crystals with large deviations from flatness, such as processed silicon wafers (which normally have large amounts of twist induced by the fabrication process) and the deliberately bent silicon wafers described in chapter 4.

The first efforts to overcome this problem were reported by Schwuttke [62], who oscillated the sample and film around the normal to the plane of incidence, as they traversed. Providing that the oscillation is large enough to include the entire reflecting range of the crystal, the whole of the sample will now diffract with high intensity for at least some of the time.

This scanning oscillator technique (SOT) works well for crystals with a small amount of distortion. However, for large distortions, the crystal will be diffracting at less than maximum intensity for a significant amount of time, since the amplitude of oscillation needs to be large enough

to include all possible misorientations. Also, this technique does lead to an increased background due to contributions from the flanks of the rocking curve.

An improvement to the SOT is a feedback system which continuously measures the diffracted intensity and rotates the sample so as to maintain it on the Bragg peak. Such a system was reported by van Mellaert and Schwuttke [63], using the algorithm described in [64], and was named automated Bragg angle control (ABAC). Using this technique, it was possible to record topographs of even severely distorted crystals, often with a significant reduction in exposure time (since the crystal was always diffracting at maximum intensity). However, the system still had limitations because of the need for a specially engineered sample holder (which limited the size of crystal which could be imaged) and dedicated electronics to provide the feedback. These factors lead to an increase in cost and a reduction in versatility of such systems.

In order to provide an inexpensive yet adaptable ABAC for the Lang camera at Durham, a system was designed to take advantage of the motor driven turntable and counting equipment already on the camera. The resulting Bragg angle controller, shown schematically in figure 3.1 is based around a microcomputer, interfaced to the camera via suitable electronics, and is described below.

3.2 The Marconi-Elliot Lang camera.

Both the traverse table and rotary table on the Marconi-Elliot Lang camera are driven by three-phase stepper

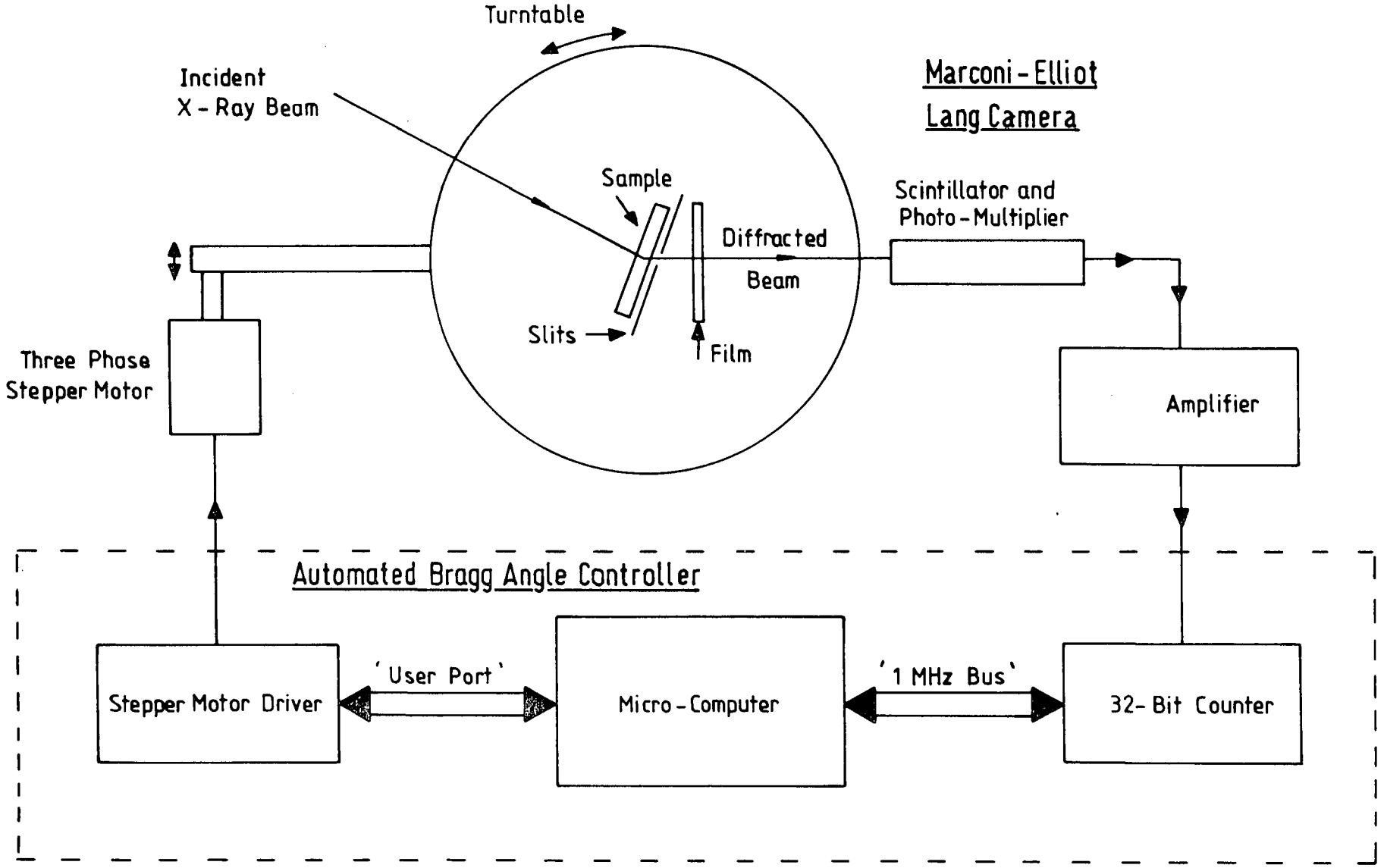

Figure 3.1
The Durham Automated Bragg Angle Controller.

motors geared to give a calibrated movement for each step of the motor. In the case of the rotary table, the motor drives a micrometer head acting against a spring loaded lever on the turntable. Suitable gearing allows samples to be rotated in 1/1000th of a degree steps. A worm screw on the traverse table similarly converts the movement of the stepper motor into a minimum stepsize of 0.01mm.

The counting equipment consists of a scintillator and photomultiplier tube, mounted on an arm co-axial with the turntable. The pulses from the photomultiplier are amplified and the count rate is normally read with an analogue rate-meter.

3.3 The Acorn "BBC" Microcomputer

It was decided to base the ABAC around an Acorn "BBC" microcomputer, chosen for its low cost and wide variety of interface ports.

The turntable stepper motor is controlled by the "User Port", which consists of eight bi-directional lines, PB0 (lowest significant bit) to PB7 (highest significant bit) and two handshake lines. The data lines are latched at either 0V or 5V when used as outputs.

The count-rate is read via the "1MHz Bus", a parallel interface with eight bi-directional data lines (D0 to D7) and eight address lines (A0 to A7). Up to 64 individually addressed devices can be accessed by the bus from the "User Applications" allocation of memory in the computer.

Details of the User Port and 1MHz Bus can be found in the BBC Advanced User Guide [65].

The connection between the computer and Lang camera is provided by an interface box, containing a stepper motor driver and 32-bit counter, the design and construction of which is described below.

3.4 The ABAC Interface Box

3.4.1 Power supply

Each coil of the stepper motor requires around 0.6A to provide sufficient holding torque for the motor. Since the resistance of each coil is 32Ω, this implies that a voltage of at least 24V is required to drive the motor. Also, to provide a rotation of 1/1000th of a degree, the motor has to be driven in half-step mode (see section 3.5.1) which requires two phases to be active simultaneously. Thus, the power supply must provide at least 1.2A continuously at a voltage of greater than 24V. To power the electronics of the counter, a stabilised 5V supply is also required.

The power supply therefore consists of a mains primary, 20V secondary, transformer, the output of which is full wave rectified and then smoothed by a 15 000μF capacitor to provide a nominal 28V dc supply.

The 5V supply for the counter is now provided by a voltage regulator fed by the 28V supply. Since this has to bring 28V down to 5V, a great deal of power is dissipated and it is therefore mounted on a heatsink on the outside of the ABAC box.

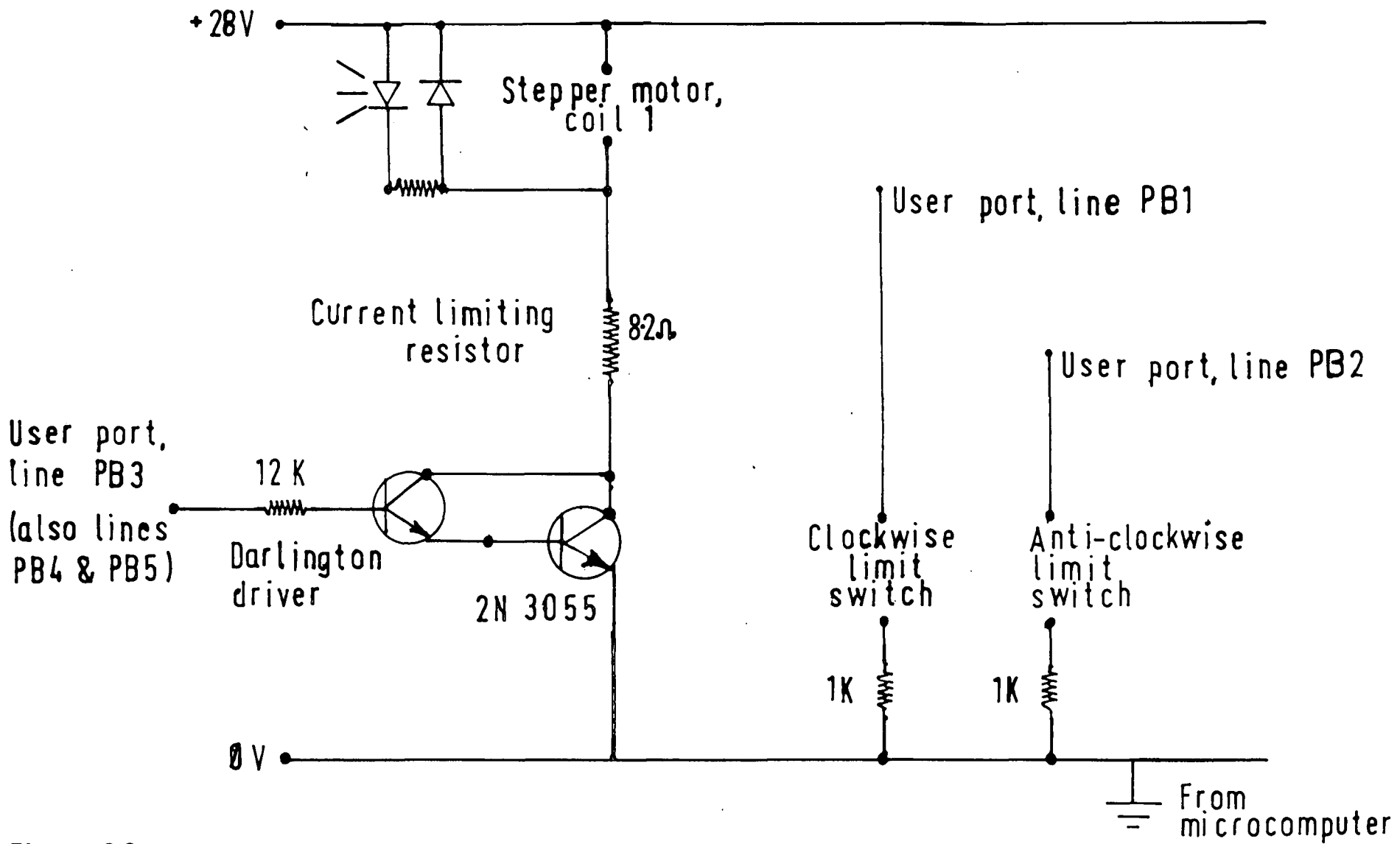

Figure 3.2

Three-Phase Stepper Motor Driver.

3.4.2 A Three-Phase Stepper Motor Driver

Figure 3.2 shows the circuit diagram for the three phase stepper motor driver. From the User Port, one line is used per phase with a further two lines being used as inputs to read the status of the clockwise and anti-clockwise limit switches on the camera turntable.

To amplify the current from the maximum of 1.5mA provided by the User port to the 0.6A needed by each phase of the stepper motor, a Darlington pair and transistor combination is used. Lines PB3, PB4 and PB5 of the port are each connected to the base of a Darlington driver (BD 679) through a current limiting resistor. As an added precaution against passing too much current through the Darlington pair, current is supplied to the collector through the stepper motor coil.

The emitter of the Darlington is then connected to the base of a high power transistor (2N 3055). The collector of this is connected via the stepper motor coil to the 28V rail of the power supply, and the emitter to the ground rail. Thus, when one of the lines from the User Port is sent high, current flows from the 28V rail through the coil and transistor to earth and will continue to flow until the line is sent low. The maximum current that can flow is limited to 0.6A by the resistance of the coil itself and an additional 8.2 series resistor.

At any time, the status of the phases (i.e. high or low) can be ascertained by three LED's on the front panel of the box, one being connected (with a current limiting resistor) in parallel with each coil.

The status of the two limit switches on the Lang camera is monitored by reading lines PB1 and PB2. These will normally return a high value and are pulled down to zero through a 1K resistor whenever the corresponding switch is closed.

3.4.3 A 32-bit counter.

The requirements for the counter are two fold. Firstly it must convert the rate of pulses from the photomultiplier into a single number, then this number must be read into the computer's memory for analysis.

The counter can be broadly split into two sections, the decoding section and the counting section. The decoding chips decode the information sent on the address lines of the bus and enable chips to be started, stopped, cleared, latched and read. The counting section consists of eight 8-bit counters arranged in two rows of four. The two sections are described individually below. Details of all the chips used in the counter circuit may be found in the TTL Data Book [66].

3.4.3.1 The counting section.

To obtain an accurate count rate, it is first necessary to know the exact time for which the pulses have been counted. Even though the counting time can be controlled by the computer fairly accurately, there will be some uncertainty as to when the counters are started and stopped. Therefore the counter employed here uses two parallel counters, one fed by the signal, the other by a 10MHz quartz oscillator. By starting and stopping both counters

simultaneously, the 10MHz counter will give the exact counting time.

The circuit is based around eight 74LS590 8-Bit binary counters with output registers, and is shown in figure 3.3. The counters will count whenever $\overline{CCKEN}$ (Clock enable) is low and stop counting whenever it is high. Data can be latched into the output registers by sending RCK high, without the need to first stop counting. Data is output from the chips on QA to QH by sending $\overline{G}$ low, QA (lowest significant bit) of each chip being connected to D0 of the 1MHz bus, with the QB's, QC's up to QH (highest significant bit) similarly connected to D1, D2 up to D7.

The signal to be counted is put into CCK of the first chip in the row (10MHz into chip 1, and the signal into chip 5), with the ripple-carry-over ($\overline{RCO}$) connected to both the $\overline{CCKEN}$ and CCK of the next chip in the row. This gives two 32-bit counters with the first counter in each row containing the least significant byte, and the fourth counter the most significant byte.

The two rows are started and stopped simultaneously by connecting $\overline{CCKEN}$ of chips 1 & 5 together, and all the chips are latched and cleared simultaneously by commoning RCK and $\overline{CCLR}$ respectively.

3.4.3.2 The decoding circuit.

The circuit diagram of the decoding circuit is shown in figure 3.4.

Page &FC of memory (also known as 'FRED') in the BBC is reserved for add on hardware to the 1MHz bus with small

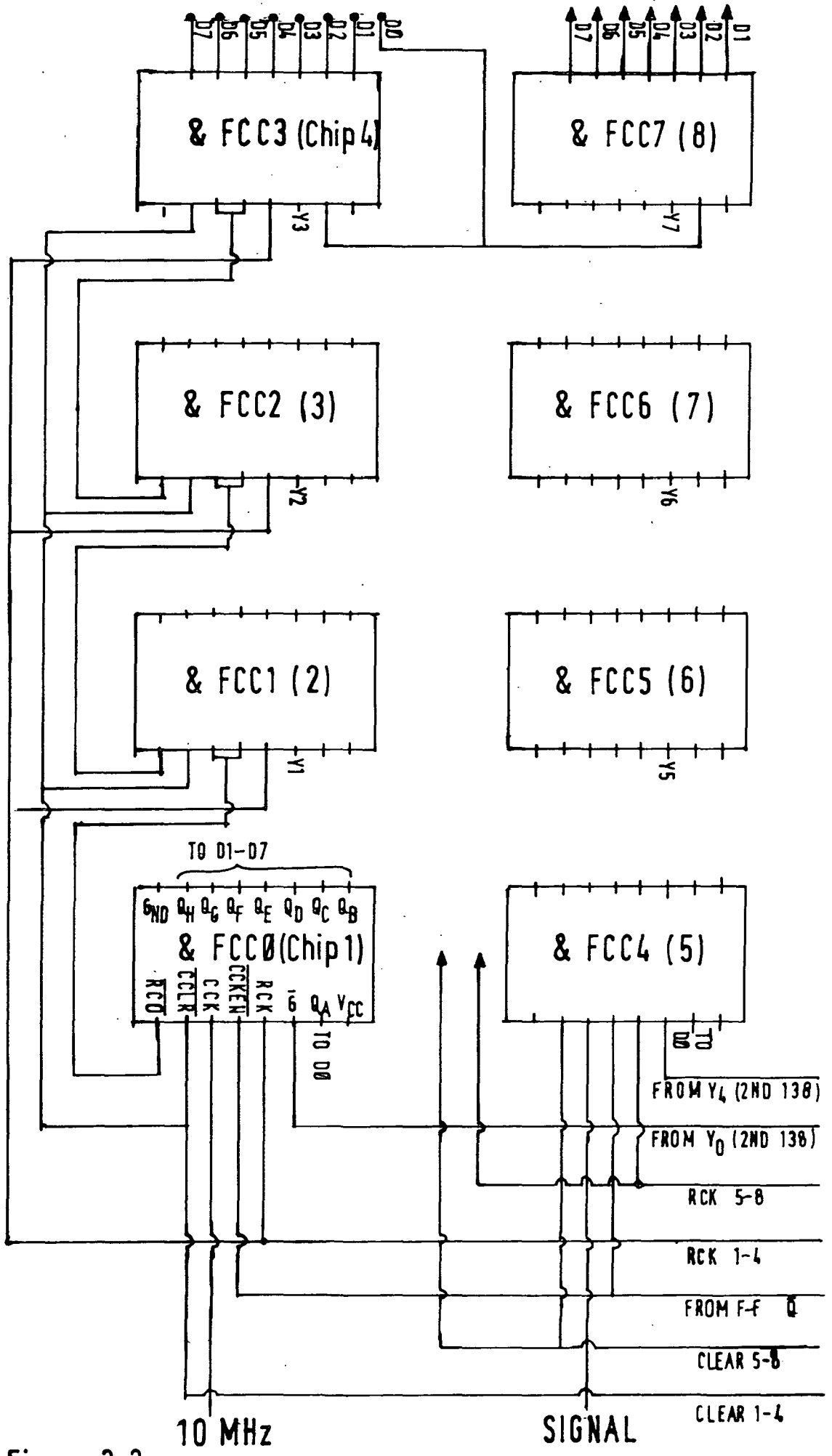

Figure 3.3
32-Bit Counter (Counting Section).

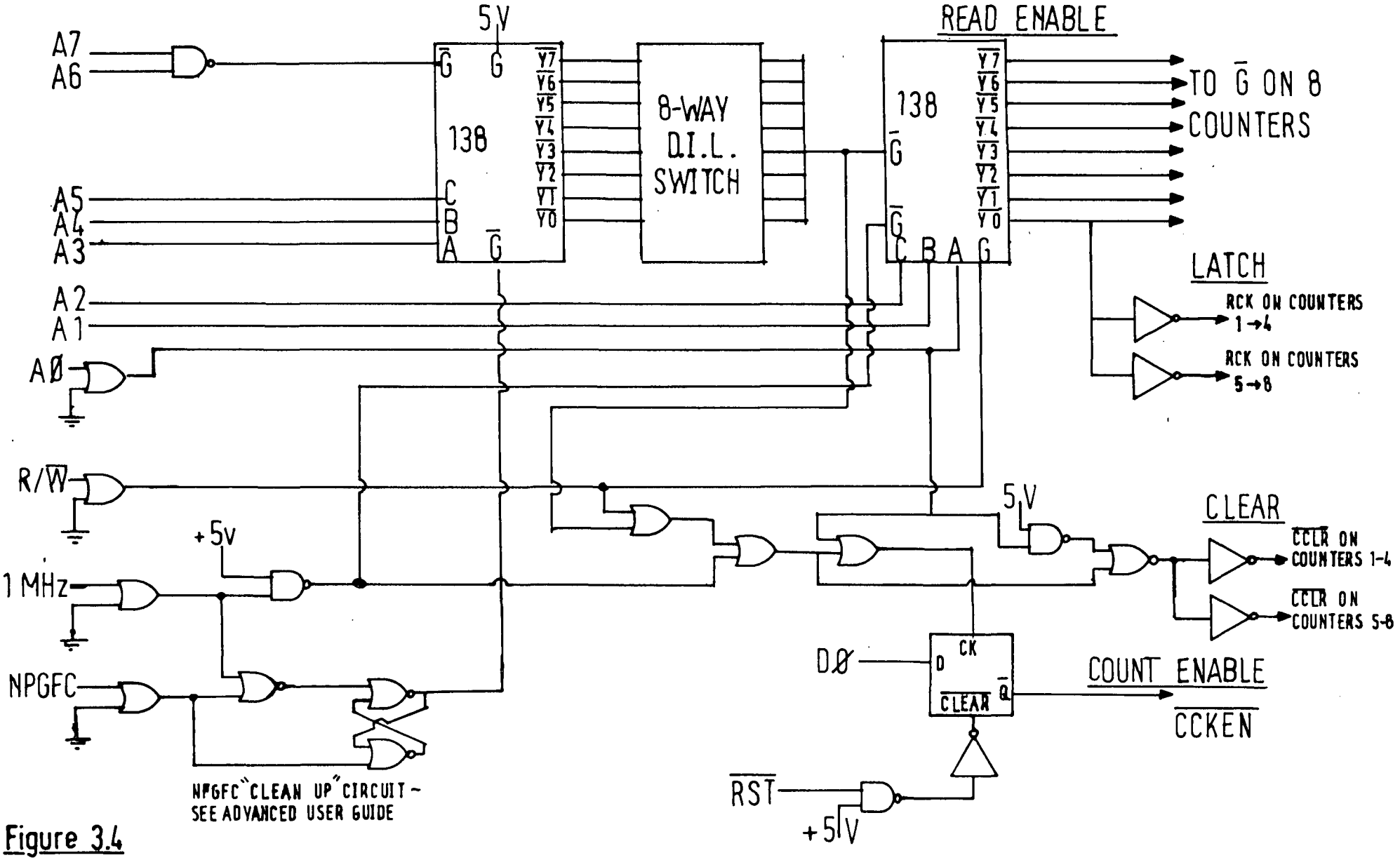

Figure 3.4

32-Bit Counter (Decoding Section).

memory requirements. Of this page, the memory between &FCC0 and &FCFE is allocated for "User Applications". When a particular device is chosen, the address is carried on lines A0 to A7, with NPGFC (Not PaGe &FC) remaining low for all addresses within FRED.

To decode the lines, two 74LS138 decoders are used. The first of these chips is used to select a board address, each board capable of having eight addressable chips (for the counter only one board is needed with an address of &FCC0). This first 138 enables the second 138 (via the eight way dual in line switch), whenever an address between &FCC0 and &FCC7 is sent. The switch provides room for further expansion to the system by allowing the board address to be changed.

The counters are enabled (i.e. started and stopped) with the D-type flip-flop, the output of which is connected to $\overline{\text{CCKEN}}$ of counters 1 and 5. When a number whose least significant bit is high (i.e. D0=1) is written to an address on the board which has A0 low (e.g. &FCC0,&FCC2,&FCC4..), Q will be sent low and counting will begin. The counters are then stopped by writing a number with D0=0 to a similar address. The counters will also be stopped by the computer being switched on or off or by a "BREAK".

By writing to the board with an address in which A0 is high, a low is sent to $\overline{\text{CCLR}}$ of all eight chips simultaneously via the two inverters, clearing all the counters.

The second 138 is used to select the chip to be read. Y0 is connected to G of counter 1, Y1 to G of counter 2, and

so on. The counter to be read is now chosen by the data on lines A2 to A0 inclusive, the lowest three bits of the address, the board address having been decoded by the first 138. The address of each counter is marked on figure 3.3.

Y0 from the second 138 is inverted and connected to RCK of all eight counters (via two inverters), ensuring that data is latched into the output registers ready for reading, whenever counter 1 is read. Although this is not necessary if the counters are stopped before being read, it is very important to ensure that data from all the counters is latched simultaneously into the output registers if the counters are read while the aquisition of data is continuing.

So, assuming a valid board address the operations can be summarised as:

Operation	Read/Write	D0	A0
Start counting	Write	High	Low
Stop counting	Write	Low	Low
Clear counters	Write	Unimportant	High
Latch data	Read from address &FCC0		
Read data	Read from counter address		

3.4.4 An opto-isolator for the 32-bit counter.

Normally, pulses from a photomultiplier are amplified to several volts and are then discriminated to give square 5V pulses. However, a discriminator was not available for the equipment at Durham, and the amplifier gave pulses with heights of between 2V and 16V. It was therefore necessary to

convert these pulses into square 5V pulses to be compatible with the TTL of the counter.

Since a height analysis of the pulses is not needed to give a measure of the diffracted intensity, it was considered unnecessary to build a discriminator, and instead, the pulses are converted to TTL by the use of the opto-isolator circuit in figure 3.5.

The 6N137 opto-isolator consists of a GaAsP input diode optically coupled to to an integrated detector comprising a photodiode, high gain linear amplifier and output transistor [67]. Providing that the input current (determined by the height of the pulse and the input resistor) is sufficient to activate the diode, an incoming pulse will give a 5V TTL output pulse. The chip also isolates the input signal from the output signal, eliminating ground loops.

3.4.5 A traverse table interrupt.

For most applications of the Lang camera, the traverse table is simply required to move backwards and forwards at a constant rate between two limits. However, for some experiments, such as step scanning section topography, described in chapter 2, it is necessary to be able to start and stop the traverse repeatedly during an exposure.

The traverse table stepper motor is driven by an Elliot controller. This has momentary action switches that start and stop the traverse, together with swiches enabling the limits to be set. The speed of traverse can be changed, but is normally left to be the slowest possible during exposure,

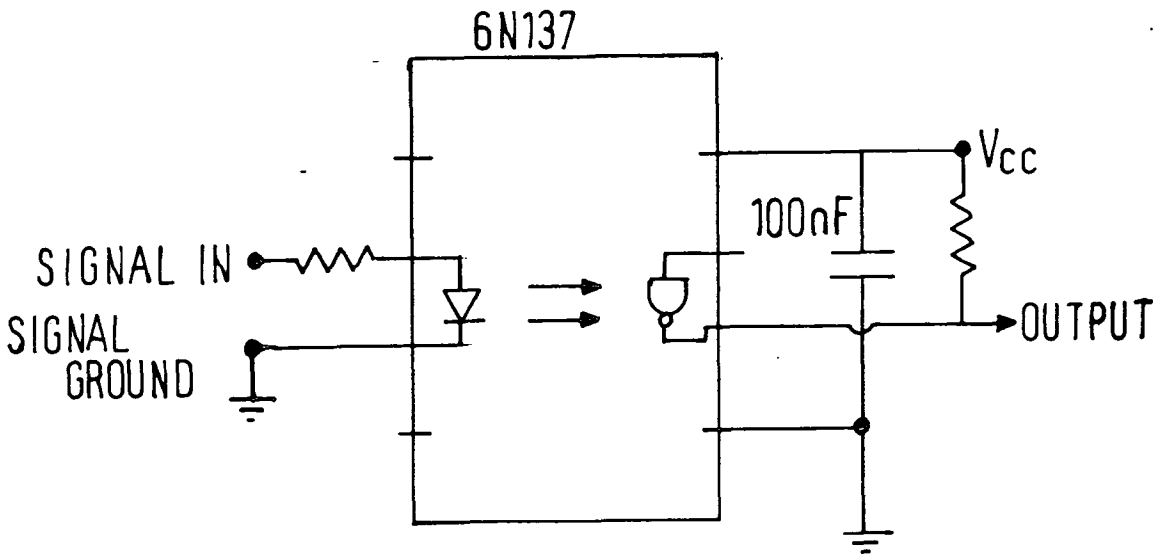

Figure 3.5

Opto-isolator circuit

to reduce vibration when the direction of traverse reverses at the limits.

Since it is unnecessary to duplicate most of the functions of the controller, it was decided to start and stop the traverse remotely by adding reed switches in parallel with the start and stop switches. Two of the remaining lines from the User Port (PB6 and PB7) are used to activate the switches, each connected to the base of a transistor, which allows current to flow from the 5V supply through the coil of the reed switch whenever the line goes high, closing the switch.

Hence, by sending PB6 high momentarily, the traverse is started and it is stopped by sending PB7 momentarily high. Since the motor is driven at a constant speed, the distance traversed is controlled by the time interval between starting and stopping the traverse.

3.5 ABAC Software

A fully anotated listing of the ABAC control program is given in appendix A. Descriptions of the Basic commands used may be found in the BBC User Guide [68] and the assembly language commands in the BBC Advanced User Guide [65].

The operation of the ABAC can be split into basic building blocks. In the first place, routines are needed to drive the stepper motor and to read the status of the turntable limit switches. Secondly, the counter must be able to be started, stopped, latched, read and cleared (though not necessarily in that order). Finally an algorithm is needed to interpret the change in the count rate and to use

this information to adjust the rotation of the sample.

The control of all of the BBC's interface ports is best effected by assembly language routines, as these access the memory locations much quicker than routines written in BASIC. Also, to provide compatibility with the BBC second processor, it is important that devices on input/ouput ports are not accessed directly from memory, but by a resident machine code routine. This OSBYTE call can be used to control a variety of the computer's functions.

Each operation of the stepper motor and counter is controlled by one of these routines, which are called from assembly language by BASIC commands. OSBYTE calls &92 and &93 are used to read from and write to the 1 MHz bus, and calls &96 and &97 to read from and write to the User Port.

3.5.1 Control of the stepper motor

For a turntable rotation of 1/1000th of a degree, the motor controlling the turntable must be moved in half step mode. That is, instead of energising the coils in the order 1, 2, 3, 1, 2 etc., they must be energised in the order 1, 1 and 2, 2, 2 and 3, 3, 3 and 1, 1, 1 and 2 etc. This gives twice as many steps per 360° as driving in normal mode.

From the User port, line PB3 is used to energise coil number 1, PB4 coil 2 and PB5 coil 3. So, to drive the motor clockwise, the following sequence of values of Y must be written to the port : 8 (coil 1), 24 (1 and 2), 16 (2), 48 (2 and 3), 32 (3), 40 (3 and 1).

To drive it anti-clockwise, the values are sent in the reverse order.

These values are contained in an array and are transferred sequentially to the OSBYTE call using FOR-NEXT loops in two BASIC procedures, one for clockwise movement, the other for anti-clockwise movement. After each step, the status of the limit switch in the direction being driven is read by the computer. If that switch is closed, then the table is driven 20/1000 of a degree away from the limit, a message appears on the screen, and the program waits for a response from the operator. In this way, it is impossible to drive the table past either the clockwise or anti-clockwise limit.

The position of the turntable in 1000ths of a degree is recorded by the variable PSN% which is continuously displayed in the corner of the computer monitor. This is updated whenever the turntable is rotated, with clockwise steps increasing its value and anti-clockwise steps decreasing it.

3.5.2 Control of the counter.

The counter is controlled by four assembly language routines, "clear", "start", "stop", and "read", which are called from the procedure PROCcount. To measure the count rate, the counting time is first set, either by the operator, or from another routine. The counters are cleared and then started, with a timing loop in the program started simultaneously. After the set counting time, the counters are stopped, and the data is read into the computer.

Referring to figure 3.3, the counters are read in the order: least significant byte of the 10MHz row (counter 1),

up to most significant byte of the signal row (counter 8). The number of counts in each counter is stored in the array NUM% (counter 1 in NUM%(0), 2 in NUM%(1), etc.) and the total number of counts in the 10MHz row is then given by:

$$X1 = NUM\%(0) + 2^8 \times NUM\%(1) + 2^{16} \times NUM\%(2) + 2^{32} \times NUM\%(3)$$

Similarly, the number of counts in the signal row is given by:

$$X2 = NUM\%(4) + 2^8 \times NUM\%(5) + 2^{16} \times NUM\%(6) + 2^{32} \times NUM\%(7).$$

Since there will be 10^7 counts in the 10MHz counter for every second the counters have been enabled, the exact counting time in seconds is now given by $X1/10^7$, and hence the count rate in counts per second by $X2 \times 10^7/X1$.

3.6 Software routines.

By using a microcomputer to control the ABAC, a variety of procedures can be built up to perform different tasks, using the routines described above. An outline of the various tasks that can be performed at present is given below.

3.6.1 Disengaging the stepper motor.

This is a routine to remove the holding torque of the motor, thus allowing the turntable to be rotated manually. It is accomplished by writing zero's to all three inputs of the stepper motor driver simultaneously, effectively "switching off" the power to the motor.

3.6.2 Count only.

The count only routine allows the count rate to be measured continuously by the computer, with the counts per second being displayed on the computer monitor. To do this, the counting time is first set by the operator. The program will then count for this time, display the counts per second on the screen, clear the counters and start counting again, continuing until the routine is interrupted by the space bar being pressed. The successive count-rates are displayed in rows of four, with new rows underneath. When the screen is full, the previous values are moved up the screen with the new values being added to the bottom of the screen. In this way, up to thirty-nine previous count-rates are displayed.

During counting, the turntable can be rotated manually by disengaging the stepper motor, using the routine described in 3.6.1.

3.6.3 Rotating the turntable via the keyboard.

This routine allows the turntable to be rotated by pressing one of two keys on the keyboard. For simplicity, the "arrow left" key from the cursor control keys is used for anti-clockwise movement and the "arrow right" key for clockwise movement.

The procedure works by redefining these two keys and then continually looking within a loop to see whether either has been pressed. If so, the motor is moved by one step for each pass of the loop during which the key is pressed. At the end of each loop, the input buffers from the keyboard are flushed to ensure that movement stops as quickly as

possible after the key is released. In practice this means that a quick key press will move the motor by just one step. Three speeds of rotation are possible by setting a time delay (using a machine code loop) between each step.

3.6.4 Rotate the turntable and count.

By combining the above two routines, the turntable can be rotated from the keyboard whilst the X-ray intensity is displayed on the computer monitor.

This routine therefore consists of the loop described in 3.6.3 with a counting procedure contained within it. For each pass of the loop, the procedure will count for a set time, display the count rate in the format described in 3.6.2, look to see if either of the arrow keys (or the space bar) have been pressed and if so, will rotate the turntable (or leave the routine). The counting time and step length are set by the operator, and since these will now limit the speed of rotation, the machine code delay loop is no longer necessary.

3.6.5 The ABAC procedure.

The feedback routine used to give automated Bragg angle control is shown in figure 3.6, and is described below. With this routine, the peak of the rocking curve is quickly found and the sample is held to within one or two steps of it at all times.

Before the computer takes over control, the operator is asked to orient the sample so that it is on part of the rocking curve. This can be done either with the cursor

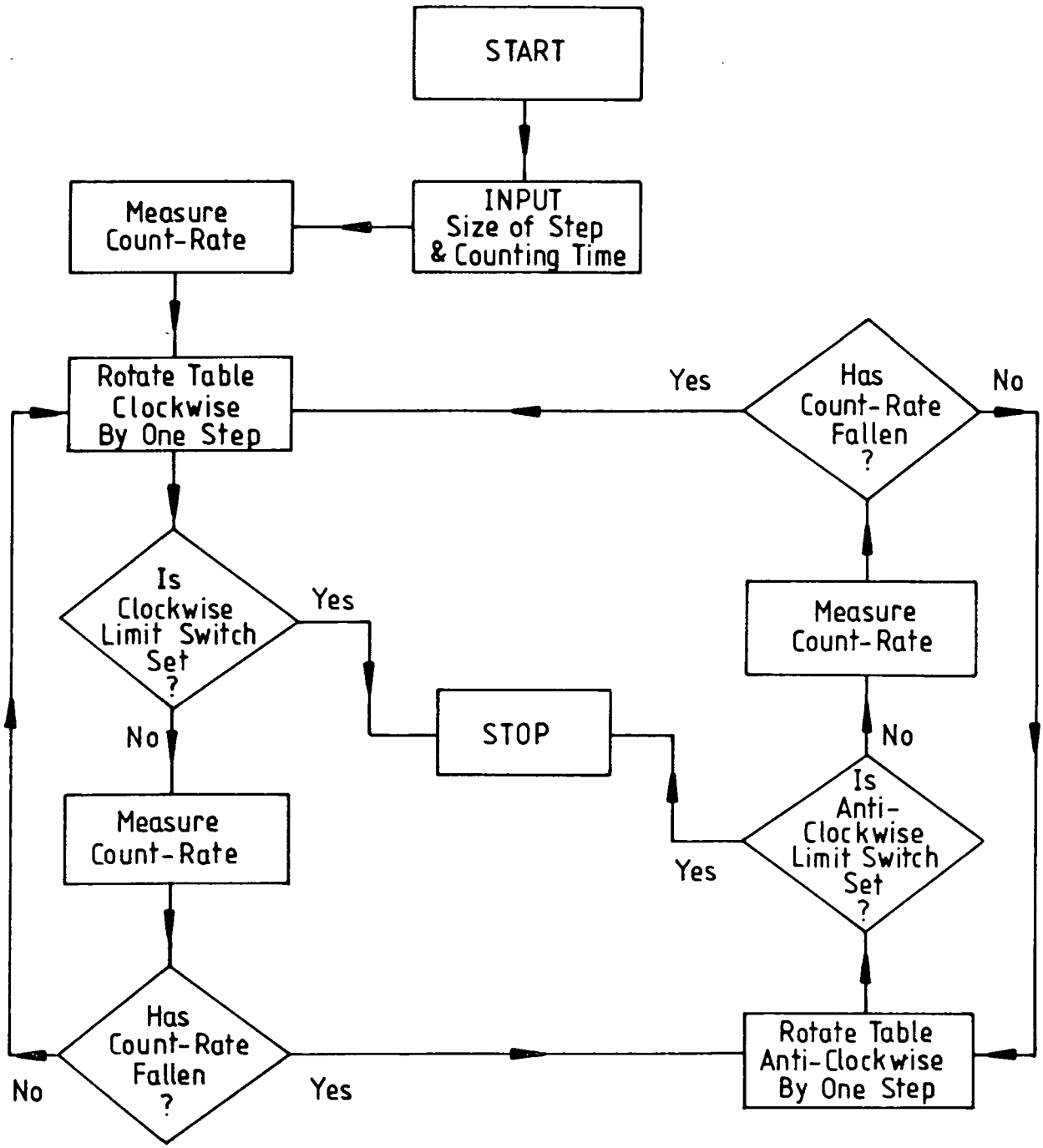

Figure 3.6

The ABAC Routine

control keys (section 3.6.3) or manually by removing the holding torque of the motor (section 3.6.1). Now, to enable the routine to react quickly enough to changes in orientation caused by the traverse, both the step size and the counting time are requested. The step size will need to be greater than the maximum misorientaion that can occur during a time roughly equal to the counting time. In most instances, a step size of two (2/1000th of a degree) works well, with a counting time of around 1 second for lightly bent crystals (R≈50m) and around 0.4 seconds for more heavily distorted ones (R≈2m).

The routine starts by measuring the diffracted intensity and then rotating the sample anti-clockwise by one step. The count rate is measured again and if the diffracted intensity is greater than the previous measurement, the sample is once more rotated in an anti-clockwise direction. However, if the diffracted intensity has dropped, then the sample is rotated in a clockwise direction and the count rate re-measured. The routine continues in this way, reversing the direction of rotation whenever there is a drop in diffracted intensity, until interrupted by the operator. This is similar in form to the algorithm used by van Mellaert and Schwuttke [64]. At all times the count rates are displayed on the screen in the format described in section 3.6.2, together with the position of the table, the maximum count rate so far recorded, and the average of the previous five count rates.

Should the turntable reach either of its limits then the routine is stopped in the way described in section

3.5.1. To allow the X-Ray shutter to be closed (and to guard against generator failure) without the turntable being rotated continuously in one direction, the turntable is not rotated whenever the count rate drops to below 20 counts per second, although the count rates are continued to be displayed. When the count rate returns to a high value, the routine continues as before.

3.6.6 Step Scanning Section Topography Routine.

By combining the ABAC routine with the traverse table interrupt (section 3.4.5) it is possible to use the Lang camera for step scanning section topography [37,38]. The routine to do this is shown in the flow diagram, figure 3.7 and works in the following way.

Firstly, the number of sections required, the exposure per section and the distance between them is entered by the operator. The routine also asks for the step size and counting time for the ABAC part of the routine. In a similar way to the ABAC routine, the crystal is oriented on part of the rocking curve and the computer takes over control.

To begin with, the Bragg peak is found using the ABAC routine for 20 seconds. After this time, the sample is held stationary and there is a delay for the desired exposure time. After the exposure is completed, the traverse table is started and the ABAC routine is entered. After the table has traversed the required distance, the traverse table is stopped, with the ABAC routine continuing, using a large counting time and small step size for 20 seconds to ensure that the crystal is close to the Bragg peak. The routine

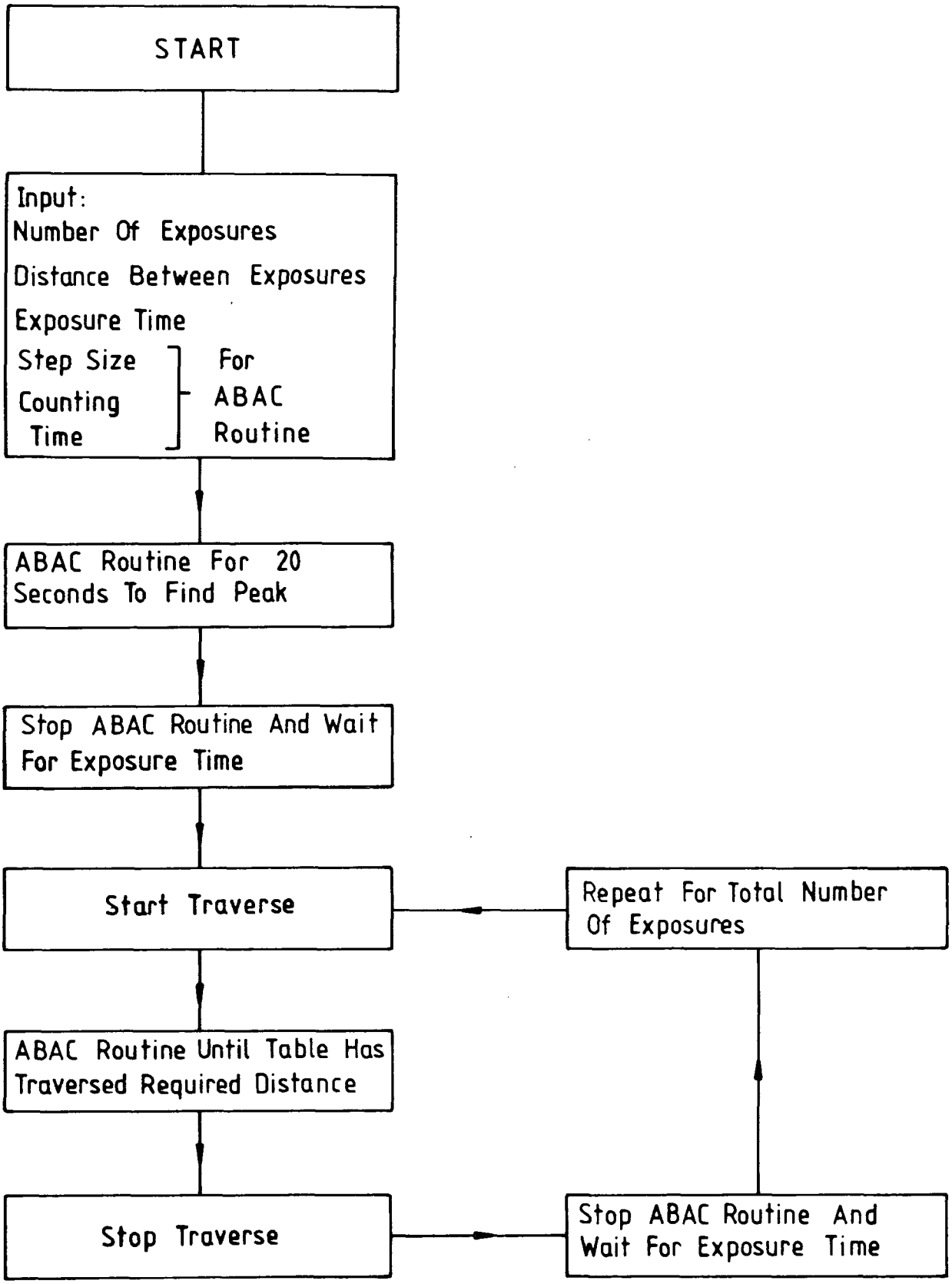

Figure 3.7

The Step-Scanning routine

again waits for the exposure time before moving the table to the next exposure, the routine being repeated for the total number of exposures.

3.7 Summary.

The Automated Bragg Angle Controller described above has been in operation for nearly three years and has worked effectively without fault since it was first installed. It has also proved to be extremely tolerent to both the large fluctuations in the diffracted intensity encountered in heavily dislocated crystals and the unstable nature of the incident beam intensity from a fifteen year old rotating anode X-ray generator. This is in many ways because of the simplicity of the design of the add on hardware and of the software routines. By utilising many of the existing features of the Lang camera, the cost and complexity of the system are kept to a minimum.

The effectiveness of the controller is demonstrated by the Lang topographs of mechanically bent wafers presented in chapter 4. It is clear from these that the whole width of the sample is evenly exposed with no loss in resolution for even the most severe distortions. Such topographs would not have been possible without a Bragg angle controller.

Chapter Four

Lang and section topography of bent crystals.

4.1 Introduction.

This chapter describes a series of experiments to investigate the influence of an impressed curvature upon the contrast of defects in Lang and section topographs. The experimental procedures required for the work are described and an explanation of the contrast differences between Lang and Hirst topographs is proposed. Finally, the systematic change in contrast with increasing bending is investigated for both Lang and section topography.

4.2 Experimental Procedure.

The samples used for this work were both cut from a four inch silicon wafer provided by British Telecom Research Laboratories. The wafer had a (111) surface, was 580μm thick and had been placed in part of a furnace which resulted in a high temperature gradient across it, causing a high density of slip dislocations as shown by the Hirst topograph of the sample, figure 4.1a. The sample had been etched on the side used as the entrance surface and lapped and polished to a smooth, strain free finish on the side used as the exit surface. No curvature could be measured by single crystal methods. Two strips were cut from the sample, each measuring approximately 15mm by 45mm and their relationship to each other and the original wafer is shown in figure 4.1b.

The samples were bent by placing them in the four line bending jig shown in figure 4.2. This consists of two 4mm

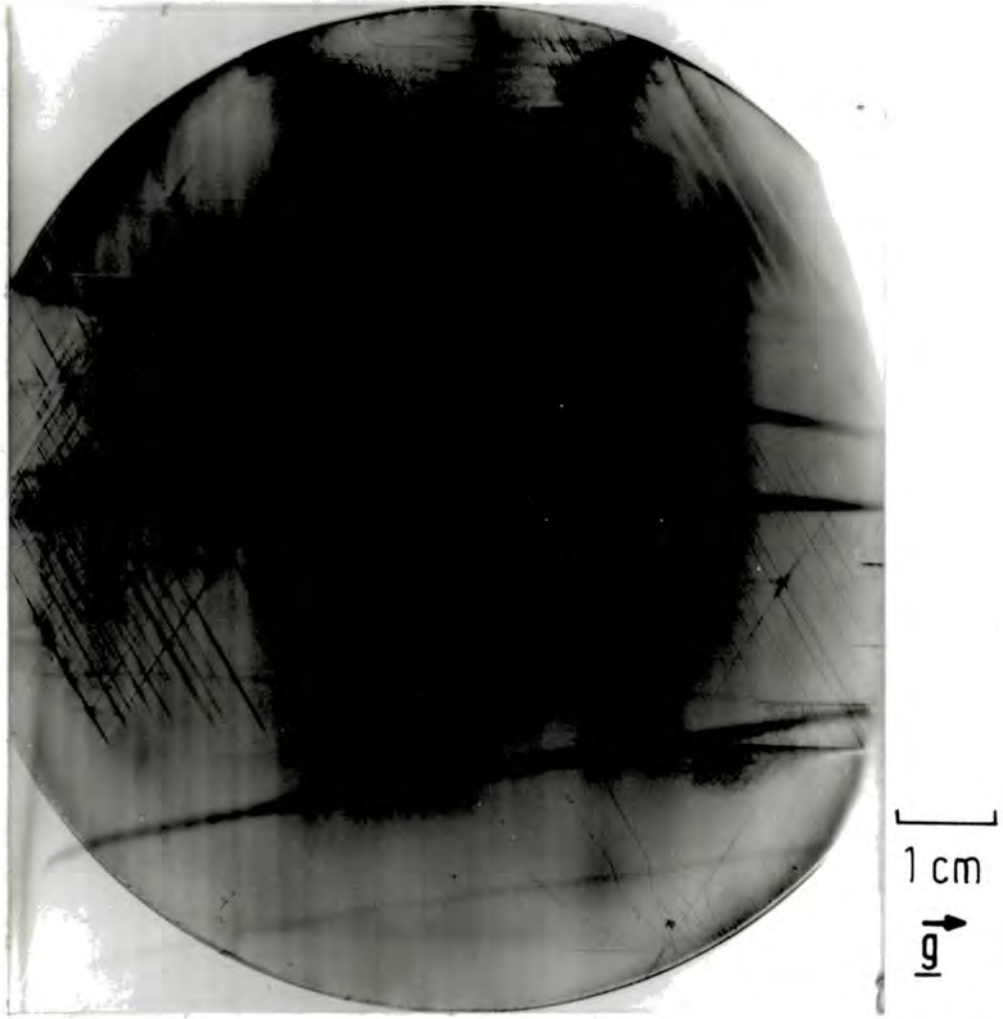

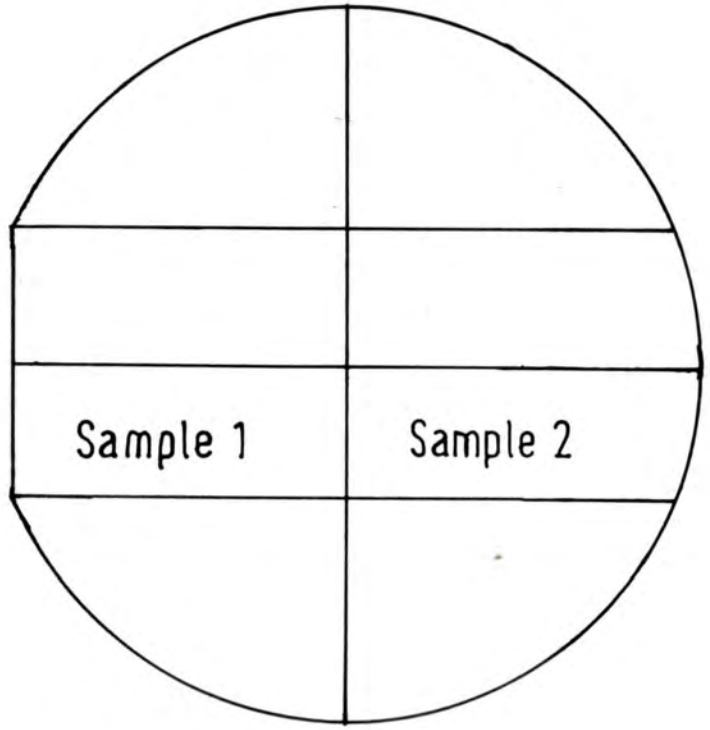

Figure 4.1
a) $2\bar{2}0$ Hirst Topograph
b) Relation of samples to original wafer

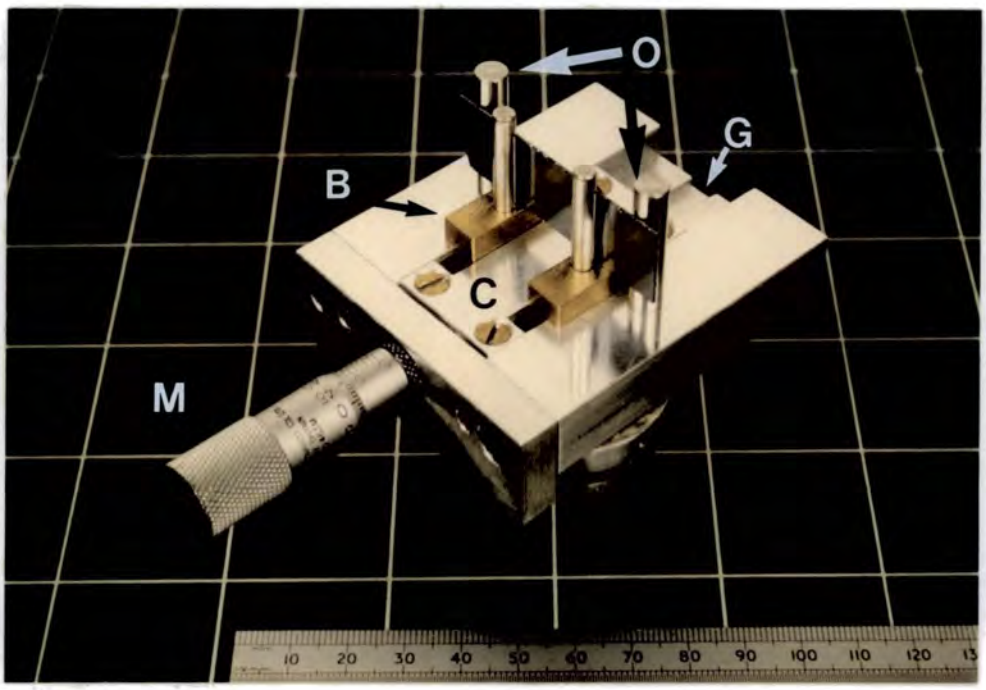

Figure 4.2

The four line bending jig used in these experiments with sample 2 in place.

diameter silver steel pins separated by 20mm, mounted on a sliding block (B) acting against two 6mm diameter fixed outer pins (O) separated by 40mm. The block fits exactly in the groove (G) ensuring that there is no sideways rocking movement and the pins are maintained perpendicular to the top surface by the closely fitting cover plate (C). The bending moment is then applied by a micrometer head (M) acting against the sliding block, the return tension being provided by the elasticity of the sample.

The jig is mounted on a goniometer which allows translational movement in two orthogonal directions so that the sample can be aligned to be directly over the rotation axis of the turntable. The goniometer also allows the jig to be tilted in a direction parallel to the sample's surface.

Since the jig was carefully made with the pins exactly perpendicular to the top and bottom surfaces, the pins could be aligned parallel to the collimating slit, which is exactly perpendicular to the turntable of the Lang camera, by levelling the top surface of the jig with the aid of a spirit level. The reading of the tilt stage for this condition was then noted and the sample adjusted for tilt by maximising the diffracted intensity of the Bragg reflection, measured for various rotations of the tilt stage. Once the optimum value of tilt had been found the tilt stage was returned to its original position, once more placing the pins parallel to the collimating slits, and the sample was tilted by placing packing under one edge. The diffracted intensity was then checked once more and final adjustments were made to the tilt. For the two samples studied here, the

bottom edges were cut exactly parallel to the $\bar{1}10$ direction and no tilt adjustment was needed. To avoid any friction between the sample and the top of the sliding block on which it rests, the crystal was placed on two human hairs, sufficiently thick to raise it off the top surface of the jig.

The curvature of the sample was found by measuring the misorientation of the Bragg planes with position along the sample, using the following procedure. The Bragg peak at one position of the traverse, preferably close to one end of the possible traverse range defined by the inner pins of the jig, was found and its angular position noted.

The crystal was then moved by a distance Δx measured on the traverse controller (section 3.2) and the average position of the Bragg peak at this point found in the same way as before. The radius of curvature was then given, providing that the direction of traverse was parallel to the unbent crystal surface by:

$$R = \frac{\Delta x}{\tan \Delta\theta_P} \qquad (4.1)$$

where $\Delta\theta_P$ is the difference between the angular position at the two points.

However, since the peak for a single crystal rocking curve is fairly broad and the vertical extent of the beam gives diffraction from a large area of the crystal, the peak position was often difficult to determine. The ABAC routine described in section 3.6.5 was therefore used. Once it has found the peak this routine oscillates around it, displaying

the average position of the turntable after every ten steps. Averaging ten of these therefore gave an average of 100 positions. Furthermore, the deviation from the mean gave an estimate of the inhomogeneity of the bending, since for perfect cylindrical bending the whole of the illuminated crystal will diffract at the same angular setting giving a small range. However, for an imperfectly bent crystal, diffraction will occur at different angular positions at different heights giving a large deviation in the position of the peak.

It is not enough however to know the overall curvature of the sample, one must also discover if the crystal is bent homogeneously, that is, cylindrically with the axis of the cylinder parallel to the pins. As stated above, non-uniform bending is usually accompanied by a large rocking curve for a ribbon incident beam, since diffraction only occurs for a small height of crystal for a particular angular postion. To check the homogeneity of the bending the vertical extent of the beam must therefore be limited and the angular position of the diffraction maximum plotted as a function of height.

In practice this was done by placing a horizontal slot cut in a lead sheet after the collimating slit so that the incident beam was limited to a height of about 1mm. The vertical position of the beam could then be simply changed by raising or lowering the slot. The position of the maximum was measured close to the top and bottom edges of the sample for several positions of the traverse. An example of the curvature uniformity map is given in table 4.1.

	Traverse position (mm)		
	8.700	9.300	9.850
Height of beam (mm)			
0	12	16	20
0.5	12	15	19
1.0	11	15	19

Table 4.1

Curvature uniformity map, showing the angular position of the Bragg peak in 1/1000th degree.

The criterion adopted for homogeneous bending was that there should be less than 2/1000th of a degree difference in the position of the peak between the top and bottom of the sample for any position of the traverse. Furthermore the crystal must have been adjusted to be within 15 minutes of arc of the optimum tilt position.

Even though the jig was carefully constructed and several modifications were made to make the bending as even as possible, it was still found to be impossible to reach the above criterion, the best uniformity being of the order of 15/1000th's of a degree difference between the top and bottom edge of the crystal. To compensate for this it was necessary to use small pieces of 10μm thick nickel foil as packing between the pins and the sample in three places. Using this rather fiddly method, it was always possible to meet the homogeneity criterion and often no difference in peak position with height could be found. Whilst the jig

could possibly have been redesigned to include a more convenient form of adjustment such as screws in the top and bottom of the pins, the above method worked well and the length of time required to construct a new jig made this course of action undesirable.

To take the topographs, the crystal was held on the peak of the rocking curve as it traversed by the ABAC described in chapter 3. The film holder was mounted securely onto the bending jig and therefore rotated with the sample. All of the topographs presented in this chapter were taken on 50μm Ilford L4 nuclear emulsion plates with $MoK\alpha_1$ radiation. The highly polished side of the sample was the exit surface and the entrance surface was taken as having an orientation of 111. The width of the collimating slits was 150μm for Lang topography and 10μm for section topography. The experimental set-up is shown in figure 4.3.

4.3 Contrast in Hirst topographs.

Although the Hirst technique described in section 2.2.5 gives comparable images to those in Lang topographs [44,69], several differences between them are obvious, most noticeably the enhanced white dynamical image and the decreased visibility of the direct image. In Hirst topographs a symmetric reflection is normally used and in this geometry no change in the propagation of x-rays within the crystal is expected because the diffracting planes remain flat, the change in tilt being exactly compensated by the dilation, giving an effective misorientation of zero [10,13,16] (section 1.5). The change in contrast is

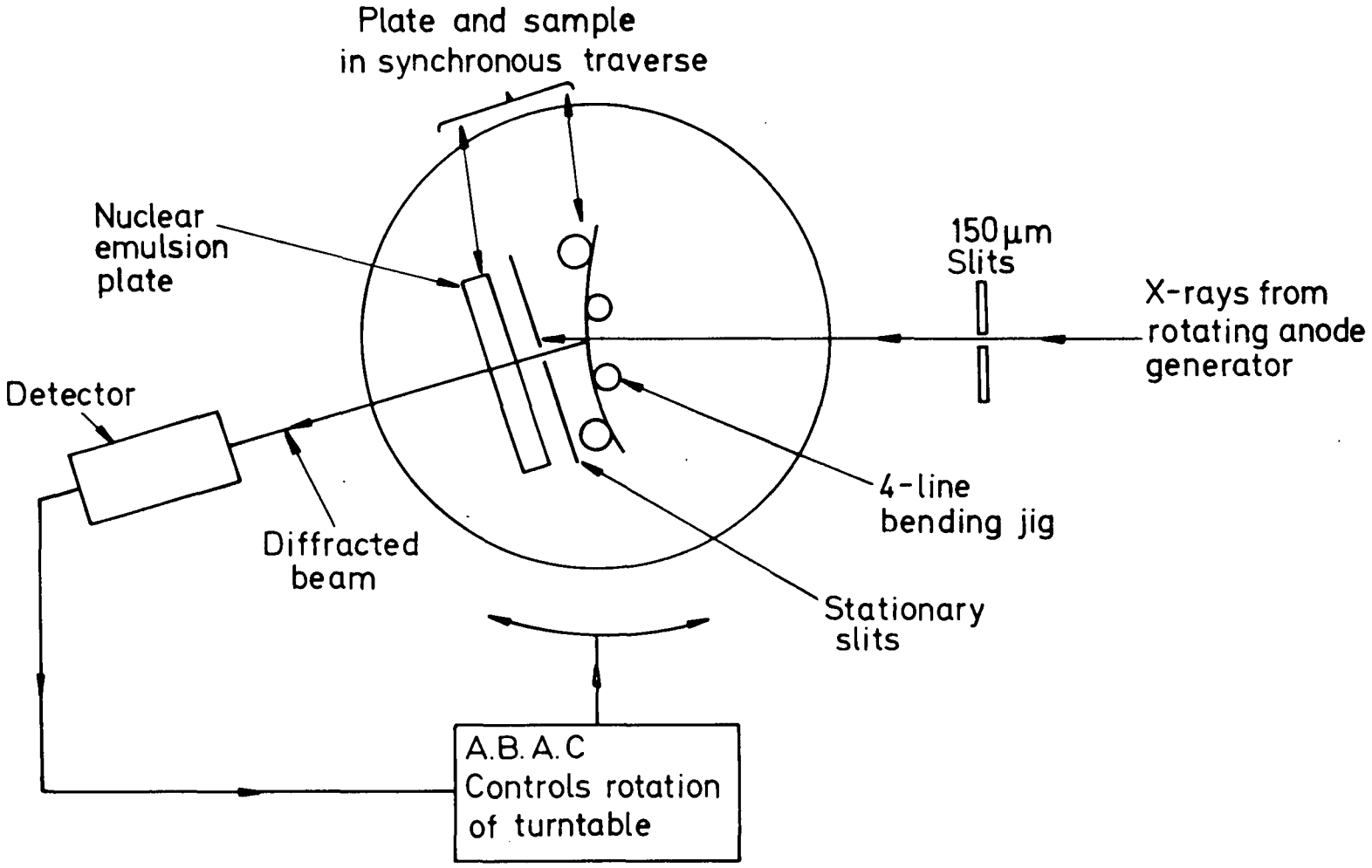

Figure 4.3

Lang Topography of Curved Crystals

therefore unexpected and the aim of the experiments described here is to discover whether the discrepencies are a real phenomenon or an artefact of the Hirst experimental procedure.

Figure 4.4a shows a $\bar{2}20$ Lang topograph (μt = 1.0)[1] of sample 1 with no bending. Two sets of inclined slip dislocations visible as lines of enhanced intensity are noteworthy and are marked by A and B. Set A is an extended pile up of dislocations parallel to <101> lying on the $1\bar{1}\bar{1}$ slip plane. The set B dislocations lie almost parallel to <110> and extend from the top (exit) surface through to the bottom (entrance) surface, having a large screw component. The end of the dislocation outcropping on the exit surface (e) is easily identified by the dynamical image being localised close to the direct image. Dislocations in set A exhibit mostly direct images whilst those in set B show the classic dark direct (d) and light dynamical (y) images separated by the grey intermediary image in which interference fringes are clearly visible.

Figure 4.4b shows the same area of crystal, homogeneously bent to a curvature of $0.008m^{-1}$ (R = 12.5m) and no difference in contrast between this and the unbent sample can be seen. Furthermore, in agreement with the Eikonal theory there is no change in the diffracted intensity upon bending. The significant contrast differences observed in the Hirst technique are therefore not explained by the effects of uniform bending.

---

[1] μt is calculated using:

$\mu = 1/2\ (1/\gamma_o + 1/\gamma_g)\ \mu_o$

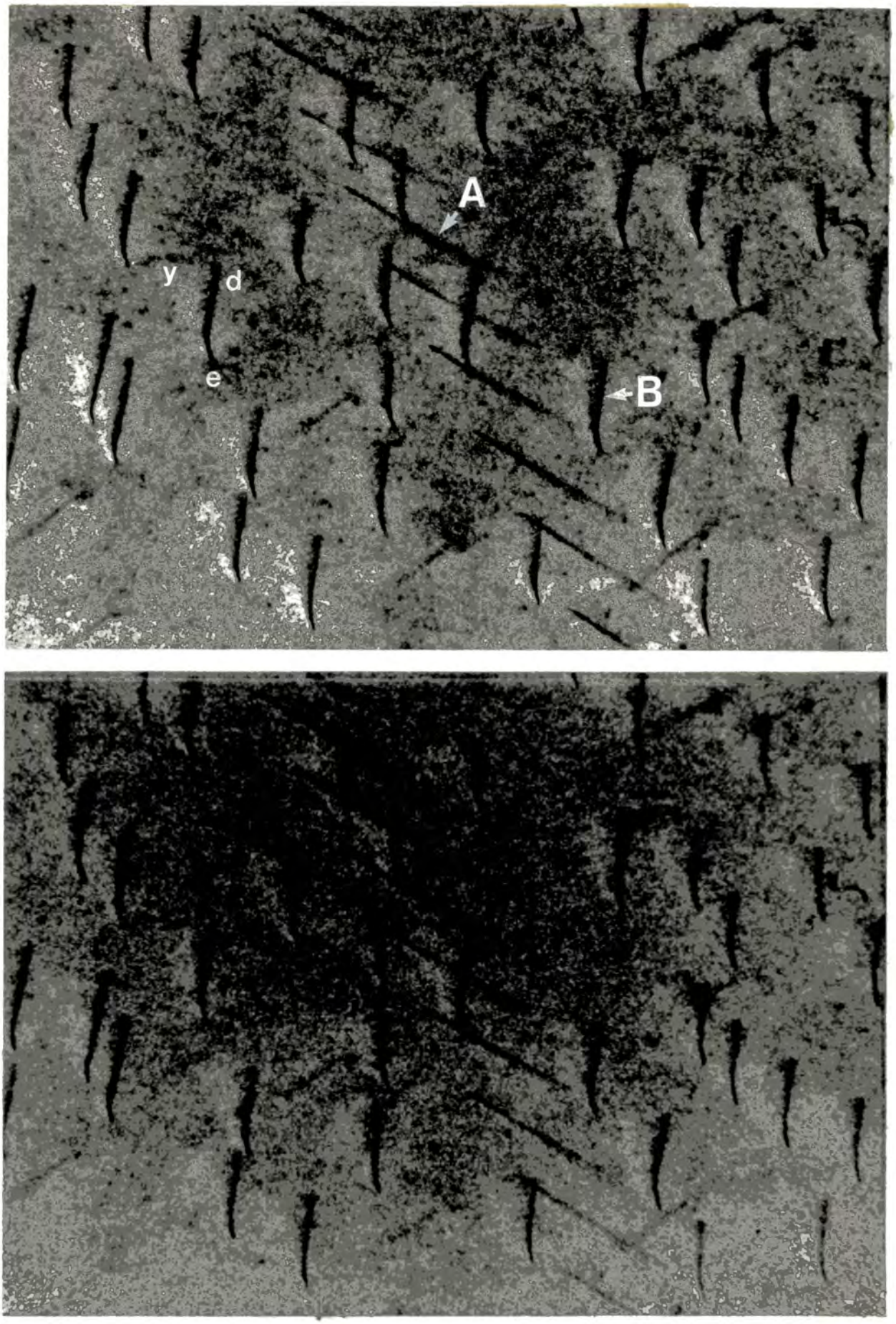

Figure 4.4

$\bar{2}20$ Lang topographs of sample 1.
a) Unbent
b) Sample homogeneously bent to R = 12.5m

Now compare figure 4.4 with figure 4.5a, the topograph of the sample bent to a curvature of $0.029m^{-1}$ (R = 35m). The sample was in this case bent inhomogeneously, that is there is a torsional moment applied about the diffracting plane normal caused by an incorrectly aligned bending pin. Unfortunately the amount of torsion was not measured, but the amount of distortion required to produce the image change is estimated in the next section.

As we can see, the torsion dramatically changes the character of the contrast. Firstly, the diffracted intensity rises by a factor of $\sim$ 1.5. Secondly, the direct images, most notably of the set A dislocations, become less visible and thirdly, a strong white dynamical image is seen extending to a greater distance than in the unbent sample and to both sides of the direct image. As the bending is increased, figure 4.5b, the extent of these white images decreases and the direct images of the set A dislocations become almost invisible. The direct images of the set B dislocations are also diffracting with similar intensity to the perfect crystal and are only visible because of the large area of depleted intensity around them.

Figure 4.6 is a topograph where the crystal has been bent to a radius of curvature of approximately 2m. The sample had been more carefully adjusted for inhomogeneous bending and as a consequence the whole of the sample is imaged. There is still approximately 1/100th of a degree difference in the peak position between top and bottom and this manifests itself in the more pronounced dynamical images and the higher diffracted intensity. These images are

a)

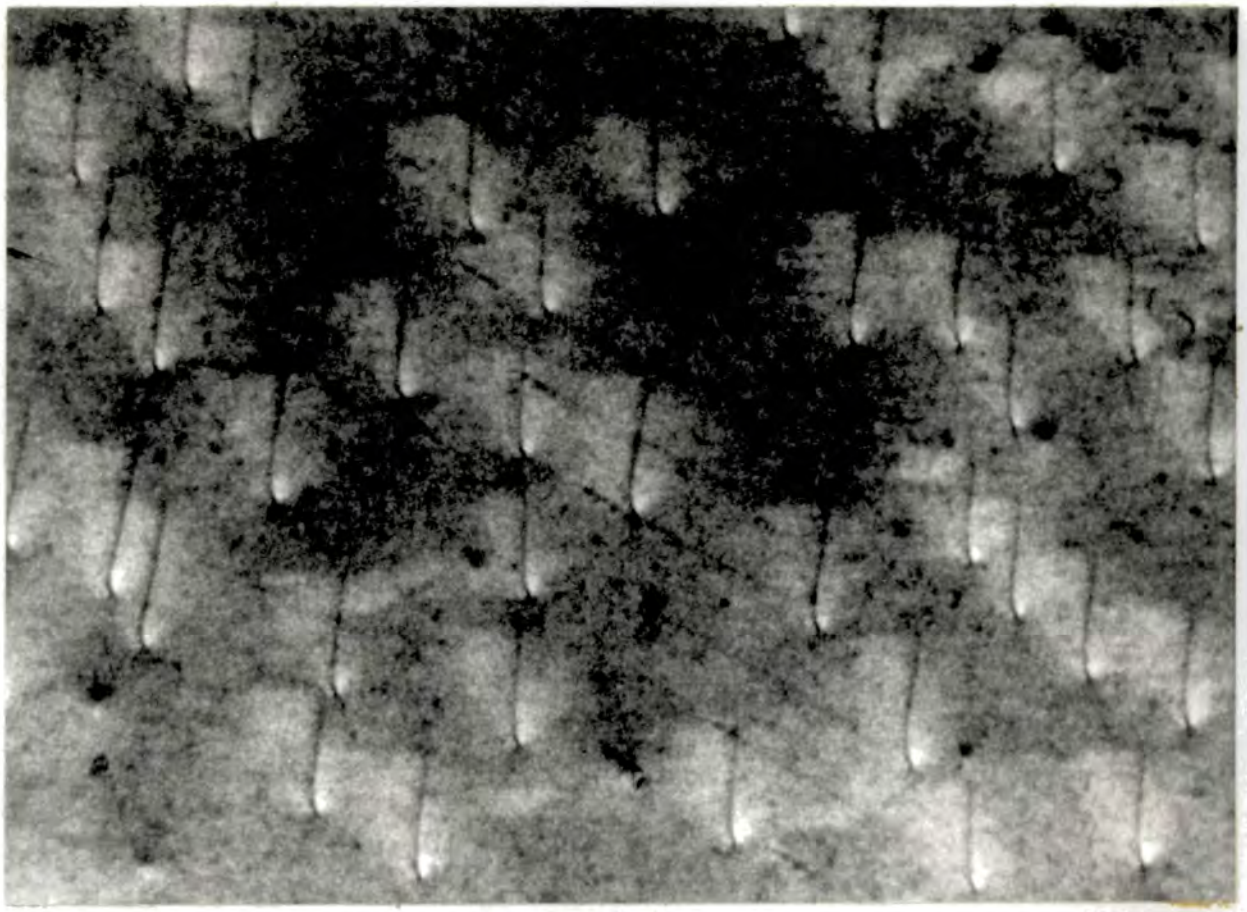

b)

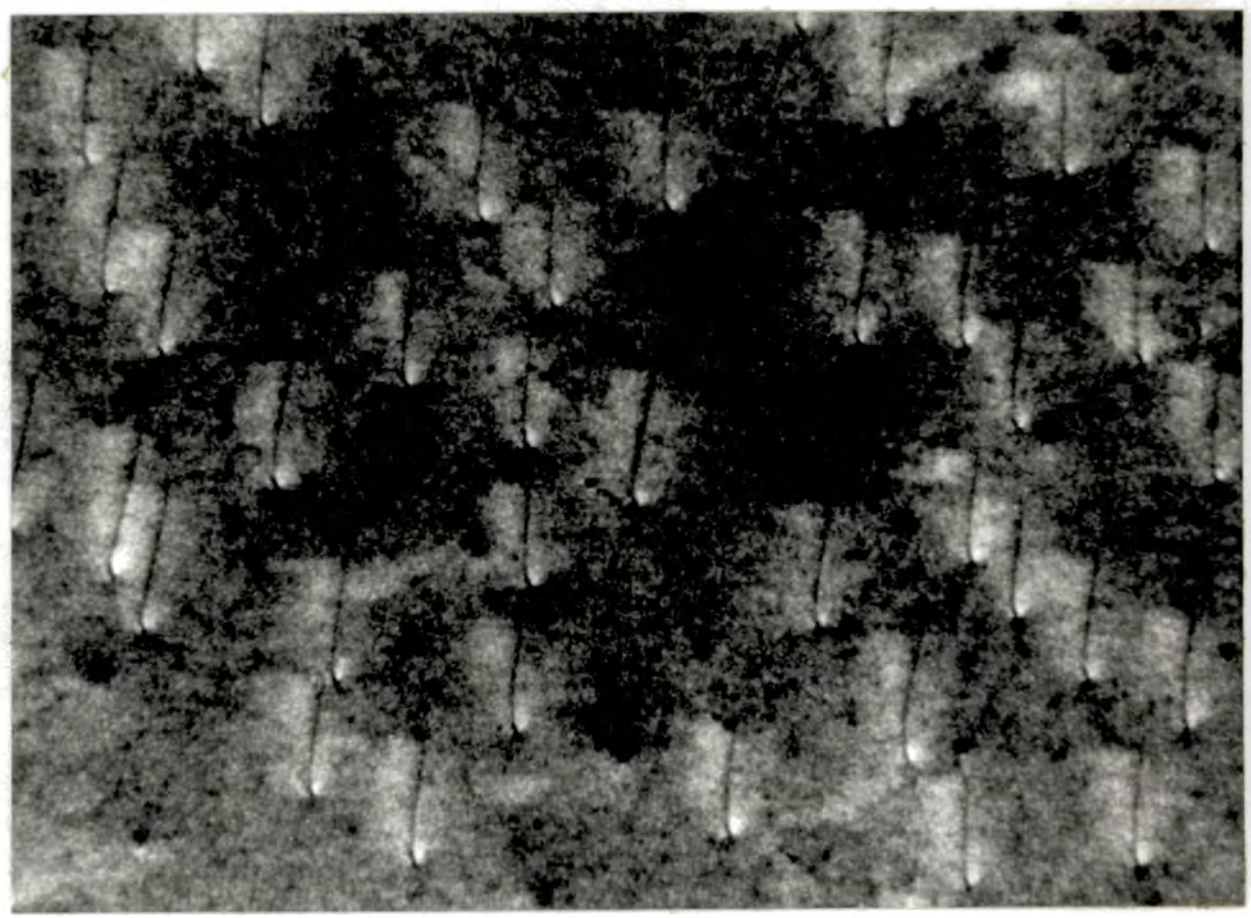

Figure 4.5

$\bar{2}20$ Lang topographs of sample 1.
a) Sample inhomogeneously bent to R = 35m
b) Sample inhomogeneously bent to R = 18m

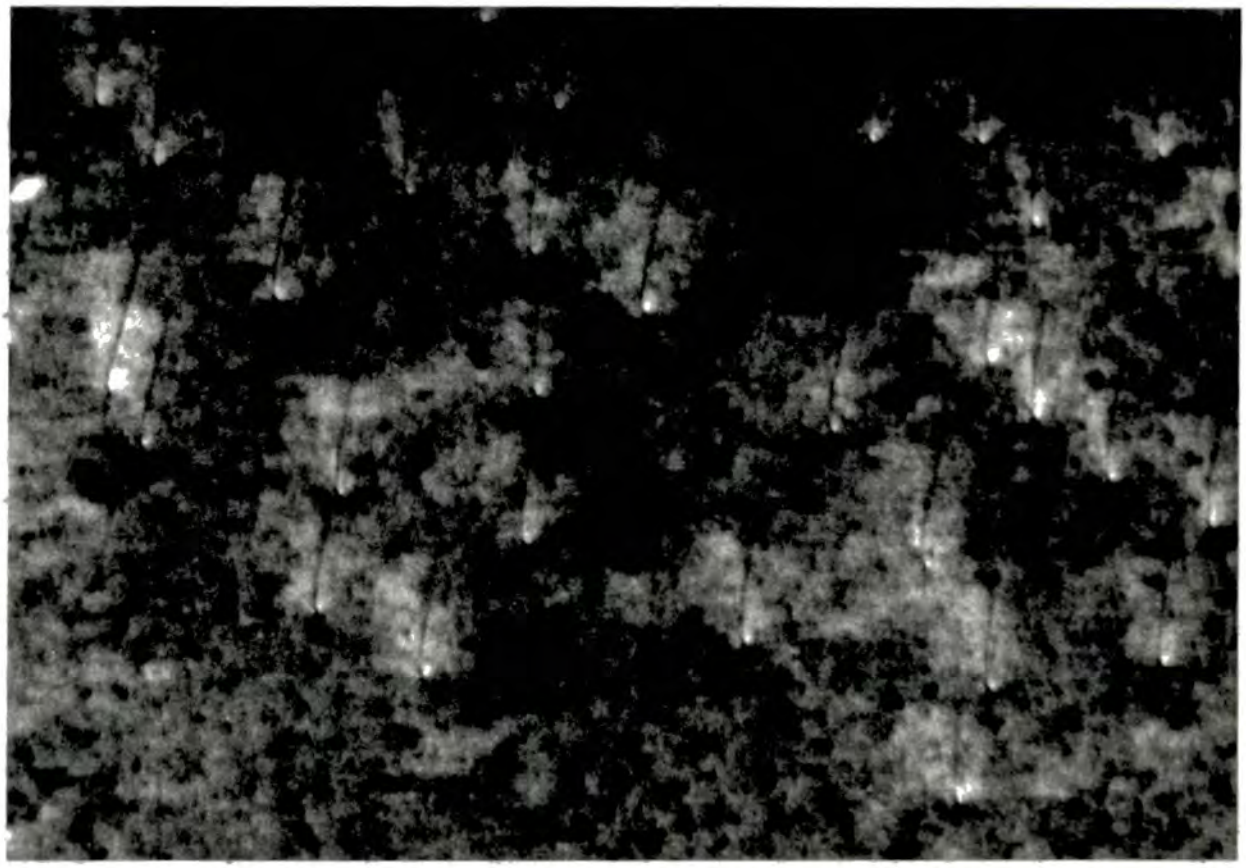

Figure 4.6

200μm

g

$\bar{2}20$ Lang topograph of sample 1.
The sample is inhomogeneously bent to R≈2m, but with a lesser degree of inhomogeneity than figure 4.5

very similar to those at R = 35m with a greater torsional moment and this suggests that the uneven bending is creating the image changes, independent of the overall curvature of the sample. The contrast seen in this topograph is very similar to that seen in the Hirst technique, although in Hirst topographs the contrast varies significantly with position on the plate.

The bending in the Hirst camera is checked by viewing the diffracted beam through an image intensifier and is adjusted until simultaneous diffraction can be seen from the whole wafer. From this work it is obvious that even when this criterion is met, there may still be some uneveness which will lead to significant contrast changes in the topograph. Furthermore, this inhomogeneity varies from point to point on the topograph giving rise to a variety of contrast effects. Since however, uneveness in bending is always accompanied by a rise in diffracted intensity it is suggested that a measurement of this should be used in conjunction with the visual technique to achieve homogeneous bending.

It is obvious that the contrast changes seen in the symmetric geometry Hirst topograph are not caused by the overall curvature of the sample but by a small inhomogeneity in the bending which has the effect of distorting the diffracting planes. Due to the unpredictable nature of the distortion it is difficult to explain the contrast changes from the topographs in this section. In order to investigate this more carefully it was decided to use an asymmetric reflection and to bend the sample homogeneously to produce a

uniform lattice curvature. This work is described in the next section.

4.4 Contrast in Lang topographs of curved crystals.

Contrast asymmetries of dislocations in distorted crystals were first observed by Saccacio [55,56] although no mechanism for the change in contrast except for a curvature of the diffracting planes was proposed. Meieran and Blech [70] showed that upon bending to a radius of curvature of 6m there is a substantial rise in the diffracted integrated intensity and the images of dislocations change contrast from black on white to white on black. There was not however any attempt to explain this contrast reversal and it was not explored for weak to intermediary bending. The aim of this section therefore is to explore the change in contrast with increasing curvature of the diffracting planes in the cylindrical bending geometry.

The theoretical basis for diffraction from a crystal with a uniform strain gradient is given in [71] and the same parameter describing the effective deformation in the case of homogeneous bending is used here, namely:

$$D = \frac{Bt\pi}{\xi_g} \qquad (4.1)$$

where t is the thickness of the crystal slab and B is given for cylindrical bending by:

$$B = -\frac{\xi_g^2}{dR}\,\frac{\sin\Psi\,[1 + \gamma_o\gamma_g(1+\nu)]}{2\pi\gamma_o\gamma_g} \qquad (4.2)$$

where R is the radius of curvature of the sample, Ψ is the angle between the surface normal and the diffracting plane and ν is Poisson's ratio, equal to 0.215 for silicon [72]. For values of $|B| \ll 1$ then Chukhovskii and Petrashens' results are identical to those given by Kato's Eikonal theory [16]. Another useful parameter for diffraction in curved crystals is given by Kalman and Weissman [73,74] the effective curvature ρ of a diffracting plane, taking into account both lattice dilation and tilt and related to the impressed curvature ρ_n by:

$$\rho = \rho_n \cos\chi \, (\sin^2\chi + \cos^2\theta_B)/\cos\theta_B \qquad (4.3)$$

Here the convention adopted is that a diffracting plane has a positive curvature when reflection occurs from the concave side of the plane. B is positive in the geometry used in these experiments as shown in figure 4.3. The sample was always bent so that the concave side was the entrance surface and the diffracting planes assumed a positive curvature.

Sample 2 was bent perfectly homogeneously and diffraction obtained from the $\bar{1}31$ reflection ($\chi = 58.5°$) with $MoK\alpha_1$ radiation ($\mu t = 1.20$) with a 111 entrance surface. The crystal was bent to radii of curvature of 82m, 69.5m, 55.5m, 34.0m and 19.5m and the values of D, B and ρ for these curvatures are given in table 4.2. Note that we are working well within the range of applicability of the Eikonal theory given by equation 1.21 since for this reflection and wavelength $R_c \approx 8m$.

R(m)	$\rho_n(m^{-1})$	$\rho(m^{-1})$	B_σ	B_π	D_σ	D_π
∞	0	0	0	0	0	0
82.0	0.012	0.011	0.022	0.027	1.06	1.30
69.5	0.014	0.013	0.026	0.032	1.25	1.54
55.5	0.018	0.016	0.034	0.041	1.63	1.97
34.0	0.029	0.026	0.055	0.066	2.64	2.64
19.5	0.051	0.045	0.096	0.117	4.60	4.61

Table 4.2

Values of ρ, B and D for π and σ polarisation states at the curvatures ρ_n used in the experiment.

As expected from both the Chukhovskii and Petrashen and Eikonal theories there is a sharp rise in the diffracted intensity upon bending. The peak intensity is plotted against ρ in figure 4.7. As we can see, an effective curvature of only $0.01m^{-1}$ is sufficient to produce a two fold increase in the peak height.

Figure 4.8 shows the $\bar{1}31$ topograph of the unbent crystal on which are marked the positions of the section topographs presented in section 4.5.2. Figures 4.9 and 4.10 show enlargements of the same area of crystal printed to give a uniform background intensity, at radii of curvature of ∞, 82m, 55.5m and 20m respectively and dramatic changes are once more visible in the images of dislocations upon bending. Two areas are interesting here, the large area of pinned slip dislocations A, which are the same in character as the individual set B dislocations in sample 1 (figure

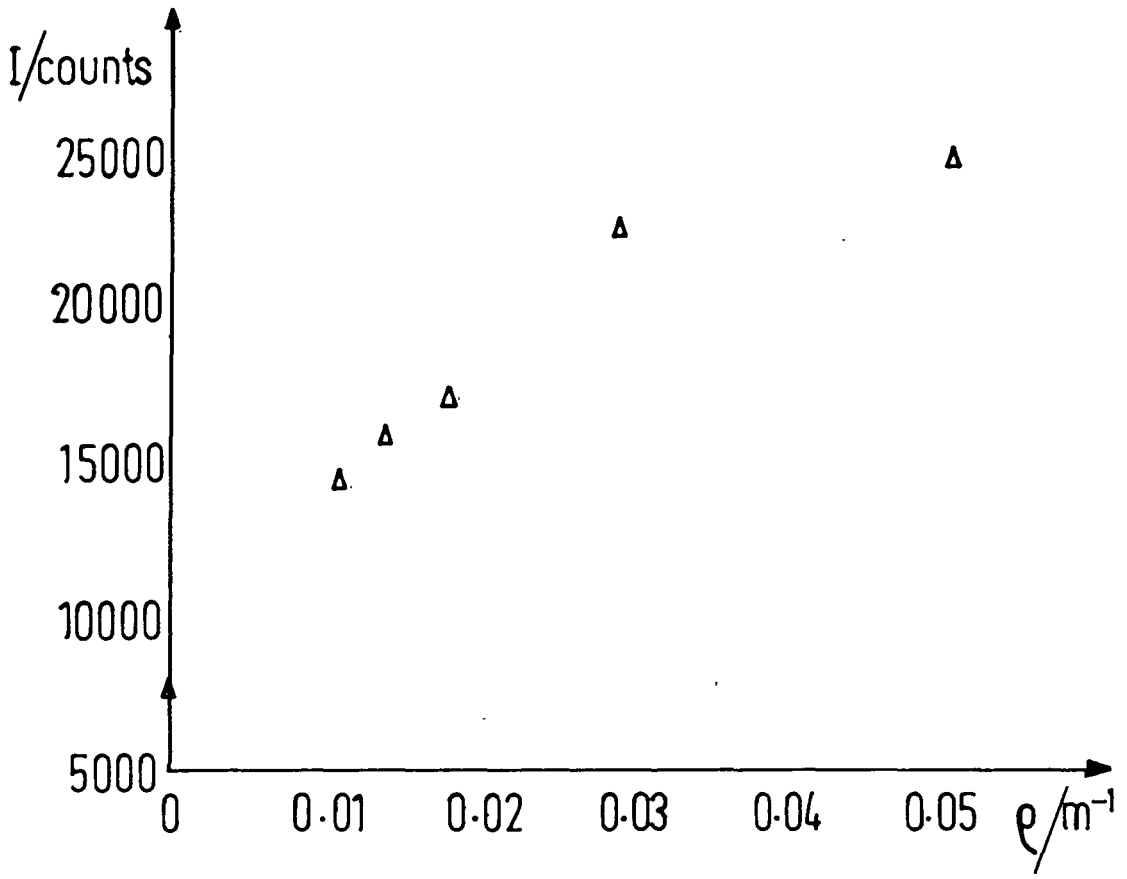

Figure 4.7
The Influence of Curvature upon Diffracted Intensity

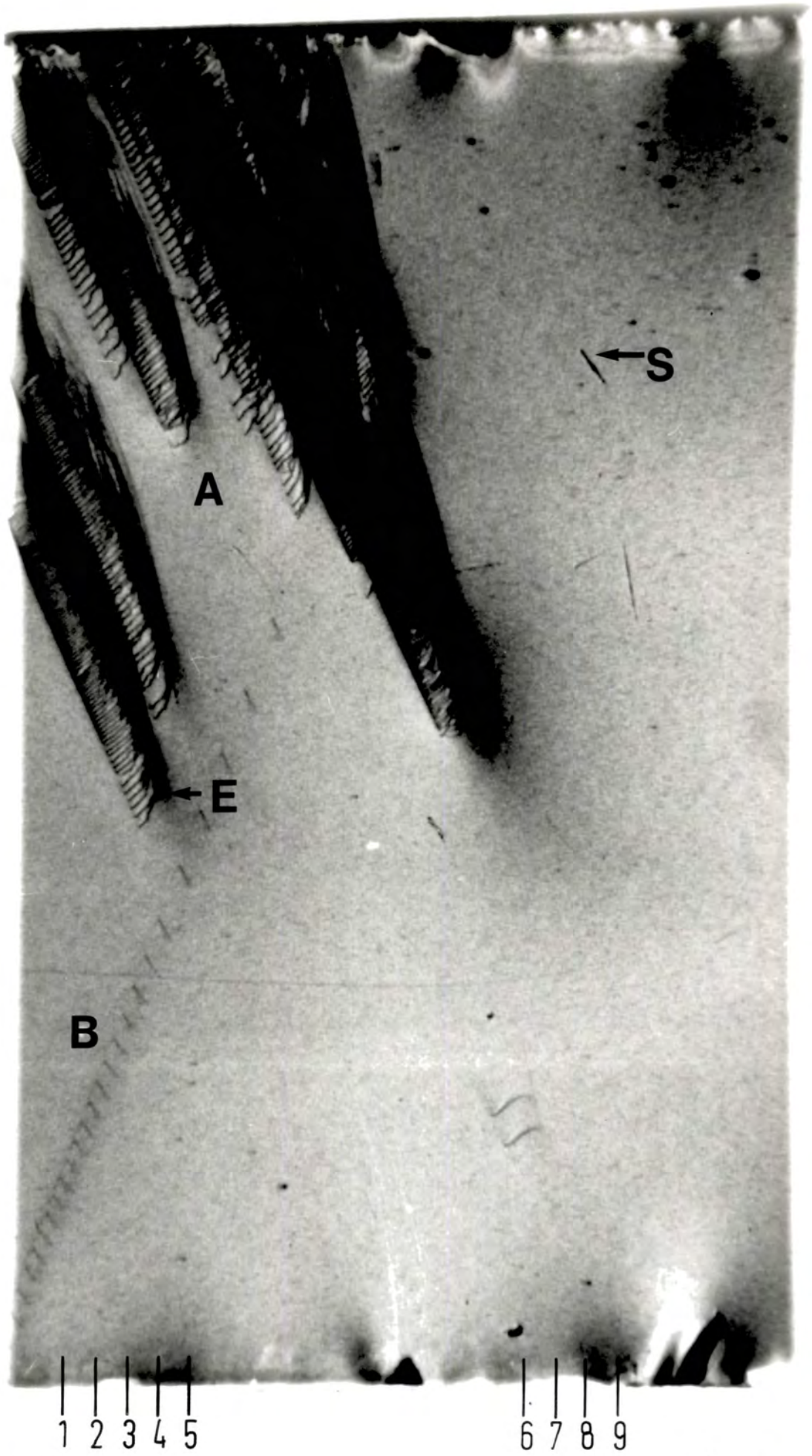

Figure 4.8
$\bar{1}31$ Lang topograph of sample 2

a)

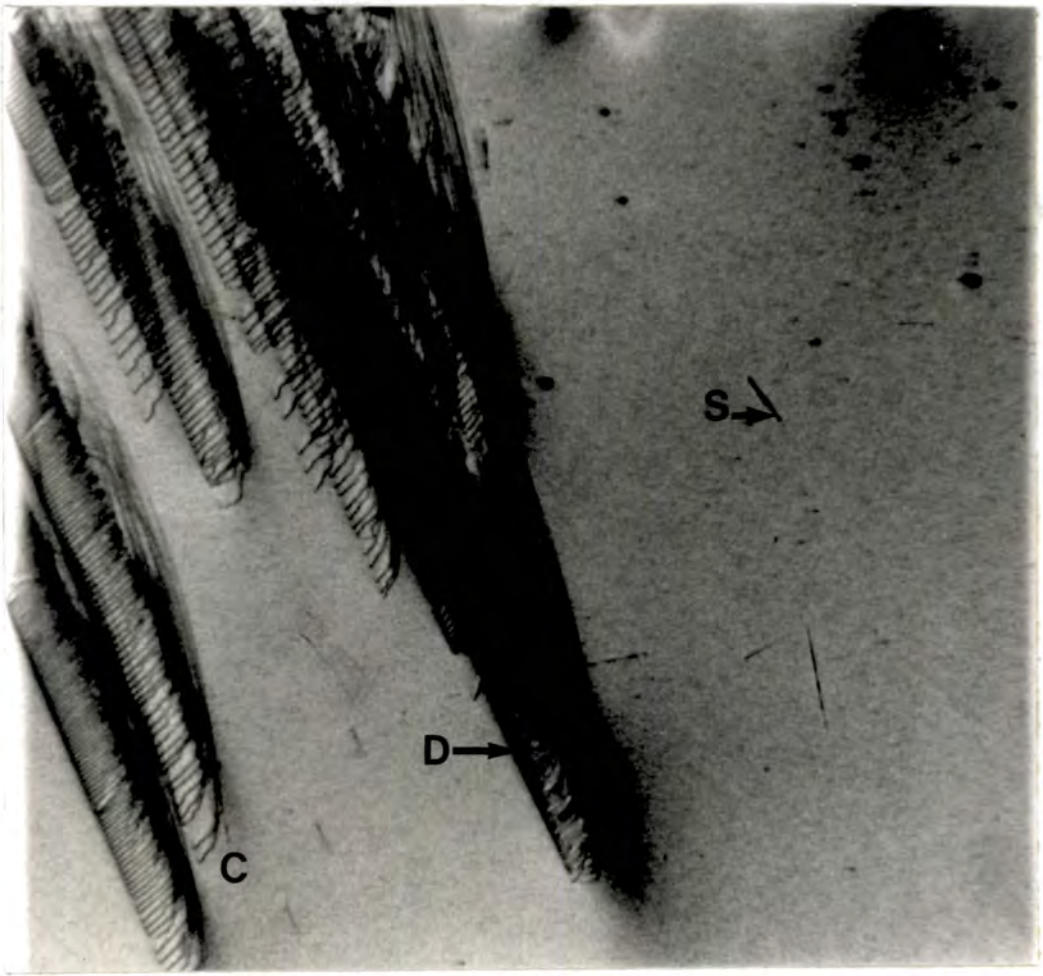

b)

Figure 4.9

$\bar{1}31$ Lang topographs of sample 2 homogeneously bent to:
a) R = ∞
b) R = 82m

$\vec{g}$ 1mm

See text for explanation of symbols

a)

b)

Figure 4.10

$\bar{1}31$ Lang topographs of sample 2 homogeneously bent to:
a) R = 55.5m
b) R = 20m

$\vec{g}$ 1mm

See text for explanation of symbols

4.4a) and the extended pile up of dislocations marked by B. As the curvature is increased, the direct images of the dislocations become less visible as observed in the topographs of the inhomogeneously bent wafer and at a radius of curvature of R = 20m the majority of the direct images are not visible.

Since the direct images can be thought of as arising mostly from parts of the crystal so heavily distorted as to be mosaic, we do not expect the long range impressed strain to have an effect on the diffracted intensity from this region since once the kinematic limit is reached there is no change in reflecting power with deformation. The decreased visibility of the direct images can therefore be attributed to the rise in the perfect crystal reflecting power which swamps the diffraction from the dislocation core. That is, if we define the contrast C as:

$$C = \frac{I_{max} - I_{min}}{I_{max} + I_{min}} \qquad (4.4)$$

we see that if the mimimum intensity I_{min} goes up then the contrast necessarily goes down.

This mechanism was also suggested by Meieran and Blech [70] and more recently by Zsoldos [75]. Since the intensity of kinematically diffracted X-rays is dependent upon the volume of heavily distorted material, we would expect direct images of individual dislocations to disappear at lower values of B and those from bundles of dislocations to be visible at higher B values. This is clearly seen from points C and D in figures 4.9 and 4.10. This condition can also be

stated as the darker the direct imager in the unbent sample the more visible it will be as B is increased.

Upon bending the white dynamical images become much more visible and extend to greater distances from the direct image. However, upon further bending they contract and eventually dominate the contrast of the dislocation for high values of B. Since dynamical effects are very sensitive to lattice strains it is unlikely that these effects can be explained by just a rise in the background intensity.

If we look at figure 4.7 we see how the change in integrated diffracted intensity is practically linear with the change in bending for small curvatures. The strain field far from the dislocation core, that is in a region of crystal not sufficiently distorted to give interbranch scattering, can either act in the same or opposite sense as the impressed strain, giving a local enhancement or depletion of intensity respectively. This would explain the large area of depleted intensity seen in the asymmetric reflection topographs and the inhomogeneously bent symmetric topographs (figures 4.5 and 4.6). However, if this is the mechanism responsible we would also expect the contrast to be reversed if the same diffraction geometry is used but the sense of the applied deformation is reversed.

That this is the case is obvious in figure 4.11, a symmetric topograph of sample 1, inhomogeneously bent to a radius of curvature of 2.6m. Here however, the twist is in the opposite sense to that in figure 4.5 and the area of depleted intensity seen in that topograph is replaced by an area of enhanced intensity extending to roughly the same

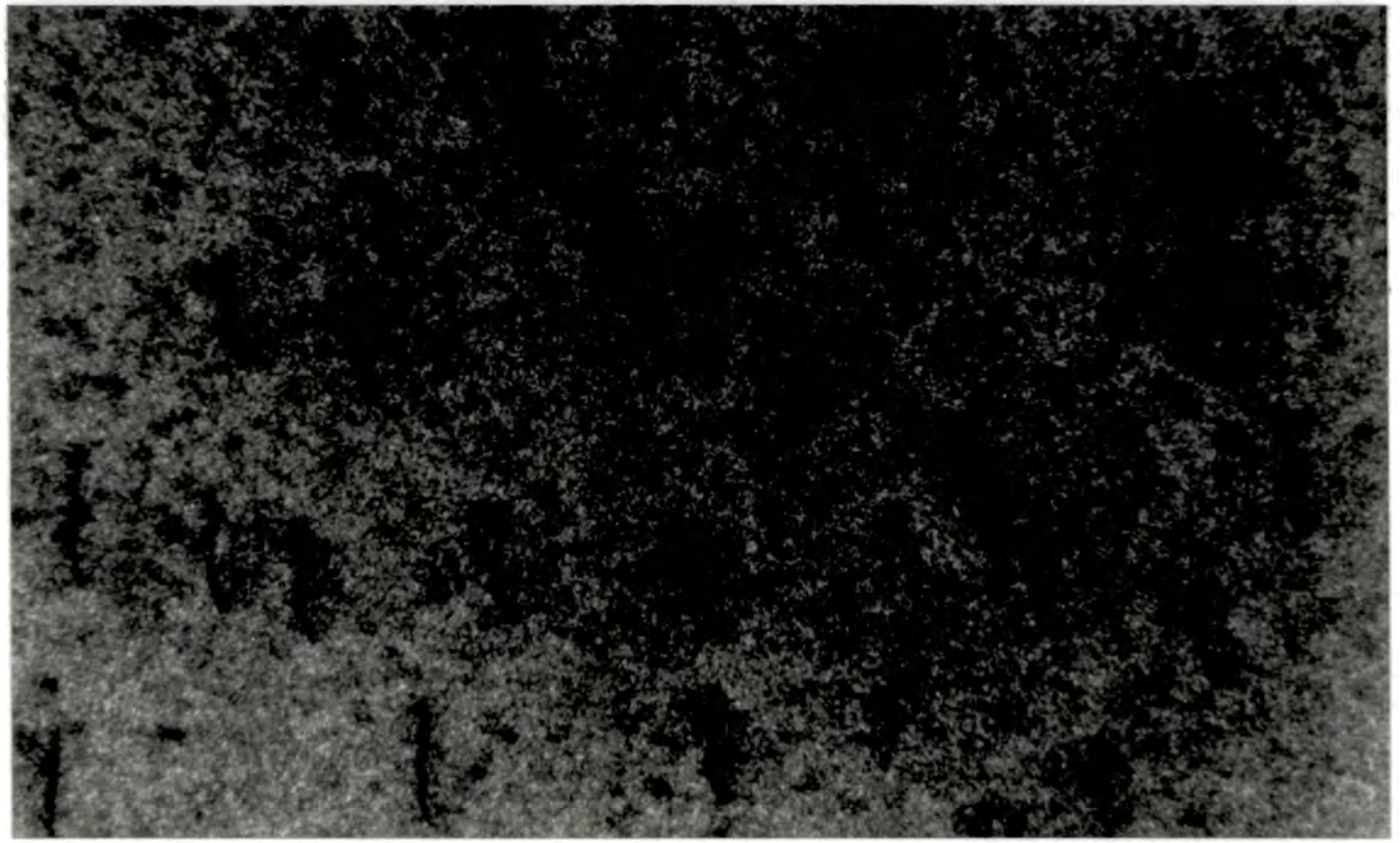

Figure 4.11

$\bar{2}20$ Lang topograph of inhomogeneously bent sample 1.
Sense of twist is opposite to that in figure 4.5. Note that the previous area of depleted intensity around the direct image is replaced by an area of enhanced intensity, extending to roughly the same distance.

distance. Similar observations have also been reported by Zsoldos [75]. Upon further bending the large white contrast contracts and dominates the contrast of the dislocations due to the invisibilty of the direct image.

Also noteworthy are the images of scratches on the exit surface of the sample (S). The visibility of the direct image once more decreases with increased bending but a strong white image also appears adjacent to it whose spatial extent does not change with increasing deformation. Since the strain field is localised at the surface, it cannot significantly change the propagation of the wavefields within the Borrmann fan and the white image can therefore best be thought of as a shadow caused by the creation of new wavefields close to the surface which cannot propagate further [76]. It is therefore likely that the contrast changes in this case arise because of the rise in the perfect crystal diffracted intensity and not by a fundamental change in the wavefields caused by the applied strain.

From this work it would appear that effective lattice curvatures of as little as $0.01m^{-1}$ are sufficient to create the contrast changes seen in topographs of inhomogeneously bent wafers. This implies that to be able to directly compare Lang and Hirst topographs, the bending homogeneity must be controlled to a tolerance close to that used in section 4.2.

Since we do not see large dynamical images associated with the scratches, the increased extent of the white image of the dislocations must be associated with changes in the

energy flow within the Borrmann fan. Such information is however lost in traverse topographs, because of their integrated nature.

To investigate in more detail the contrast effects produced by homogeneous bending, section topographs were also taken at several positions of the crystal for each radius of curvature. Section topographs have the added advantage that they can be simulated successfully in a realistic time using the Takagi-Taupin equations. The experimental results and some simulations are presented below.

4.5 Section topography of curved crystals.

The section topographs in this section are all of sample 2 and were taken at exactly the same curvatures as the Lang topographs. The positions of the sections for each curvature were checked using dental film, which gave sufficient resolution to enable the crystal to be aligned to within 20μm of the same position for each curvature. This is 5% of the width of the base of the Borrmann fan for the 131 reflection and 4.5% for the 440 reflection.

4.5.1 Symmetric reflection.

Figures 4.12 and 4.13 show section topographs using the $\bar{4}40$ symmetric reflection (μt = 1.09) with $\theta_B = 21.6^\circ$. Figures 4.12a and 4.13a are enlargements of parts of the unbent section and figures 4.12b and 4.13b are the same regions in the crystal bent to a radius of curvature of 17.5m. Ostensibly there is no difference in contrast between

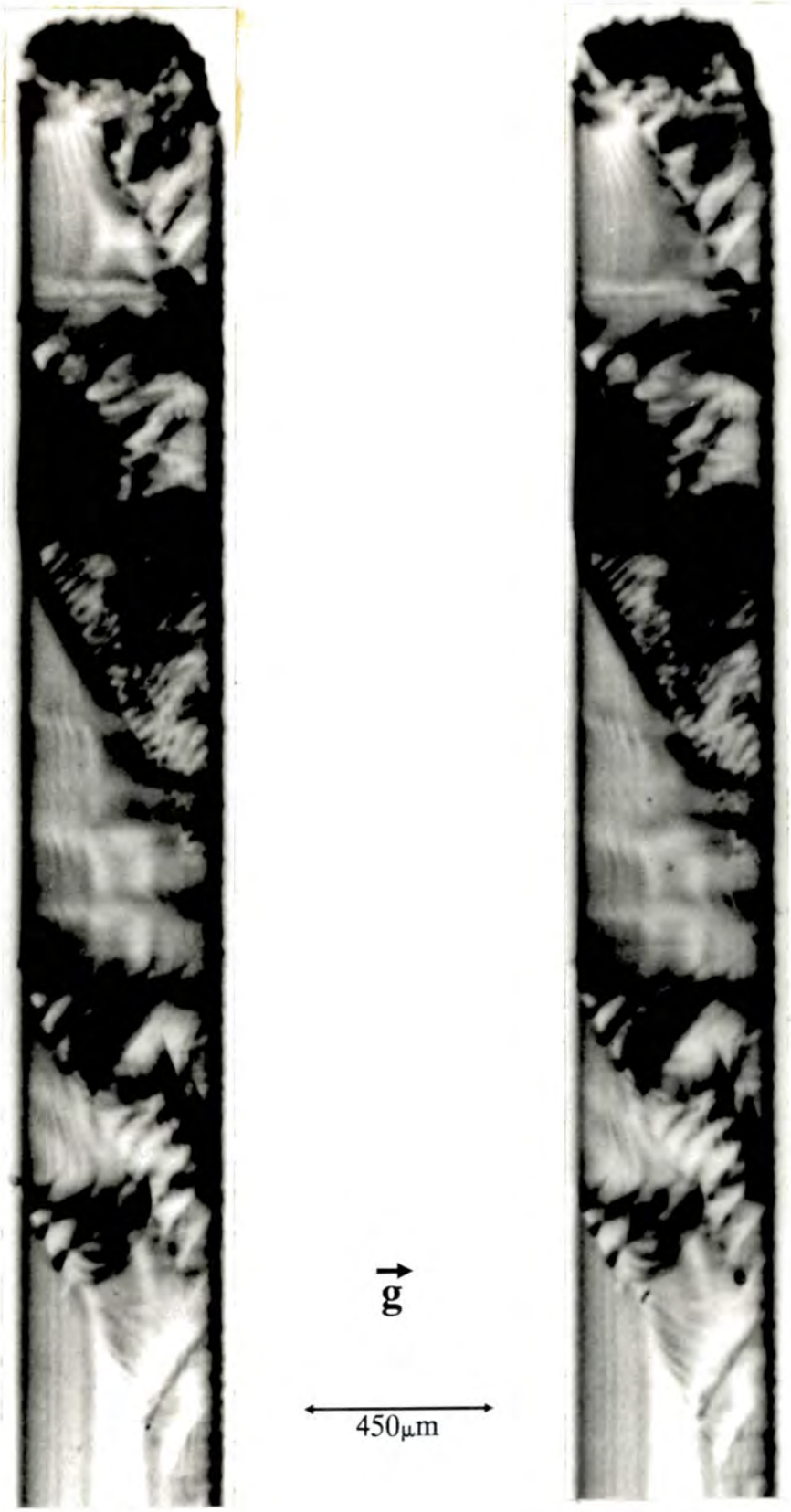

Figure 4.12

$\bar{4}40$ Section topographs of homogeneously bent sample 2.
a) $R = \infty$
b) $R = 17.5\text{m}$

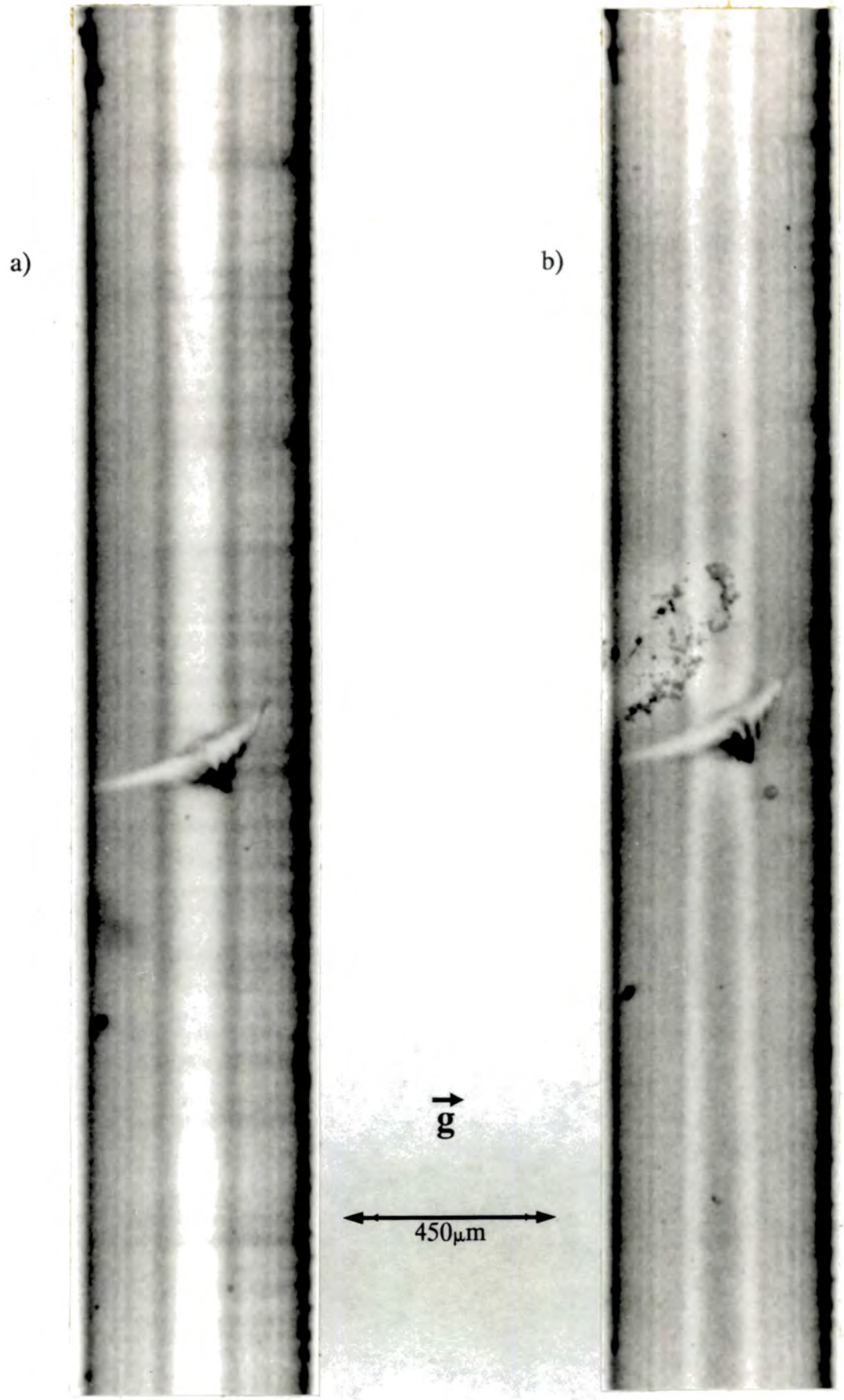

Figure 4.13

$\bar{4}40$ Section topographs of homogeneously bent sample 2.
a) R = ∞
b) R = 17.5m

the images in the bent and unbent crystal and no rise in diffracted intensity occurred upon bending, in agreement with the homogeneously bent $\bar{2}20$ reflection of sample 1 (figure 4.4). There are however changes in the fringe patterns in the fine structure of images of dislocations and also in the parallel Kato fringes. These show a phase change in the centre of the section, that is close to the exact Bragg condition, whilst towards the edges the period and phase are identical in both cases.

This change in phase is surprising since in the symmetric geometry no curvature of the wavefields in the Borrmann fan is predicted by the Eikonal theory. Using the Eikonal theory, a lattice distortion has the effect of migrating the tie-point along the dispersion surface. For a very small distortion this migration will produce the greatest change in the direction of energy flow for each wavefield close to the exact Bragg conditon, $\eta = 0$ since here there is a large angular amplification effect (section 1.4.8). Since wavefields from different branches curve in opposite directions for a given curvature, the spatial overlap between them will change and we can expect a change in the interference pattern, that is in the Kato fringes.

Thus, for very small curvatures significant changes in phase will only be present close to the exact Bragg condition, that is at the centre of the section pattern, in agreement with the experimental results. Similar changes in the fringe pattern have been observed by White and Chen [77] and these have been simulated using a numerical integration of the Takagi-Taupin equations by Green and Tanner [78].

They showed that a phase change occurs in the symmetric geometry even for perfectly homogeneous bending, although not of the same magnitude as seen here. A change in phase is also predicted for the case of fanning planes with B = 0 by Chukhovskii and Petrashen [71, 79].

The cause of the change in contrast seen in these experiments is therefore unclear, although perfect bending will be difficult to obtain in practice and an undetectable inhomogeneity is possibly the reason.

4.5.2 Asymmetric reflection.

Figures 4.14 to 4.17 show $\bar{1}31$ section topographs of sample 2 at the same radii of curvature as the Lang topographs, the numbers referring to the position of the section in relation to the sample, shown in the Lang topograph, figure 4.8. Sections 1 to 5 were taken on the same plate using a step scanning technique, as were sections 6 to 9.

Upon bending a large change in the Pendellosung fringes is seen. These become more localised at the centre of the section, showing less contrast with increased bending and becoming invisible for R < 34m. Such changes in the fringes have been previously observed [57,77] and are adequately explained by the Eikonal theory. Also interesting is the sensitivity of the Pendellosung fringes to local lattice strains in the vicinity of a dislocation. Referring to figure 4.14 and the dislocation marked D, we see that for ρ = 0 the dislocation has very little effect on the shape of the Pendellosung fringes whilst for R = 82m these fringes

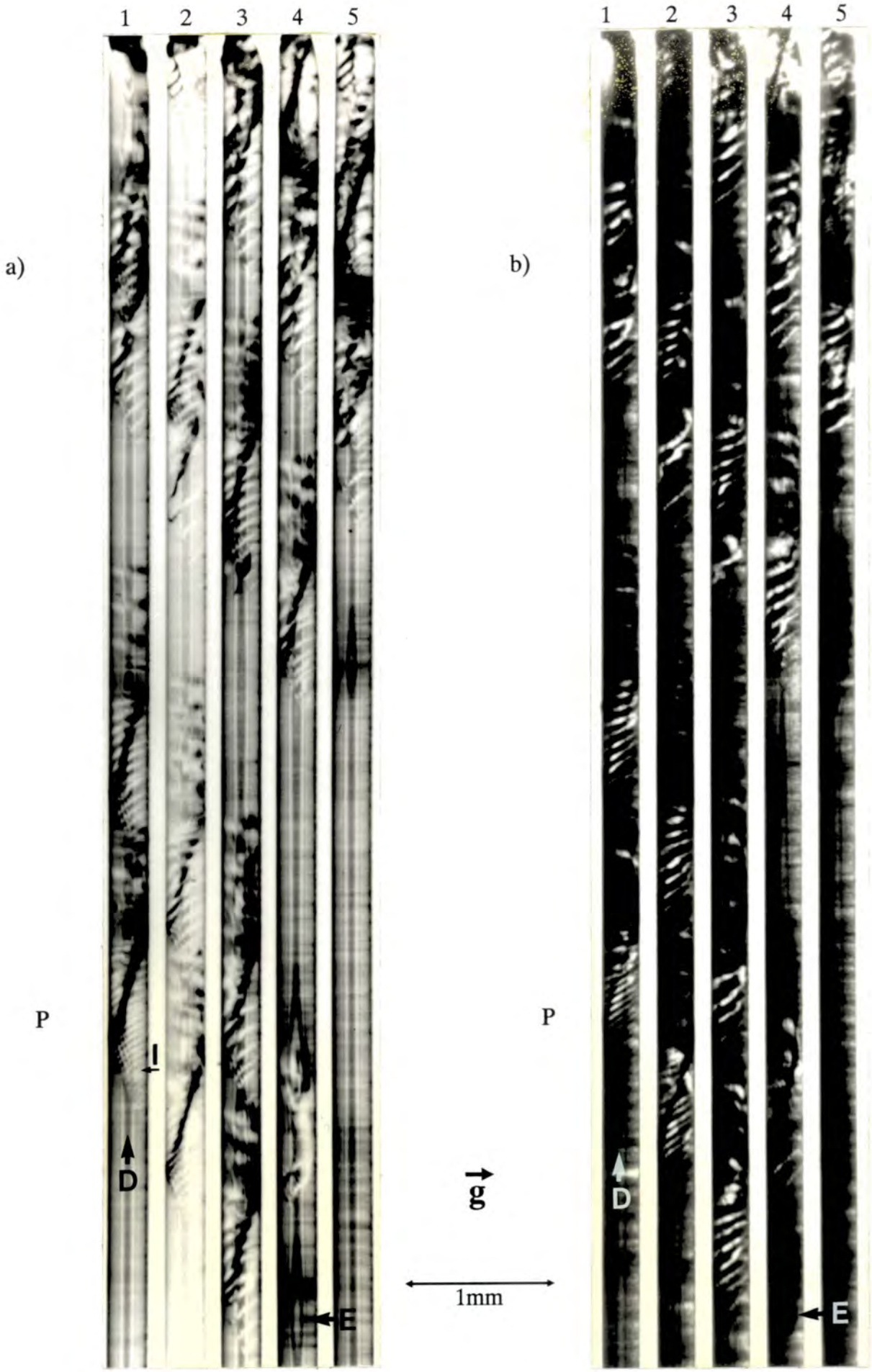

Figure 4.14

$\bar{1}31$ Section topographs of homogeneously bent sample 2.
a) $R = \infty$
b) $R = 82m$

See text for explanation of symbols

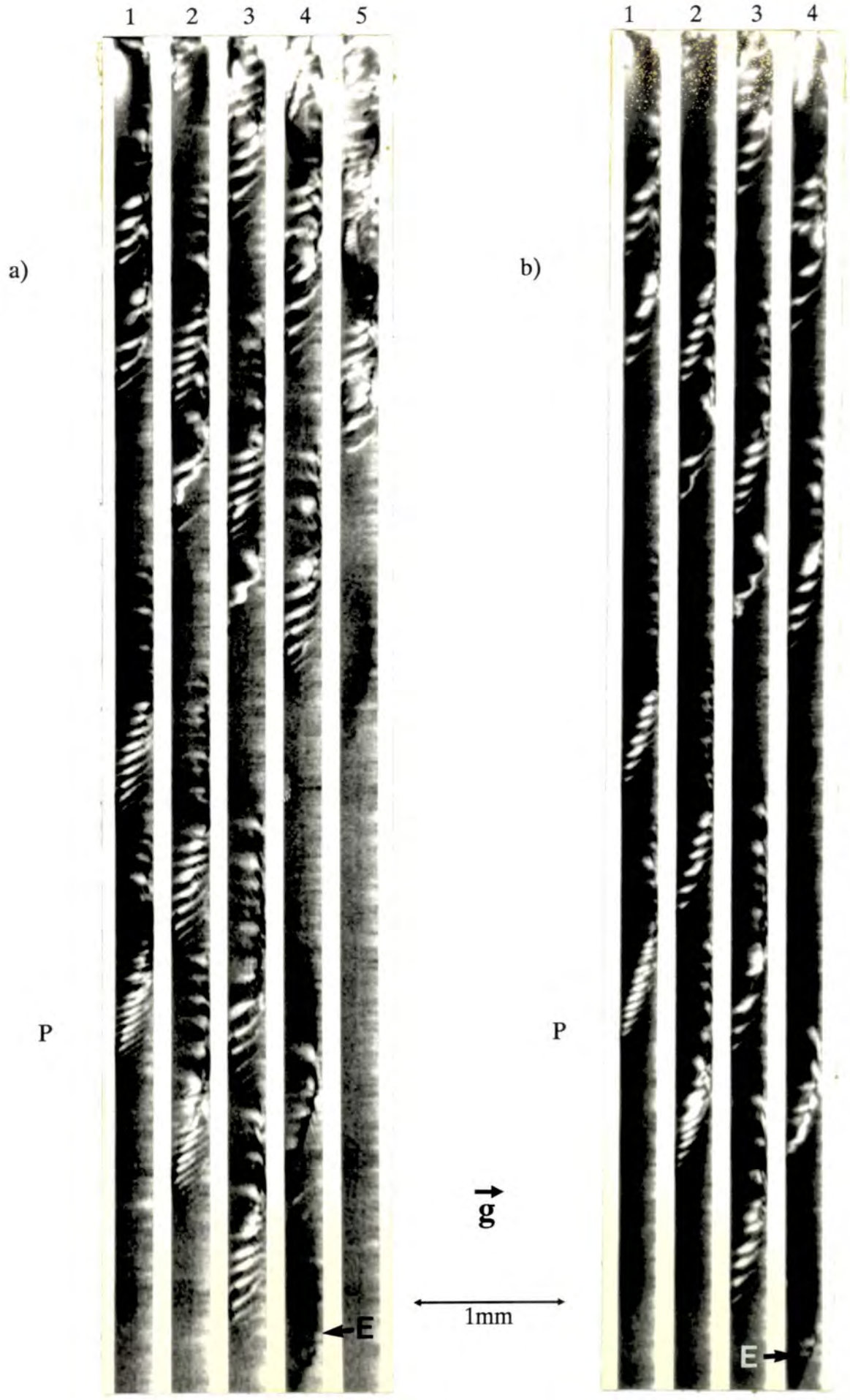

Figure 4.15

$\bar{1}31$ Section topographs of homogeneously bent sample 2.
a) R = 55.5
b) R = 20m

See text for explanation of symbols

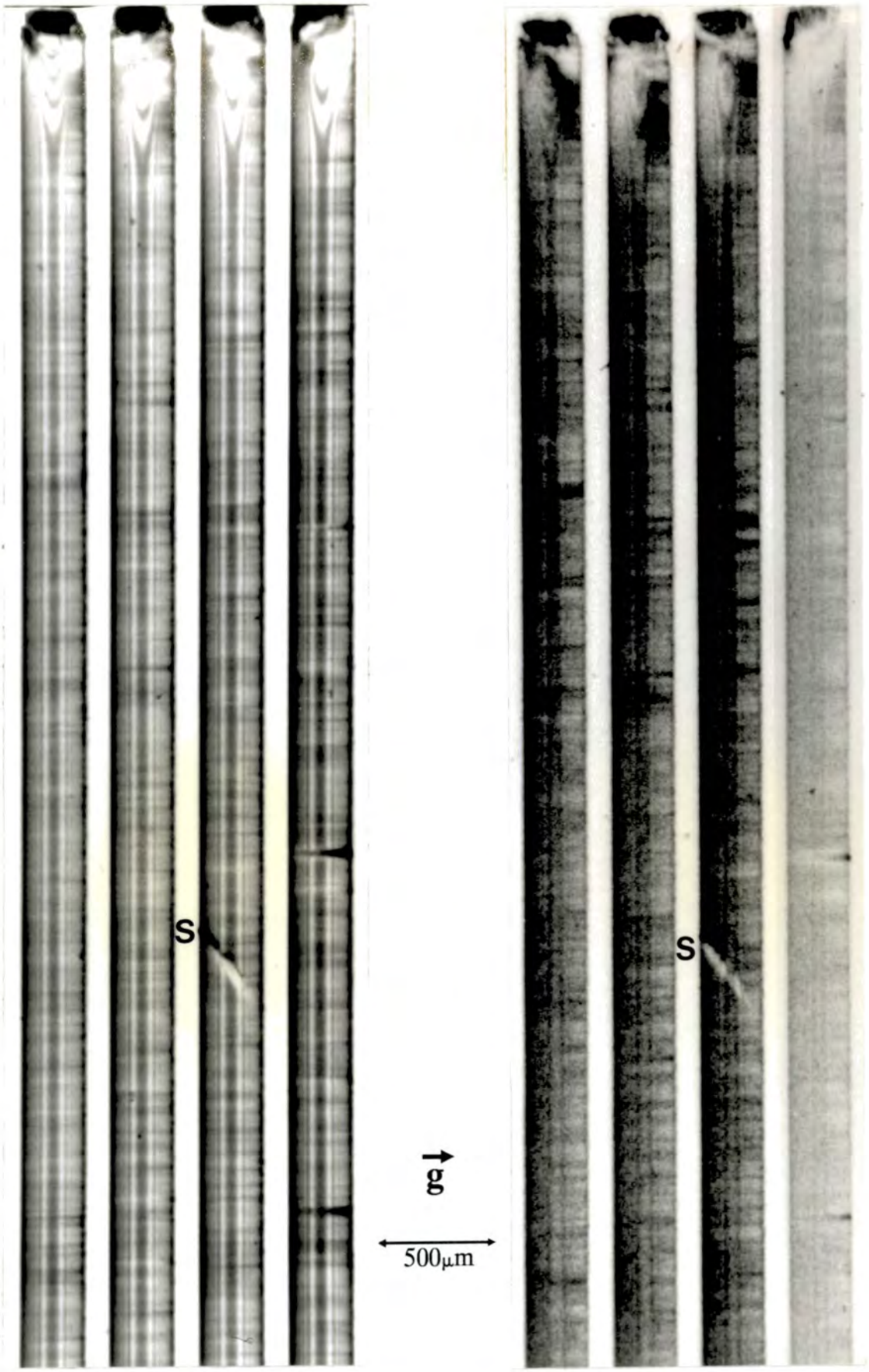

a) b)

Figure 4.16

$\bar{1}31$ Section topographs of homogeneously bent sample 2.
a) $R = \infty$
b) $R = 82m$

See text for explanation of symbols

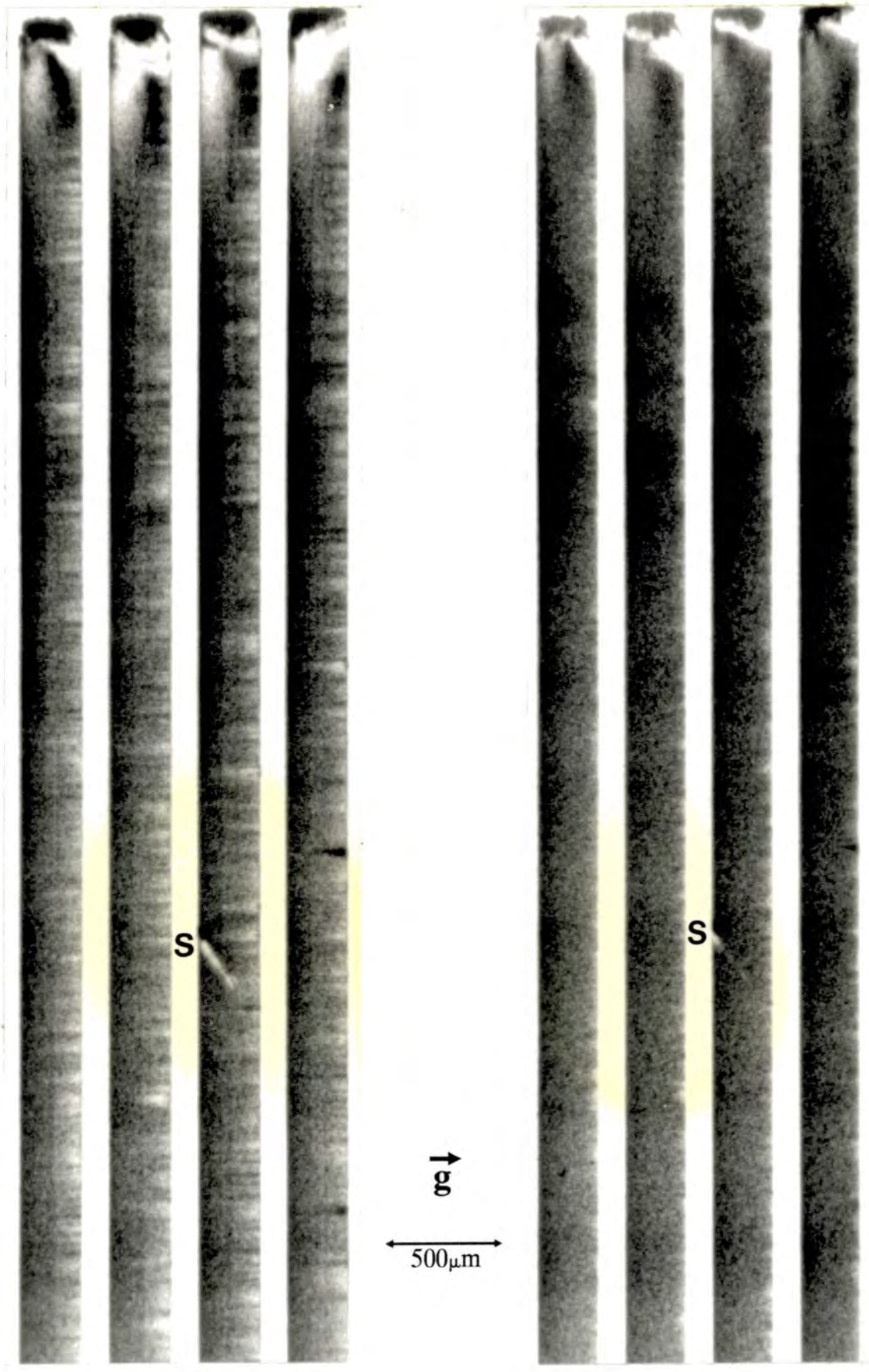

a) b)

Figure 4.17

$\bar{1}31$ Section topographs of homogeneously bent sample 2.
a) R = 55.5m
b) R = 20m

See text for explanation of symbols

are considerably distorted in the region of the dislocation. This effect has also been observed by Chukhovskii and Petrashen [80] and is explained by the phase difference between branch 1 and 2 wavefields having a linear dependence on the local strain field only for a non-zero value of B.

The sensitivity of these fringes to quite moderate bending conditions means that care should be taken when using asymmetric reflections to examine processed wafers, as there will be some ambiguity as to whether poor fringe visibility is due to the presence of a long range strain or to lattice disorders such as microdefects.

The region marked E in figure 4.14 shows interesting contrast changes upon bending. The area in question is also marked on figure 4.8 and as we can see the section topograph is very close to, but does not cross, the bundle of dislocations marked by Q. This is shown by the lack of a direct image in the section topograph. The strain field around these dislocations is sufficient however to distort the local fringe pattern. As the bending increases, a dark image is formed in the shape of the bundle which upon further bending, (figure 4.15) becomes more localised and gives rise to white dynamical images at R = 34m. This enhanced intensity agrees well with the Lang topograph and can be explained by the long range strain field acting in the same sense as that around the dislocation, thus giving a local enhancement of intensity greater than that in the perfect crystal. At higher bending it is likely that the added strain is sufficient to give rise to interbranch scattering giving a localised dark image and white dynamical

image, the previous enhancement being swamped by the rise in diffracted intensity from the perfect crystal.

The sections show, as was reported in 4.3, the lack of change of the images of scratches upon bending. Figures 4.16 and 4.17 show section number 8 which cuts the scratch marked S on the Lang topograph (figure 4.8). This changes very little in shape or contrast up to a curvature of $0.029m^{-1}$ when further bending causes a contraction of the extent of the dynamical image. Again this is because of a rise in background intensity rather than a change in the propagation of the X-rays around the scratch.

Figures 4.16 and 4.17 also show drastic changes in the images of back (entrance) surface damage with curvature. Since the back surface has not been polished, there are a considerable number of localised strain centres. In the unbent crystal these are evident as dark spots if the direct beam cuts the strain centre, with streaks of either enhanced or depleted intensity running horizontally from entrance to exit surface. For a small curvature, these streaks become wider and show greater contrast, dominating the perfect crystal image. The great sensitivity to additional bending is because the small extent of the strain field can to some degree alter the propagation of all wavefields within the Borrmann fan. Thus small changes in this strain are magnified to give large changes in the image contrast. At a curvature of $0.051m^{-1}$ the enhanced images are again masked by the rise in background intensity, the white images contracting and becoming localised at the entrance surface. This change in contrast is the most likely explanation for

the increased mottling seen in the Hirst and inhomogeneously bent Lang topographs.

Generally, images of dislocations show enhanced white dynamical images at low curvatures which become more localised as the bending increases and finally dominate the contrast of the dislocation. Those showing only dynamical images however, become invisible at much lower bending. The direct image decreases in contrast and eventually becomes completely invisible. This is seen in figures 4.14 and 4.15 for the series of pinned dislocations marked by P. From the unbent section and with reference to the Lang topograph we can see that these extend from the top surface into the crystal roughly parallel to 011 and are pinned by bundles of dislocations running parallel to and close to the back surface.

For small curvatures, direct, intermediary and dynamical images are visible although the complicated interference patterns marked by I disappear. Note that at large curvatures the invisibility of the direct images makes depth profiling of the dislocations impossible. The change of contrast to localised white images explains the previous observations of white dislocation images in Lang topographs of bent crystals [70].

It should be noted though that at the curvatures studied here the direct image does not change from black to white but merely becomes invisible, and this suggests that the appearance of the dislocations as white on black is associated with interbranch scattering from the region

adjacent to the core of the dislocation and not diffraction from the heavily distorted core itself.

Figures 4.18 shows the contrast of individual dislocations at R = ∞ and R = 82m lying parallel to the 110 direction. Also shown are simulations kindly supplied by Dr Green, which show excellent agreement with the experimental results.

The use of the long range strain to identify the sense of deformation associated with a dislocation and hence the sense of its Burgers vector was proposed by Meieran and Blech [70]. Figure 4.19 shows how the image of the dislocation in the bent wafer is critically dependent upon the Burgers vector, even though changing the Burgers vector does not necessarily change the image in the unbent section. The use of a small curvature coupled with simulations is therefore a way of uniquely identifying the Burgers vectors of dislocations and was used here to classify the dislocation as having $\mathbf{b} = 1/_2[01\bar{1}]$.

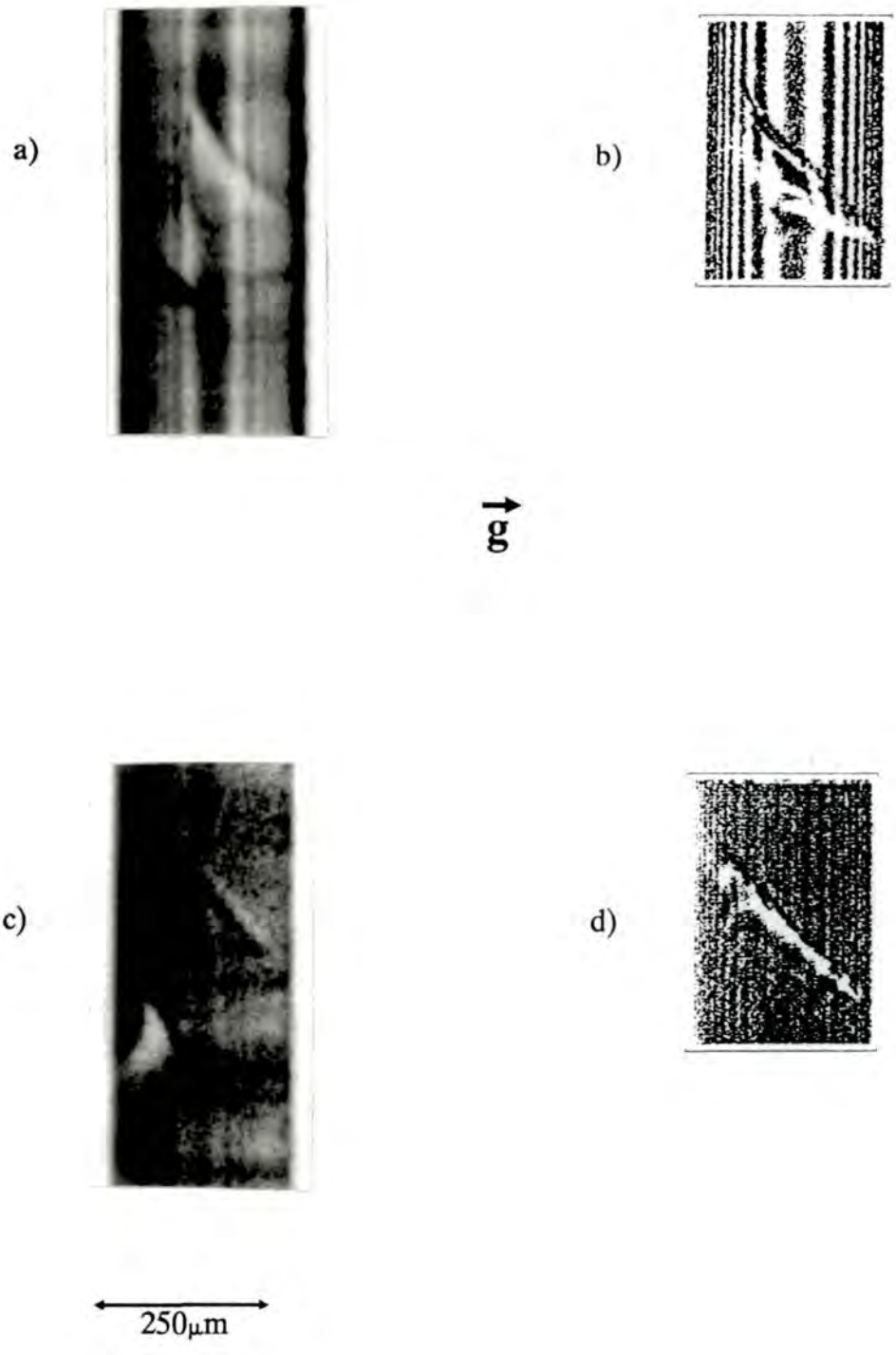

Figure 4.18

Experimental and simulated $\bar{1}31$ Section topographs of homogeneously bent sample 2.
a) Experimental and b) Simulation for R = ∞
c) Experimental and d) Simulation for R = 82m

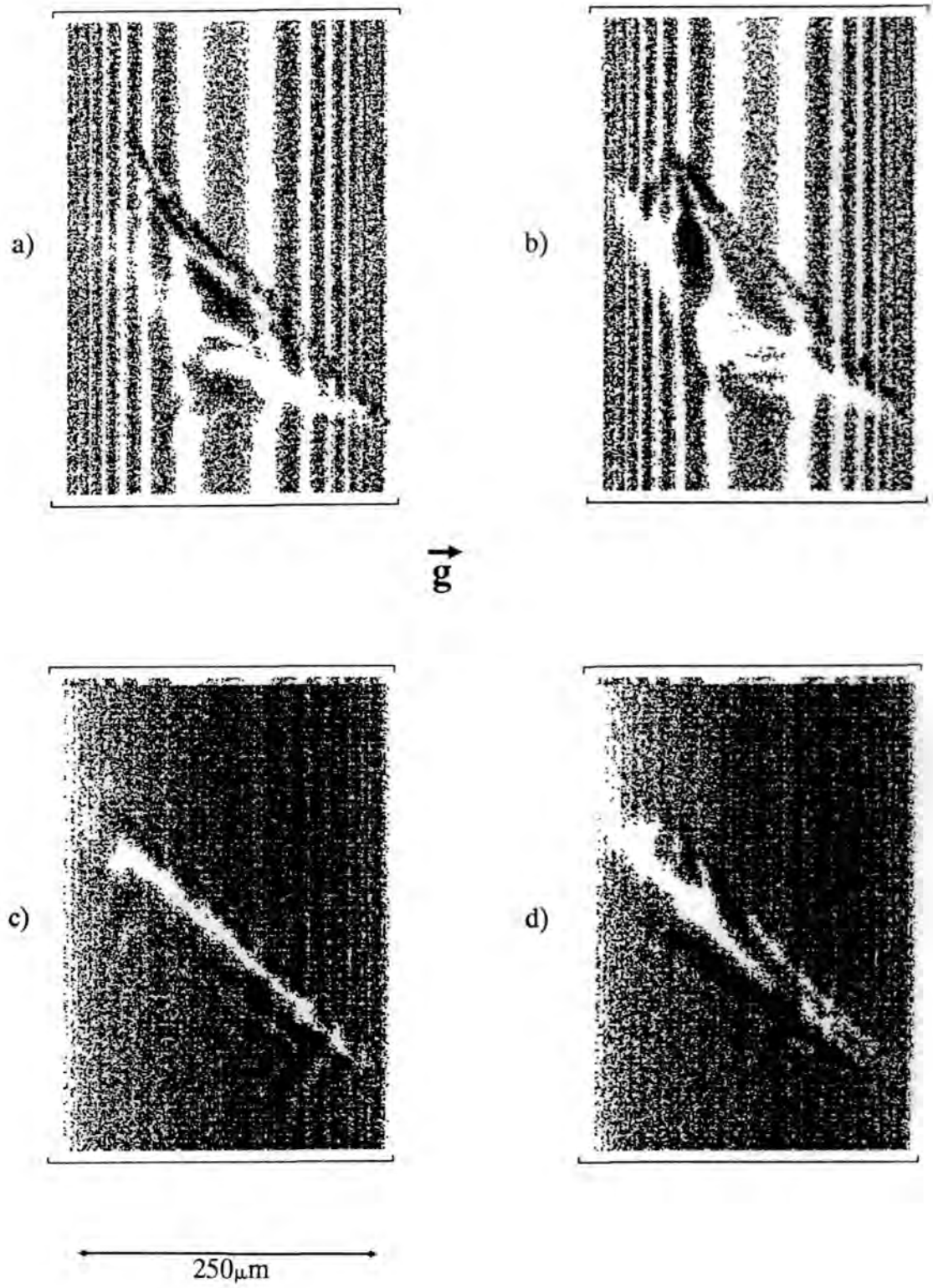

Figure 4.19

Simulated $\bar{1}31$ Section topographs of homogeneously bent sample 2, showing the sensitivity of defect contrast to the Burgers vector in curved crystals

a) $R = \infty$; $\mathbf{b} = 1/2[01\bar{1}]$ b) $R = \infty$; $\mathbf{b} = 1/2[110]$
c) $R = 55.5$m; $\mathbf{b} = 1/2[011]$ d) $R = 55.5$m; $\mathbf{b} = 1/2[110]$

Chapter Five

Glancing angle double crystal topography with synchrotron radiation.

5.1 Introduction.

This chapter describes the examination and characterisation of a fully processed bipolar device wafer by X-ray topography using synchrotron radiation. The merits of single crystal (white radiation) reflections are briefly discussed, however the bulk of the chapter is concerned with the technique of glancing angle Bragg geometry double crystal topography. By the use of several reflections and exploiting the wavelength tunability of the synchrotron radiation, the depth penetration of the X-rays into the sample was varied and the best conditions for examining both devices and defects explored.

The sample to be examined was half of a 4 inch diameter silicon wafer, with a nominal (111) surface plane, which had been fully processed to form bipolar type integrated circuits. Bipolar integrated circuits are made up of n-p-n and p-n-p transistors, and a cross section through a typical device is shown in figure 5.1. Unfortunately, precise details of the wafer examined here were not available for commercial reasons, but the transistors consisted of emitters which were phosphorus doped to 8 or 9 x 10^{19} atoms.cm^{-3} (n^+ type) to a depth of 1.4μm and bases which were boron doped to 3 x 10^{18} atoms.cm^{-3} (p type) to a depth of 3.3μm. The devices are fabricated upon a 20μm thick n-

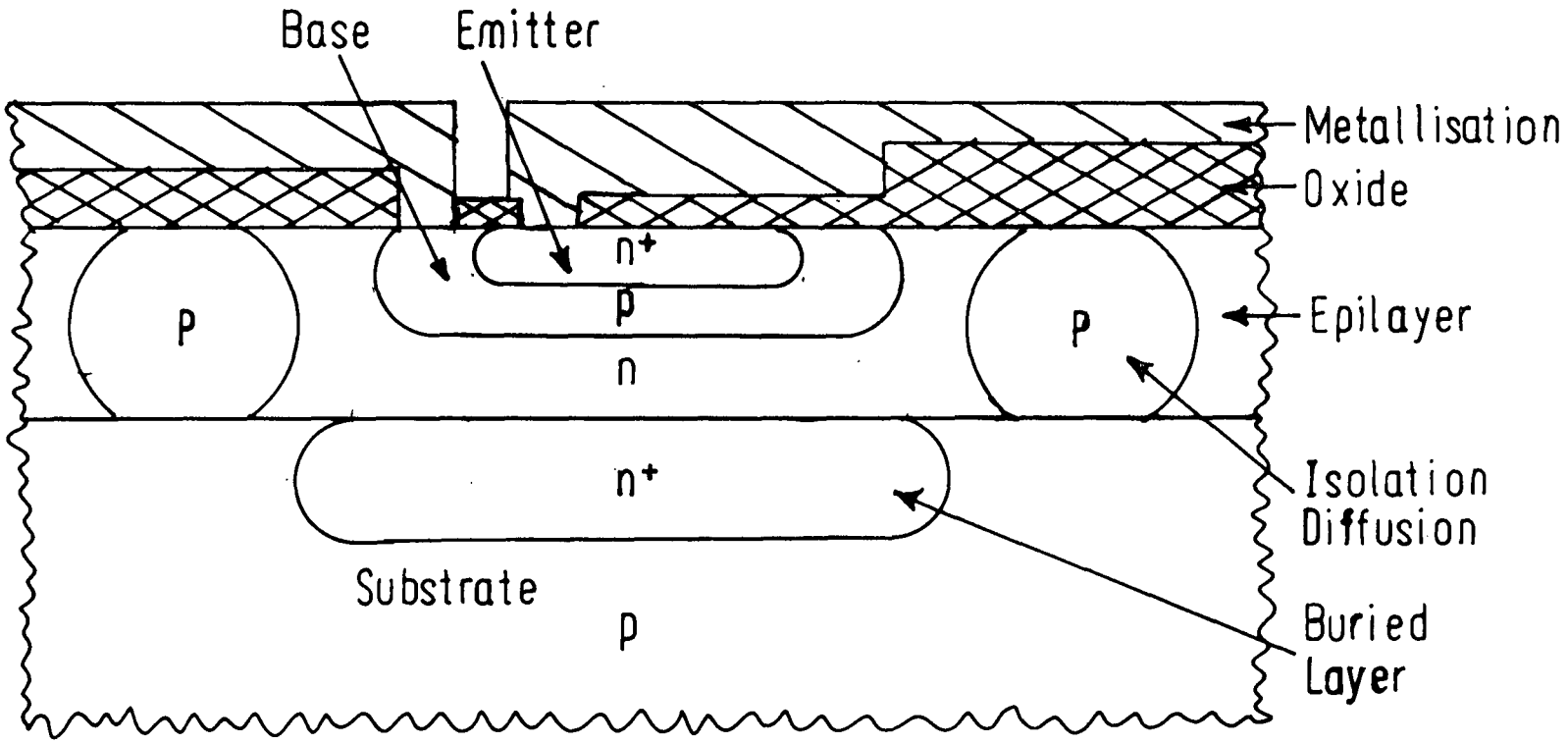

Figure 5.1
Section through typical Bipolar device

type epilayer grown on a Czochralski p-type silicon substrate.

The wafer was first examined using Lang and section topography, which showed a high concentration of microdefects in the crystal bulk (figure 5.2). These are associated with interstitial impurities such as oxygen and carbon, which upon thermal annealing form two types of defect, type A and type B. Type B defects are small and have too small a strain field to be individually resolved by single crystal topography. The type A defects however are typically 1 to 3 μm in size and have been observed to be dislocation loops [81]. The formation of these defects has been associated with the formation of oxide precipitates [82] but their precise nature and cause is the matter of some debate, a good summary of which may be found in [83].

The microdefects obscure details of the device structure in the Lang topograph making it unsuitable for the examination of process related defects. The section topograph however indicated the presence of a microdefect-free region below the wafer surface, and it was therefore decided to examine the wafer using reflection topography.

5.2 White radiation topography.

Before setting up the double crystal experiment, it was decided to make use of a low intensity beam of around 20mA to make some preliminary investigations of the crystal with white radiation topography.

The first choice of reflection was a surface symmetric <111> reflection, with λ chosen to be $\sim$ 1Å, by setting the

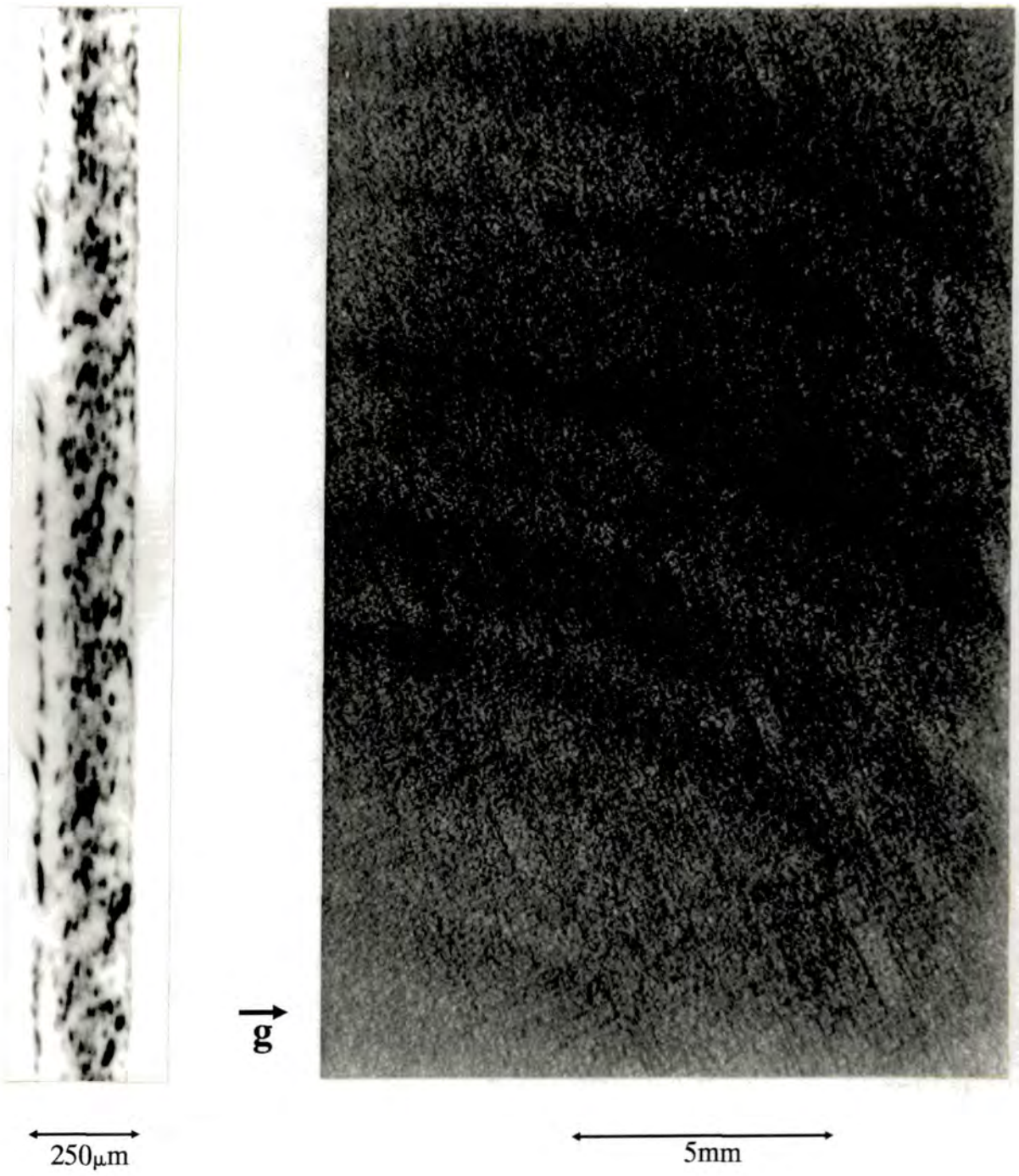

Figure 5.2

a) $\bar{2}20$ Section topograph, MoKα1 radiation. Device side of wafer (exit surface) is on the left.

b) $2\bar{2}0$ Lang topograph, MoKα1 radiation.

angle of incidence and hence θ_B at $\sim 10^\circ$. No further setting up was required, except to limit the vertical and horizontal extent of the incident beam by the means of slits, and to position the sample in the beam with a plate positioned at $2\theta_B$, perpendicular to the diffracted beam. Even with the very low intensity (by SRS standards), an exposure time of only 10 seconds was required.

In the direction parallel to the plane of incidence and for a plate placed perpendicular to the diffracted beam, images will be foreshortened by a factor given by the aspect ratio. In the Bragg geometry, the aspect ratio is given by:

$$b/a = \sin(\theta_B + \chi) \qquad (5.1)$$

where b is the length of the image of a line of length a on the crystal surface, and χ is the angle between the diffracting planes and the surface as shown in figure 5.4. The aspect ratio is an important consideration when deciding upon a reflection geometry.

The <111> reflection has an aspect ratio of approximately 0.2, making it unsuitable for examining the device structure and process related defects. The aspect ratio could be improved by using a larger Bragg angle, but this would increase the penetration depth of the X-rays and would limit the area of the wafer that could be examined in one exposure. For these reasons the surface symmetric reflection is unsuitable for examining device wafers, although this reflection did show contrast from defects in the substrate.

On the same plate there was an asymmetric reflection present which, from its position and aspect ratio, could be identified as having $\theta_B \approx 26^\circ$ and $\chi = 20^\circ$. To properly expose this an exposure time of approximately four times that for the 111 reflection was required. Due to the insensitivity to orientation of the white radiation method, diffraction occurs simultaneously from the whole of the illuminated area, even though the sample has a small process induced curvature (see section 5.3.3). One would expect this to lead to uniform contrast from the epilayer and device areas since the doped areas will diffract at the same angle as the epilayer, although at a slightly different wavelength because of the effective mismatch between them. The appearance of the devices as white contrast on a dark background (figure 5.3a) can therefore only be explained by absorption of the diffracted X-rays in this area by metallisation on the wafer surface.

Within the device area, very little contrast is visible, although there is a dark stripe of enhanced intensity running along the lower edge of some devices. This can be considered as extinction contrast, where the heavily distorted region at the interface between the device and the epilayer "pumps out" of the incident beam X-rays of wavelengths not normally satisfying the Bragg condition. This contrast is similar in form to that observed by Blech and Meieran [49], with the exception that in their experiment enhanced intensity was given because the angular divergence of the incident beam was greater than the reflecting range of the crystal (see section 2.3.1). In the

epilayer between chips, contrast is visible from some defects such as the dislocations indicated by the arrows, but no defects are visible in the device areas.

The final white radiation experiment was to place the sample surface at a glancing angle of $\sim 2^{\circ}$ with the incident beam, the plate being placed above and parallel to the wafer surface. The resulting topograph consisted of many overlapping reflections making it difficult to distinguish details. In some areas however, the images from different reflections were sufficiently separated to give good resolution and contrast and an example is shown in figure 5.3b. This shows very similar contrast to 5.3a, including the enhanced intensity at the device edges. However, a large area of depleted intensity above the devices is visible due to the absorption of the incident beam by the device areas, which effectively casts a shadow of the devices.

The area of heavily dislocated crystal indicated by A is also noteworthy on this topograph. This consists of a crossed grid network of dislocations running parallel to the <110> directions, and is formed to partially relieve the stress caused by the contraction of the silicon lattice which occurs when a dopant of smaller ionic radius is diffused into the silicon lattice. These misfit dislocations have been widely reported, observed by a variety of techniques [84-87], and are generally accepted to be either pure edge or 60° dislocations lying in the plane parallel to the surface and with Burgers vectors of type a/2(110).

The white radiation methods described here have several obvious advantages for the examination of processed wafers.

They are experimentally very simple, require very short exposure times, are capable of giving a range of reflections for a single exposure and their insensitivity to orientation enables large areas of curved wafers to be imaged. Surface symmetric reflections have a limited use whereas asymmetric reflections with a glancing angle of incidence can be used to limit the depth penetration of the X-rays, to give an aspect ratio close to unity and are capable of imaging dislocations and other large distortions. The single crystal technique is not however capable of imaging the small strains created by the diffusion and masking processes and is thus unsuitable for examining details of the device structure or of process induced defects.

5.3 Glancing angle double crystal topography.

To obtain a higher sensitivity to strain and misorientation, it was decided to use the double crystal technique in the +- setting with a highly asymmetric second reflection. Some parallel settings were used, however because of the low angular divergence of the beam in the plane of incidence, the non-parallel +- setting is also highly strain sensitive.

5.3.1 Experimental procedure.

The results described here were obtained during the course of several visits to the SRS. The majority of the experiments were carried out on station 7.5, using radiation from a standard 1.2T bending magnet. Some results however were obtained on station 9.4 using radiation from the 5T

wiggler magnet, which is more intense and extends to shorter wavelengths. For the work described here however, the wiggler station had no advantages over the normal line except for shorter exposure times. It also presented practical problems due to increased short wavelength scatter which necessitated more careful shielding of the experiment from noise.

The double crystal cameras on both stations are very similar in design, with the 2θ (goniometer) arm aligned in the vertical plane to take advantage of the highly polarised nature of the radiation, since in this geometry the incident X-rays are almost entirely σ-polarised. The size of the incident beam is limited firstly by entrance slits at the point where the beam enters the experimental hutch and then by one or more sets of remotely controlled slits nearer the first crystal.

Rapid initial alignment of the sample and beam conditioner is achieved by using the following procedure. The goniometer arm is oriented horizontally, that is, parallel to the incident beam, with the aid of a permanently attached spirit level. The sample is now mounted on the second axis, making sure that the wafer surface is directly on axis with the use of an alignment laser fixed to the back wall of the hutch. The sample is rotated so that the processed side is facing the incident beam and is roughly perpendicular to it and its orientation is ascertained with a back reflection Laue using a pinhole on the incident beam. With subsequent Laue's the tilt of the sample is adjusted so that the nominal surface plane (which is often several

degrees off the actual wafer surface) is perpendicular to the incident beam and the zone containing the desired reflection is parallel to the plane of incidence. The beam conditioner is now mounted on the first axis and the process repeated. In this way, both crystals are exactly aligned with known orientations and can be accurately rotated by means of calibrated rotation stages to within a fraction of a degree of the Bragg angle.

The goniometer arm is now rotated by $2\theta_1$, and the beam conditioner is rotated to give an angle of θ_1 between the incident beam and diffracting planes, where θ_1 is the Bragg angle for the beam conditioner selected to diffract a particular wavelength from the polychromatic incident beam. It is essential now to check that the once diffracted beam passes directly over the second axis and this is done by removing the sample goniometer, carefully noting its position and replacing it with a pointer. The position of the diffracted beam relative to this pointer is then quickly found with the aid of a polaroid film placed behind it, the pointer being visible by virtue of its shadow cast in the scattered radiation. If the diffracted beam does not pass through the axis then it can be adjusted by a simple rotation of the first axis. Note that this moves the position of the beam by selecting a different wavelength and is therefore not a valid procedure when using characteristic radiation laboratory sources when both θ_1 and $2\theta_1$ must be adjusted.

At this point the second crystal is shielded as much as possible from scattered radiation to reduce fogging of the

film emulsion. This is achieved by enclosing the incident beam in lead piping between the entrance slits and the slits nearest the beam conditioner, and then completely encasing the beam conditioner in lead, allowing only two apertures, one for the incident and one for the diffracted beam. These apertures must not cut either the incident or diffracted beam or they too will act as sources of scattering. It is also usually desirable to enclose as much of the diffracted beam as is practicable by means of more lead piping. It is worth spending extra time at this stage to ensure a good signal to noise ratio on the topograph, especially if a large area of the sample is to be imaged.

The second crystal is now remounted and rotated to give an approximate angle of incidence of $\theta_B - \chi$. A detector consisting of a scintillator and photomultiplier tube is attached radially to the second axis at an angle of $2\theta_B$ to the goniometer arm. The experimental set-up at this stage is shown schematically in figure 5.4.

The reflection can now be quickly found (on a good day!) by scanning the second axis, using a small incident beam to avoid saturation of the detector. For processed wafers, which have a significant rocking curve width, the second reflection can usually be found by rotating the axis continually at a medium speed and using a ratemeter to observe the peak. Furthermore, by using the audio output the peak is found with a minimum of concentration. For highly perfect crystals however it is necessary to scan the axis in steps of the order of seconds of arc, measuring the intensity after each step. Luckily this can be done

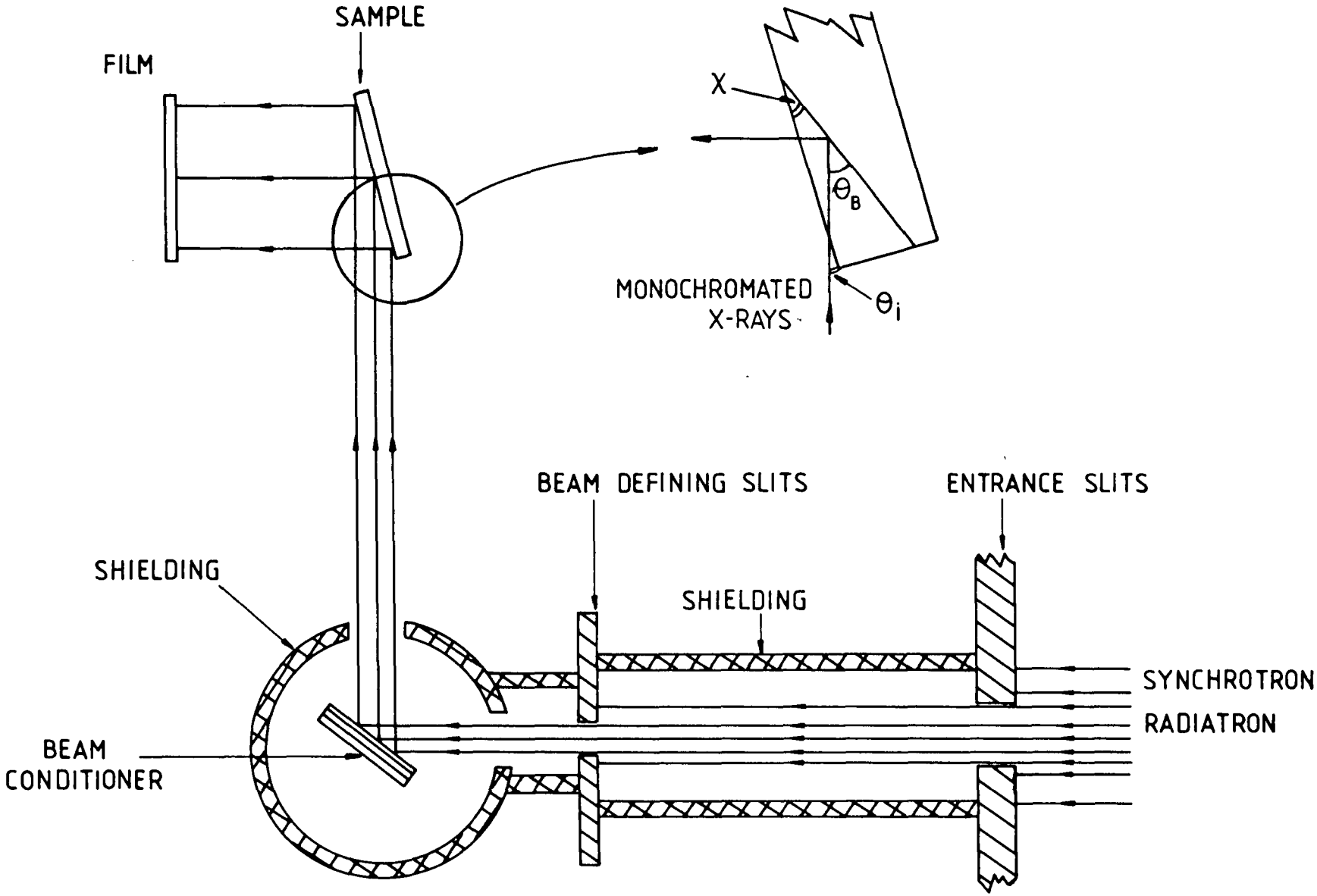

Figure 5.4
Experimental set-up for glancing angle double crystal topography with synchrotron radiation

automatically, the computer stopping the scan when the diffracted intensity rises above the level set by the operator.

5.3.2 Choice of reflections.

When choosing which reflections to use in a double crystal experiment several factors have to be taken into consideration. As already mentioned, a parallel setting is not needed for a high strain sensitivty, although the Bragg angles for the two crystals should still be kept as close as possible. To this end, the first crystal can be considered as a beam conditioner, selecting a wavelength and shaping the beam incident on the second crystal.

For the second crystal, we want a reflection which limits the penetration of the X-rays into the sample and gives an aspect ratio close to unity, that is $\theta_B + \chi$ close to 90°. The range of possible Bragg angles is also limited to $\chi < \theta_B < 90^\circ$ which obviously limits the possible wavelengths that can be used to $2d\sin\chi < \lambda < 2d$. Two important parameters describe the penetration of X-rays into a crystal in the Bragg geometry, the extinction distance ξ_g (equation 1.18) and the penetration depth P. In, or very close to the range of total Bragg reflection ($-1 < \eta < 1$) the incident beam diminishes very rapidly in intensity (section 1.4.7) and at a depth of $\xi_g/_{2\pi}$ below the surface is reduced in intensity by a factor of $1/_e$ [88].

In asymmetric reflections ξ_g is given by: [89]

$$\xi_g = \frac{1}{r_e |C| \lambda |F|} \cdot \{|\sin(\theta_B - \chi)|\sin(\theta_B + \chi)\}^{0.5} \quad (5.2)$$

where the symbols are the same as defined in equation 1.18. In cases of low photoelectric absorption and close to the exact Bragg condition, the depth to which the crystal will be imaged will be primarily dependent upon this quantity.

Away from the exact Bragg condition and in heavily distorted crystals, extinction is less important and the penetration of the X-rays is controlled by ordinary photoelectric absorption. The intensity of the incident beam will be reduced by a factor of 1/e at a depth of P_1 perpendicularly below the surface given by:

$$P_1 = \mu^{-1}\sin(\theta_B - \chi) \qquad (5.3)$$

and a once diffracted beam will be reduced by a factor of 1/e at the surface if diffraction occurred at a perpendicular depth of P_2 given by: [90]

$$P_2 = \mu^{-1}[\mathrm{cosec}|\theta_B + \chi| + \mathrm{cosec}(\theta_B - \chi)]^{-1} \qquad (5.4)$$

It is this parameter that is used here when considering the depth penetration far from the exact Bragg condition.

Both ξ_g and P_2 are dependent upon wavelength and reflection and therefore the continuous range of wavelengths available at the SRS allows the depth sensitivity to be varied over a wide range. It is convenient when working at the SRS to have a table of Bragg angles, ξ_g's and P_2's for a particular reflection at different wavelengths and two very simple programs using equations 5.2 and 5.4 were written to give these, using the values of f_a and μ given in [1]. Printouts for several of the most widely used reflections are given in Appendix B.

Using these tables it was decided to use the following reflections, the 115 (χ = 38.9°), 224 (χ = 19.5°) and 220 (χ = 35.3°). The values of θ_B, θ_i, ξ_g and P_2 for these reflections at the wavelengths used are given below in table 5.1.

The first crystal was a high purity, dislocation free, 4 inch diameter, 15mm thick silicon crystal with a (111) surface plane. The first reflection is chosen to give a $2\theta_1$ of approximately 90° since this places the second crystal as far as possible from the direct beam, making shielding of the sample and film from scattered radiation easier. The other consideration for the choice of the first reflection is the suppression of harmonic contamination. This arises

h k l	λ (Å)	θ_B(Deg)	θ_i(Deg)	Aspect ratio	ξ_g(μm)	P_2(μm)
115	1.80	59.5	20.5	0.99	16.0	11.7
224	1.80	54.3	34.8	0.96	13.7	16.2
115	1.80	50.0	11.0	1.00	13.4	10.2
224	1.55	44.4	24.9	0.90	13.2	20.0
224	1.35	37.5	18.1	0.84	12.6	23.5
115	1.55	47.9	8.9	1.00	12.4	9.4
115	1.50	45.9	6.9	1.00	11.3	8.3
115	1.35	40.2	1.3	0.98	5.4	2.3
224	0.78	20.6	1.1	0.64	4.8	10.0
220	2.70	44.7	9.4	0.98	3.8	2.0

Table 5.1

Values of the Bragg angle, angle of incidence, aspect ratio, extinction distance and penetration depth for the reflections and wavelengths used in the experiment.

because of the 1st order diffraction at λ having the same Bragg condition as the 2nd order diffraction at $\lambda/2$, 3rd order at $\lambda/3$ and so on, and can make interpretation of the results very difficult because of the superposition of many different reflections. For the first experiments carried out on the wiggler line, a 224 first reflection was used to spread the incident beam, which results in contamination at all higher orders. Even though the 115 reflection used for the second reflection does not have a harmonic at $\lambda/2$, the radiation from the wiggler line still has appreciable intensity at $\lambda/3$ and therefore some harmonic contamination will be present.

It was found however that since the horizontal and vertical extent of the beam could be made large (up to 40mm by 20mm) without causing excessive scatter and the angle of incidence for the second crystal was small, the incident beam did not require spreading. This enabled a surface symmetric 333 first crystal reflection to be used which has the advantage of not having a harmonic at $\lambda/2$, and although it does have a harmonic at $\lambda/3$, this is not a problem on the standard beam line for the wavelengths used since the intensity of the X-rays drops very sharply for wavelengths shorter than ~ 0.7Å. For the 220 reflections though, the 333 reflection could not select suitable wavelengths at convenient angles and therefore unfortunately, a 220 first crystal reflection had to be used with resulting contamination at all higher orders.

5.3.3 General observations.

Figure 5.5 shows a single exposure for the 115 reflection at λ = 1.6Å (exposure time 2 minutes at 197mA, using wiggler radiation). The contrast from the device areas is now striking when compared with figures 5.2 and 5.3, and a large area of the crystal is imaged but with markedly different contrast depending on the position on the plate. The difference in contrast arises because the whole of the angular diffracting range of the sample is present on one topograph due to a small process induced curvature. Areas with different lattice parameters or with slightly different orientations diffract at different Bragg conditions and this is reflected in the position on the plate at which they give strong intensity.

Note that the topograph shows two bands of strong diffracted intensity marked by the arrows A and B. The diffraction at A is mainly due to the devices and at B is due to the epilayer. At first sight therefore it is surprising that in this topograph the two diffractions are not complementary, that is, there is a strong intensity in the channels (here, the term channel is used to describe the areas between individual chips) at both A and B. Also, on closer inspection the channels diffract to some extent at every position on the plate between these two points. This rather complicated diffraction profile arises because of the variation of lattice parameter with depth of the epilayer. Since, as is shown later in this section, the device side of the wafer is concave, the epilayer must have a smaller lattice parameter than the substrate and in order for this

to be accommodated without the generation of misfit dislocations at the interface, the lattice parameter must vary continuously with depth between that of the substrate and that of the epilayer.

At point B enhanced intensity is seen in the channels for all reflections and wavelengths and hence diffraction must be occurring within one or two microns of the surface. The top of the epilayer must therefore satisfy the Bragg condition at this point and the penetration depth is described by ξ_g. As we move away from the exact Bragg condition, the penetration is described by P_2 and the X-rays penetrate to this depth or to a depth at which they are strongly diffracted by crystal with a suitable lattice parameter. Generally therefore, the further we move from the Bragg condition for the surface layers, the larger the value of lattice parameter required to satisfy the Bragg condition and hence the greater the depth penetration. At point A, for reflections with a large P_2 such as the 224 reflection at λ = 1.35Å the X-rays penetrate to the substrate and this leads to a dark band running across both devices and channels, whilst for the 115 reflection at λ = 1.35Å the peaks from the devices and the epilayer do indeed become complementary. Topographs with large values of P_2 as in figure 5.6, the 224 reflection at λ = 1.55Å, also show up striations running across the channels which correspond well with the pattern of microdefects seen in figure 5.1.

Note also how at point B there is a thin band in the middle of the channels, indicated by the letter E which diffracts at a position slightly displaced compared to the

epilayer. This is because of a local relaxation of the lattice, most probably caused by a variation in the oxide thickness.

Clearly, in the single exposure topograph we have a visual sense of the effective mismatch of diffused regions with respect to the epilayer or substrate. The diffracted intensity of a particular device can be followed as it moves through the range of reflection as for the area marked by C. The position at which it diffracts most strongly can then be compared with the position at which strong diffraction occurs for the epilayer or substrate and the effective mismatch between the two calculated using the simple expression:

$$\Delta d/d = - \frac{\Delta\theta}{\tan \theta_B} \qquad (5.5)$$

where $\Delta\theta$ is related to the spatial separation of the two areas on the plate by:

$$\Delta\theta = \frac{1}{\sin(\theta_B + \chi)} \cdot \frac{\Delta x}{R} \qquad (5.6)$$

and R is the radius of curvature of the sample.

The curvature of the sample can be found using the above expression, by rotating the sample by a known angle and measuring the displacement of the diffraction maximum. This can be done by either taking several topographs or by making a multiple exposure on one plate, with a small rotation of typically 10 seconds of arc of the sample between exposures. The multiple exposure method shown in figure 5.7, the 115 reflection at λ = 1.5Å with a rotation

of 20 seconds of arc between exposures, is perhaps the most useful, giving bands of equal misorientation from which it is easy to calculate the radius of curvature. It does not however give the sense of the curvature since the direction of movement of the peak for a given direction of rotation is not recorded and therefore single exposures must be used to ascertain this. The resulting images are also difficult to interpret because of the superposition of diffracted intensity from several points on the rocking curve. However, the multiple exposure technique is preferable to a series of single exposures when looking for defects because of the large area of sample imaged on one plate. Furthermore, it was found that the defects (section 5.3.4) were equally visible in both techniques and therefore, from a materials viewpoint the multiple exposure method is to be preferred, giving the most information in the most convenient form, in the shortest time and at the least cost.

The curvature of the sample using figure 5.7 can be seen to be similar over the whole of the area imaged in figure 5.5 since the diffraction bands are equally spaced, and the radius of curvature is easily calculated to be 105m. From single exposures furthermore, the device side of the wafer is shown to be concave since a clockwise rotation of the sample moves the diffracting stripe up. This value for R gives an effective mismatch between the devices and epilayer of 120ppm, which agrees qualitatively with the expected strain for the dopant concentrations given by Fukuhara and Takano [91,92]. It is surprising though, that the epilayer should have a smaller lattice parameter than the device

areas since the diffusion of boron and phosphorous causes a contraction of the silicon lattice [93]. However, since the strong diffraction from the channels is also seen between individual devices at the same position, this is perhaps because the area we can see has been heavily boron doped to form isolation barriers (figure 5.1), and this has caused a lattice contraction greater than that caused by the emitter and base diffusions.

So far we have seen how the single exposure when combined with the multiple exposure, can give a value of the effective mismatch for the devices within the chip. This mismatch is not however the only mechanism which gives contrast of the devices. Referring to figure 5.11, the 115 reflection at λ = 1.6Å, we see how the device marked by C is diffracting with the same intensity as the background and is only delineated by contrast at its edges. This contrast is a result of the local misorientation of the lattice at the interface between the device and epilayer which occurs to accomodate the difference in lattice parameter between the two areas.

It is interesting to see how this contrast is critically dependent upon the position on the plate and hence the position on the rocking curve. Figure 5.8 shows the 115 reflection at λ = 1.55Å and the change in contrast of the device is clearly visible. At the low angle side of the rocking curve, that is the bottom of the topograph, the top of the device shows depleted intensity (white contrast) whereas the bottom shows enhanced intensity (black contrast). However at the point where the device is

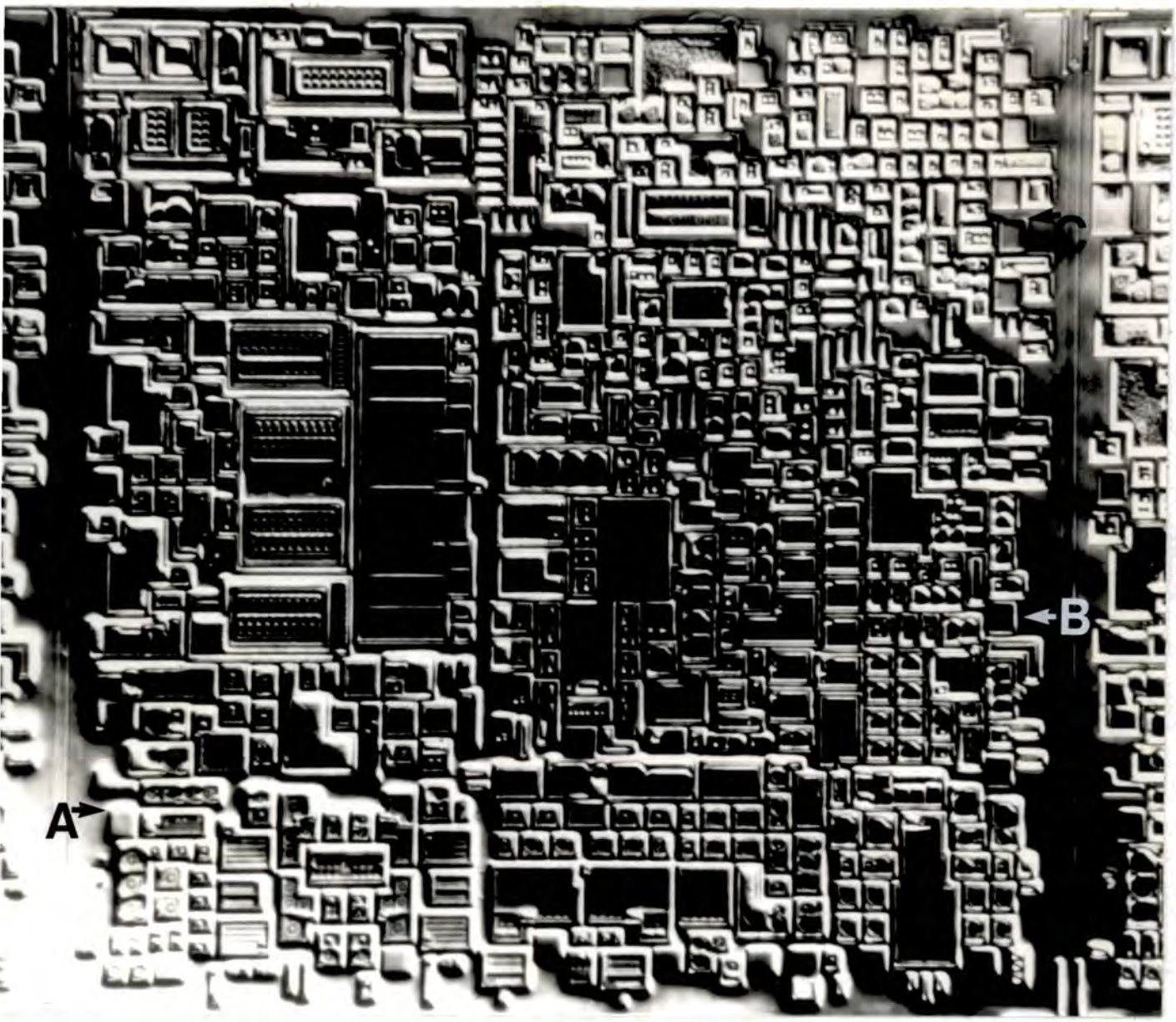

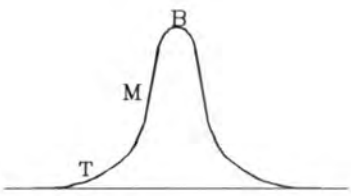

Point A
Device on low angle side of rocking curve

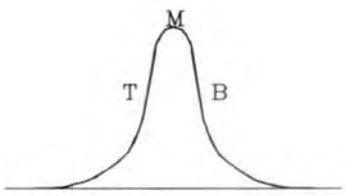

Point B
Device exactly on the Bragg peak

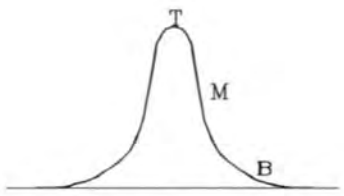

Point C
Device on high angle side of rocking curve

Figure 5.8

115 double crystal topograph, $\lambda = 1.55$Å (SRS) showing the variation of contrast of a device with position on the rocking curve. The sketches refer to the points marked on the topograph. B ≡ bottom edge of device; M ≡ middle of device; T ≡ top edge of device.

diffracting strongly, the two edges show white contrast and at the high angle side, the top shows black contrast and the bottom white contrast. This contrast reversal can be explained either by considering the Du Mond diagram (section 2.2.4) or more clearly by considering the position of the device on the double crystal rocking curve shown schematically at the side of figure 5.8. Since the device has a larger lattice parameter than the surrounding lattice it exerts a compressive force at its edges. This leads to the lattice planes being curved by an equal amount on all sides of the device but in a different sense to the diffraction vector on opposite edges.

If we represent the misorientation of the lattice parallel to **g** by a shift along the θ axis of the rocking curve, the device can be simplified to three equally spaced diffracting points on it. Note that this is a crude approximation since the misorientation varies continuously with distance from the edge, but is nonetheless a useful concept to explain the contrast mechanism. At point A, the device is at the low angle side of the rocking curve which means that the bottom edge is at a greater θ and therefore diffracts with greater intensity whilst the top edge is further from the Bragg condition and thus appears white. At the position where the device satisfies the exact Bragg condition (point B) the top and bottom edges necessarily diffract with less intensity and show white contrast, and at point C the bottom edge does not diffract whilst the top edge diffracts strongly. Since the area surrounding the device diffracts at an angle which puts it outside the

reflecting range at this point, this contrast is confined to the diffused area.

This contrast is a good indicator of the degree of strain present at the interface, as can be seen from the device marked by D in figure 5.5. The greater the strain then the greater the angle (and therefore distance on the plate) between the point where the device is diffracting strongly and where enhanced intensity can still be seen from the edge. There is, using this criterion, obviously a high strain gradient present at the edge of device D. The spatial extent of the enhanced intensity also contracts as θ is increased until it is confined to a small band at the interface. This shows that the most intense strain is present very close to the edge, and decays with distance away from it. The presence of large strain gradients in processed wafers is one cause of crystallographic defects and dislocation loops are observed originating from a large number of these edges (section 5.3.4).

The contrast rule described above holds well for all of the devices, but the contrast in the area immediately surrounding them is less simple to explain. The difficulty arises because of the presence of oxide and metallisation films which are not imaged but which nonetheless exert localised strains at their edges. Without more detailed information on the configuration of the devices it is therefore not possible to explain all of the fine structure seen in this area. Several general observations can however be made. At the point where the devices are diffracting white contrast can be seen adjacent to the devices,

complementary to enhanced intensity within them. This effect arises because energy is taken out of the direct beam to form the diffracted beam within the diffused area, leading to a reduction in intensity incident on the adjacent area. From the separation of this shadow and the edge of the device, a simple calculation shows that for the 115 reflection at λ = 1.55Å, diffraction is occurring at a depth of approximately 8μm. Furthermore, this separation varies with position on the rocking curve, consistent with the model of a depth dependent lattice parameter described earlier. Obviously since P_2 for this experiment is greater than 8μm, this gives a good indicator of the lattice mismatch at a given depth.

At the point where the epilayer is diffracting strongly, the area immediately surrounding the devices shows a similar contrast reversal with position on the rocking curve as the device shown in figure 5.8. This effect is expected since the diffused area necessarily exerts a compressive force on the surrounding lattice.

For very low angles of incidence such as the 115 reflection at λ = 1.35Å shown in figure 5.9, the white shadow described above is very noticeable and actually obscures details of device structure and defects. Low angles of incidence should therefore be avoided if possible when looking for process induced defects. They do however show some very interesting dynamical effects, most noticably fringes adjacent to the edges of devices at the point where the channels are strongly diffracting. Presumably dynamical effects are present in this region for all reflections but

are not visible due to geometrical effects. The appearance and nature of these fringes is discussed in greater depth in chapter 6.

The sensitivity to lattice strain and tilt is greatest on the flank of the rocking curve (2.2.4) and this is clearly shown in these topographs. Figure 5.10 shows the same area of the wafer observed at two points on the rocking curve. At the point where the devices are diffracting, very little detail can be seen, whilst in the flank the fine structure is clearly visible. The contrast is again a mixture of lattice mismatch and lattice strain. Double crystal topography obviously gives sufficient resolution to distinguish between different device structures and as shown in section 5.3.4 is capable of imaging many process related defects.

5.3.4 Defects.

Several types of defect show up clearly in the double crystal topographs, the most common of which are shown in figure 5.11, the 115 reflection at λ = 1.6Å. Two types of defect are worthy of note in this picture, the heavily dislocated area marked A and the dislocation loops marked by B.

Area A is so heavily dislocated that it is not possible to individually resolve the dislocations. It is likely however that these are misfit dislocations similar to those shown in figure 5.3b, created by a high dopant concentration, since they are confined to the diffused area [84-86]. Figures 5.12 and 5.13 show that these defects are

aligned parallel to the 110 direction and also that they appear in many other devices (marked by an arrow). At first it was considered that these were images of scratches on the surface of the wafer but their high density makes this improbable and none could be seen when the wafer was examined under an optical microscope. It is possible that they once again take the form of a crossed grid network if the dislocations parallel to 011 and 101 are 60° dislocations with Burgers vectors in the 111 plane, since for those dislocations **g.b** = 0 and they will not be highly visible. These straight dislocations show up with most clarity in the 224 and 220 reflections.

Whilst the type A dislocations can be attributed directly to the contraction of the lattice caused by dopant diffusion, the origin of the type B dislocations is not so straightforward. The formation of dislocations outside the diffused area was first reported by Sato and Arata [94] and were postulated as a mechanism for emitter push. Loops similar to those shown here have also been observed by limited projection topography [95]. Work by Fairfield and Schwuttke [96,97] who coined the term emitter-edge dislocations for the loops, showed them to be generated by a high strain gradient at the diffused-undiffused interface, created by the combined action of the lattice contraction of the diffused area and the stress at the edges of the oxide window formed to define the diffused area.

These results agree well with the loops observed here, since they are in all cases associated with those devices which show a high strain gradient at their edges. The

dislocations consist of concentric loops going into the crystal, extending to a distance of typically 100-200μm with the tips of the loops pointing in the 011 direction, in agreement with TEM studies by Lawrence [86]. The emitter-edge dislocations were very common in this sample and could be clearly seen at all positions of the rocking curve, although the tips of the loops were most visible at the point where the devices were diffracting, implying that the loops penetrate quite deeply into the crystal. Note that the dislocations have widths of typically 10-20μm because of the high strain sensitivity of the double crystal technique. Emitter-edge dislocations are extremely deleterious to the performance of integrated circuits since they penetrate deeply into devices and can cause emitter to collector shorts [98]. Identification of these loops enabled the manufacturers to eliminate them by raising the deposition temperature of the dopants.

5.4 Conclusions.

Several general conclusions can be drawn from this work about the best experimental conditions for examining processed silicon wafers. To begin with, the limitation of the depth of penetration of the X-rays is critical. Although one would expect the extinction distance ξ_g to be the crucial factor in this respect, for all the wavelengths and reflections used here, the X-ray beam is severely attenuated within 3μm of the surface, comparable to the diffusion depths. Also, the range of angles over which the crystal satisfies the exact Bragg condition is small compared to the

area imaged in one topograph and hence for most of the crystal the depth penetration is primarily limited by photoelectric absorption described by P_2. If P_2 is large, as for the 224 reflection and the 115 reflection for $\lambda > 1.5$Å, the background, that is diffraction from crystal further below the surface, acts to obscure images of the devices.

At first sight, the 115 reflection with a λ of approximately 1.5Å appears to give the best contrast, and does give very clear, sharp images with high resolution. It is clear however when comparing it with topographs that have a small ξ_g and P_2 such as the 115 at 1.35Å (figure 5.9) or the 220 reflection at λ = 2.7Å shown in figure 5.14 that much detail is not present in this reflection.

Interpretation of the topograph is made easier by arranging to have an aspect ratio close to unity since measurements can be made directly from the plate without need for correction. An aspect ratio of unity is not however essential and a distortion of up to 70% is tolerable, the only experiment in which the aspect ratio made visibility difficult being the 224 at λ = 0.78Å which has b/a = 0.64. Care should however be taken to avoid angles of incidence below approximately 5° since this leads to a considerable white shadow which often obscures images of devices and defects. The low angle of incidence does give rise to some very interesting dynamical effects, most notably the appearance of fringes at the edges of devices.

From the above discussion the 220 reflection at λ = 2.7Å does appear to satisfy the above criteria very well but the 220 topographs presented here should not be relied upon

when considering contrast effects because of the high proportion of harmonics with different penetration depths which go to make up the resulting image. Whilst the 224 reflection would from these arguments appear to be unsuitable, it does still give good device contrast and is useful for imaging a greater depth of crystal, giving images of microdefects in the crystal bulk.

If one is examining the wafer for defects then one multiple exposure will probably be sufficient to image a large area of the wafer and show defects clearly. In addition, one or two single exposure topographs will enable the sense of curvature and hence the sign of the mismatch of devices to be determined as well as allowing contrast mechanisms to be studied.

Finally, it should be remembered that the preceding discussion is concerned with a {111} surface oriented wafer and whilst the general conclusions can be used with any wafer orientation, the specific reflections and wavelengths must be tailored to suit the experiment.

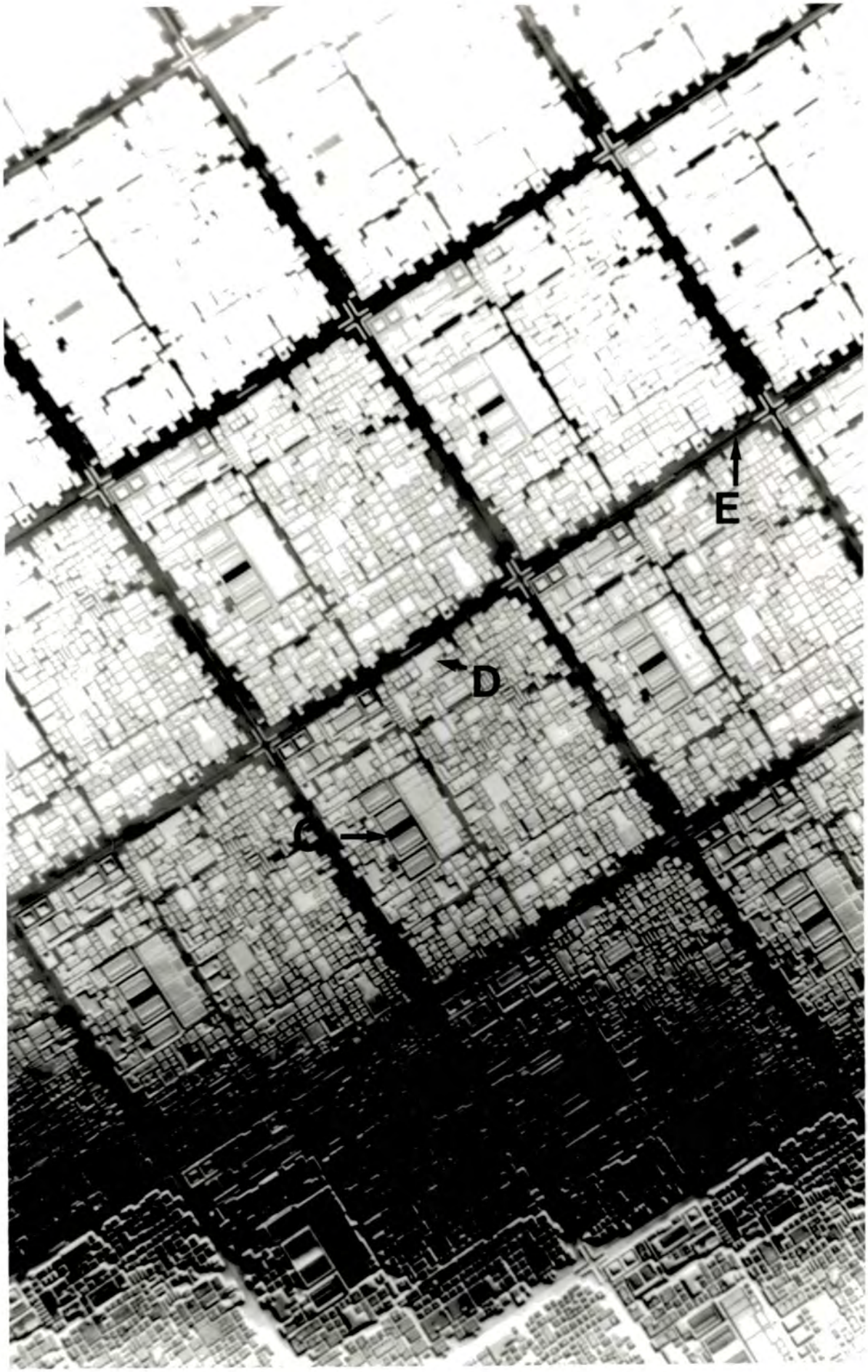

Figure 5.5
Double Crystal Topograph (SRS)
115 Reflection $\lambda = 1.6$ Å

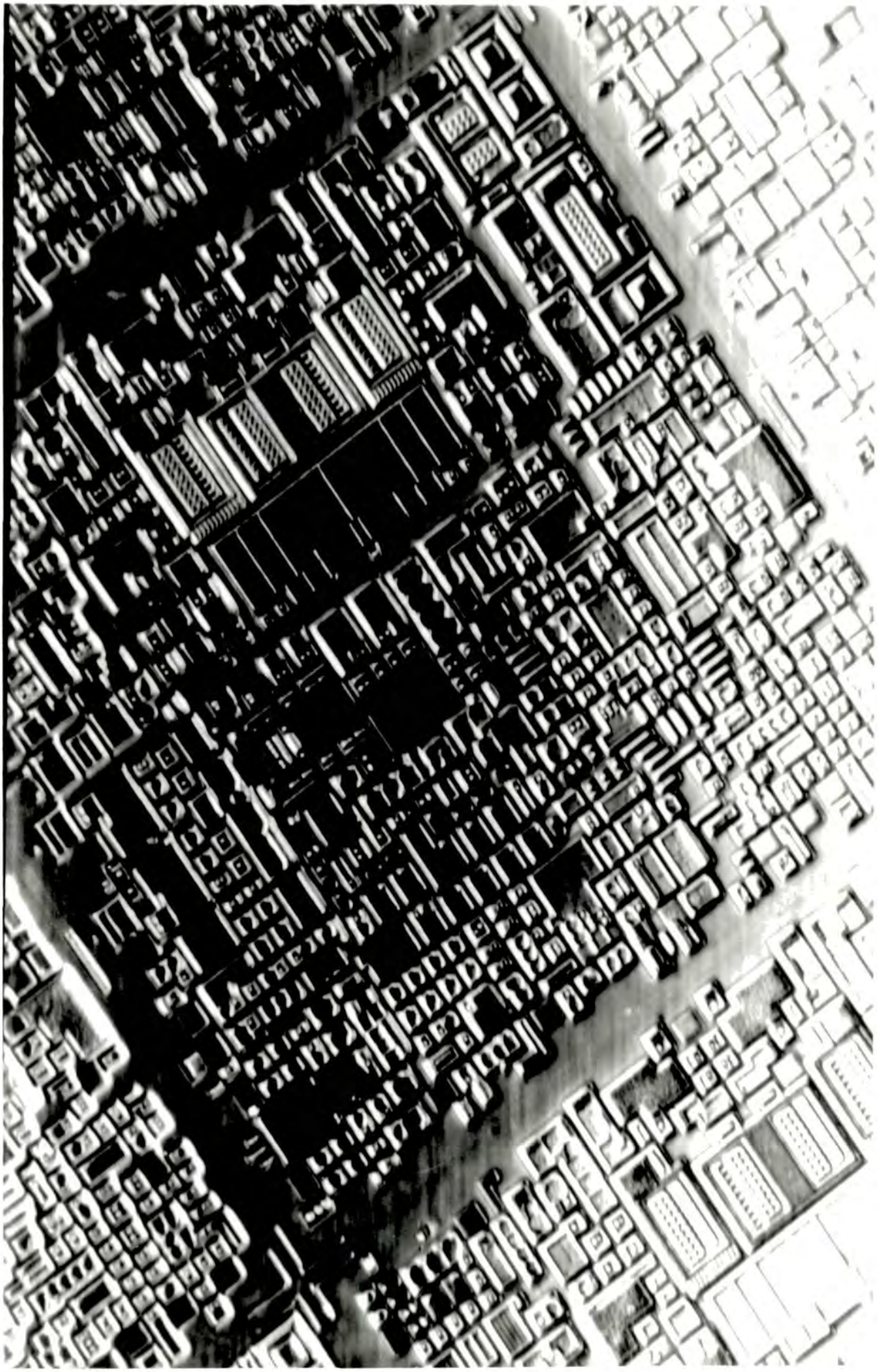

Figure 5.6
Double crystal topograph (SRS)
224 reflection, λ =1.55 Å. See text for details

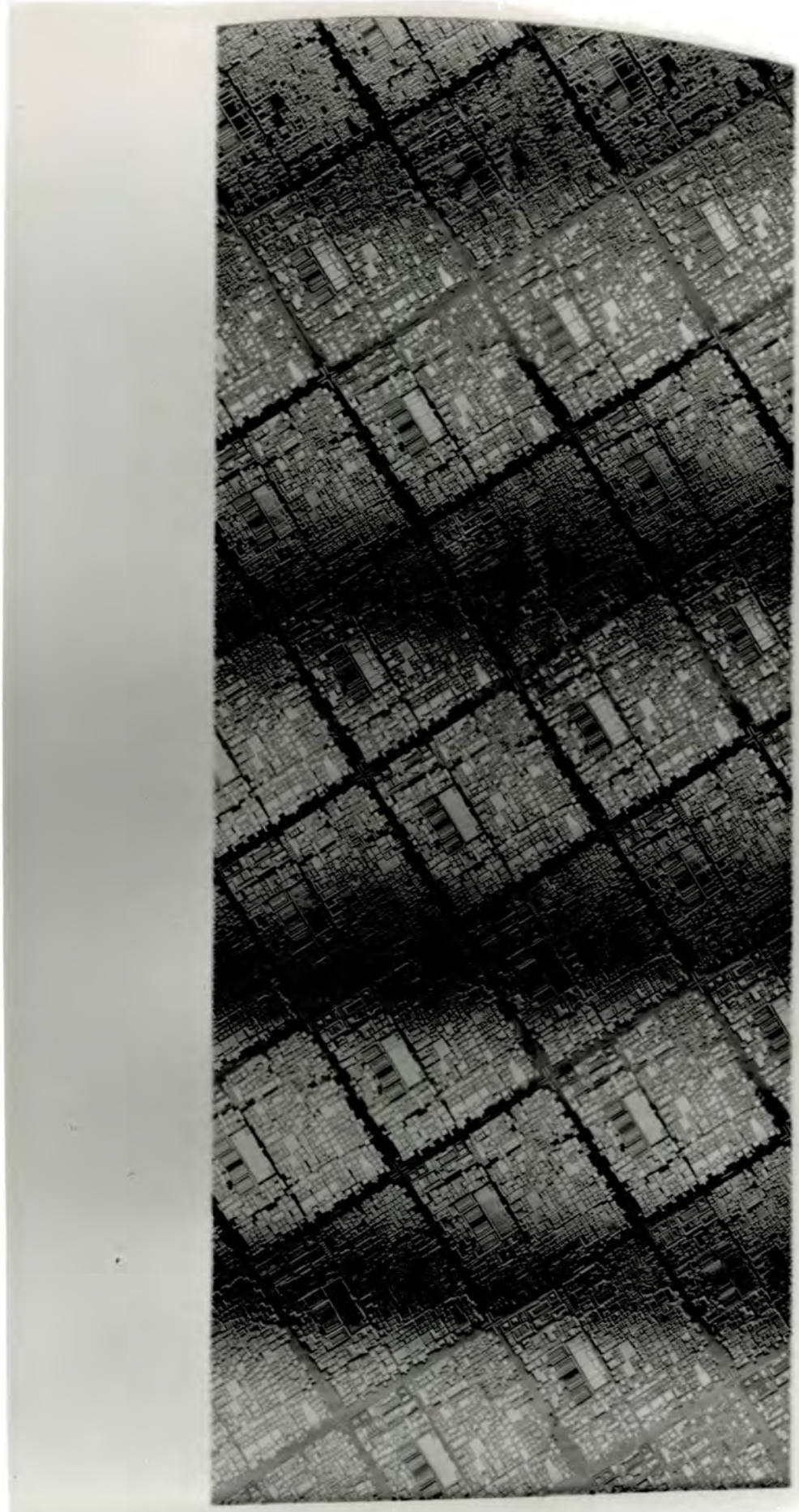

Figure 5.7
Double Crystal Topograph (SRS)
115 Reflection λ = 1.5 Å (Multiple Exposure)

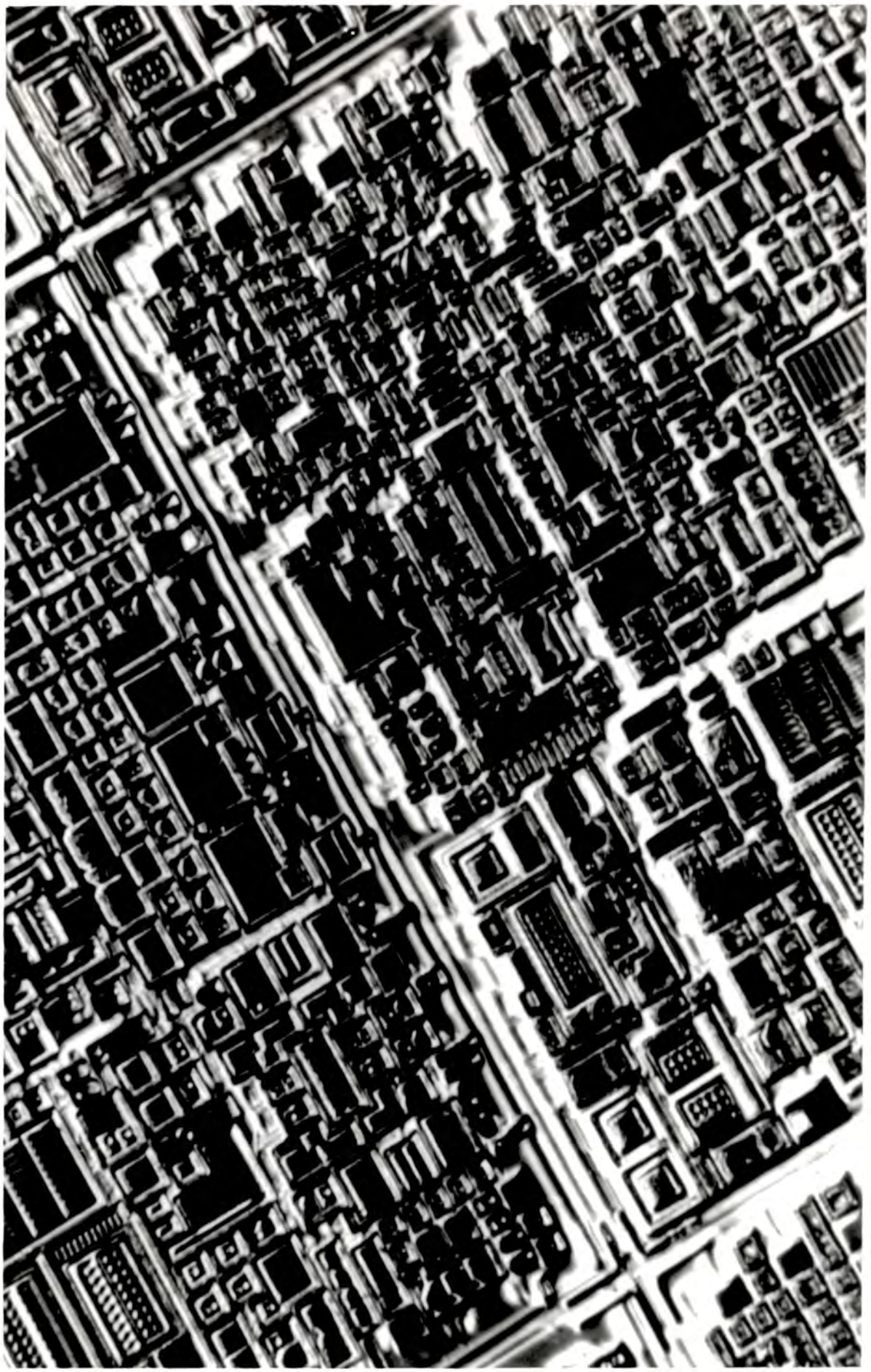

Figure 5.9
Double crystal topograph (SRS)
115 reflection, λ=1.35 Å. See text for details

a)

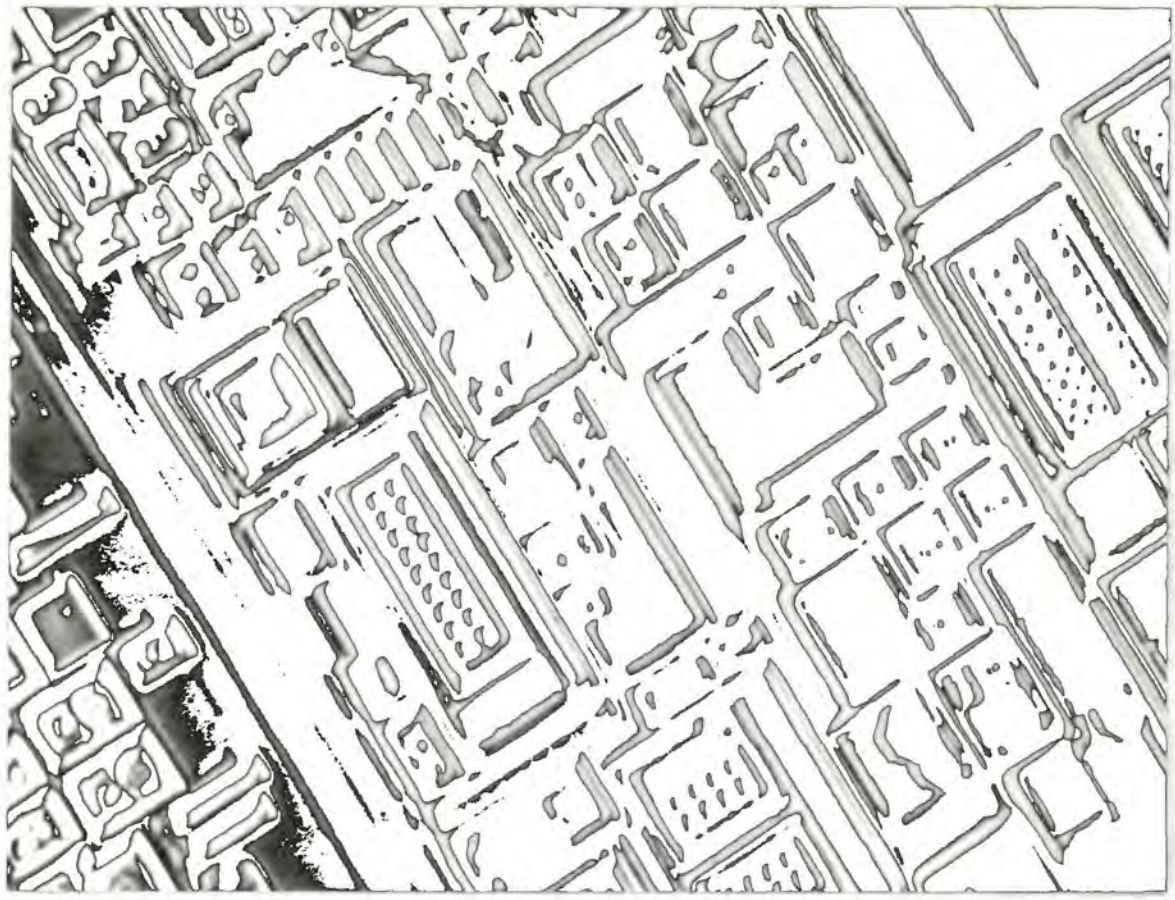

b)

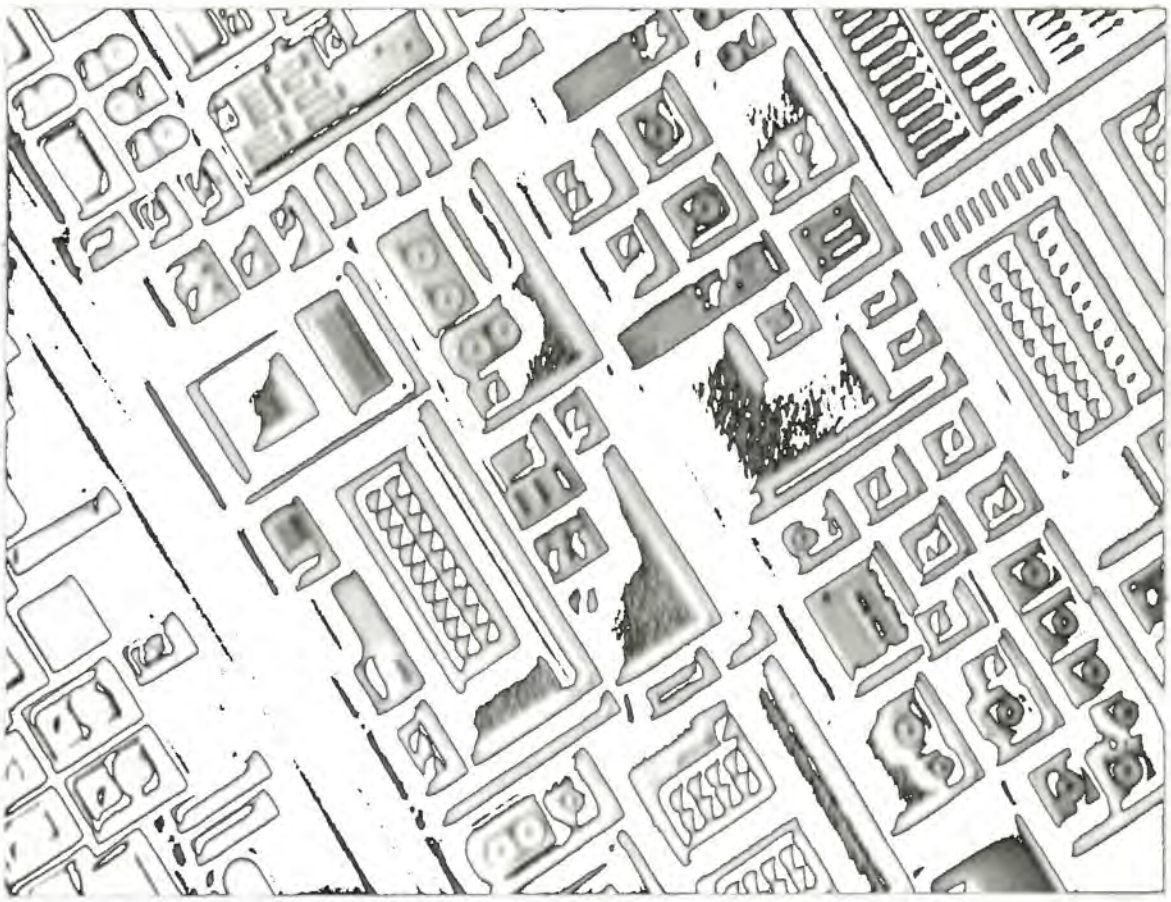

Figure 5.10

400μm

Double crystal topographs (SRS) 115 reflection, $\lambda = 1.6$Å.
a) Exact Bragg condition.
b) Same area but diffraction is from flank of rocking curve. Note the better resolution and contrast for this condition.

g

Figure 5.11
Double crystal topograph (SRS)
115 reflection, λ=1.60 Å. See text for details

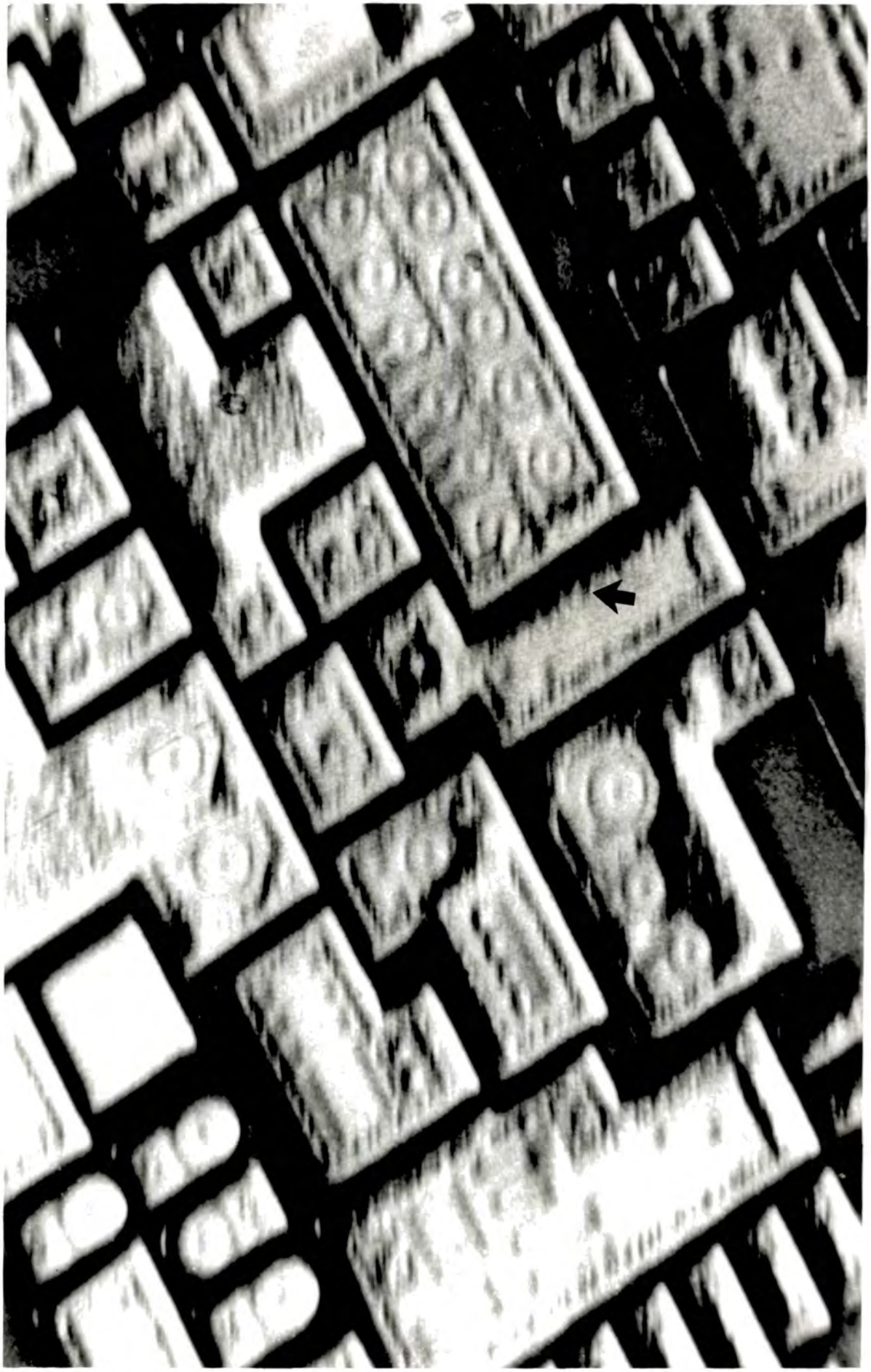

Figure 5.12
Double crystal topograph (SRS)
224 reflection, λ =1.55 Å. See text for details

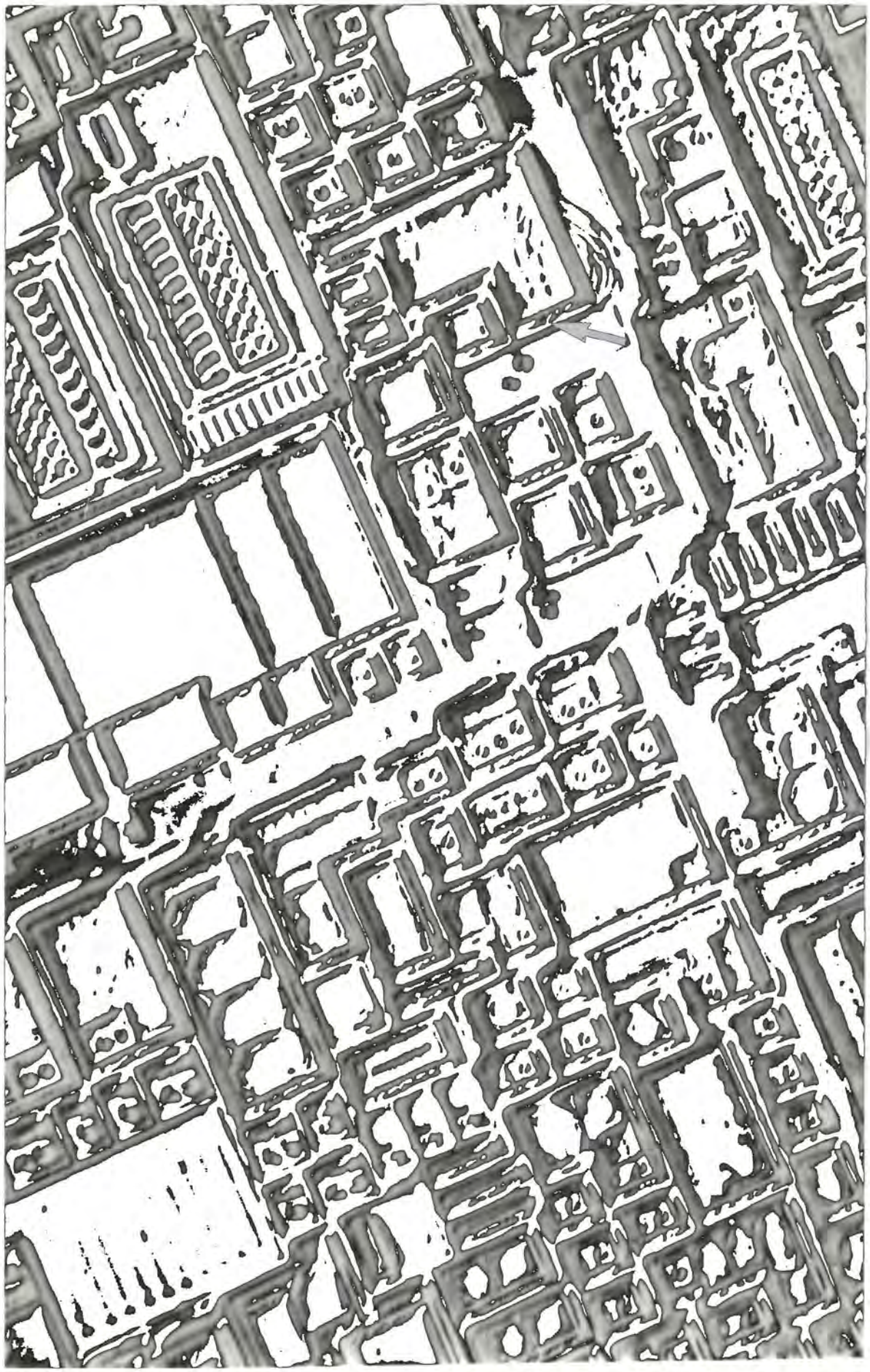

Figure 5.13
Double crystal topograph (SRS)
220 reflection, $\lambda = 2.70$ Å. See text for details

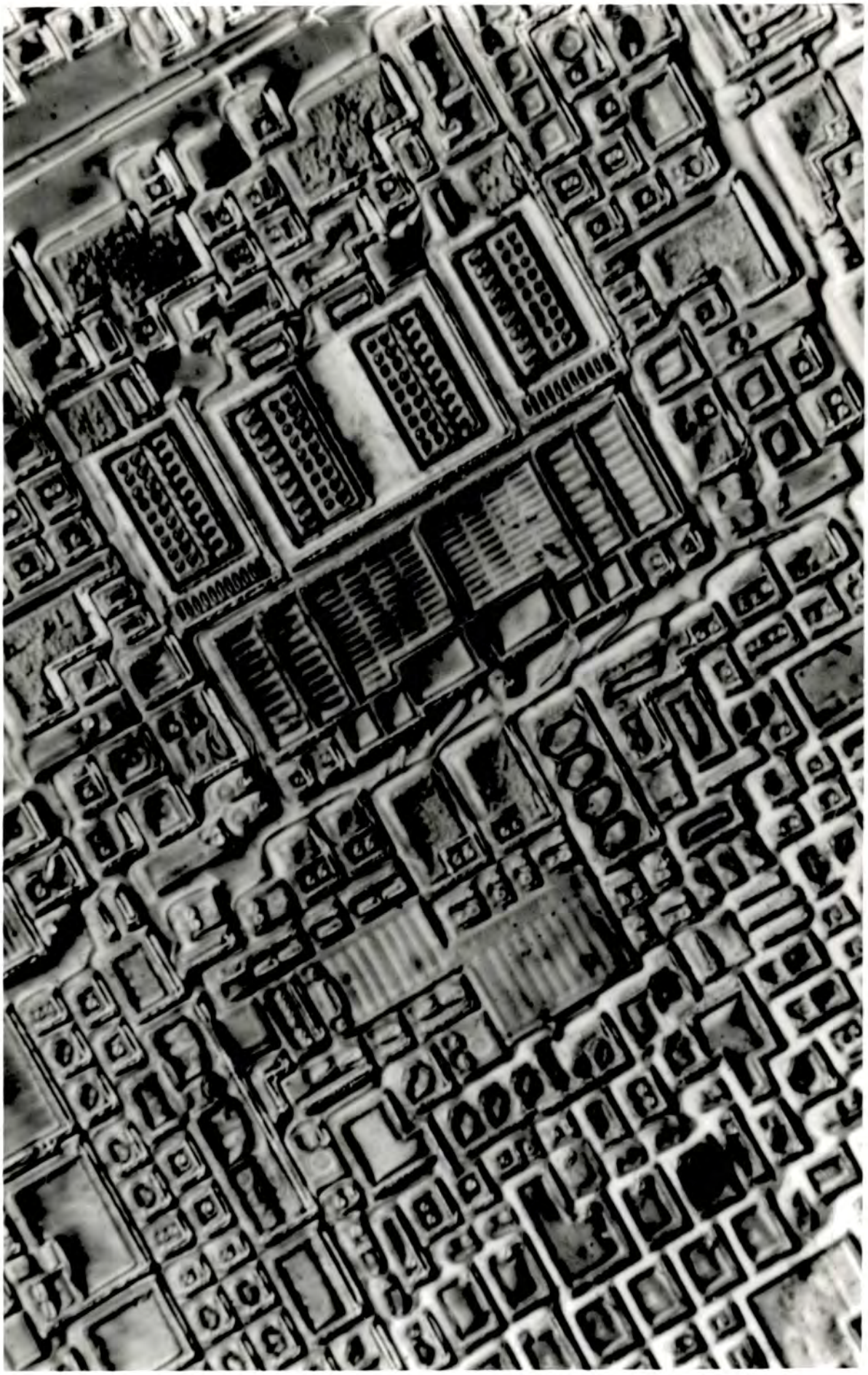

Figure 5.14
Double crystal topograph (SRS)
220 reflection, $\lambda = 2.70$ Å. See text for details

Chapter Six

Comparison of topographic techniques for the examination of processed silicon wafers.

6.1 Introduction

This chapter describes the characterisation of a fully processed wafer from the GEC CMOS production line by Lang, section and synchrotron radiation double crystal topography. The three techniques are compared and their relative merits and disadvantages discussed. Finally, the formation of interference fringes in Bragg case topography of bent crystals is explored for both this and the bipolar device wafer examined in the previous chapter.

The sample is a small strip measuring 35mm by 10mm, cut from a wafer from the Hirst Research Centre CMOS line. The substrate is 001 orientation Sb doped (n-type) with a 5μm P doped epilayer (n^+-type) and had been subjected to the following processing schedule:

Ion Implantation:

n-field, p-well, p-channel

Furnacing:

Initial oxidation, nitride deposition, p-well drive-in, field oxidation, gate oxidation.

No oxide-dielectric layers have been removed.

A section through a typical CMOS device is shown in figure 6.1. In these experiments the $\bar{2}20$ reflection with $MoK\alpha_1$ radiation ($\mu t = 0.86$) was used for the Lang topography

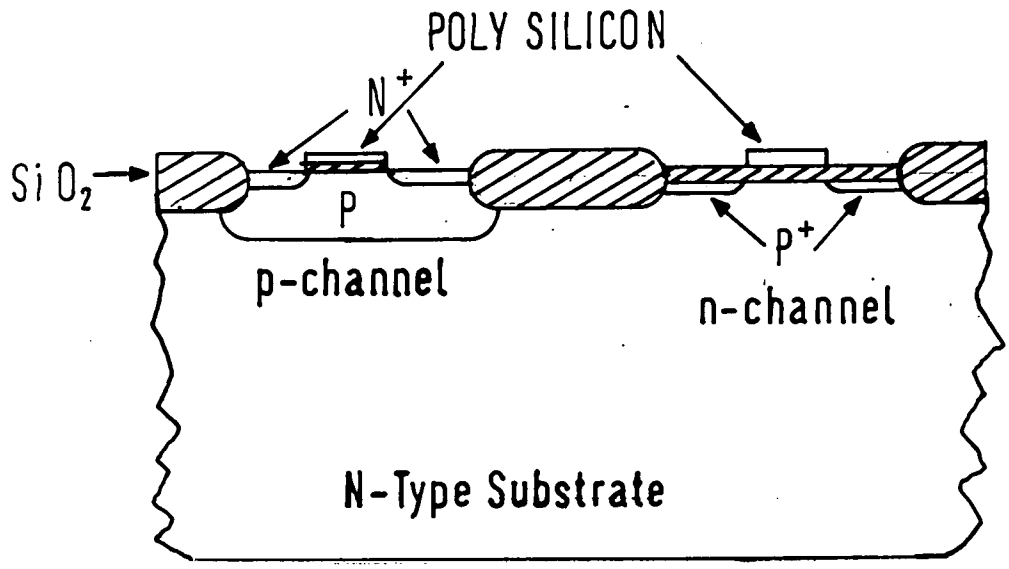

Figure 6.1

Section through a Complimentary MOS (CMOS) Device

and the $\bar{4}40$ reflection with $MoK\alpha_1$ radiation ($\mu t = 0.94$) for the section topography. The double crystal topographs were taken using the geometry shown in figure 5.4 with the 224 reflection at a wavelength of 1.36Å ($\chi = 35.26^{o}$, $\theta_B = 37.9^{o}$, $\theta_i = 2.5^{o}$) selected from the polychromatic incident beam by a 333 surface symmetric reflection from a highly perfect beam conditioner. From the previous chapter it is obvious that this is not an ideal geometry for studying the device structure because of the low angle of incidence, however it was chosen primarily to investigate the appearance of fringes previously seen at device edges in the bipolar wafer. These results are discussed in section 6.3.

6.2 Comparison of techniques

Figures 6.2 to 6.7 show a comparison between the three techniques. The positions of the section topographs shown in figures 6.6 and 6.7 relative to the Lang topograph is marked on figure 6.2a. Figure 6.2b shows a multiple exposure double crystal topograph with an angular step of 10 arcseconds between exposures. The rather poor resolution on this figure is because the topograph was exposed on medium speed film to ascertain the sample curvature. The remaining double crystal topographs shown in figures 6.3 to 6.5 are all single exposures. The topographs in figures 6.3 to 6.5 are reproduced at the same magnification from the plate but the Lang topograph suffers an extra horizontal magnification of 0.98 and the double crystal topograph a vertical magnification of 0.95. The section topographs shown in figures 6.6 and 6.7 have been reproduced at a slightly

higher magnification to show the fine structure more clearly.

It is evident from the transmission topographs that there is a high density of dislocations towards the top of the sample. Since the sample is cut from close to the edge of the wafer, these are probably associated with stresses formed in the wafer during furnacing. As can be seen from the section topographs they are evenly distributed through the crystal volume. Furthermore, the Lang topograph shows that the vast majority of them outcrop on the device side of the wafer. In the heavily dislocated region however, it is impossible to resolve individually all of the intersections with the surface. However, comparing the Lang with the double crystal topograph in figure 6.3 we see that there is a one to one correlation between these outcrops and the contrast marked by A in the double crystal topograph. This enables the position of the dislocation outcrop to be identified and several of these are shown on the diagram. It is now clear from the double crystal topograph that many of the dislocations penetrate through devices and as such will be extremely deleterious to device performance (see, for example [98]). Further enlargement of this area, shown in figures 6.8 and 6.9 shows that many of these dislocation outcrops are connected by straight dislocation lines, many longer than 200μm in length, parallel to the $\bar{1}10$ direction. Since the maximum depth penetration of the X-rays for this reflection is only of the order of 5μm (P_2 = 4μm) these must lie very close to the surface and are therefore most probably confined to the 5μm epilayer, suggesting that they

are misfit dislocations formed at the substrate/epilayer interface. Again, many of these appear to pass through devices and are therefore undesirable. Note also how they are superficially similar to the edges of processed areas indicated by B and should not be confused with them.

Very clear on the Lang topograph is the contrast formed by the identification number which has been scratched on the back of the wafer. Such numbers have been shown to generate dislocations [99], [100] because of the high stress concentration associated with them, although in this case none appear to have been formed. From the section topographs it is clear that the strain field from the numbers is large enough to create direct images which extend to the centre of the section and in some cases through to the left hand margin, that is the exit surface. This implies that there is a considerable strain due to the scratches present on the device side of the wafer. That this is the case is borne out by the outline of the numbers being clearly visible in the reflection topographs as shown in figures 6.3b and 6.4b Especially note the area marked C in figure 6.4b, where the strain field close to the exit surface is sufficient to create strong localised images. The influence of the scratches can also be seen in the bending of the Bragg reflection fringes discussed in section 6.3.3, as can be seen in figure 6.16 where the number 7 has caused a considerable distortion of the fringes.

It is obvious therefore that the scribed marks are not only deleterious because of the possibility of dislocation generation but also because they can create a considerable

localised distortion of the lattice at the device surface which may affect the circuit's performance. For these reasons it is suggested that the practice of identifying wafers by mechanical scribing be replaced by non-mechanical methods such as laser scribing. This initiative has already been taken by GEC Hirst Research Laboratories as a result of the Alvey collaboration of which this thesis forms a part.

Devices show different contrast in different techniques. Contrast in the double crystal technique has been discussed in depth in chapter 5 and therefore will not be explored here, however it is interesting to note the differences between this and contrast in the Lang technique. Generally, devices in the Lang technique show up because of large distortions which give dark direct images on the plate. Oxide and metallisation films give no contrast in the symmetric geometry except at the edges for which $\mathbf{g}.\mathbf{l} = 0$, where $\mathbf{l}$ is a vector parallel to the edge of the film; this is clearly shown by the areas marked by D in figure 6.5. For these reasons, the contrast on Lang topographs often bear little relation to the device geometry making the technique unsuitable for examining device related faults. When compared with the double crystal technique we see how the latter gives contrast from diffused and film covered areas and thus has a good correlation with the device architecture. Furthermore, using the two together, it is often possible to distinguish between diffused areas and oxide or metallisation which often mask other contrast in the double crystal topograph.

Devices in the section technique show a variety of contrasts. Here the case when the device side is on the exit surface is considered. When one cuts the direct beam, a very dark direct image is formed, with the width of the image indicating the depth to which the crystal is heavily distorted, if not the depth of the diffusion [101]. Only the direct image can be used as a measure of the depth and the contrast of this varies dramatically with the position of the device with respect to the base of the Borrmann fan. Figures 6.10a to 6.10d show the contrast from the same type of device cutting the Borrmann fan at different positions, shown approximately in the accompanying sketches. In figure 6.10a the device just touches the direct beam and the direct image is limited to a thin dark image on the exit surface, with the long range strain field still being sufficient to bend the Pendellosung fringes. As the device fully crosses the direct beam, figure 6.10b, the direct image increases in width, reaching a maximum size which it does not exceed. This position should therefore be used as a test of the depth of diffusion, since two identically fabricated devices will show direct images extending to the same depth.

If the device is very close to the direct beam and within the Borrmann fan, it may give rise to the contrast shown in figure 6.10c. Here, the direct image extends to the same distance from the edge of the section as for the case in which the device fully cuts the direct beam, but does not give contrast at the edge of the section pattern. This in some cases produces contrast similar to that from a spherical strain centre [102] as shown in the region marked

Figure 6.2

a) $\bar{2}20$ Lang topograph of the CMOS sample.
b) 224 Double crystal topograph (SRS) of the same sample, $\lambda = 1.36$Å

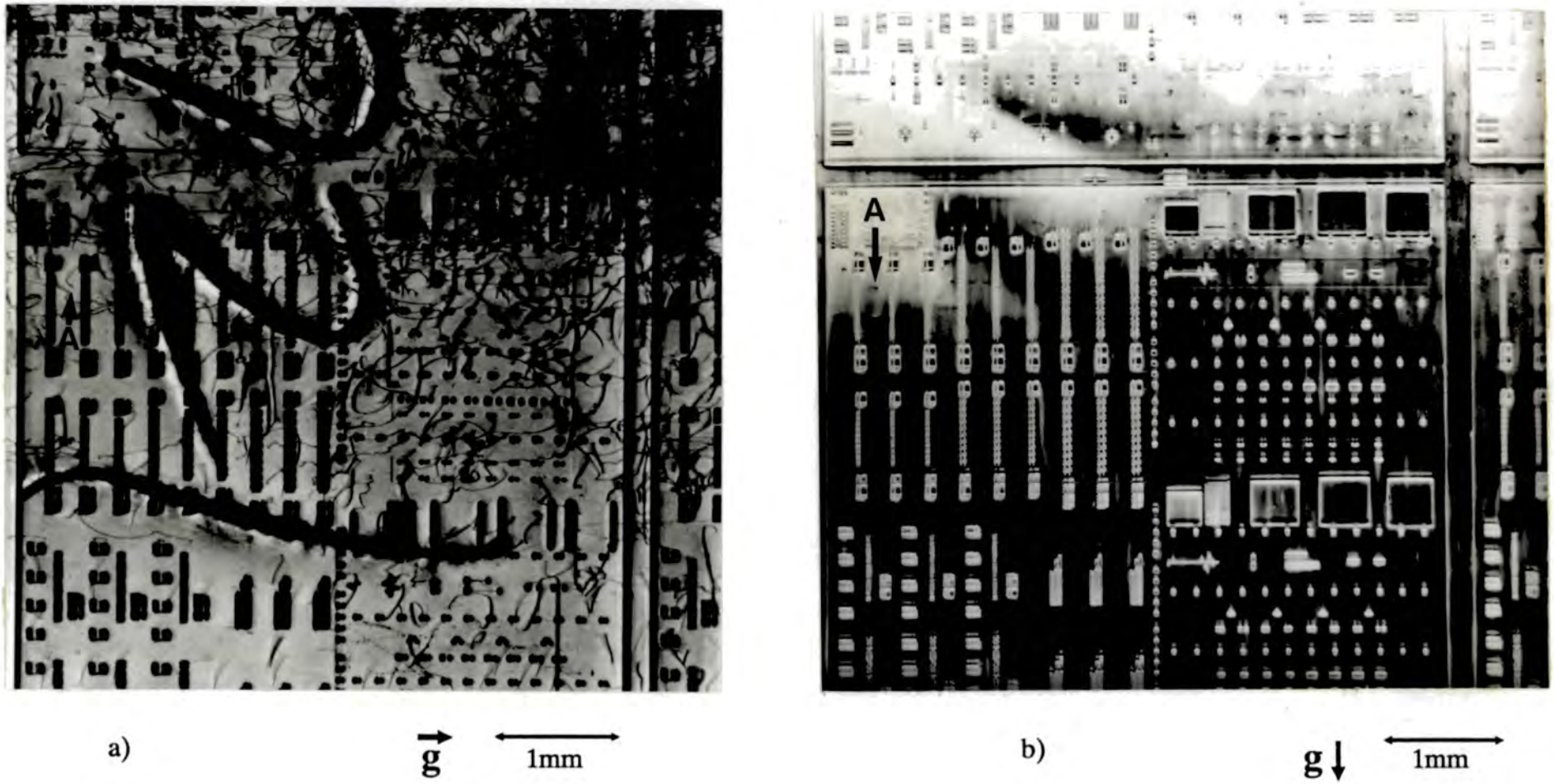

Figure 6.3

Lang and double crystal topographs of the same area of the CMOS sample.

a) $\bar{2}20$ Lang topograph.
b) 224 Double crystal topograph (SRS), $\lambda = 1.36$Å

See text for explanation of symbols

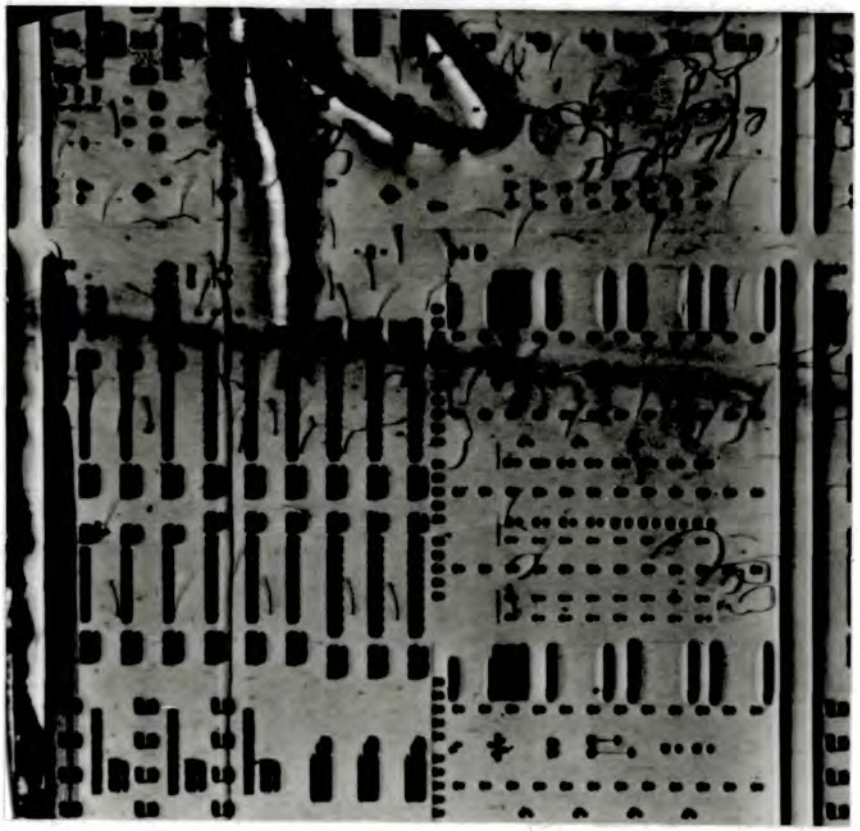

a) $\vec{g}$ 1mm

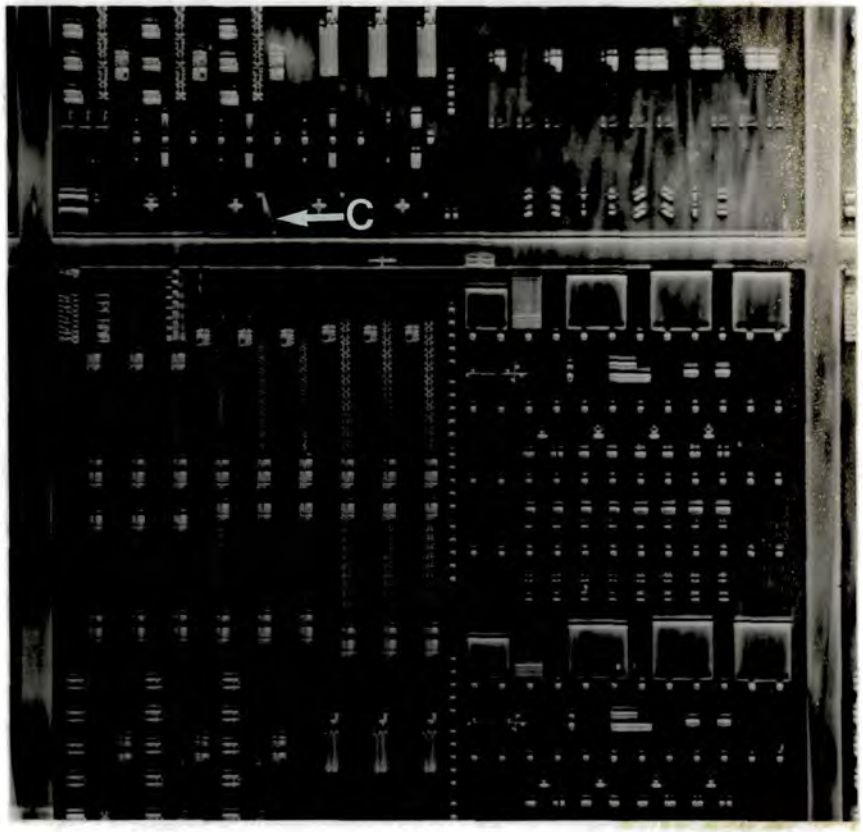

b) g 1mm

Figure 6.4

Lang and double crystal topographs of the same area of the CMOS sample.

a) $\bar{2}20$ Lang topograph.
b) 224 Double crystal topograph (SRS), $\lambda = 1.36$Å

See text for explanation of symbols

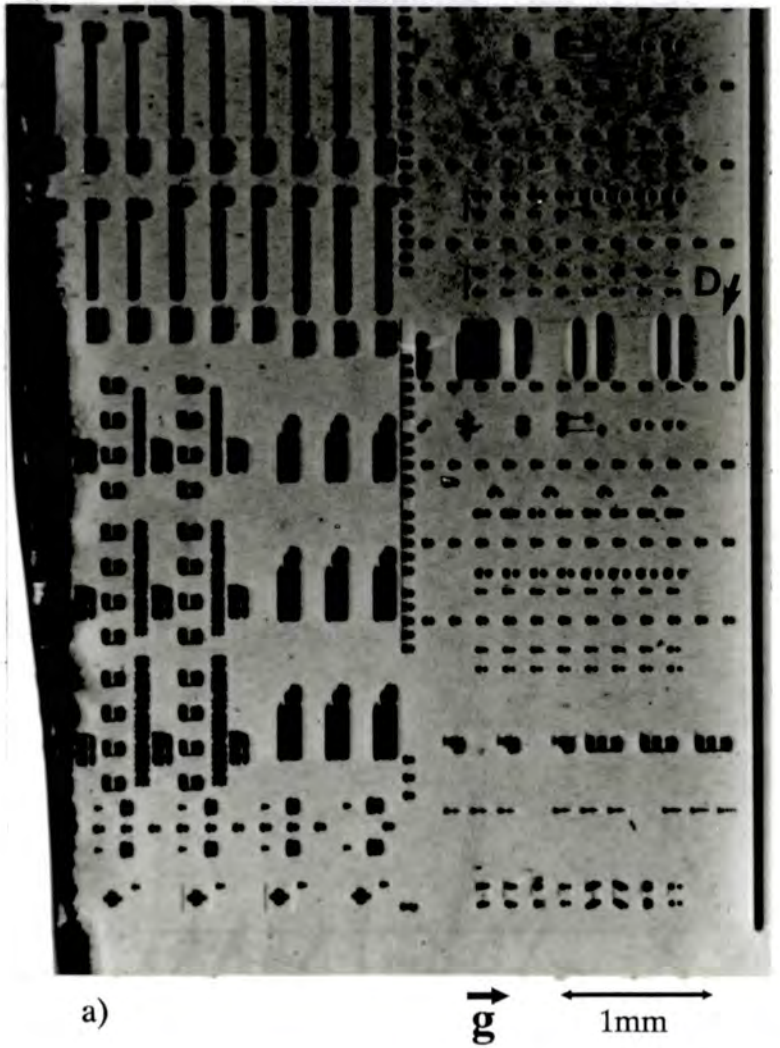

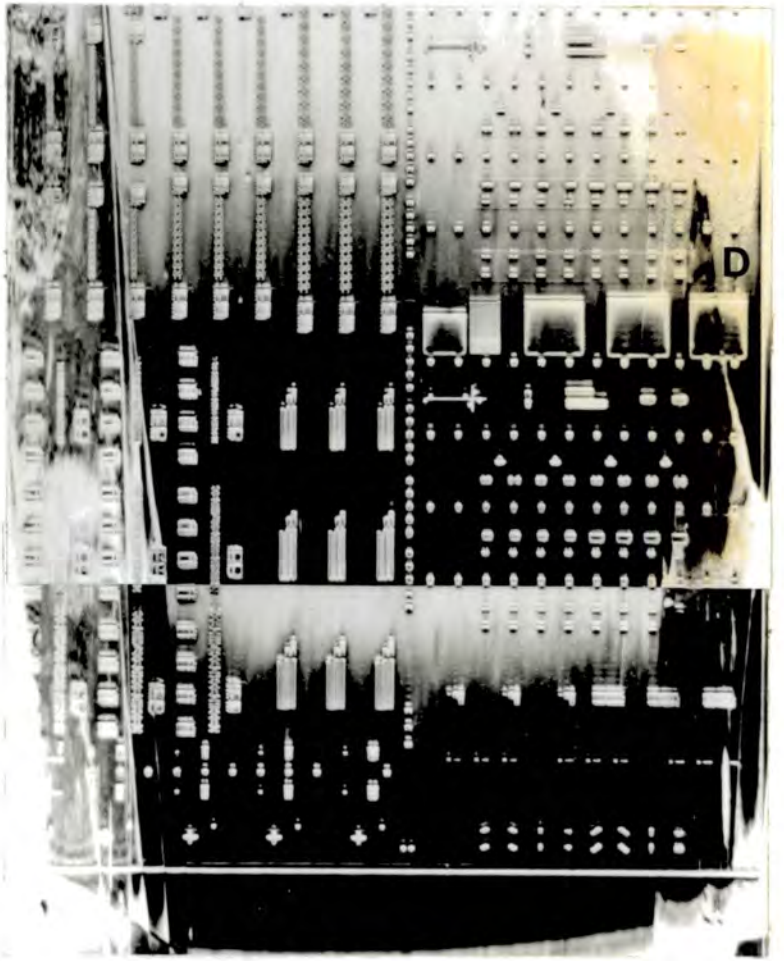

Figure 6.5

Lang and double crystal topographs of the same area of the CMOS sample.

a) $\bar{2}20$ Lang topograph.
b) 224 Double crystal topograph (SRS), $\lambda = 1.36$Å

See text for explanation of symbols

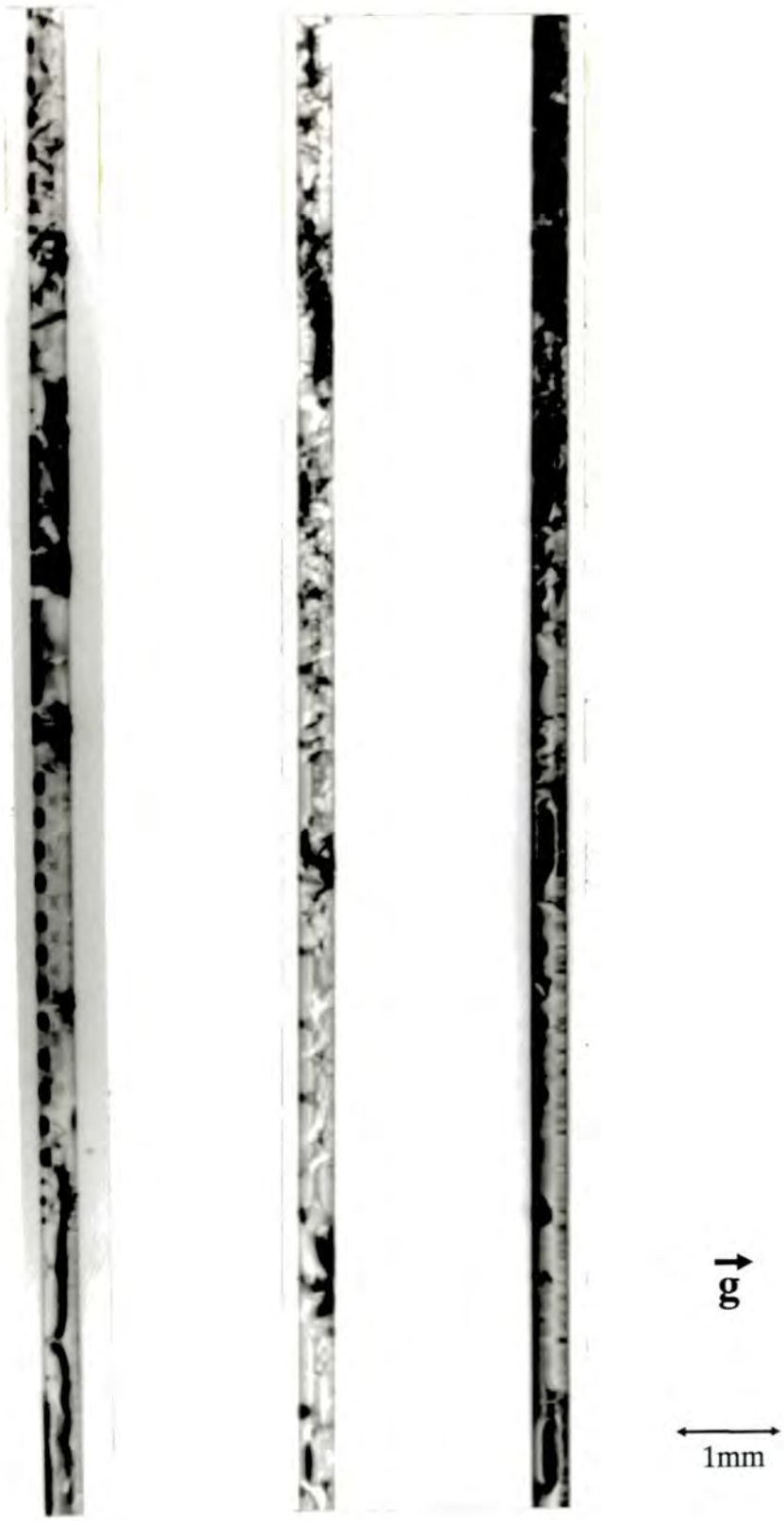

Figure 6.6

Upper portion of the $\bar{4}40$ section topographs of the CMOS sample. The numbers refer to the positions of the sections marked on figure 6.2a.

See text for explanation of symbols

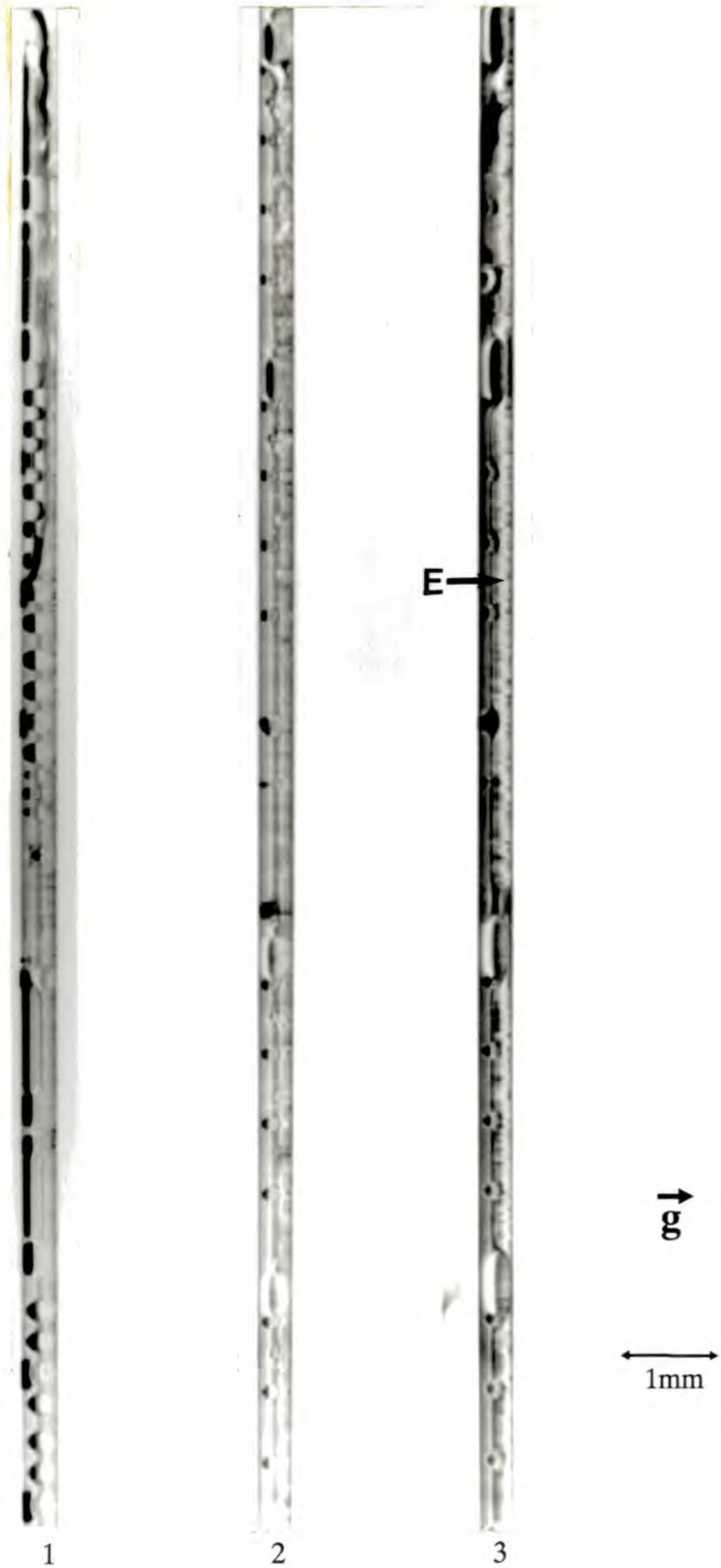

Figure 6.7

Lower portion of the $\bar{4}40$ section topographs of the CMOS sample. The numbers refer to the positions of the sections marked on figure 6.2a.

See text for explanation of symbols

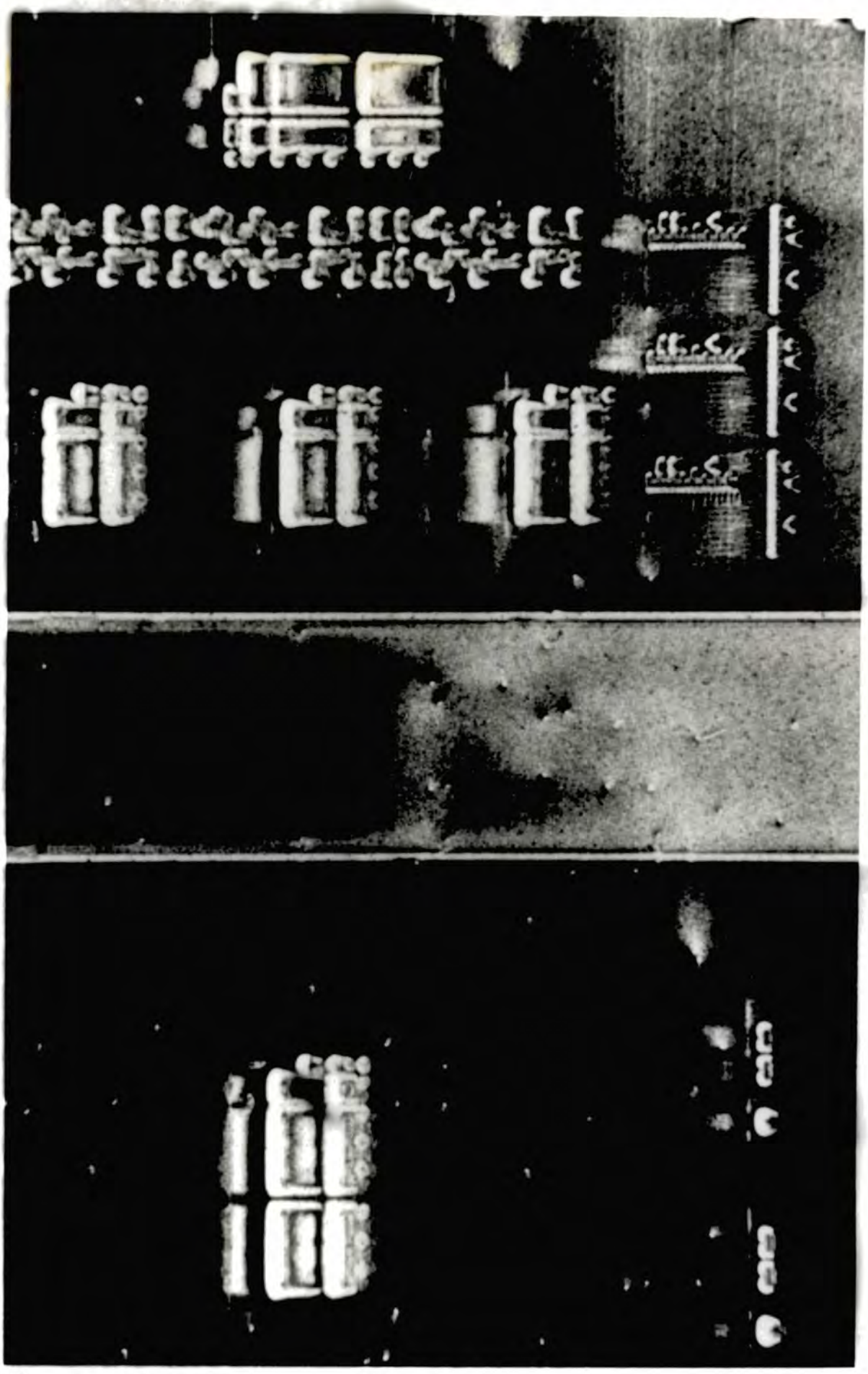

Figure 6.8
Double crystal topograph (SRS)
224 reflection, λ =1.36 Å. See text for details

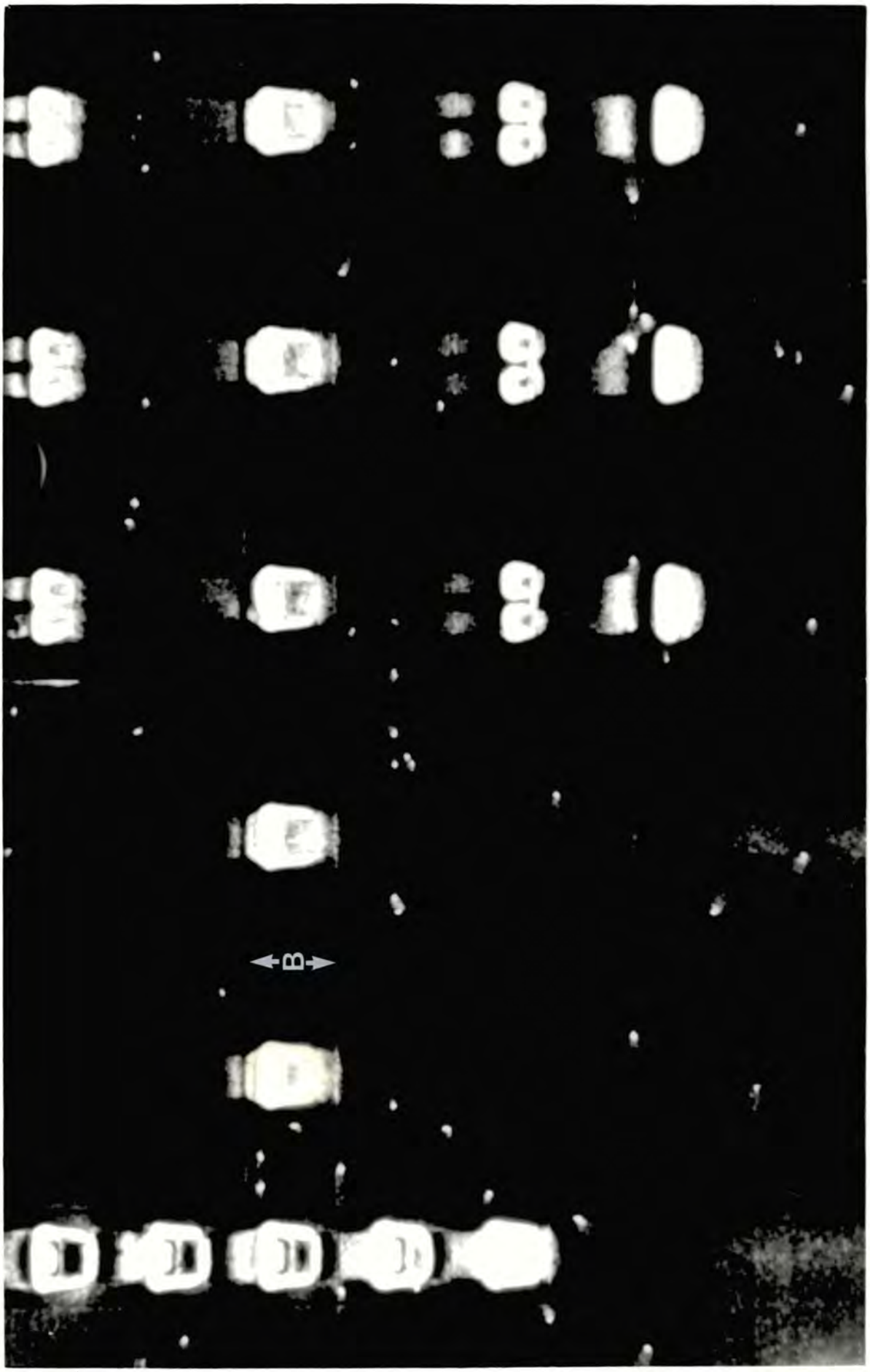

Figure 6.9
Double crystal topograph (SRS) 224 reflection, λ =1.36 Å. See text for details

by A and the two should not be confused. This highlights the need to take section topographs at several positions on the crystal to determine uniquely the cause of the observed contrast. Finally, when the heavily distorted region no longer crosses the direct beam but is very close to it, the device contrast is dominated by weak dynamical images as shown in figure 6.10d.

When the device is covered by the Borrmann fan but no longer cuts the direct beam, the direct image decreases in intensity and finally disappears, the device giving rise solely to dynamical effects in the form of additional fringes, localised to the area of the strain [53]. Whilst these fringes do not give information about the depth profile of the defect, they may be of some use for quality control, since identically manufactured devices will have very similar strain fields and hence give very similar dynamical effects.

Towards the bottom of the sample and evident in the section topograph, are small black dots close to the exit surface, indicated by the marker A in figure 6.12b. Corresponding contrast is not visible in the Lang topograph but can clearly be seen in the surface-sensitive double crystal method. From the double crystal topograph these look at first sight like outcrops of dislocations similar to those seen in the upper region of the sample. However, the section topograph shows the limited depth penetration of the defects and also that they appear as small dark dots with no visible dynamical image, at different depths below the surface.

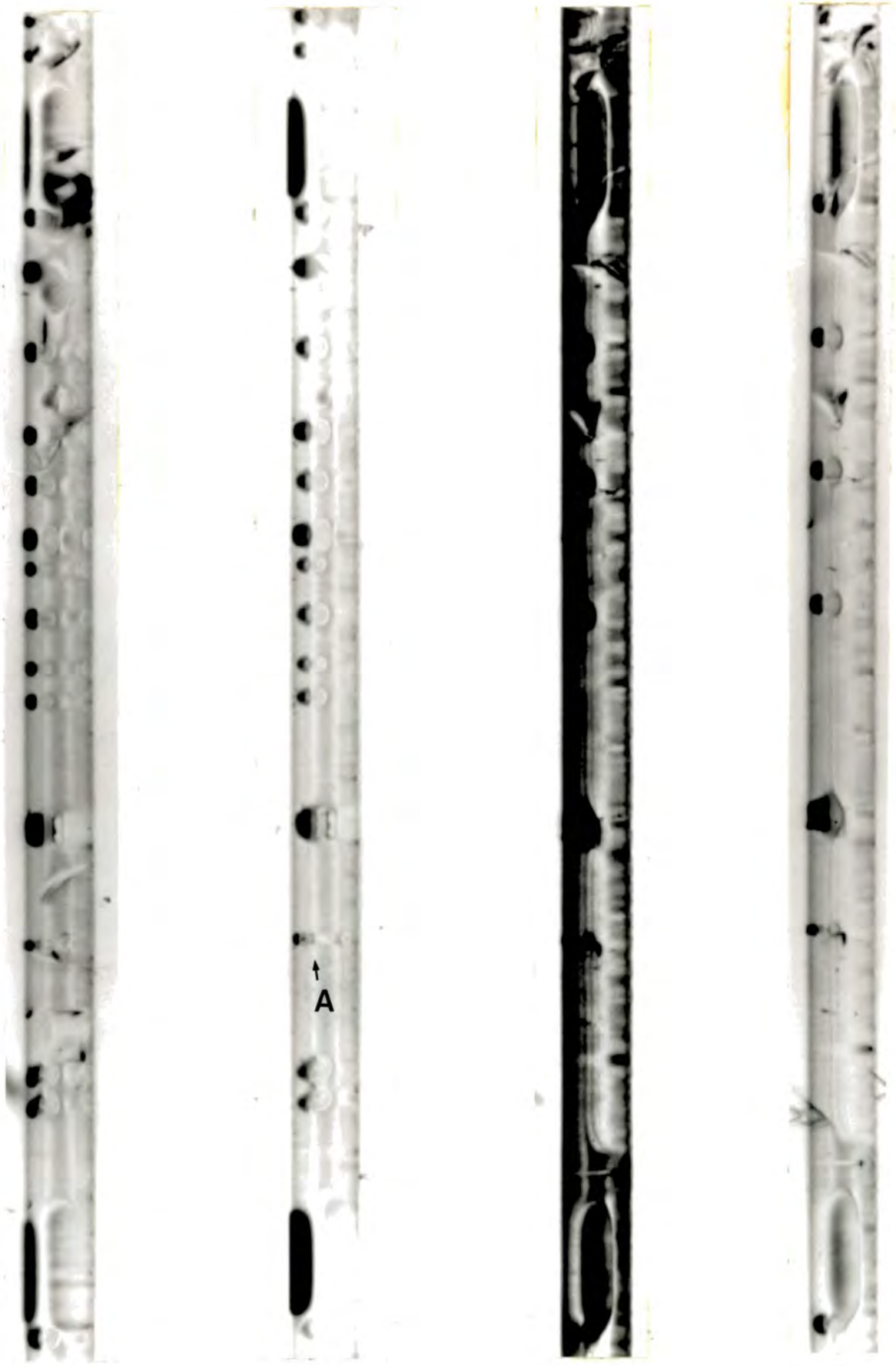

Figure 6.10

$\bar{4}40$ section topographs showing the dependence of contrast upon the position of a device relative to the Borrmann fan.
See overleaf for explanatory sketches and refer to text for details.

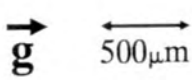

Upon closer examination, figure 6.11, the double crystal topograph reveals that the defects take the form of elongated ovals lying with the long axes parallel to two orthogonal 110 directions. This, together with the evidence from the section topographs that the defects are limited to within a few microns of the surface implies that the defects are stacking faults confined to the epitaxial layer, formed at the interface with the substrate [103,104]. Indeed, etch studies and anomalous transmission topography [105] on a sample from the same batch have confirmed the presence of a high density of stacking faults. They also showed the presence of some partial dislocations although in the studies reported here the defect contrast was always of the same character, showing no evidence of partials. This once again shows the importance of using a variety of techniques to uniquely determine the nature of crystal defects.

Whilst it is only the direct image which can give depth information in section topographs, the dynamical effects are also extremely good indicators of the crystal perfection and should not be ignored. The presence of straight, parallel Pendellosung fringes in section topographs indicates the absence of unimaged microdefects. Note how in region E of figure 6.7 the strain field from back surface damage is sufficient to destroy the fringes close to the exit surface although they are still present towards the centre of the section. This gives a good indication of the degree of strain associated with the back surface.

The exposure time for section topographs of processed wafers should therefore be a compromise between the

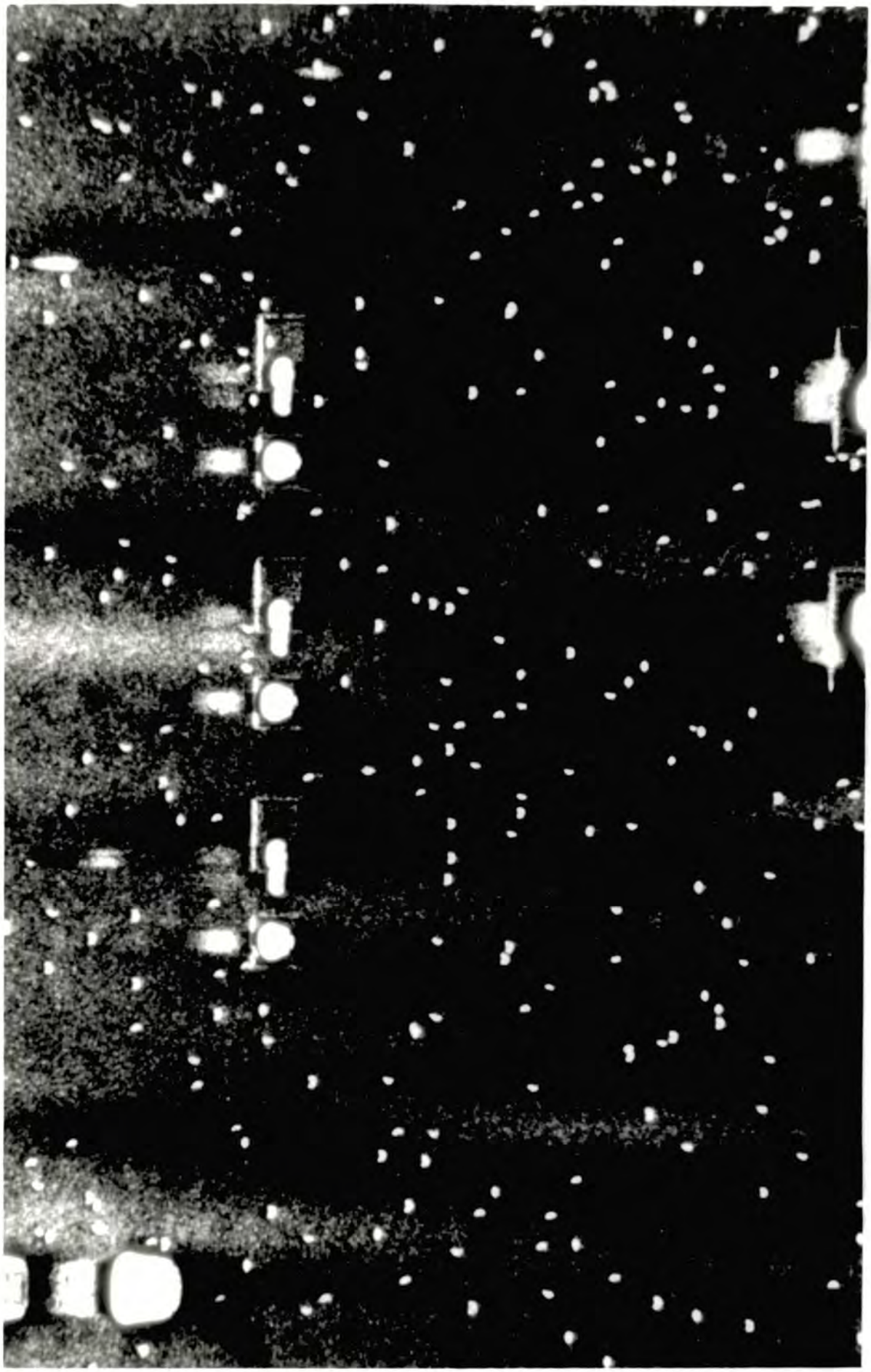

Figure 6.11
Double crystal topograph (SRS)
224 reflection, λ =1.36 Å. See text for details

reasonably short exposures required to expose the direct images, sufficient to show the depth of devices and heavily distorted regions, and the longer exposures neeeded to properly display the dynamical effects. The much greater detail given by a longer exposure is clearly shown in figure 6.12, where figure 6.12a has been exposed for two hours and figure 6.12b for four hours with the same experimental conditions. It is clear that for examining the depth distribution of defects and the gross strain associated with processed areas, the slightly underexposed topograph gives sufficient detail. This has great implications for the routine assessment of device wafers by section topography, where clearly time is of the essence.

6.3. Bragg case interference fringes

6.3.1. Previous work

During the examination of the bipolar wafer described in chapter 5, it was noticed that for angles of incidence below about 5^{o}, fringes could clearly be seen at the edges of many devices. These are shown in figure 6.13, the 115 reflection at $\lambda = 1.35$Å. That fringes are visible at all is surprising, considering that we are dealing with a singly polarised beam with little divergence in the plane of incidence. We would therefore expect plane wave conditions to predominate, leading to the formation of only one beam inside the crystal and no interference effects. Fringes in the Bragg case have been observed for a divergent incident beam [106,107] for undeformed crystals, and remarkably similar fringes to the ones seen here were observed in a

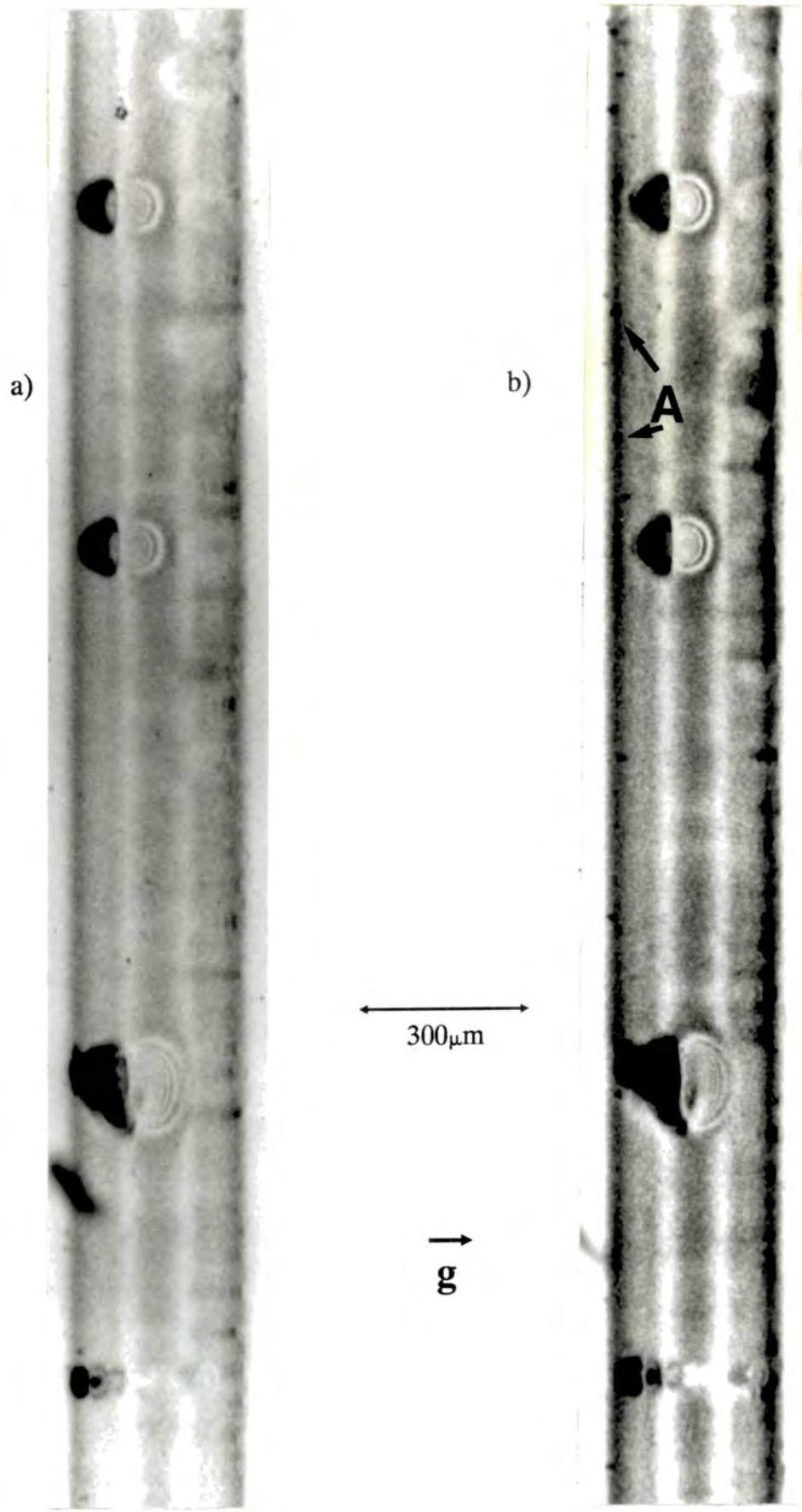

Figure 6.12

$\bar{4}40$ section topographs showing the effect of exposure time upon resolution

a) Two hour exposure
b) Four hour exposure

See text for
explanation of symbols

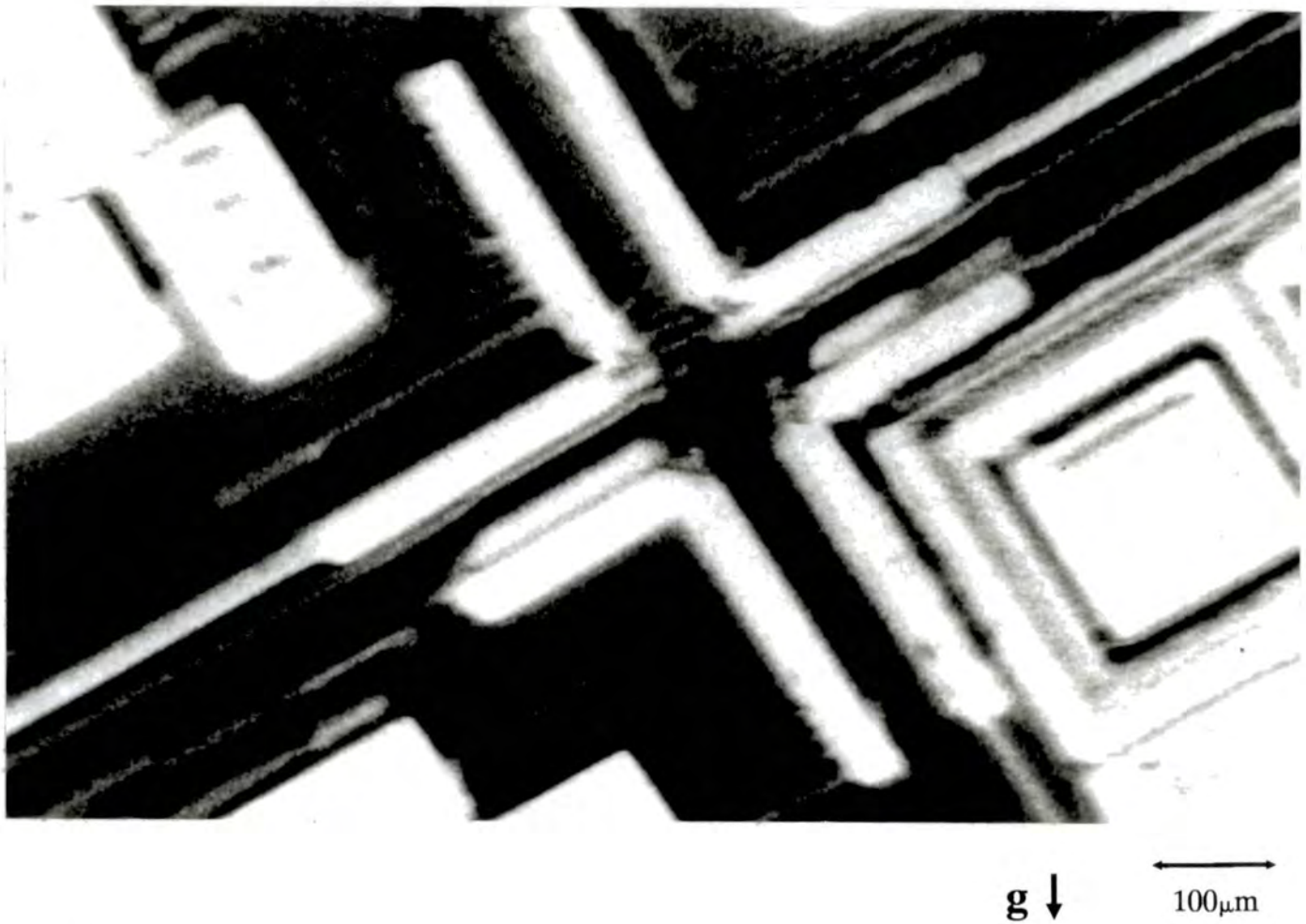

Figure 6.13

115 double crystal topograph, $\lambda = 1.35$Å (SRS), of the bipolar wafer described in chapter 5.

Note the appearance of fringes at the edges of devices.

deformed crystal [108]. In Chen's experiment a section slit was used, leading to a narrow divergent beam, and the sample was cylindrically bent. The period of the fringes varied significantly with increasing curvature and a reasonable match was obtained to Chukhovskii's theory for the propagation of X-rays in a medium with a uniform strain gradient (USG) [79]. Similar fringes have also been observed by Bak-Misuik et al [109], using the same experimental geometry as Chen. In their experiment however, the results are complicated by the fact that the bending moment was applied by growing an oxide layer on one side of the wafer, and the fringes were only observed close to the edges of windows cut in the oxide. Thus , it is not clear whether the fringes arise because of the long range curvature as claimed by Misuik et al, or because of the short range, rapidly varying curvature close to the oxide. Since fringes were only seen at the edges of devices in the double crystal topographs this work has some relevance to the results presented here. More recently, Chukhovskii and Petrashen [80] have observed similar fringes, again using a spherical wavefront and attribute them to the interference of Bloch waves at the surface which have undergone successive internal reflections. This concept of a waveguide leads to enhanced values of ξ_g as reported previously by Chen. A simple parameter for the fringe spacing is given in the paper and the author's results are compared with this theory in section 6.3.3.

6.3.2 Experimental Procedure

Since fringes were only observed at low angles of incidence for the bipolar wafer, the experimental geometry for this work was chosen to give an angle of incidence of approximately 2^{o}. Conveniently, the sample was supplied as a long rectangular strip, which meant that its curvature could be easily changed in the direction parallel to the long edge without imposing a significant curvature in the orthogonal direction. This meant that the dependence of the fringes upon the long range strain could be easily investigated. The as-mounted sample had a significant curvature which was constant over most of its length, as can be seen in fig 6.2b. The curvature in this case is 28m and the entrance surface, which is the device side of the wafer, is convex.

The sample was firmly secured at four points at the lower edge of the sample as shown in figure 6.14a and was bent by placing thin strips of foil under the upper edge, also visible in the same photograph, giving a cantilever type arrangement. The sample was bent twice, leading eventually to the lower part of the sample being bent concavely, the middle being essentially flat and the upper part remaining convex with a curvature of $50m^{-1}$. Topographs were taken at different rotations of the sample to image a large area of the crystal, but on individual plates for each position to avoid the overlapping of successive images. This also allowed the sense of the curvature at any point on the sample to be determined.

The complete experimental set-up is shown in figure 6.14b.

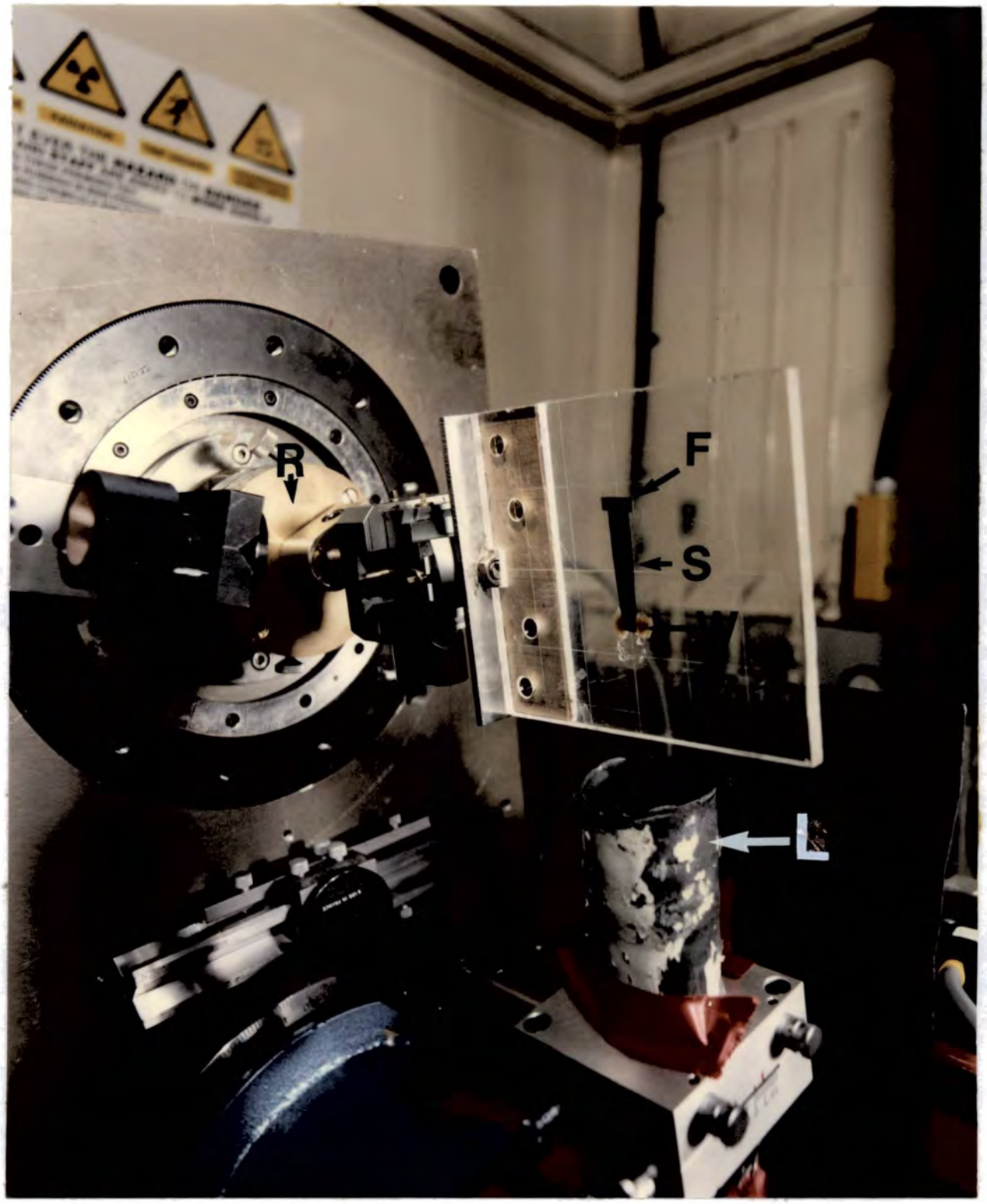

Figure 6.14a)

Close up of the CMOS sample mounted on the double crystal camera in the SRS topography hutch, showing the sample (S), bending foil (F), fixing wax (W), rotation stage (R) and shielding (L).

Figure 6.14b)

Complete experimental set up for glancing angle double crystal topography using the double crystal camera in the SRS topography hutch.
The photograph shows the 2θ arm (G), first axis (1) with beam conditioner (B) in place, second axis (2) with sample holder (H) in place, beam defining slits (S), detector (D), plate holder (P), inter-axis slits (I) and shielding (L).

6.3.3 Results

Fringes were only seen in the bipolar wafer for angles of incidence below 7° and only in the part of the wafer where the crystal close to the surface satisfied the Bragg condition, that is in the band of diffraction marked B in figure 5.5. The latter is not surprising since we would expect there to be dynamical effects only where the wavefields can propagate in perfect crystal close to the exact Bragg condition. The former is probably because of the geometrical problem of resolving the fringes, since even though interference between wavefields may be occurring in the crystal for angles of incidence greater than 7°, the diffracted and direct beam directions $\mathbf{s}_g$ and $\mathbf{s}_o$ are such that the beams emerging from the exit surface are bunched much closer together making it impossible to resolve individual fringes.

That the fringes were only observed at device edges implies that either the boundary is acting as a slit and hence a source of spherical wavefronts similar to the section slit used in previous experiments, or that the shorter range strain field close to the interface is significant to the formation of the fringes. This question is considered later on.

In the CMOS wafer, fringes were also seen in many places, but again only associated with device edges. Interestingly, fringes that were observed in the bent crystal disappeared in the region that became essentially flat, suggesting that the phenomenon is indeed related to the long range strain field. A simple calculation using

equation 5.6 and the divergence of the incident beam shows that the radius of curvature of this region is of the order of 3000m. This effect is shown in figure 6.15. The character of the fringes is insensitive to the sense of the deformation, showing the same general nature whether the entrance surface is concave or convex. That is, the first maximum is always separated from the device by a broad minimum, with the fringes showing roughly the same periodicity and decrease in visibility with increasing order.

One area of the crystal was chosen for closer examination, close to the channel between individual chips, where there is a silicon oxide interface. This was in the upper part of the crystal which remained convex for each degree of applied bending. The curvature did however change significantly. Figures 6.16a to 6.16c show enlargements of this area at radii of curvature of 28m, 38m and 47m respectively. Note that this is the overall curvature, measured over several millimetres and that the curvature closer to the interface will be slightly different because of the strain field associated with it [109]. As can be seen, the fringes are very similar for each value of bending but show a significant variation in the periodicity of the fringes. As the curvature increases, the fringe spacings decrease and the visibility of the higher order fringes improves. This finding is similar to that previously reported [80,108] and can be explained by using Chukhovskii's USG theory.

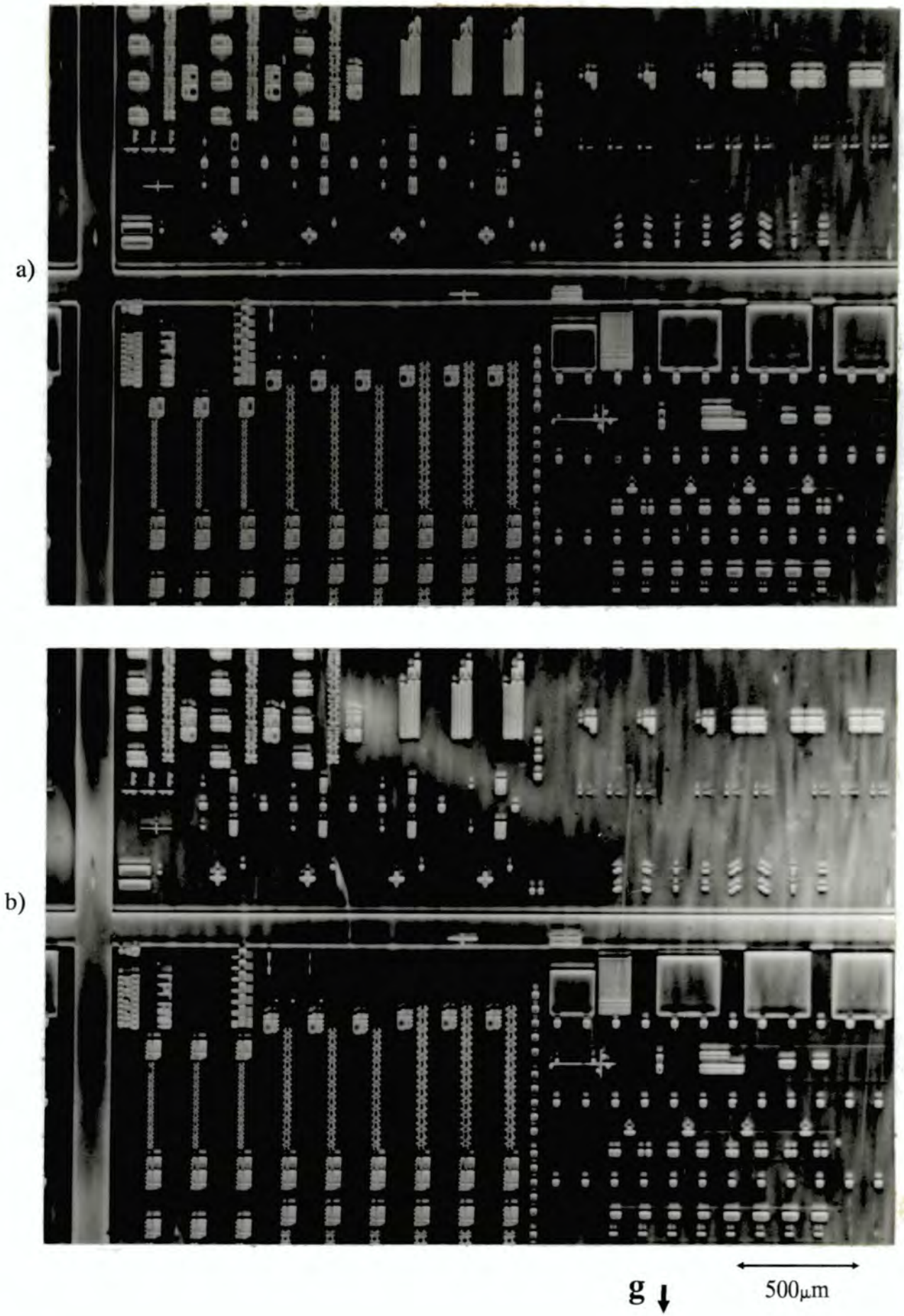

Figure 6.15

224 double crystal topographs, $\lambda = 1.36$Å (SRS), of the same area of the CMOS sample.
a) Sample is bent to R≈50m in this area.
b) Sample is essentially flat; note the disappearance of fringes for this condition

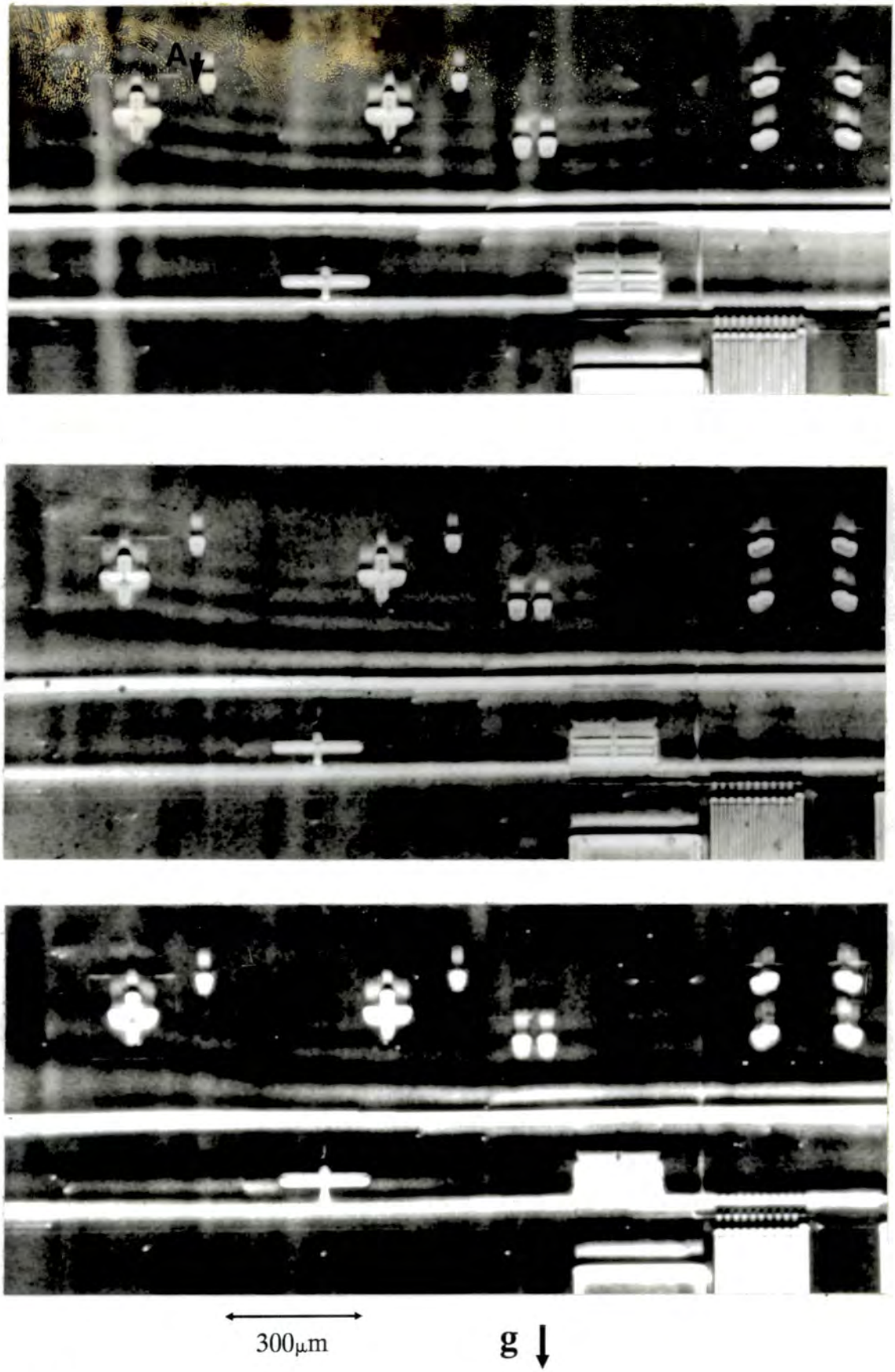

Figure 6.16

224 double crystal topographs, $\lambda = 1.36$Å (SRS), of the same area of the CMOS sample for different overall curvatures, R.

a) R = 28m
b) R = 38m
c) R = 47m

Chukhovskii predicts the relationship for the position of the first fringe maximum, x in relation to the slit of:

$$x^3 \propto 1/B^2 \qquad (6.1)$$

where B is the USG parameter defined in equation 4.2. Figure 6.17 shows a plot of the present results and as can be seen they do show the same trend, although there are too few data points to give a definitive comparison between theory and experiment.

When the result from the bipolar wafer is plotted on the same graph however, it does not provide a good fit with the other data points. This is due to the curvature close to the devices which cannot be accurately determined. The short range curvature will be essentially the same for the three CMOS data sets but will be significantly different for the bipolar wafer because of the different fabrication processes used in the two types of device. The influence of an additional strain field on the fringes is clearly shown in the region marked A on figure 6.16. Here, the additional curvature from the scribed identification number on the back surface causes a considerable distortion of the fringes. This not only shows the extent of the strain field induced by the numbers but also the sensitivity of the fringes to impressed curvature.

Another relationship predicted by Chukhovskii is that the position of the fringes x_n go as:

$$x_n = [16\pi(2n-1)/(5B^2)]^{1/3} \qquad (6.2)$$

where n is the order of the fringe maximum.

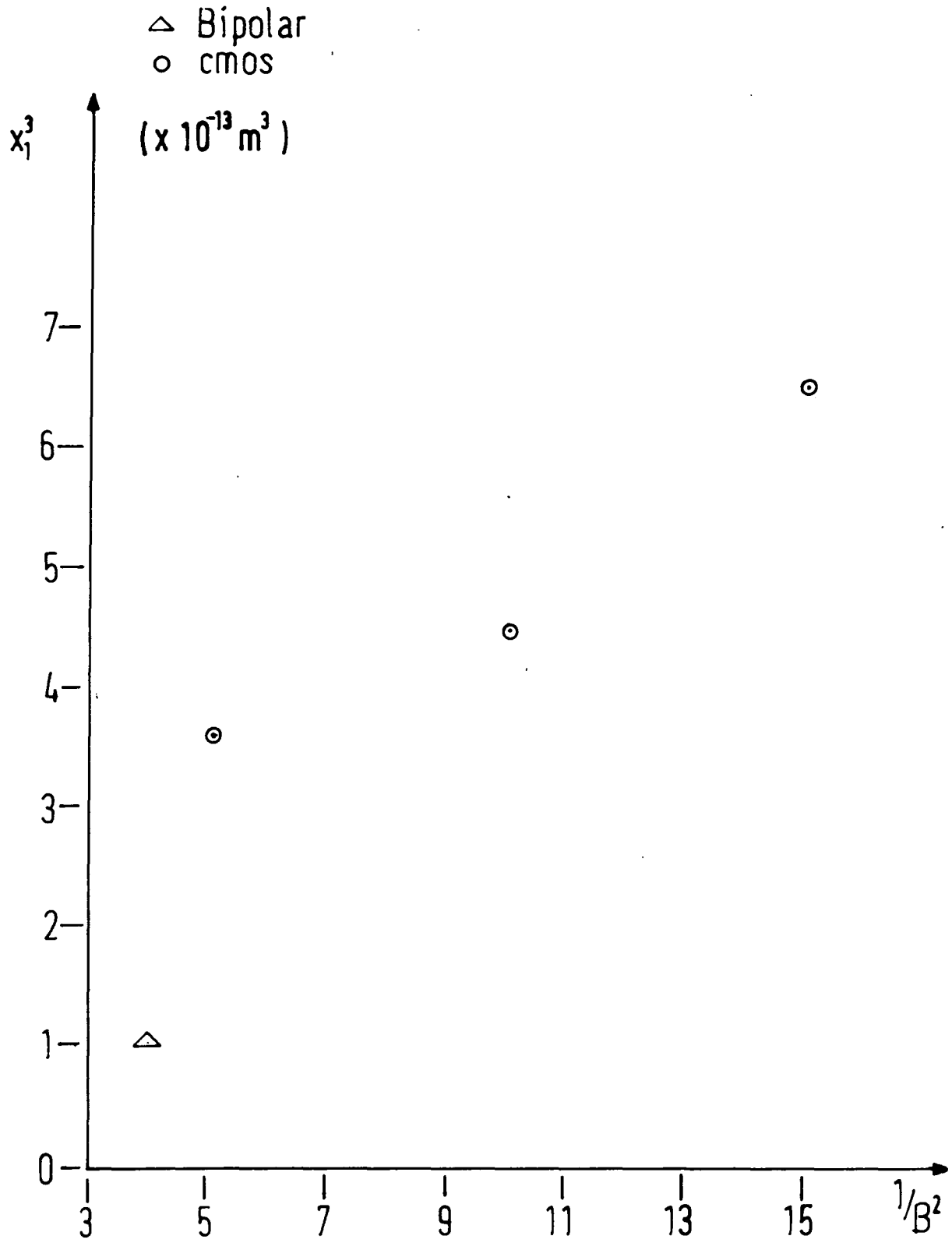

Figure 6.17
Position of 1st fringe maximum against $1/B^2$

Figure 6.18 shows a plot of x_n^3 against n for the three curvatures studied. As can be seen this does not give a good straight line as predicted by the theory although an increased curvature does lead to a smaller gradient consistent with the $B^{-2/3}$ relationship. A possible reason why the experimental results do not match the theory is again because of the short range strain field. This leads to a higher curvature close to the device which rapidly decreases to the long range curvature as we move away from the interface. This gives a larger value of B close to the device and hence a smaller gradient associated with the first one or two fringes, consistent with the results plotted in figure 6.18. These results throw doubt upon the validity of Bak Misuiks technique of measuring fringe spacings close to an oxide edge, since even though a rough estimate of the additional curvature is used, no account is taken of its variation with distance from the interface.

The above results are consistent with Chukhovskii's theory of X-ray propagation in crystals with an USG and therefore suggest that the fringes are being caused by the enhanced extinction distance in bent crystals. The problem still remains however, of why an experiment using an essentially plane polarised beam of X-rays gives similar results to those obtained using unpolarised radiation with a spherical wavefront. In particular, one does not expect interference effects when wavefields from only one branch of the dispersion surface are excited. The mechanism which links the two situations is the short range, rapidly varying strain field associated with the device-substrate interface,

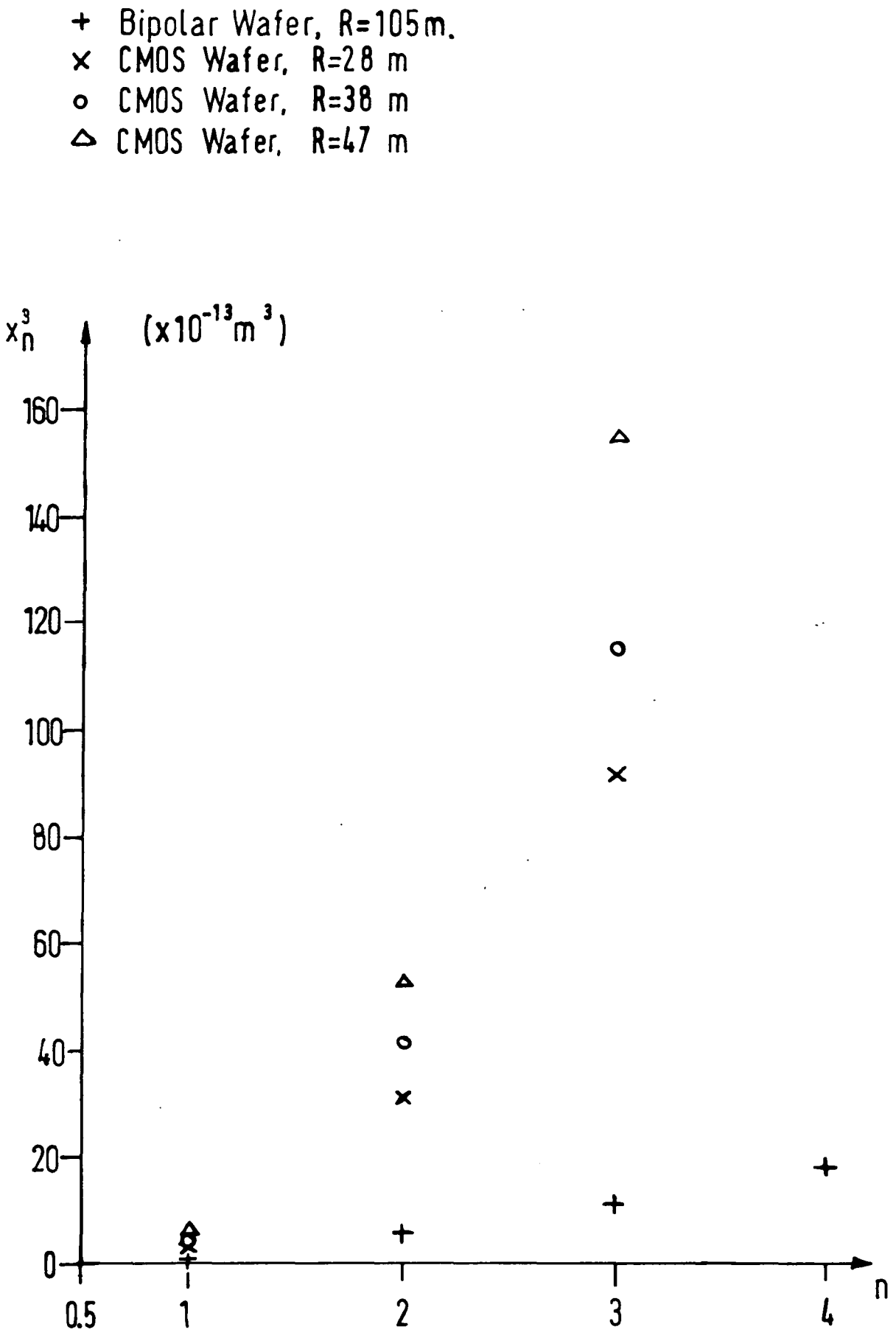

Figure 6.18

Position of fringe maximum against fringe order for the curvatures studied

since fringes are not seen isolated in perfect crystal and disappear when the sample is flat. It is likely that this area enables both branches of the dispersion surface to be excited since the orientation of the dispersion surface with respect to the incident beam changes very rapidly over a short distance, leading to the effect of a spherical wavefront. The edge of the device could possibly be acting as a slit, which then acts as a source of divergent wavefields but this is unlikely since fringes would then be seen associated with many more shallow devices rather than just those with a large strain gradient as is observed in the experiments.

What is needed now is a simulation of these results to see whether the short range strain field has a significant effect on the fringes. Also a more complete data set is required, using a sample with carefully controlled interfaces instead of the unpredictable ones caused by the necessary superposition of oxide, diffusion and metallisation effects in the integrated circuits studied here.

Chapter Seven

Summary

This thesis has shown the suitability of X-ray topography for the non-destructive examination of processed silicon wafers at all stages in the processing schedule.

Contrast differences between the Hirst and Lang topography techniques have been shown to be due to inhomogeneous bending which imposes a curvature upon the diffracting planes. A curvature of as little as 100m is sufficient to produce the enhanced dynamical images in the Lang technique that are seen in the Hirst technique. Inhomogeneous bending also decreases the visibility of the direct images, implying that for maximum defect visibility the bending should be adjusted to be as homogeneous as possible. Since inhomogeneous bending is always accompanied by a significant increase in diffracted intensity from the perfect crystal, it is suggested that this be used as a test of the bending conditions in the Hirst technique.

In asymmetric reflections, there is a sharp rise in diffracted intensity upon homogeneous cylindrical bending. For large curvatures (R=20m), the images of dislocations change contrast from black on grey to white on grey. This is not due however to the direct image changing contrast but to a combination of two effects. The rise in diffracted intensity from the perfect crystal tends to swamp the direct images, causing them to disappear and at the same time the spatial extent of the dynamical images decrease and become localised around the dislocation core.

The contrast effects seen in the Lang topographs are seen more clearly in the section topographs taken under the same bending conditions. In the symmetric geometry with homogeneous bending, a phase change is seen in the Pendellosung fringes and some differences can be seen in the fine structure of dislocation images. These are unexpected, since the diffracting planes should remain flat in this geometry, but are probably explained by the high strain sensitivity of both the fringes and the intermediary images which means that they are affected by an otherwise undetectable inhomogeneity.

In the asymmetric geometry, bending reduces the visibility of the fringes, and care should therefore be taken in interpreting the absence of fringes in curved crystals since there will be some ambiguity as to whether it is due to curvature or unimaged microdefects.

The long range strain has been used with the aid of simulations based on the Takagi-Taupin equations to identify the Burgers vector of an individual dislocation. In the unbent crystal several Burgers vectors give similar contrast, but the addition of the long range strain gives a unique contrast for each Burgers vector. This is obviously a powerful technique and more work needs to be done with different experimental geometries and defect types to test its range of validity.

Examination of a processed bipolar device wafer using glancing angle double crystal topography with synchrotron radiation and a variety of reflections and wavelengths has determined the best conditions for the examination of

processed wafers. The wavelength tuneability of the SRS allows the depth penetration of the X-rays to be continuously varied. This surface sensitivity enables both devices and process related defects to be imaged over a large area to a high resolution and contrast, allowing a range of defects to be identified. The best experimental geometries have been determined, including the choice of a first reflection.

Processed wafers normally have a significant curvature and this limits the area that can be imaged on one plate. By rotating the sample by a few seconds of arc and taking an exposure on the same plate for each position a large area of the wafer can be imaged. In general this multiple exposure technique is the most convenient when looking for defects since a large area of crystal is imaged on one plate in a relatively short time. Furthermore it has been shown that the defects are equally visible when using either a multiple or a single exposure technique. When combined with two single exposures the multiple exposure method also allows the sense and magnitude of the wafer curvature to be determined as well as its uniformity over the sample.

The single exposure gives a visual sense of lattice mismatch and if the overall curvature of the sample is found using the multiple exposure method, it is possible to determine the effective mismatch between individual devices and the substrate by the spatial separation of their diffraction maxima.

Asymmetric reflections are essential to give a low depth penetration of the X-rays and a good aspect ratio on

the plate. Two parameters are important when considering the depth of crystal which will be imaged, the penetration depth P_2 and the extinction distance ξ_g. Of these the most useful is usually P_2 (based on photoelectric absorption), since the wafer curvature means that only a narrow strip of material satisfies the exact Bragg condition for a particular angular setting and the depth penetration is only dependent upon extinction within this limited range.

Although low angles of incidence give low penetration depths, they should be avoided when looking for defects since they give rise to large areas of depleted intensity which obscure details of devices and defects. Generally therefore, the experimental geometry should be chosen to give a low depth penetration for angles of incidence greater than about 5°.

It would be useful now to see if these general conclusions can be extended to a wider range of process types, wafer orientations and substrate materials than the limited range studied in this thesis.

Lang, section and double crystal topography have been compared for the examination of a CMOS device wafer. It has been shown how the use of three such complementary techniques can characterise most of the defects within the sample. Contrast can generally be easily correlated between the techniques, allowing the spatial and depth distribution of the defects to be non-destructively determined.

Double crystal topographs indicate that the practice of scratching identification numbers on the back surface of wafers before processing, already known to be a source of

dislocations, also produces a significant localised strain on the device side of the wafer, which may adversely affect the electrical performance of the chip.

The contrast of devices in section topography has also been studied and it has been shown that the apparent depth of the device varies depending on its position relative to the Borrmann fan. This shows the need to take section topographs at several positions to uniquely determine the depth profile of processed areas. Underexposed section topographs give sufficient information to determine the depth of defects and diffused areas, although information on dynamical effects and small distortions is lost. This makes the section topography technique more attractive for the routine assessment of processed wafers.

Fringes have been observed in double crystal topographs obtained at the SRS for angles of incidence below about 5°. These were shown to be dependent on the overall curvature of the sample, but only appeared at the edges of devices. The behaviour of the fringes agreed with the theory of Chukhovskii and Petrashen [80], although the experiment was complicated by the presence of the short range rapidly varying strain field close to the edge of the device. It is postulated however that it is this short range strain field which gives rise to the fringes, allowing both wavefields in the crystal to be excited, even though the incident beam is essentially a linearly polarised plane wave.

A more complete data set is now required to test this theory, using a more predictable short range strain field, such as that close to an oxide edge, than that given by the

combination of oxide, diffusion and metallisation in the wafers studied here. Simulations using the superposition of the short range and long range strain fields would help to clarify the role of the short range strain in the formation of the fringes.

References

1 International tables for X-ray Crystallography, Volume III, (D.Reidel, Dordecht), 1983

2 L.V. Azaroff et al, **X-ray Diffraction**, (McGraw-Hill, London (1974)

3 R.W. James, **The Optical Principles of the Diffraction of X-rays** (G. Bell and Sons, London, 1948)

4 W.H. Zachariasen, **Theory of X-ray Diffraction in Crystals**, (Dover Publications, New York 1967)

5 M.M. Woolfson, **An Introduction to X-Ray Crystallography**, (Cambridge University Press, 1970)

6 B.H. Batterman and H. Cole, Rev. Mod. Phys. 36, 681 (1964)

7 A. Authier, in **Advances in Structure Research by Diffraction Methods**, (edited by Brill and Mason), 3, 1 (1970)

8 Z.G. Pinsker, **Dynamical Scattering of X-rays in Crystals**, (Springer-Verlag, Berlin, Heidelberg, New York, 1978)

9 M. Hart, Rep. Prog. Phys. 34, 435 (1971)

10 P. Penning, PhD Thesis, published in **Philips Res. Rept. Supplements number 5**, 1 (1966)

11 M. Kohler, Ann. Phys. **18**, 265 (1933)

12 U. Bonse, Z. Phys. **177**, 385 (1964)

13 P. Penning and D. Polder, Philips Res. Rept. **16**, 419 (1961)

14 N. Kato, J. Phys. Soc. Japan **18**, 1785 (1963)

15 N. Kato, J. Phys. Soc. Japan **19**, 67 (1964)

16 N. Kato, ibid., 971 (1964)

17 S. Takagi, Acta Cryst. **15**, 1311 (1962)

18 S. Takagi, J. Phys. Soc. Japan **26**, 1239 (1969)

19 D.Taupin, Bull. Soc. Fr. Mineral. Cristallogr. **87**, 469 (1964)

20 A. Authier, C. Malgrange and M.Tournarie, Acta Cryst. **A24**, 126 (1968)

21 Y. Epelboin, Materials Science and Engineering, **73**, 1 (1985)

22 L.G. Schulz, J. Metals 6, 1082 (1954)

23 A. Guinier and J. Tennevin, Acta Cryst. 2, 133 (1949)

24 B.K. Tanner, **X-Ray Diffraction Topography**, (Pergamon Press, Oxford, 1976)

25 A.R. Lang, in **Diffraction and Imaging Techniques in Material Science, Volume II, 2nd edition**, (edited by Amelinckx et al), 623 (North Holland, 1978)

26 U.K. Bonse, M. Hart and J.B. Newkirk, Adv. X-ray Analysis **10**, 1 (1967)

27 G. Hildebrandt, J. Phys. E: Sci. Instrum. **15**, 1140 (1982)

28 G. Dionne, J. Appl. Phys. **38**, 4094 (1967)

29 B.K. Tanner and C.J. Humphreys, J. Appl. Phys. D: Appl. Phys. **3**, 1144 (1970)

30 W.F. Berg, Naturwissenschaften **19**, 391 (1931)

31 C.S. Barrett, Trans. AIME **161**, 15 (1945)

32 J.B. Newkirk, Trans. AIME **110**, 1465 (1958)

33 J.B. Newkirk, Trans. AIME **215**, 483 (1959)

34 E.M. Juleff and R.G. Wolfson, J. Appl. Phys. **37**, 2178 (1966)

35 E.M. Juleff, A.G. Lapierre III and R.G. Wolfson, Adv. X-Ray Analysis **10**, 173 (1967)

36 A.R. Lang, Acta Met. **5**, 358 (1957)

37 A.L. Andersen and L. Gerward, Phys. Stat. Sol. **A23**, 537 (1974)

38 S. Kawado and J. Aoyama, Appl. Phys. Lett. **34**, 428 (1979)

39 A.R. Lang, Acta Cryst. **12**, 249 (1959)

40 W.L. Bond and J. Andrus, Am. Mineralogist 37, 622 (1952)

41 U. Bonse and E. Kappler, Z. Naturforschung 13a, 348 (1958)

42 M. Hart, Science Progress (Oxford) 56, 429 (1968)

43 M. Renninger, Adv. X-ray Analysis 10, 32 (1967)

44 C.A. Wallace and R.C.C. Ward, J. Appl. Cryst. 8, 281 (1975)

45 N. Kato and A.R. Lang, Acta Cryst. 12, 787 (1959)

46 N. Kato, Acta Cryst. 14, 526, 627, (1961)

47 A.R. Lang, Z. Naturforschung 20a, 636 (1965)

48 E.S. Meieran and I.A. Blech, J. Appl. Phys. 36, 3162 (1965)

49 I.A. Blech and E.S. Meieran, J. Appl. Phys. 38, 2913 (1967)

50 G.H. Scwuttke and J.K. Howard, J. Appl. Phys. 39, 1581 (1968)

51 E.S. Meieran and I.A. Blech, Phys. Stat. Sol. 29, 653 (1968)

52 N. Kato and J.R. Patel, J. Appl. Phys. 44, 965 (1973)

53 J.R. Patel and N. Kato, ibid., 971 (1973)

54 Y. Ando, J.R. Patel and N. Kato, ibid., 4405 (1973)

70 E.S. Meieran and I.A. Blech, J. Appl. Phys. 43, 265 (1972)

71 F.N. Chukhovskii and P.V. Petrashen, Acta Cryst. A33, 311 (1977)

72 J.P. Hirthe and J. Lothe **Theory of Dislocations** (McGraw Hill, 1968)

73 Z.H. Kalman and S. Weissman, J. Appl. Cryst. 12, 209 (1979)

74 Z.H. Kalman and S. Weissman, J. Appl. Phys. 43, 265 (1972)

75 L. Zsoldos, Presented at the I.U.C. 13th International Congress, Hamburg, 1984. Acta Cryst. A40 Supplement (1984)

76 B.R. Lawn, Adv. X-ray Analysis 11, 385 (1968)

77 G.E. White and H. Chen, Materials Letts. 2, 347 (1984)

78 G.S. Green and B.K. Tanner, Inst. Phys. Conf. Ser. No. 87: Section 9, 627, (1987)

79 F.N. Chukhovskii, K.T. Gabrielyan and P.V. Petrashen, Acta Cryst. A34, 610 (1978)

80 F.N. Chukhovskii and P.V. Petrashen, Acta Cryst. A44, 8, (1988)

81 J.R. Patel and A. Authier, J. Appl. Phys. 46, 118 (1975)

82 K. Furusho, Jap. J. Appl. Phys. **46**, 118 (1975)

83 K.V. Ravi, **Imperfections and Impurities in Semiconductor Silicon**, (Wiley and Sons, New York, 1981)

84 H.J. Queisser, J. Appl. Phys. **32**, 1776 (1961)

85 G.H. Schwuttke and H.J. Queisser, J. Appl. Phys. **33**, 1540 (1962)

86 J.E. Lawrence, J. Electrochem. Soc. **113**, 819 (1966)

87 W. Wierzchowski, Phys. Stat. Sol. (a) **88**, 77 (1985)

88 Reference [8], page 279

89 R.W. Armstrong, in **Characterisation of Crystal Growth Defects by X-ray Methods** ed. B.K. Tanner and D.K. Bowen, 353 (Plenum Press, New York, 1980)

90 ibid., 518

91 A. Fukuhara and Y. Takano, Acta Cryst. **A33**, 137 (1977)

92 A. Fukuhara and Y. Takano, J. Appl. Cryst. **10**, 287 (1977)

93 Pearson and Bardeen, Phys. Rev. **75**, 865 (1949)

94 Y. Sato and H. Arata, Jap. J. Appl. Phys. **3**, 511 (1964)

95 I.A. Blech, E.S. Meieran and H. Sello, Appl. Phys. Lett. **7**, 176 (1965)

96 G.H. Schwuttke and J.M. Fairfield, J. Appl. Phys. **37**, 4394, (1966)

97 J.M. Fairfield and G.H. Schwuttke, J. Electrochem. Soc. **115**, 415 (1968)

98 Reference [83], page 262

99 G.H. Schwuttke, IBM Scientific Report AFCRL-70-0110 (1970)

100 P.J. Halfpenny, (GEC Hirst Research Laboratories), Private Communication

101 M.J. Hill, IEEE Transactions on Electron Devices, **ED-23**, 839 (1976)

102 S. Cui, G.S. Green and B.K. Tanner, Symposium Q, MRS Fall Meeting, Boston (1988) submitted

103 Reference [83], page 165

104 G.H. Schwuttke, J.Appl. Phys. 34, 3127 (1963)

105 P.J. Halfpenny and C. Dineen, Private Communication

106 A.R. Lang and Z.H. Mai, Proc. R. Soc. Lond. **A368**, 313 (1979)

107 T. Uragami, J. Phys. Soc. Japan 27, 147 (1969)

108 H. Chen, Materials Letters 4, 65 (1986)

109 J. Bak-Misiuk, J. Gronkowski, J. Hartwig and W. Wierzchowski, Phys. Stat. Sol. (a) 99, 345 (1987)

Appendix A

Listing of the ABAC control program

A.1 Introduction

This appendix gives an annotated listing of the automated bragg angle controller (ABAC) software described in chapter three. The reader is referred to that chapter for a functional description of the program. Annotations are given to the right of each column, these are not REM statements and as such are not present in the executable version of the software.

```
 10 MODE7
 20 *FX21,0
 30 *KEY 10 "OLD |M RUN |M"
 40 PSN%=A%:DTHETA%=C%:MIN%=D%
 50 FLAG%=0
 60 inttime%=0
 70 DIM SP%(5):DIM ROCK%(300):REM SPEED & ROCKING CURVE
 80 DIM PNTR%(6):REM STEP NUMBER-POINTER
 90 DIM NUM%(8):REM INPUT FROM COUNTERS
100 DIM GAP% 300
110 FOR I%=0 TO 2 STEP 2
120 P%=GAP%
130 [ OPT I%
140 \***********************          Delay loop for routine to
150 .delay \DELAY PROGRAM              rotate stepper motor from
160 \***********************          the keyboard.
170 \
180 \ TWO'S COMPLEMENT OF LOOP COUNTER
190 CLC
200 LDA &80
210 EOR #&FF
220 ADC #01
230 STA &80
240 LDA &81
250 EOR #&FF
260 ADC #0
270 STA &81
280 \ SET TIMER TWO TO ONE SHOT MODE
290 LDA #&96
300 LDX #&6B
310 JSR &FFF4
320 TYA
330 AND #&DF
340 TAY
350 LDA #&97
360 LDX #&6B
370 JSR &FFF4
380 \ SET LOW ORDER TIMER COUNTER
390 LDX #&68
400 LDY #&5B
410 JSR &FFF4
420 .timer   \ LOAD HIGH ORDER COUNTER AND START TIMER(SET TO .1ms/STEP)
430 LDA #&97
440 LDY #3
450 LDX #&69
460 JSR &FFF4
470 .loop \TEST TIME OUT FLAG IN IFR
480 LDA #&96
490 LDX #&6D
500 JSR &FFF4
510 TYA
520 AND #&20
530 BEQ loop
540 \ TIMED OUT INCREMENT LOOP COUNTER
550 INC &80
560 BNE timer
570 INC &81
580 BNE timer
590 \ LOOP COUNTER =0 -END
600 RTS
610 \
620 \********************
630 \STEP MOTOR PROGRAM
640 \********************
650 \
660 .set LDA #&97 \SET DDRB -PB1,PB2 INPUTS
670 LDX #&62                           Set lines PB1 and
680 LDY #&F9                           PB2 of the User Port
690 JSR &FFF4                          as inputs for limit
700 RTS                                switch sensing.
710 .step
720 LDA #&97 \WRITE VALUE TO PORT      Write a number to the
730 LDX #&60                           User Port (transferred
740 JSR &FFF4                          from PROCclock or
750 LDA #&96 \READ VALUE FROM PORT     PROCanticl).
760 LDX #&60
770 JSR &FFF4                          Read status of limit
780 STY &8A \ PUT IN &8A               switches, store the
790 RTS                                number returned in
800 \                                  memory location &8A
810 \********************
820 \COUNTER PROGRAM                   Routine to control
830 \********************              the 32-bit counter
840 \
850 .start
860 LDY #1 \ D0 HIGH START COUNTING
870 LDA #&93                           Write to 1MHz Bus.
880 LDX #&C0 \ A0 LOW COUNTER ENABLED
890 JSR &FFF4
900 RTS
910 .stop
920 LDY #0                             D0 low, stop counting.
930 LDA #&93
940 LDX #&C0
950 JSR &FFF4
960 RTS
970 .read                              Read counter, chip to
980 LDA #&92                           read is defined in
990 JSR &FFF4                          PROCcount.
1000 STY &82 \ VALUE READ IN &82       Store number in memory
1010 RTS                               location &82.
1020 .clear
1030 LDA #&93                          A0 high, clear counters.
1040 LDX #&C1 \ A0 HIGH
1050 JSR &FFF4
1060 RTS                               End of assembly language
1070                                   section.
1080 NEXT
1090 REM SET PNTR%(1)TO PNTR%(6)
1100 PNTR%(1)=8:PNTR%(2)=24:PNTR%(3)=16:PNTR%(4)=48:PNTR%(5)=32:PNTR%(6)=40
1110 CALL set:LOC%=B%+1:PROCstop
1120 CLS                               The Array PNTR% contains
1130 VDU 23,1,0;0;0;0;                 the values of Y required
1140 PROCupdate                        to drive motor in 1/2
1150 PROCmenu                          step mode.
1160 END
1170 REM*****************************************
1180 REM
1190 REM CLOCKWISE STEP PROCEDURE      Routine to drive motor
1200 REM ************************      clockwise.
1210 DEF PROCclock
1220 IF STPNUM%=0 THEN 1270
1230 FOR Z%=1 TO STPNUM%:LOC%=LOC%+1:IF LOC%=7 THEN LOC%=1
1240 Y%=PNTR%(LOC%):CALL step:PSN%=PSN%+1:DUM%=?&8A-PNTR%(LOC%)
1250 IF DUM%=2 THEN PROCclimit         Read status of clockwise
1260 NEXT                              limit switch.
1270 ENDPROC
1280 REM
```

```
1290 REM ANTICLOCKWISE STEP PROCEDURE                Routine to drive motor
1300 REM ****************************                anticlockwise.
1310 DEF PROCanticl
1320 IF STPNUM%=0 THEN 1370
1330 FOR Z%=1 TO STPNUM%:LOC%=LOC%-1:IF LOC%=0 THEN LOC%=6
1340 Y%=PNTR%(LOC%):CALL step:PSN%=PSN%-1:DUM%=?&8A-PNTR%(LOC%)
1350 IF DUM%=4 THEN PROCalimit                       Read status of anti-
1360 NEXT                                            clockwise limit switch.
1370 ENDPROC
1380 REM
1390 REM COUNTING PROCEDURE
1400 REM ******************
1410 DEF PROCcount
1420 CALL clear                                      Clear the counters.
1430 CALL start                                      Start the counters.
1440 BBC%=TIME:REPEAT:UNTIL TIME-BBC%+CNTTM%         Delay loop.
1450 CALL stop                                       Stop the counters.
1460 FOR I%=0 TO 7
1470 X%=&C0+I%                                       Read from each chip
1480 CALL read:NUM%(I%)=?&82                         in turn.
1490 NEXT
1500 X1=NUM%(0)+256*NUM%(1)+65536*NUM%(2)+16777216*NUM%(3)
1510 X2=NUM%(4)+256*NUM%(5)+65536*NUM%(6)+16777216*NUM%(7)
1520 CNTSEC%=INT(X2*1E7/X1+0.5)                      Work out counts/sec.
1530 ENDPROC
1540 REM
1550 REM CLOCKWISE LIMIT PROCEDURE                   Routine to drive
1560 REM **************************                  motor off clockwise
1570 DEF PROCclimit                                  limit switch.
1580 STPNUM%=20:PROCanticl
1590 CLS:PRINT TAB(8,11);"CLOCKWISE LIMIT REACHED"
1600 PRINT TAB(8,12);"************************"
1610 VDU 28,0,24,39,23:CLS:PRINTTAB(7);"Press any key to continue"
1620 VVV%=GET:CLS:VDU 28,0,22,39,3
1630 PROCmenu
1640 ENDPROC
1650 REM
1660 REM ANTICLOCKWISE LIMIT PROCEDURE               Routine to drive motor
1670 REM *****************************               off anticlockwise
1680 DEF PROCalimit                                  limit switch.
1690 STPNUM%=20:PROCclock
1700 CLS:PRINT TAB(6,11);"ANTICLOCKWISE LIMIT REACHED"
1710 PRINT TAB(6,12);"*****************************"
1720 VDU 28,0,24,39,23:CLS:PRINTTAB(7);"Press any key to continue"
1730 WWW%=GET:CLS:VDU 28,0,22,39,3
1740 PROCmenu
1750 ENDPROC
1760 REM
1770 REM IMMEDIATE MOVEMENT OF ST.MOTOR              Drive motor from
1780 REM *******************************             cursor control keys.
1790 DEF PROCimmed
1800 *FX 4,1                                         Redefine cursor control
1810 CLS                                             keys.
1820 PRINT TAB(0,2);"SPEED 1-3(SLOW TO FAST) ? (4 TO END) "
1830 I=GET:I=I-48:IF I<1 OR I>4 THEN 1820
1840 IF I=4 THEN 1990
1850 CLS:VDU 28,20,1,39,0:PRINT TAB(12);"SPEED=";I:VDU 28,0,24,39,23
1860 PRINT "Press S.Bar to change speed,E/e to End":VDU 28,0,22,39,3
1870 SP%(1)=300:SP%(2)=50:SP%(3)=1
1880 VAR%=SP%(I):VAR0%=VAR% MOD 256:VAR1%=VAR% DIV 256
1890 *FX 12,1                                        Set auto-repeat period
1900 REPEAT                                          of keys to 1/100th sec.
1910 *FX 15,1                                        Flush keyboard buffers.
1920 MV%=GET
1930 IF MV%=137 THEN PROCdeclock                     Look to see which key
1940 IF MV%=136 THEN PROCdeanticl                    has been pressed.
1950 UNTIL MV%=32 OR MV%=&65 OR MV%=&45              Stop when space bar or
1960 IF MV%=&65 OR MV%=&45 THEN 1990                 E or e pressed.
1970 VDU 28,0,24,39,23:CLS:VDU 28,0,22,39,3
1980 GOTO 1820
1990 *FX 12,0                                        Reset auto repeat
2000 *FX 4,0                                         Reset Cursor keys.
2010 VDU 28,20,1,39,0:CLS:VDU 28,0,24,39,1:CLS
2020 PROCupdate
2030 ENDPROC
2040 REM
2050 REM CLOCKWISE MOVEMENT WITH DELAY               Movement of stepper
2060 REM *****************************               motor with delay loop
2070 DEF PROCdeclock                                 for PROCimmed.
2080 LOC%=LOC%+1:IF LOC%=7 THEN LOC%=1
2090 Y%=PNTR%(LOC%):CALL step:PSN%=PSN%+1:DUM%=?&8A-PNTR%(LOC%)
2100 PROCupdate
2110 IF DUM%=2 THEN PROCclimit
2120 IF VAR%=1 THEN 2140
2130 ?&80=VAR0%:?&81=VAR1%:CALL delay                Call assembly language
2140 ENDPROC                                         delay loop.
2150 REM
2160 REM ANTICLOCKWISE MOVEMENT WITH DELAY
2170 REM *********************************
2180 DEF PROCdeanticl
2190 LOC%=LOC%-1:IF LOC%=0 THEN LOC%=6
2200 Y%=PNTR%(LOC%):CALL step:PSN%=PSN%-1:DUM%=?&8A-PNTR%(LOC%)
2210 PROCupdate
2220 IF DUM%=4 THEN PROCalimit
2230 IF VAR%=1 THEN 2250
2240 ?&80=VAR0%:?&81=VAR1%:CALL delay
2250 ENDPROC
2260 REM
2270 REM ROCKING CURVE PROCEDURE                     Routine for single crystal
2280 REM ************************                    rocking curves.
2290 DEF PROCrock
2300 CLS:H%=0:V%=0
2310 INPUT TAB(0,2);"Anticlkws. Adjstmnt.(1000th deg.)";STPNUM%
2320 PROCanticl
2330 PROCupdate
2340 INPUT TAB(0,3);"Count Time (100th sec.)";CNTTM%
2350 INPUT "Step Length (1000th deg.)";STPNUM%
2360 INPUT "Total No. of Points";N%
2370 CLS:VDU 28,0,24,39,23:PRINT TAB(8);"Press S.bar to stop."
2380 VDU 28,0,22,39,3
2390 IROCK%=0
2400 REPEAT
2410 IROCK%=IROCK%+1
2420 PROCcount
2430 ROCK%(IROCK%)=CNTSEC%
2440 PRINT TAB(H%*10,V%);ROCK%(IROCK%)
2450 PROCtab
2460 SR%=INKEY(0)
2470 IF IROCK%=N% OR SR%=32 THEN 2500
2480 PROCclock
2490 PROCupdate
2500 UNTIL IROCK%=N% OR SR%=32
2510 N%=IROCK%
2520 VDU 28,0,24,39,23:CLS:VDU 28,0,22,39,3
2530 REM FIND MAXIMUM IN ARRAY
2540 IROCKMAX%=1:MAX%=ROCK%(1)
2550 FOR K%=2 TO N%
2560 IF MAX%>ROCK%(K%) THEN 2580
```

```
2570 MAX%=ROCK%(K%):IROCKMAX%=K%
2580 NEXT
2590 PSNMAX%=PSN%+STPNUM%*(IROCKMAX%-N%)
2600 REM FIND MINIMUM IN ARRAY
2610 IROCKMIN%=1:MIN%=ROCK%(1)
2620 FOR K%=2 TO N%
2630 IF MIN%<ROCK%(K%) THEN 2650
2640 MIN%=ROCK%(K%):IROCKMIN%=K%
2650 NEXT
2660 PSNMIN%=PSN%+STPNUM%*(IROCKMIN%-N%)
2670 MAXC%=MAX%-MIN%
2680 REM FIND 1ST POINT > HALF MAXIMUM
2690 HALF%=MAXC%/2
2700 K%=0
2710 REPEAT
2720 K%=K%+1
2730 UNTIL (ROCK%(K%)-MIN%)>HALF%
2740 HALFNO%=K%:HALFPNT%=ROCK%(K%)
2750 PSNHALF%=PSN%+STPNUM%*(HALFNO%-N%)
2760 REM FIND SLOPE BETWEEN HALFMAX AND MAX
2770 DTHETA%=PSNMAX%-PSNHALF%
2780 CLS:PRINT TAB(0,2);"Min' cnt= ";MIN%;" at Psn.= ";PSNMIN%
2790 PRINT TAB(0,4);"Max' cnt= ";MAX%;" at Psn.= ";PSNMAX%
2800 PRINT TAB(0,6);"\ width at \ max'(1000th Deg.) = ";DTHETA%
2810 PRINT TAB(0,8);"Save rocking curve on disk?(Y/N)":DD%=GET
2820 IF DD%=89 OR DD%=121 THEN PROCsave
2830 PRINT TAB(0,8);"                                "
2840 VDU 28,0,24,39,23:CLS
2850 PRINT "Press any key to continue."
2860 ABC%=GET
2870 CLS:VDU 28,0,22,39,3
2880 ENDPROC
2890 REM
2900 REM PROCEDURE TO MAINTAIN PEAK INTENSITY                ABAC Routine.
2910 REM ************************************
2920 DEF PROCpeak
2930 XYZ%=-1
2940 IF ANS%=56 THEN 2950 ELSE 2960
2950 IF XYZ%=89 OR XYZ%=121 THEN 2960 ELSE 2980
2960 CLS:INPUT"COUNT TIME (100th Sec) ";CNTTM%
2970 INPUT"STEP LENGTH (1000th Deg) ";STPNUM%
2980 VDU 28,0,24,39,23
2990 PRINT TAB(5);"Press space bar to stop."
3000 VDU 28,0,22,39,3
3010 IF ANS%=56 THEN 3030
3020 CLS
3030 H%=0:V%=8
3040 PROCcount
3050 SB%=INKEY(0)
3060 IF SB%=32 THEN 3440
3070 COUNT1%=CNTSEC%
3080 PRINT TAB(H%*10,V%);COUNT1%:PROCtab
3090 PROCmax(COUNT1%)
3100 IF COUNT1%<20 THEN 3040
3110 IF TIME>=inttime% AND ANS%=56 THEN 3490
3120 COUNTT%=COUNT1%:tot%=1
3130 COUNTL%=COUNT1%
3140 IF ANS%=56 THEN 3170
3150 PRINT TAB(10,4);"START TRAVERSE NOW"
3160 PRINT TAB(10,5);"******************"
3170 PROCaclkcount
3180 IF SB%=32 THEN 3440
3190 COUNT2%=CNTSEC%
3200 PRINT TAB(H%*10,V%);COUNT2%:PROCtab
3210 PROCavg(COUNT2%)
3220 IF TIME>=inttime% AND ANS%=56 THEN 3490
3230 IF COUNT2%<20 THEN PROCnocounts
3240 IF SB%=32 THEN 3440
3250 IF COUNT2%<=COUNTL% THEN 3290
3260 COUNTL%=COUNT2%
3270 IF COUNT2%>COUNTMAX% THEN PROCmax(COUNT2%)
3280 GOTO 3170
3290 COUNTL%=COUNT2%
3300 PROCclkcount
3310 IF SB%=32 THEN 3440
3320 COUNT3%=CNTSEC%
3330 PRINT TAB(H%*10,V%);COUNT3%:PROCtab
3340 PROCavg(COUNT3%)
3350 IF TIME>=inttime% AND ANS%=56 THEN 3490
3360 IF COUNT3%<20 THEN PROCnocounts
3370 IF SB%=32 THEN 3440
3380 IF COUNT3%>COUNTL% THEN 3410
3390 COUNTL%=COUNT3%
3400 GOTO 3170
3410 IF COUNT3%>COUNTMAX% THEN PROCmax(COUNT3%)
3420 COUNTL%=COUNT3%
3430 GOTO 3300
3440 VDU 28,0,24,39,23:CLS
3450 IF ANS%=56 THEN 3490
3460 PRINT TAB(10);"Continue Y/N ? "
3470 XYZ%=GET
3480 IF XYZ%=89 OR XYZ%=121 THEN 2940
3490 VDU 28,16,2,39,0:CLS:VDU 28,0,24,39,23:CLS
3500 VDU 28,0,2,15,1:CLS:VDU 28,0,22,39,3
3510 ENDPROC
3520 REM
3530 REM PROCEDURE TO UPDATE POSITION        Display current position
3540 REM ****************************        of stepper motor on screen
3550 DEF PROCupdate
3560 VDU 28,0,1,15,0
3570 PRINT "Position="
3580 PRINT TAB(9,0);"      "
3590 PRINT TAB(9,0);PSN%
3600 VDU 28,0,22,39,3
3610 ENDPROC
3620 REM
3630 REM PROC' TO PRINT TABS                 Print tabs to display
3640 REM ********************                counts in rows of four.
3650 DEF PROCtab
3660 H%=H%+1:IF H%=4 THEN 3670 ELSE 3680     H%=Horizontal pointer
3670 H%=0:V%=V%+2                            V%=Vertical poi nter
3680 IF V%<19 THEN 3710                      Once screen is full,
3690 V%=18                                   new values are added
3700 VDU 10,10                               to bottom line.
3710 ENDPROC
3720 REM
3730 REM MENU PROCEDURE
3740 REM ***************
3750 DEF PROCmenu
3760 REPEAT
3770 CLS
3780 PRINT TAB(0,0);"1. RESET POSITION COUNTER."
3790 PRINT TAB(0,2);"2. ADJUST THETA VIA CURSOR CNTL. KEYS."
3800 PRINT TAB(0,4);"3. ROCKING CURVE OF SAMPLE."
3810 PRINT TAB(0,6);"4. A.B.A.C. "
3820 PRINT TAB(0,8);"5. DISENGAGE S.MOTOR."
3830 PRINT TAB(0,10);"6. DISPLAY/PLOT ROCKING CURVE."
3840 PRINT TAB(0,12);"7. COUNT ONLY."
```

```
3850 PRINT TAB(0,14);"8. STEP SCANNING SECTION TOPOGRAPH."
3860 PRINT TAB(0,16);"9. ADJUST THETA AND COUNT."
3870 PRINT TAB(0,18);"Enter desired No.(Space Bar to End)."
3880 *FX15,0
3890 ANS%=GET
3900 IF ANS%=49 THEN PSN%=0
3910 IF ANS%=50 THEN PROCimmed
3920 IF ANS%=51 THEN PROCrock
3930 IF ANS%=52 THEN PROCabac
3940 IF ANS%=53 THEN PROCdiseng
3950 IF ANS%=54 THEN PROCplot
3960 IF ANS%=55 THEN PROCconcount
3970 IF ANS%=56 THEN PROCstepscan
3980 IF ANS%=57 THEN PROCcountmove
3990 PROCupdate
4000 UNTIL ANS%=32                                  Exit program when space-
4010 A%=PSN%:B%=LOC%-1:C%=DTHETA%:D%=MIN%           bar is pressed.
4020 VDU 23,1,1;0;0;0;                              Turn cursor on
4030 ENDPROC
4040 REM
4050 REM ABAC PROCEDURE                             Set up procedure for
4060 REM ***************                            ABAC routine.
4070 DEF PROCabac
4080 CLS
4090 VDU 28,0,3,39,1
4100 PRINT TAB(6);"Set on peak of rocking curve"
4110 PRINT TAB(6);"****************************"
4120 VDU 28,0,22,39,3
4130 *FX15,0
4140 PRINT TAB(0,6);"Adjustment of theta by:"
4150 PRINT TAB(10,8);"M: Manual control."
4160 PRINT TAB(10,10);"C: Cursor control keys."
4170 PRINT TAB(10,12);"N: No adjustment."
4180 ANS5%=GET
4190 IF ANS5%=77 OR ANS5%=109 THEN 4200 ELSE 4210
4200 FLAG%=1:QW%=89:CNTTM%=50:PROCconcount:GOTO 4240
4210 IF ANS5%=67 OR ANS5%=99 THEN PROCcountmove:GOTO 4240
4220 IF ANS5%=78 OR ANS5%=110 THEN 4240ELSE 4080
4230 IF ANS%=56 THEN 4240
4240 VDU 28,0,3,39,1:CLS:VDU 28,0,22,39,3
4250 IF ANS%=56 THEN ENDPROC ELSE PROCpeak
4260 ENDPROC
4270 REM
4280 REM PROC' TO DISENGAGE S. MOTOR
4290 REM ***************************
4300 DEF PROCdiseng
4310 CLS:PRINT TAB(0,6);"Stepper motor disengaged."
4320 PRINT TAB(0,7);"**************************"
4330 Y%=0:CALL step                                 Write 0 to stepper motor
4340 VDU 28,0,24,39,23:PRINT "Press any key to re-engage."
4350 GG%=GET:Y%=PNTR%(LOC%):CALL step               Re-energise previously
4360 CLS:VDU 28,0,22,39,3                           active phases.
4370 ENDPROC
4380 REM
4390 REM PROCEDURE TO SAVE ROCKING CURVE ON DISK
4400 REM ***************************************
4410 DEF PROCsave
4420 CLS:INPUT "ENTER DRIVE NUMBER";DR$
4430 OSCLI("DRIVE "+DR$)
4440 INPUT '"FILENAME = ";FIN$
4450 INPUT '"COMMENT ";COM$
4460 INPUT '"DATE ";DATE$
4470 PRINT"ARE THESE CORRECT ?"
4480 GFG%=GET
4490 IF GFG%=78 OR GFG%=110 THEN 4440
4500 R%=OPENOUT FIN$
4510 PRINT#R%,COM$,DATE$,MAXC%,DTHETA%,N%,STPNUM%
4520 FOR FF%=1 TO N%
4530 PRINT#R%,ROCK%(FF%)-MIN%
4540 NEXT
4550 CLOSE#R%
4560 *DRIVE 0
4570 ENDPROC
4580 REM
4590 REM PROCEDURE TO CHAIN "PLOT"                  Load and run plotting
4600 REM **************************                 program, kept as a seperat
4610 DEF PROCplot                                   program because of lack of
4620 C%=DTHETA%:D%=MIN%                             memory in graphics mode.
4630 A%=PSN%:B%=LOC%-1
4640 CHAIN"P.PLOT"
4650 ENDPROC
4660 REM
4670 REM PROCEDURE FOR CONTINUOUS COUNTING          Count and display values
4680 REM **********************************         continuously on screen.
4690 DEF PROCconcount
4700 IF FLAG%=1 THEN 4750
4710 IF ANS%=56 THEN PROCdispexpno ELSE 4730        For step scanning routine.
4720 GOTO 4810
4730 CLS:PRINT TAB(5,5);"Disengage stepper motor(Y/N)?"
4740 QW%=GET
4750 exptime%=0
4760 IF QW%=78 OR QW%=110 THEN 4800
4770 VDU 28,0,3,39,2:PRINT TAB(6);"**Stepper motor disengaged**":VDU 28,0,22
4780 Y%=0:CALL step
4790 IF FLAG%=1 THEN 4810
4800 CLS:INPUT TAB(5,10);"COUNT TIME (100th's sec.) = ";CNTTM%
4810 FLAG%=0:H%=0:V%=0
4820 VDU 28,16,1,39,0:PRINT "COUNT TIME = ";CNTTM%:VDU 28,0,22,39,3
4830 VDU 28,0,24,39,23:CLS
4840 PRINT TAB(5);"Press space bar to stop."
4850 VDU 28,0,22,39,3
4860 CLS
4870 COUNTT%=0:tot%=0
4880 REPEAT
4890 ST%=INKEY(0)
4900 PROCcount
4910 PRINT TAB(H%*10,V%);CNTSEC%:PROCtab
4920 IF ANS%=56 THEN PROCdispexptm
4930 IF ANS%=56 AND TIME>=exptime% THEN ST%=43210
4940 UNTIL ST%=32 OR ST%=43210:REM 43210 HAS NO NUMERICAL SIGNIFICANCE
4950 VDU 28,16,1,39,0:CLS:VDU 28,0,22,39,3
4960 VDU 28,0,24,39,23:CLS
4970 IF ANS%=56 THEN 5000
4980 PRINT TAB(10);"REPEAT (Y/N)?":TT%=GET
4990 IF TT%=89 OR TT%=121 THEN 4800
5000 CLS:VDU 28,0,22,39,3
5010 Y%=PNTR%(LOC%):CALL step
5020 VDU 28,0,3,39,2:CLS:VDU 28,0,2,15,1:CLS:VDU 28,0,22,39,3
5030 ENDPROC
5040 REM
5050 REM DISPLAY AVG. COUNT                         Display average of
5060 REM ********************                       last five counts.
5070 DEF PROCavg(count%)
5080 COUNTT%=COUNTT%+count%
5090 tot%=tot%+1
5100 IF tot%<5 THEN 5150
5110 tot%=0
5120 VDU 28,16,2,39,1:PRINT "Avg.Cnt. = ";INT(COUNTT%/5);"        "
```

```
5130 VDU 28,0,22,39,3
5140 COUNTT%=0
5150 ENDPROC
5160 REM
5170 REM DISPLAY MAX' COUNT                          Display maximum count
5180 REM ******************                          so far.
5190 DEF PROCmax(Q%)
5200 COUNTMAX%=Q%
5210 VDU 28,16,1,39,0:PRINT "Max.Cnt. = ";Q%;"       ":VDU 28,0,22,39,3
5220 ENDPROC
5230REM
5240REM DISPLAY AVG. POSITION                        Display average of
5250REM **********************                       last ten angular
5260DEF PROCavgp(psn%)                               positions.
5270 PSNT%=PSNT%+psn%
5280 tot1%=tot1%+1
5290 IF tot1%<10 THEN 5360
5300 tot1%=0
5310 @%=&20105
5320 VDU 28,0,2,15,1:CLS:PRINT "Avg.Psn =";INT(PSNT%*10+.5)/100
5330 @%=10
5340 VDU 28,0,22,39,3
5350 PSNT%=0
5360 ENDPROC
5370 REM
5380 REM STEP SCANNING PROCEDURE
5390 REM ************************
5400 DEF PROCstepscan
5410 expno1%=1
5420 PROCsetupscan
5430 CLS:PRINTTAB(8,0);"Step scanning routine"       Set up parameters
5440 PRINTTAB(8,1);"**********************"         for routine.
5450 VDU 23,1,1;0;0;0;
5460 INPUTTAB(0,3);"Stepsize(mm) between exposures";STPSIZE:inttime1%=INT(26
5470  PRINTTAB(0,5);"Exposure per point :"
5480 INPUTTAB(0,6);"Hours   :";hours
5490 INPUTTAB(0,7);"Minutes :";mins
5500 exptime%=INT(360000*hours+6000*mins+.5)
5510 INPUTTAB(0,9);"No of exposures ";expno%
5520 INPUTTAB(0,11);"Count time for ABAC (100th Sec) ";CNTTM1%
5530 INPUTTAB(0,13);"Step size for ABAC (1000th Deg) ";STPNUM1%
5540 VDU 23,1,0;0;0;0;
5550 PRINTTAB(0,18);"Are these correct (Y/N) ?"
5560 DDT%=GET
5570 IF DDT%=89 OR DDT%=121 THEN 5580 ELSE 5430
5580 CLS:PRINTTAB(0,10);"Mount plate on holder,then"
5590 PRINTTAB(0,12);"press any key to continue."
5600 IGG%=GET
5610 PROCsettle                                      Use ABAC routine to
5620 IF SB%=32 THEN 5860                             find peak.
5630 PROCexpose
5640 IF ST%=32 THEN 5860
5650 IF expno%=1 THEN 5790
5660 FOR expno1%=2 TO expno%                         Repeat for number
5670 TIME=0                                          of exposures.
5680 PROCstart                                       Start traverse.
5690 STPNUM%=STPNUM1%:CNTTM%=CNTTM1%:inttime%=inttime1%
5700 PRINTTAB(5,6);"Traversing by ";STPSIZE;" mm."
5710 PROCpeak                                        ABAC during traverse.
5720 PROCstop                                        Stop traverse.
5730 IF SB%=32 THEN 5860
5740 PROCsettle
5750 IF SB%=32 THEN 5860
5760 PROCexpose                                      Hold on peak during
5770 IF ST%=32 THEN 5860                             exposure.
5780 NEXT
5790 PRINTTAB(0,10);"EXPOSURE FINISHED-CLOSE THE SHUTTER"
5800 PRINTTAB(0,11);"************************************"
5810 VDU 28,0,24,39,23
5820 PRINTTAB(3);"PRESS THE SPACE BAR TO CONTINUE"
5830 REPEAT:UNTIL INKEY(-99):CLS
5840 *FX15,0
5850 VDU 28,0,22,39,3
5860REM
5870 ENDPROC
5880 REM
5890 REM INTRO FOR STEP SCAN ROUTINE
5900 REM ****************************
5910 DEFPROCsetupscan
5920 CLS:PRINTTAB(8,0);"Step Scanning Routine"
5930 PRINTTAB(8,1);"**********************"
5940 PRINTTAB(0,3);"Before proceeding,drive traverse table "
5950 PRINTTAB(0,5);"to one extreme of the desired traverse."
5960 PRINTTAB(0,7);"Then press space bar to continue."
5970 REPEAT:UNTIL INKEY(-99)
5980 CLS:PROCabac
5990 ENDPROC
6000 REM
6010 REM START TRAVERSE
6020 REM ***************
6030 DEFPROCstart
6040 Y%=PNTR%(LOC%)+64:CALL step                     Send PB6 High.
6050 Y%=PNTR%(LOC%):CALL step                        Send PB6 low.
6060 ENDPROC
6070 REM
6080 REM STOP TRAVERSE
6090 REM **************
6100 DEFPROCstop
6110 Y%=PNTR%(LOC%)+128:CALL step                    Send PB7 high.
6120 Y%=PNTR%(LOC%):CALL step                        Send PB7 low.
6130 ENDPROC
6140 REM
6150 REM LET ABAC SETTLE IN STEP SCAN                Use ABAC routine to
6160 REM ****************************                make sure that you are
6170 DEFPROCsettle                                   on the peak of the
6180 CLS:PRINTTAB(5,4);"LETTING ABAC SETTLE"         rocking curve.
6190 PRINTTAB(5,5);"********************"
6200 STPNUM%=2:CNTTM%=200:inttime%=6000              Stepsize 2/1000th deg.,
6210 TIME=0:PROCpeak                                 counttime 2 sec for 1 min
6220 IF SB%=32 THEN ENDPROC
6230 CLS:PRINTTAB(5,4);"LETTING ABAC SETTLE"
6240 PRINTTAB(5,5);"********************"
6250 STPNUM%=1:CNTTM%=200:inttime%=6000              Stepsize 1/1000th deg.,
6260 TIME=0:PROCpeak                                 countime 2sec for 1 min.
6270 VDU 28,16,2,39,0:CLS:VDU 28,0,24,39,23:CLS
6280 VDU 28,0,2,15,1:CLS:VDU 28,0,22,39,3
6290 ENDPROC
6300 REM
6310 REM GIVE A DELAY (FOR EXPOSURE)
6320 REM ****************************
6330 DEFPROCexpose
6340 CNTTM%=100:TIME=0:PROCconcount
6350 CLS:VDU 28,0,22,39,3
6360 ENDPROC
6370 REM
6380 REM DISPLAY EXPOSURE TIME                       Display remaining time
6390 REM **********************                      of exposure.
6400 DEF PROCdispexptm
```

```
6410 secslft%=exptime%-TIME+6000
6420 hrslft%=secslft% DIV 360000
6430 minslft%=(secslft% MOD 360000) DIV 6000
6440 VDU28,0,3,39,2:PRINT;"Exposing for ";hrslft%  ;" Hours and ";minslft%;"
6450 VDU 28,0,22,39,3
6460 ENDPROC
6470 REM
6480 REM DISPLAY EXPOSURE NUMBER
6490 REM ************************
6500 DEFPROCdispexpno
6510 VDU 28,0,2,15,1
6520 PRINT;"Exposure no:";expno1%
6530 VDU 28,0,22,39,3
6540 ENDPROC
6550 REM
6560 REM COUNT AND MOVE A-CLOCKWISE PROCEDURE       Count and move motor
6570 REM ************************************       from cursor control keys.
6580 DEFPROCaclkcount
6590 CALL clear
6600 CALL start
6610 BBC%=TIME
6620 PROCanticl
6630 PROCupdate
6640 PROCavgp(PSN%)
6650 SB%=INKEY(0)
6660 REPEAT:UNTIL TIME >= BBC%+CNTTM%
6670 CALL stop
6680 FOR I%=0 TO 7
6690 X%=&C0+I%
6700 CALL read:NUM%(I%)=?&82
6710 NEXT
6720 X1=NUM%(0)+256*NUM%(1)+65536*NUM%(2)+16777216*NUM%(3)
6730 X2=NUM%(4)+256*NUM%(5)+65536*NUM%(6)+16777216*NUM%(7)
6740 CNTSEC%=INT(X2*1E7/X1+0.5)
6750 ENDPROC
6760 REM
6770 REM COUNT AND MOVE CLOCKWISE PROCEDURE
6780 REM ************************************
6790 DEFPROCclkcount
6800 CALL clear
6810 CALL start
6820 BBC%=TIME
6830 PROCclock
6840 PROCupdate
6850 PROCavgp(PSN%)
6860 SB%=INKEY(0)
6870 REPEAT:UNTIL TIME >= BBC%+CNTTM%
6880 CALL stop
6890 FOR I%=0 TO 7
6900 X%=&C0+I%
6910 CALL read:NUM%(I%)=?&82
6920 NEXT
6930 X1=NUM%(0)+256*NUM%(1)+65536*NUM%(2)+16777216*NUM%(3)
6940 X2=NUM%(4)+256*NUM%(5)+65536*NUM%(6)+16777216*NUM%(7)
6950 CNTSEC%=INT(X2*1E7/X1+0.5)
6960 ENDPROC
6970 REM
6980 REM NO COUNTS PROCEDURE                        Routine to stop
6990 REM ********************                       movement of motors
7000 DEFPROCnocounts                                when counts drop to
7010 PROCcount                                      less than 20Hz-displaying
7020 SB%=INKEY(0)                                   counts on screen.
7030 PRINTTAB(H%*10,V%);CNTSEC%:PROCtab
7040 PROCavg(CNTSEC%)
7050 IF CNTSEC%>20 OR SB%=32 THEN ENDPROC ELSE 7010
7060 ENDPROC
7070 REM
7080 REM MOVE WITH C.CNTRL KEYS AND COUNT
7090 REM ********************************
7100 DEF PROCcountmove
7110 CLS:INPUT TAB(10,3);"Count time";CNTTM%
7120 INPUT TAB(10,5);"Step size";STPNUM%
7130 *FX 4,1
7140 CLS:VDU 28,0,24,39,23
7150 PRINTTAB(5);"Press space bar to stop":VDU 28,0,22,39,3
7160 *FX 12,1
7170 COUNTMAX%=0
7180 H%=0:V%=8
7190 REPEAT
7200 MV%=INKEY(0)
7210 *FX15,1
7220 IF MV%=137 THEN PROCclock ELSE 7240
7230 PROCupdate
7240 IF MV%=136 THEN PROCanticl ELSE 7260
7250 PROCupdate
7260 PROCcount
7270 PRINTTAB(H%*10,V%);CNTSEC%:PROCtab
7280 IF CNTSEC%>COUNTMAX% THEN PROCmax(CNTSEC%)
7290 UNTIL MV%=32
7300  CLS:VDU 28,0,24,39,23:CLS:VDU 28,16,1,39,0:CLS:VDU 28,0,22,39,3
7310 *FX 12,0
7320 *FX 4,0
7330 ENDPROC
```

Appendix B

Tables of ξ_g and P_2

B.1 Introduction

This appendix contains tables of extinction distances, ξ_g and penetration depths, P_2 for a variety of reflections and a continuous range of wavelengths. The tables are calculated using equations 5.2 and 5.4 using the values of f_a and μ contained in [1].

Crystal Type : Si

Surface h,k,l : 1 1 1

Reflection h,k,l : 1 1 5

Angle between surface and reflecting plane : 38.94 Degrees

Wavelength (Angstroms)	Angle of Incidence,(Deg's)	Bragg Angle (Deg's)	Extinction Distance,(Microns)	Penetration Depth,(Microns)
1.35	1.30	40.24	5.40	2.30
1.40	3.12	42.06	8.10	4.82
1.45	4.99	43.93	9.91	6.76
1.50	6.92	45.86	11.30	8.25
1.55	8.93	47.87	12.43	9.37
1.60	11.02	49.96	13.37	10.21
1.65	13.20	52.14	14.17	10.82
1.70	15.49	54.43	14.86	11.26
1.75	17.92	56.86	15.47	11.55
1.80	20.52	59.46	16.01	11.74
1.85	23.33	62.27	16.48	11.88
1.90	26.44	65.38	16.91	11.81
1.95	29.97	68.91	17.30	11.83
2.00	34.18	73.12	17.65	11.74
2.05	39.83	78.77	17.97	11.65

Crystal Type : Si

Surface h,k,l : 1 1 1

Reflection h,k,l : 2 2 0

Angle between surface and reflecting plane : 35.26000001 Degrees

Wavelength (Angstroms)	Angle of Incidence,(Deg's)	Bragg Angle (Deg's)	Extinction Distance,(Microns)	Penetration Depth,(Microns)
2.25	0.61	35.87	1.14	0.25
2.30	1.54	36.80	1.78	0.59
2.35	2.48	37.74	2.21	0.88
2.40	3.43	38.69	2.56	1.12
2.45	4.39	39.65	2.84	1.34
2.50	5.37	40.63	3.08	1.52
2.55	6.36	41.62	3.29	1.67
2.60	7.36	42.62	3.48	1.80
2.65	8.38	43.64	3.65	1.92
2.70	9.42	44.68	3.80	2.01
2.75	10.48	45.74	3.94	2.09
2.80	11.56	46.82	4.07	
2.85	12.66	47.92	4.19	
2.90	13.79	49.05	4.30	
2.95	14.94	50.20	4.40	
3.00	16.12	51.38	4.49	
3.05	17.33	52.59	4.58	
3.10	18.58	53.84	4.66	
3.15	19.86	55.12	4.73	
3.20	21.19	56.45	4.81	
3.25	22.57	57.83	4.87	
3.30	24.00	59.26	4.94	
3.35	25.49	60.75	5.00	
3.40	27.05	62.31	5.05	
3.45	28.71	63.97	5.11	
3.50	30.46	65.72	5.16	
3.55	32.34	67.60	5.20	
3.60	34.39	69.65	5.25	
3.65	36.66	71.92	5.29	
3.70	39.24	74.50	5.34	
3.75	42.34	77.60	5.37	
3.80	46.51	81.77	5.41	

Crystal Type : Si

Surface h,k,l : 1 1 1

Reflection h,k,l : 2 2 4

Angle between surface and reflecting plane : 19.47 Degrees

Wavelength (Angstroms)	Angle of Incidence,(Deg's)	Bragg Angle (Deg's)	Extinction Distance,(Microns)	Penetration Depth,(Microns)
0.75	0.30	19.77	2.57	3.02
0.80	1.68	21.15	5.75	13.35
0.85	3.08	22.55	7.41	19.76
0.90	4.48	23.95	8.56	23.74
0.95	5.91	25.38	9.42	25.88
1.00	7.34	26.81	10.10	26.97
1.05	8.80	28.27	10.65	27.37
1.10	10.28	29.75	11.11	27.21
1.15	11.78	31.25	11.49	26.79
1.20	13.30	32.77	11.81	26.13
1.25	14.85	34.32	12.09	25.32
1.30	16.43	35.90	12.34	24.44
1.35	18.05	37.52	12.55	23.53
1.40	19.69	39.16	12.74	22.61
1.45	21.38	40.85	12.90	21.72
1.50	23.11	42.58	13.05	20.85
1.55	24.89	44.36	13.18	19.98
1.60	26.73	46.20	13.30	19.16
1.65	28.63	48.10	13.41	18.37
1.70	30.60	50.07	13.50	17.62
1.75	32.66	52.13	13.59	16.91
1.80	34.82	54.29	13.67	16.24
1.85	37.10	56.57	13.75	15.67
1.90	39.52	58.99	13.81	14.93
1.95	42.13	61.60	13.88	14.42
2.00	44.98	64.45	13.93	13.87
2.05	48.16	67.63	13.99	13.38
2.10	51.85	71.32	14.04	12.86
2.15	56.43	75.90	14.08	12.41
2.20	63.47	82.94	14.12	11.94

Crystal Type : Si

Surface h,k,l : 0 0 1

Reflection h,k,l : 2 2 4

Angle between surface and reflecting plane : 35.26000001 Degrees

Wavelength (Angstroms)	Angle of Incidence,(Deg's)	Bragg Angle (Deg's)	Extinction Distance,(Microns)	Penetration Depth,(Microns)
1.30	0.64	35.90	2.64	1.29
1.35	2.26	37.52	4.77	3.93
1.40	3.90	39.16	6.08	5.95
1.45	5.59	40.85	7.05	7.49
1.50	7.32	42.58	7.82	8.65
1.55	9.10	44.36	8.46	9.50
1.60	10.94	46.20	9.00	10.13
1.65	12.84	48.10	9.47	10.57
1.70	14.81	50.07	9.87	10.87
1.75	16.87	52.13	10.23	11.05
1.80	19.03	54.29	10.54	11.15
1.85	21.31	56.57	10.83	11.22
1.90	23.73	58.99	11.08	11.10
1.95	26.34	61.60	11.31	11.07
2.00	29.19	64.45	11.52	10.95
2.05	32.37	67.63	11.71	10.84
2.10	36.06	71.32	11.89	10.66
2.15	40.64	75.90	12.05	10.49
2.20	47.68	82.94	12.20	10.28